The BABAR Level 1 Electromagnetic Calorimeter Trigger & a Measurement of the Branching Ratio of $B^0 \rightarrow J/\Psi K^0_s$

By

David Charles Hamilton Wallom

H.H. Wills Physics Laboratory, University of Bristol

A dissertation submitted to the University of Bristol in accordance with the requirements for the degree of Doctor of Philosophy in the Faculty of Science

Abstract

During the last year the *BABAR* detector at SLAC has been collecting data to try to further our fundamental understanding of the universe very shortly after the big bang. The design requirements for the experiment were understandably tight and to this end a very high performance calorimeter trigger was required. The design for the system used the inputs from 280 segments or towers within the calorimeter to provide input. The basic operation of the trigger uses sums of these towers operating over the whole θ strip to provide an energy sum that is compared against a set of thresholds. As well as these energy dependent triggers 2 positional triggers exist, one for the forward endcap of the calorimeter and the other for the rear of the barrel. The rear positional trigger is primarily used for Bhabha event selection whilst the forward trigger can be used for background rejection. The trigger has now been operating successfully for the entire Run-1 period.

To perform a measurement on *CP* violation within the neutral B meson system the $\mathrm{B}^0 \rightarrow \mathrm{J}/\Psi \mathrm{K}^0_s$ decay channel is most important. The K^0_s daughter can decay either through a pair of oppositely charged π or through a pair of π^0's. As a further check on the behaviour of the calorimeter system and as a cross-check for results given at ICHEP 2000 in Osaka and recent papers submitted for publication by the collaboration a measurement of the branching ratio of $\mathrm{B}^0 \rightarrow \mathrm{J}/\Psi \mathrm{K}^0_s$, with the K^0_s decaying through the π^0 mode is made. This is then corrected to provide the overall $\mathrm{B}^0 \rightarrow \mathrm{J}/\Psi \mathrm{K}^0_s$ measurement.
The final measurement used 58.15 fully reconstructed B mesons giving:

$$\frac{B^0 \rightarrow J/\Psi K^0_s}{B^0 \rightarrow X} = 8.65 \pm 0.6(Stat)^{+0.48}_{-0.99}(Sys) \times 10^{-4} \quad (1)$$

AUTHOR'S DECLARATION

I declare that the work in the dissertation was carried out in accordance with the Regulations of the University of Bristol. The work is original except where indicated by special reference in the text and no part of the dissertation has been submitted for any other degree.

Any views expressed in the dissertation are those of the author and in no way represent those of the University of Bristol.

The dissertation has not been presented to any other University for examination either in the United Kingdom or overseas.

SIGNED: DATE:

Acknowledgements

I would like to take this opportunity to thank the many people that have helped in the completion of this thesis. Not least my family for their unswerving support throughout my education. My father in particular has been a constant figure to look up to throughout the 26 years of my existence.

During my work on the trigger I found a source of constant ideas and encouragement from Paul Dauncey, a person who was always ready to give that little bit of extra help and advice when needed most. Also Jason Mcfall was always available to give that little bit of help and also a few rather nice meals!

I'd also like to thank the Dataflow group, Mike Huffer, Rowan Hamilton, Chris O'Grady and Iain Scott, not only for an awful lot of help just after I'd arrived at SLAC with a lot of electronics and a VME crate, but also those tricky C++ problems that you can easily get into with realtime programming.

When working with the Neutral Analysis Working group I found a very dedicated group of people that were a source of constant help when needed most and in particular Christos Touramanis and David Payne, without whom my work would have wandered off into many a blind alley.

Back in Bristol, the absolute best backup for my physics analysis was given by Nicolo De Groot, as well as some gentle (and not so gentle) encouragement on when I should be submitting my thesis.

During my stay in California I met many really cool people, not the least of which are Mickey, Jamie, Nicole, Marjan, Iain and Eve. All of whom contributed to one of the best eighteen months in my life, including some very memorable nights out all over the Bay Area.

During the winters that I was out at SLAC everyone from the little community there will remember my near constant wish every Friday night to go and visit the mountains and the massive amounts of snow that they have. Many thanks are due to Fergus Wilson, Jon Fullwood and Phil Clark for keeping me company on many of these trips, plus as well as Paul Gravener who really didn't know what had hit him after an 11 hour flight to San Fransisco only to be greeted by a maniac dragging him straight up to Tahoe before the jet lag had even had a chance to appear!

Since returning to the UK to finish my thesis I can only really mention one person, the best girl in the world, Kerri Winship who didn't mind many a really interesting evening watching me bang away on the keyboard trying to shape the motley collection of notes and books into something that might be reasonably called a thesis.

Contents

List of Figures

List of Tables

Chapter 1

Introduction

With the LEP detectors at CERN now being removed in preparation for the LHC and its experiments and the Fermilab detectors currently under upgrade this has been deemed by history to be the time for the smaller experiments to push forward our boundaries of knowledge. Two experiments that stand out are *BABAR* at the Stanford Linear Accelerator Center in California and BELLE at the KEKB accelerator in Japan. Both detectors are situated at asymmetric colliders, with the electrons and positrons having different energies. This induces a boost to the centre of mass system. A direct result of this is any differences between the B and $\bar{B}$ lifetimes can be measured using the now measurable decay lengths.

During the immediate aftermath of the Big Bang the sea of particles created contained equal proportions of matter and anti-matter. Within a very short period though this must have grown to be a large difference. The universe as we know it now has virtually no anti-matter naturally present and this invites us to ask the question: "Where did the anti-matter go?" According to the early standard model, *CP* symmetry was a given. In 1964 it was found by Christensen, Cronin, Fitch and Turlay that within the Kaon system the decay $K_L \rightarrow \pi\pi$ was actually *CP* violating and as such could not be currently explained. It was later shown that this effect would also be seen in the neutral B-meson system.

The *BABAR* detector in combination with PEP-II is a factory design. B-mesons are created in unprecedented numbers. It is required that the detector runs at a very high efficiency. To this end the design criteria for all components involved in the running of *BABAR* were very tight. The overall construction of the *BABAR* detector is described with current performance comparisons with design values as described in the Final Design Report[1].

The University of Bristol's involvement on a hardware level was as one of the prime partners in the design, construction and operation of the Level 1 Electromagnetic Calorimeter Trigger along with the Rutherford Appleton Laboratory (RAL), Royal Holloway and Bedford New College and Imperial College. This involved the initial design studies progressing through prototyping the electronic boards designed both at Bristol and the Rutherford Appleton Laboratory and then onto final testing and commissioning out at SLAC. It was necessary to provide expert coverage of the system especially throughout the first few months of operation so that all caveats of operation could be studied and, if they were to turn into problems, fixed.

For the investigation of *CP* Violation in the B meson system the so called golden channel is $B^0 \rightarrow J/\Psi K^0_s$. The K^0_s decays through either $\pi^+\pi^-$or a pair of π^0's. Since the branching ratio for the charged mode is larger and the charged pions easier to detect with high efficiency and purity, this was the channel of choice by *BABAR* to provide preliminary results.

Due to my involvement with the Calorimeter group I decided to further investigate the neutral mode. As validation analyses the lifetime of the K^0_s and the branching ratio for $B^0 \rightarrow J/\Psi K^0_s$, $K^0_s \rightarrow \pi^0\pi^0$are measured. A comparison of systematics applicable for both channels will also be made.

Initially upon starting my PhD I was required to learn C++ so as to write online and test code for the EMT system. This was initially to test the preproduction boards both at Bristol and RAL so as to complete the final design process for the system. After completing of this then the production phase could begin and I moved to SLAC. Whilst there I was initially to complete the final integration of the online code with the Dataflow hardware and software.

After completion of the first pair of production trigger processor boards these were flown to SLAC so as to complete testing. At this point I was asked to head the on-site effort for the EMT in particular liaison with the trigger management and subsystem online groups. My responsibility extended to all parts of the system including hardware, software and monitoring code whilst other more senior members of the team were back in the UK.

As *BABAR* moved toward first event taking it became necessary for the online system experts from each subsystem to familiarise themselves with the entire experiments online and Run Control systems. This meant that during the initial cosmic ray testing

phase of the detector commissioning we were all required to work as Data Acquisition System experts.

Once the detector had been rolled onto the beamline and initial commissioning of PEP-II had started then the eight DAQ experts were required to cover twenty four hours per day, seven days per week. During this period I was also one of two EMT experts that were required to provide 24 hour on-call cover for the system. This continued until a member of Bristol University staff arrived and then the next year's student, so that I could reduce my trigger responsibilities and start to concentrate on analysis.

At this point Bristol had not chosen a physics analysis channel and so I chose to work with the Neutral Analysis working group due to the relevance to the calorimeter and EMT systems. Initially this consisted of checking the behaviour of the Geometric and Kinematic fitter when applied to a neutral particle with neutral daughters. This then continued with the charmonium working group using what I had already learnt of the behaviour of K^0_s to the neutral K^0_s decay channel of the $B^0 \rightarrow J/\Psi K^0_s$ decay mode.

Chapter 2

CP Violation and mixing in the B Meson System

2.1 Introduction

This chapter is an introduction to the basic physics of *BABAR*. We will start with a generalised discussion of *CP* violation for neutral mesons and then move on to the only system this has currently been seen in, i.e. the Kaon system. This will then be extended to the B meson system. The three possible mechanisms for *CP* violation will be discussed, leading to the CKM matrix parameterisation and the unitarity triangle representation. Finally we discuss the importance of the channel $\mathrm{B}^0 \rightarrow \mathrm{J}/\Psi \mathrm{K}^0_s$ to the measurement of $\sin 2\beta$.

2.2 General CP Violation and Mixing in Neutral Mesons

2.2.1 General Formalism for Mixing

For this section a generalisation for all neutral psuedoscalar mesons (K^0, D^0, B^0 & B^0_s) will be represented as P^0 and $\bar{P}^0$. These are both eigenstates of the strong interaction Hamiltonian and are described here by $|P^0\rangle$ and $\left|\bar{P}^0\right\rangle$ each having the opposite flavour content but the same mass.

The transitions $\langle P^0|\hat{\mathrm{T}}_s\left|\bar{P}^0\right\rangle$ and $\left\langle\bar{P}^0\right|\hat{\mathrm{T}}_s|P^0\rangle$ where $\hat{\mathrm{T}}_s$ is the strong interaction transition operator, are impossible since they result in zero value matrix elements. If instead the weak Hamiltonian is used, the mixing transitions $\langle P^0|\hat{\mathrm{T}}_w\left|\bar{P}^0\right\rangle$ and $\left\langle\bar{P}^0\right|\hat{\mathrm{T}}_w|P^0\rangle$ are then possible. The conclusion drawn from this is that these states cannot be eigen states of the total Hamiltonian ($H = H_s + H_w$). This further implies that they are stationary states with no simple $e^{-iEt/\hbar}$ time dependence. This creates the en-

vironment where the $|P^0\rangle$ and $\left|\bar{P}^0\right\rangle$ can mix and decay into states normally forbidden.

In general the formalism required to describe the evolution of a state is of the form below;

$$|\psi(t)\rangle = a(t)\left|P^0\right\rangle + b(t)\left|\bar{P}^0\right\rangle + decay\ states \tag{2.1}$$

Taking $P^0(t)$ and $\bar{P}^0(t)$ to be probability amplitudes of having a P^0 or $\bar{P}^0$ meson at a time t and using the coupled Schrôdinger equation to describe the time dependence of $P^0(t)$ and $\bar{P}^0(t)$ this can be rearranged as:

$$i\hbar\frac{d}{dt}\begin{pmatrix} P^0(t) \\ \bar{P}^0(t) \end{pmatrix} = \begin{pmatrix} H_{11} & H_{12} \\ H_{21} & H_{22} \end{pmatrix}\begin{pmatrix} P^0(t) \\ \bar{P}^0(t) \end{pmatrix} \tag{2.2}$$

where $H_{11} = \langle P^0|\hat{\mathrm{T}}_w\,|P^0\rangle$, $H_{22} = \left\langle \bar{P}^0\right|\hat{\mathrm{T}}_w\left|\bar{P}^0\right\rangle$, $H_{12} = \langle P^0|\hat{\mathrm{T}}_w\left|\bar{P}^0\right\rangle$, $H_{21} = \left\langle \bar{P}^0\right|\hat{\mathrm{T}}_w\,|P^0\rangle$. The processes of CPT and CP conservation imply that $H_{11} = H_{22}$ and $H_{12} = H_{21}^*$ respectively. If the matrix H is split into its hermitian and anti-hermitian parts then:

$$H = M - \frac{i}{2}\Gamma \tag{2.3}$$

with $M = M^\dagger$ and $\Gamma = \Gamma^\dagger$

M and Γ are the hermitian mass and decay matrices. M is described as the dispersive part due to contribution from processes involving intermediate virtual states, M_{11} and M_{22} are due to constituent quark masses and their binding energy whilst M_{12} and M_{21} are due to virtual processes in the transitions $P^0 \to \bar{P}^0$ and $\bar{P}^0 \to P^0$. From these CPT requires that $M_{12} = M_{21}^*$, $M_{11} = M_{22} = M_0$ and $\Gamma_{11} = \Gamma_{22} = \Gamma_0$.

Γ is due to processes involving real intermediate states and is known as the absorptive part with Γ_{11} and Γ_{22} due to the $P^0 \to f$ and $\bar{P}^0 \to f$ decay states whilst Γ_{12} and Γ_{21} are due to the $P^0 \to f \to \bar{P}^0$ and $\bar{P}^0 \to f \to P^0$ where f is a common state between the 2 eigenstates.

By diagonalising equation 2.2 we are able to determine q/p, the fraction of $\bar{P}_0/P_0$, to a sign as:

$$p\left|P^0\right\rangle \pm q\left|\bar{P}^0\right\rangle \tag{2.4}$$

$$\Rightarrow\ \frac{q}{p} = \left(\frac{H_{21}}{H_{12}}\right)^{1/2} = \left(\frac{M_{12}^* - i\frac{\Gamma_{12}^*}{2}}{M_{12} + i\frac{\Gamma_{12}}{2}}\right)^{1/2} \tag{2.5}$$

By convention the linear combinations that diagonalise equation 2.2 give:

$$\left|P^0_{1,2}\right\rangle \equiv \frac{1}{\sqrt{|p|^2+|q|^2}}\left\{p\left|P^0\right\rangle \pm q\left|\bar{P}^0\right\rangle\right\} \tag{2.6}$$

This has the effect of making the description of the time evolution much more straightforward:

$$\left|P^0_1,t\right\rangle = P_1(t)\left|P^0_1\right\rangle \text{ where } P_1(t) = e^{-i(m_1-\frac{1}{2}\Gamma_1)t} \tag{2.7}$$

$$\left|P^0_2,t\right\rangle = P_2(t)\left|P^0_2\right\rangle \text{ where } P_2(t) = e^{-i(m_2-\frac{1}{2}\Gamma_2)t} \tag{2.8}$$

with

$$m_{1,2} = M_{11} \pm \mathrm{Re}\sqrt{H_{12}H_{21}} \tag{2.9}$$

$$\Gamma_{1,2} = M_{11} \mp 2\mathrm{Im}\sqrt{H_{12}H_{21}} \tag{2.10}$$

giving:

$$\Delta m - \frac{i}{2}\Delta\Gamma = 2\sqrt{H_{12}H_{21}}$$

The study of various different meson systems needs a slightly differing form of the solution to equation 2.2.1 to be used. For the Kaon where $\Delta M \gg \Delta\Gamma$ in states formed by the strong interaction at t=0 we use:

$$\left|P^0(t)\right\rangle = \frac{\sqrt{|p^2|+|q^2|}}{2p}\left\{P_1(t)\left|P^0_1\right\rangle + P_2(t)\left|P^0_2\right\rangle\right\} \tag{2.11}$$

$$\left|\bar{P}^0(t)\right\rangle = \frac{\sqrt{|p^2|+|q^2|}}{2q}\left\{P_1(t)\left|P^0_1\right\rangle - P_2(t)\left|P^0_2\right\rangle\right\} \tag{2.12}$$

For the $B^0-\bar{B}^0$ system the following is more useful:

$$\left|P^0(t)\right\rangle = f_+(t)\left|P^0\right\rangle + \frac{q}{p}f_-(t)\left|\bar{P}^0\right\rangle \tag{2.13}$$

$$\left|\bar{P}^0(t)\right\rangle = \frac{p}{q}f_-(t)\left|P^0\right\rangle + f_+(t)\left|\bar{P}^0\right\rangle \tag{2.14}$$

where

$$f_\pm(t) = \frac{1}{2}\left(e^{-i\left(m_1-\frac{i}{2}\Gamma_1\right)t} \pm e^{-i\left(m_2-\frac{i}{2}\Gamma_2\right)t}\right) \tag{2.15}$$

2.2.2 General Formalism for CP violation

For the case of CP violation let us once again use the general case of P^0 and $\bar{P}^0$. Also let the value of $(CP)^2 = 1$.

$$CP\left|P^0\right\rangle = e^{i\xi}\left|\bar{P}^0\right\rangle, \quad CP\left|\bar{P}^0\right\rangle = e^{-i\xi}\left|P^0\right\rangle \tag{2.16}$$

The choice of phase in which to define this transformation is completely arbitrary from equation 2.2.1. The probability amplitudes for the transitions are:

$$\left\langle P^0 \right| \hat{T}_w \left| \bar{P}^0 \right\rangle = H_{12} = M_{12} - \frac{i}{2}\Gamma_{12} \tag{2.17}$$

$$\left\langle \bar{P}^0 \right| \hat{T}_w \left| P^0 \right\rangle = H_{21} = M_{12}^* - \frac{i}{2}\Gamma_{12}^* \tag{2.18}$$

Since if *CP* symmetry is conserved $H_{12} = H_{21}^* \Rightarrow M_{12} = M_{12}^*$ and $\Gamma_{12} = \Gamma_{12}^*$, therefore:

$$\mathrm{Im}\left(M_{12}^*\Gamma_{12}\right) = 0 \text{ CP Conserving} \tag{2.19}$$

$$\mathrm{Im}\left(M_{12}^*\Gamma_{12}\right) \neq 0 \text{ CP Violating} \tag{2.20}$$

$\Rightarrow$

$$\frac{q}{p} = 1 \text{ CP Conserving} \tag{2.21}$$

$$\left|\frac{q}{p}\right| \neq 1 \text{ CP Violating} \tag{2.22}$$

If **H** exhibits *CP* violation the $\langle P_1^0 | P_2^0 \rangle$ is non zero. This means that the states $|P_1^0\rangle$ and $|P_2^0\rangle$ are not orthogonal and therefore not eigenstates.

2.3 *CP* Violation in the neutral Kaon System

Since the lifetimes of the K_S^0 and K_L^0 are so different this can be used to produce a pure beam of K_L^0 for study. This was used by Lande *et al*[2]. The two states of the Kaon can be described by:[3]

$$\left|K_1^0\right\rangle = \frac{1}{\sqrt{2}}\left(|K_0\rangle + \left|\bar{K}^0\right\rangle\right) \; CP = +1 \tag{2.23}$$

$$\left|K_2^0\right\rangle = \frac{1}{\sqrt{2}}\left(|K_0\rangle - \left|\bar{K}^0\right\rangle\right) \; CP = -1 \tag{2.24}$$

The final state of the $\pi^+\pi^-$ (a *CP* eigenstate with CP = +1) can only be produced without *CP* violation by the $|K_1^0\rangle$ decay, whilst the decay $\pi^+\pi^-\pi^0$, having CP = -1 is only produced by $|K_2^0\rangle$. Therefore the discovery of the decay $|K_L^0\rangle \rightarrow \pi^+\pi^-$ in 1964 by Cronin *et al* [4], indicated that *CP* violation was present in the Kaon system. This implies that the *CP* and mass eigenstates are no longer equal and *CP* violation by

mixing must be occurring, ie $\left|\frac{q}{p}\right| \neq 1$. $\left|\frac{q}{p}\right|$ may be parameterised by $\frac{1-\epsilon}{1+\epsilon}$. ϵ may be described as the complex parameter which is used to describe the *CP* violation in mixing.
$\Rightarrow$

$$\left|K_S^0\right\rangle = \frac{\left|K_1^0\right\rangle + \epsilon \left|K_2^0\right\rangle}{\sqrt{1+\left|\epsilon\right|^2}} \tag{2.25}$$

$$\left|K_L^0\right\rangle = \frac{\left|K_2^0\right\rangle + \epsilon \left|K_1^0\right\rangle}{\sqrt{1+\left|\epsilon\right|^2}} \tag{2.26}$$

The currently accepted values are $|\epsilon| = (2.285 \pm 0.019) \times 10^{-3}$ and its phase $\Phi = (43.49 \pm 0.08)^o$ [5]. Equations 2.25 and 2.26 may be rewritten to include the flavour basis states $|K^0\rangle$ and $\left|\bar{K}^0\right\rangle$:

$$\left|K_S^0\right\rangle = \frac{1}{\sqrt{2\left(1+\left|\epsilon\right|^2\right)}}\left((1+\epsilon)\left|K^0\right\rangle - (1-\epsilon)\left|\bar{K}^0\right\rangle\right) \tag{2.27}$$

$$\left|K_L^0\right\rangle = \frac{1}{\sqrt{2\left(1+\left|\epsilon\right|^2\right)}}\left((1+\epsilon)\left|K^0\right\rangle + (1-\epsilon)\left|\bar{K}^0\right\rangle\right) \tag{2.28}$$

The lifetimes of the two types of K mesons are [13]:

$$\tau_{K_S} = (8.934 \pm 0.008) \times 10^{-11} s$$
$$\tau_{K_L} = (5.17 \pm 0.04) \times 10^{-8} s$$

2.4 *CP* Violation in the B meson system

When a $P^0\bar{P}^0$ pair are created from a $Q\bar{Q}$ bound state such as the $\Upsilon(4S)$ they are free to oscillate between the 2 states in a correlated manner. The result of this is that the anti-symmetry of the wave function is maintained by the time evolution, i.e. when one of the mesons produced is measured, and for example tagged as a B^0 then the other instantly becomes a $\bar{B}^0$. This allows a time dependent measurement of the *CP* asymmetry.

The idea of the bound state mixing can now be applied to the B meson system. The 2 eigenstates are expected to show a slight difference in their lifetimes due to the contribution of decay channels common to both, though these are $\mathcal{O}(10^{-3})$ [5].

$$\frac{\Delta\Gamma_{B_d}}{\Gamma_{B_d}} = \mathcal{O}(10^{-2}) \tag{2.29}$$

There is a mass difference between the two eigenstates though and this is currently measured at [13]:

$$x_d = \frac{\Delta m_{B_d}}{\Gamma_{B_d}} = 0.723 \pm 0.08 \tag{2.30}$$

Model independently we may assume $\Delta\Gamma_B \ll \Delta m_B$ and from this equation 2.15 may be simplified as follows:

$$f_+(t) = e^{-\left(im+\frac{\Gamma}{2}\right)t} \cos\left(\frac{\Delta m_B t}{2}\right) \tag{2.31}$$

$$f_-(t) = ie^{-\left(im+\frac{\Gamma}{2}\right)t} \sin\left(\frac{\Delta m_B t}{2}\right) \tag{2.32}$$

There are three types of *CP* violation that the B-meson can exhibit once the time evolution of the meson is known. These are listed below and then described in their respective sections.

- *CP* violation in mixing (Indirect), where the 2 neutral mass eigenstate mixtures cannot be chosen to be *CP*-eigenstates.
- *CP* violation in decay (Direct), occurring in both charged and neutral systems this is where the decay amplitude for a decay is not equal to that for its *CP*-conjugate process.
- *CP* violation in interference (Interference), this is for decays both with and without mixing, where the final states are the same for both the B^0 and $\bar{B}^0$.

2.4.1 *CP* Violation in mixing

Since it is possible for a final state f to be produced from an initial B^0, there must exist somewhere between the time $t = 0$ and $t = t_{decay}$ mixing between the B^0 and $\bar{B}^0$ states. Therefore the following relationship defines whether *CP* violation occurs from this condition.

$$\left|\frac{q}{p}\right| = \left(\frac{M_{12}^* - i\Gamma_{12}^*/2}{M_{12} - i\Gamma_{12}/2}\right)^{1/2} \neq 1 \Rightarrow \text{CP Violation} \tag{2.33}$$

For this to occur the physical B meson mass eigenstates are not *CP* eigenstates. This therefore requires a phase between M_{12} and Γ_{12}. Within the B meson system *CP*

violation is observed by looking for asymmetries in the semileptonic decays to *CP* conjugate states. The amount of *CP* violation is described as:

$$a_{SL} = \frac{\Gamma(\bar{B}^0(t) \to l^+\nu X) - \Gamma(B^0(t) \to l^-\nu X)}{\Gamma(\bar{B}^0(t) \to l^+\nu X) + \Gamma(B^0(t) \to l^-\nu X)} \tag{2.34}$$

$$= \frac{\left|\frac{p}{q}\right|^2 - \left|\frac{q}{p}\right|^2}{\left|\frac{p}{q}\right|^2 + \left|\frac{q}{p}\right|^2} \tag{2.35}$$

The measurement of this type of *CP* violation requires a time dependent measurement of B decays from mixing since the decay width difference is not great enough to produce a pure beam of single state mesons as in the Kaon system. The expected value of this asymmetry is $\mathcal{O}(10^{-2})$[6]

2.4.2 *CP* Violation in decay

For the processes $B \to f$ and $\bar{B} \to \bar{f}$ the decay amplitudes can be labelled as A_f and $\bar{A}_{\bar{f}}$. Therefore the following describes *CP* violation in decay.

$$\left|\frac{\bar{A}_{\bar{f}}}{A_f}\right| \neq 1 \Rightarrow \text{CP} \quad \text{Violation} \tag{2.36}$$

Contributing to both A_f and $\bar{A}_{\bar{f}}$ are both the Weak and Strong phases and so the contributions to the decay amplitudes are from the magnitude A_i, a weak phase term $e^{i\phi_i}$, and a strong phase term $e^{i\delta_i}$. Since the transition $B \to f$ may be a sum of many separate transitions then the amplitude A_f may be given as:

$$A_f = \sum_i A_i e^{i(\delta_i + \phi_i)} \tag{2.37}$$

Rearranging equation 2.36 to include this for both A_f and $\bar{A}_{\bar{f}}$ gives:

$$\left|\frac{\bar{A}_{\bar{f}}}{A_f}\right| = \left|\frac{\sum_i A_i e^{i(\delta_i - \phi_i)}}{\sum_i A_i e^{i(\delta_i + \phi_i)}}\right| \tag{2.38}$$

If this relation is not unity then *CP* conservation is violated. This is called *CP* violation in decay and is commonly described as Direct *CP* violation . In practice there must be at least 2 different strong and weak phases present for the transition $B \to f$. An example of this is the Kaon system discussed in section 2.3 and rates may be written as

$$\Gamma_1 = \left|A_1 e^{i(\delta_1 + \phi_1)} + A_2 e^{i(\delta_2 + \phi_2)}\right|^2 \tag{2.39}$$

$$\Gamma_2 = \left|A_1 e^{i(\delta_1-\phi_1)} + A_2 e^{i(\delta_2-\phi_2)}\right|^2 \tag{2.40}$$

The asymmetry between the amplitudes A and $\bar{A}$ is given by

$$\left|\bar{A}\right|^2 - |A|^2 \propto 2A_1A_2 \sin(\phi_1 - \phi_2)\sin(\delta_1 - \delta_2) \tag{2.41}$$

This is totally independent of phase conventions and clearly physically meaningful. Therefore any *CP* asymetries within the charged B meson system are from *CP* violation in decay. In terms of the decay amplitudes the amount of *CP* violation is given by

$$a_f = \frac{|A|^2 - \left|\bar{A}\right|^2}{|A|^2 + \left|\bar{A}\right|^2} \tag{2.42}$$

Constraints on this are that the final state f can only be produced from the specific flavour of the B^0 and the *CP* violation is independent of any mixing between the B^0 and $\bar{B}^0$.

2.4.3 *CP* Violation in the Interference between decays with and without mixing

Let us consider the case of neutral B mesons decaying to a final *CP* eigenstate f_{CP}. It is possible for both the B^0 and $\bar{B}^0$ to decay to this final state. A measurable quantity for this is as follows:

$$\lambda \equiv \frac{q}{p}\frac{\bar{A}_{f_{CP}}}{A_{f_{CP}}} = \eta_{f_{CP}}\frac{q}{p}\frac{\bar{A}_{\bar{f}_{CP}}}{A_{f_{CP}}} \tag{2.43}$$

Within this description $\eta_{f_{CP}} = \pm 1$ describing the *CP* eigenvalue for the f_{CP} state. It is clear that if *CP* is conserved then $\left|\frac{q}{p}\right| = 1$ and in turn $\left|\bar{A}_{\bar{f}_{CP}}/A_{f_{CP}}\right| = 1$. This indicates that no relative phase must exist between q/p and $\bar{A}_{\bar{f}_{CP}}/A_{f_{CP}}$.
Therefore:

$$\lambda \neq \pm 1 \Rightarrow CP \text{ violation} \tag{2.44}$$

This means that it is possible for *CP* violation to still exist even if $|q/p| = 1$ and $\left|\bar{A}_{\bar{f}_{CP}}/A_{f_{CP}}\right| = 1$. Let us consider the decay widths of neutral mesons. It is useful to consider the CP asymmetry in the form:

$$a_f(t) = \frac{\Gamma\left(\bar{B}^0(t) \to f\right) - \Gamma\left(B^0(t) \to f\right)}{\Gamma\left(\bar{B}^0(t) \to f\right) + \Gamma\left(B^0(t) \to f\right)} \tag{2.45}$$

to measure the ratio and sum of the two decay widths. This implies that:

$$a_f(t) = \frac{(1-|\lambda|^2)\cos\Delta Mt - 2\mathrm{Im}(\lambda)\sin\Delta Mt}{1+|\lambda|^2} \tag{2.46}$$

which is nonzero if any of the types of *CP* violation are present. If *CP* violation in *decay* or *mixing* are absent though, this may be simplified since $|\lambda| = 1$ as:

$$a_{f_{CP}} = -\mathrm{Im}\lambda_{f_{CP}}\sin(\Delta M_B t) \tag{2.47}$$

2.5 *CP* violation within the Standard Model and The CKM Matrix

The generation of masses for the quarks is done through the Yukawa couplings to the neutral Higgs field:

$$\mathcal{L}_{Yukawa} = -\left(\bar{u}_L \mathbf{m} \bar{u'}_R + \bar{d'}_L \bar{\mathbf{m}} \bar{d}_R + h.c.\right)\left(1 + \frac{1+\Phi_0}{\upsilon}\right) \tag{2.48}$$

Within this context Φ is the scalar Higgs field and υ is its vacuum expectation value, $\bar{u'}_{L,R}$ and $\bar{d'}_{L,R}$ are the flavour space three component vectors for the up and down quarks and $\mathbf{m}, \bar{\mathbf{m}}$ are the arbitrary complex 3x3 mass matrices. In order to define the physical flavour states we must diagonalise $\mathbf{m}, \bar{\mathbf{m}}$. Therefore $\mathbf{m}_D = V_L \mathbf{m} V_R^\dagger$ and $\bar{\mathbf{m}}_D = \bar{V}_L \bar{\mathbf{m}} \bar{V}_R^\dagger$ and hence the charged-current couplings become:

$$\mathcal{L}_{Yukawa} = \frac{g}{\sqrt{2}}\left\{\bar{u}_L \gamma^\mu W_\mu^+ \mathbf{V} d_L + \bar{d}_L \gamma^\mu W_\mu^- \mathbf{V} u_L\right\} \tag{2.49}$$

From this the most important term for *CP* violation is $\mathbf{V}$ which is a 3x3 unitary matrix known as the Cabibbo, Kobayashi, Maskawa Matrix, V_{CKM} [7] and [8]. This defines the mixing of quark flavours and is shown in equation 2.50.

$$V_{CKM} = V_{uL} V_{dL}^\dagger = \begin{pmatrix} V_{ud} & V_{us} & V_{ub} \\ V_{cd} & V_{cs} & V_{cb} \\ V_{td} & V_{ts} & V_{tb} \end{pmatrix} \tag{2.50}$$

This is a complex matrix with 18 parameters, though its unitary nature reduces this to 9 constants and 9 free variables. Three of these are the Euler angles which leaves six pure phase parameters. Rearrangement of $\mathbf{V}$ to include these phases in the quark fields transforms $\mathbf{V}$ to $\mathbf{V'}$:

$$V'_{CKM} = \begin{pmatrix} e^{-i(\phi_1-\xi_1)}V_{ud} & e^{-i(\phi_1-\xi_2)}V_{us} & e^{-i(\phi_1-\xi_3)}V_{ub} \\ e^{-i(\phi_2-\xi_1)}V_{cd} & e^{-i(\phi_2-\xi_2)}V_{cs} & e^{-i(\phi_2-\xi_3)}V_{cb} \\ e^{-i(\phi_3-\xi_1)}V_{td} & e^{-i(\phi_3-\xi_2)}V_{ts} & e^{-i(\phi_3-\xi_3)}V_{tb} \end{pmatrix} \tag{2.51}$$

Through matrix rotation it can be seen that 5 of the phases may be removed but the 6th (δ_{CKM}) cannot. This is the source of *CP* violation within the Standard Model.

The parameterisation of the CKM matrix is done using the unitary property since it can also be represented as a product of rotational matrices. This was first done by Kobayashi and Maskawa but the preferred parameterisation is now by Chau and Keung[10]. In all there are 36 matrices with the usual choice being shown in equation 2.52.

$$\begin{aligned} V_{CKM} &= R_{23}(\theta_{23}, 0) \times R_{13}(\theta_{13}, -\delta) \times R_{13}(\theta_{12}, 0) \qquad (2.52) \\ &= \begin{pmatrix} c_{12}c_{13} & s_{12}c_{13} & s_{13}e^{-i\delta_{CKM}} \\ -s_{12}c_{23} - c_{12}s_{23}s_{13}e^{i\delta_{CKM}} & c_{12}c_{23} - s_{12}s_{23}s_{13}e^{i\delta_{CKM}} & s_{23}c_{13} \\ s_{12}s_{23} - c_{12}c_{23}s_{13}e^{i\delta_{CKM}} & -c_{12}s_{23} - s_{12}c_{23}s_{13}e^{i\delta_{CKM}} & c_{23}c_{13} \end{pmatrix} \end{aligned}$$

where $c_{ij} \equiv \cos\theta_{ij}$ and $s_{ij} \equiv \sin\theta_{ij}$. The three $\sin\theta_{ij}$ are the three real mixing parameters. These are the Euler angles and δ is the phase and source of *CP* violation. There are several conditions that apply to the CKM matrix if *CP* violation is to be exhibited. The Euler angles must not be either 0 or 2π, whilst δ must not be either 0 or π. From this there are eight conditions on the phases and angles for *CP* violation to occur. Unfortunately this alone is not quite enough for *CP* violation. If you have a pair of either up or down quarks and their masses are equal then you are able to remove only one Euler angle and the phase. Therefore there are 14 conditions in order for *CP* violation to be present in the Standard Model with 36 different parameterisations. Luckily however a single relation was found for the 14 parameters as shown below [11]. In the parameterisation as used in equation 2.52 this is:

$$J = \left| s_{13}s_{12}c_{13}^2 s_{13}c_{23}s_{23}\sin\delta \right| \qquad (2.53)$$

To get round the numerous parameterisations possible Wolfenstein [12] noticed that $|V_{cb}| \approx |V_{us}|^2$ and it had been previously shown that $|V_{cb}| \gg |V_{ub}|$ which implied that $c_{13} \approx 1$. It is therefore possible to rewrite V_{CKM} as below after the small angle approximation has been used:

$$V = \begin{pmatrix} 1 - \lambda^2/2 & \lambda & A\lambda^3(\rho - i\eta) \\ -\lambda & 1 - \lambda^2/2 & A\lambda^2 \\ A\lambda^3(1 - \rho - i\eta) & -A\lambda^2 & 1 \end{pmatrix} \qquad (2.54)$$

2.5.1 Current status and constraints on the CKM matrix

Due to the need for the quark mixing parameters to be measured using processes involving the weak interaction only these could most easily be affected by the possible

	Method	Value
$\|V_{ud}\|$	Nuclear β decays	0.9737 ± 0.0008
$\|V_{us}\|$	Semileptonic Hyperon & Kaon decays	0.2196 ± 0.0023
$\|V_{cd}\|$	Deep Inelastic Neutrino scattering	0.2240 ± 0.0016
$\|V_{cs}\|$	Semileptonic decays of charm mesons	1.04 ± 0.16
$\|V_{cb}\|$	Inclusive and exclusive semileptonic B meson decays to charm final states	$(40.4 \pm 1.8)10^{-3}$
$\|V_{ub}\|$	Lepton energy spectrum in semileptonic B decays	$\frac{\|V_{ub}\|}{\|V_{cb}\|} = 0.08 \pm 0.02$
$\|V_{tb}\|$	The decay $t \to bl^+\nu_l$	$\frac{\|V_{tb}\|^2}{\|V_{td}\|^2+\|V_{ts}\|^2+\|V_{tb}\|^2} = 0.99 \pm 0.29$

Table 2.1: *Currently measured parameters of V_{CKM} [13]*

new physics beyond the Standard Model. The methods that are used to measure the parameters of the CKM matrix are as follows:

- Direct Measurements of SM tree level processes
- Unitarity, i.e. relations between the CKM elements since $V_{CKM}^{\dagger} V_{CKM} = 1$
- Indirect Measurements of SM loop processes.

From this various elements of the CKM matrix have been determined as summarised in table 2.1. The experimental methods employed are given in detail in references [14] and [15]. These results lead us to the total constraints on the CKM matrix as shown in equation 2.55.

$$|V| = \begin{pmatrix} 0.9745 - 0.9760 & 0.2170 - 0.2240 & 0.0018 - 0.0045 \\ 0.2170 - 0.2240 & 0.9737 - 0.9753 & 0.0360 - 0.0420 \\ 0.0040 - 0.0130 & 0.0350 - 0.0420 & 0.9991 - 0.9994 \end{pmatrix} \tag{2.55}$$

These direct measurement constraints can be further enhanced using the unitarity constraint that we introduced initially. Unitarity leads to the formation of 6 orthogonality relationships these are described in more detail in [16]. The most important of these relationships for the description of CP violation within the B meson system is shown in equation 2.56.

$$V_{ub}^* V_{ud} + V_{cb}^* V_{cd} + V_{tb}^* V_{td} = 0 \tag{2.56}$$

This can be represented on an argand diagram as in fig 2.1. The usual representation has all three values divided by $|V_{cd}V_{cb}^*|$ with a phase convention chosen so that $V_{cd}V_{cb}^*$

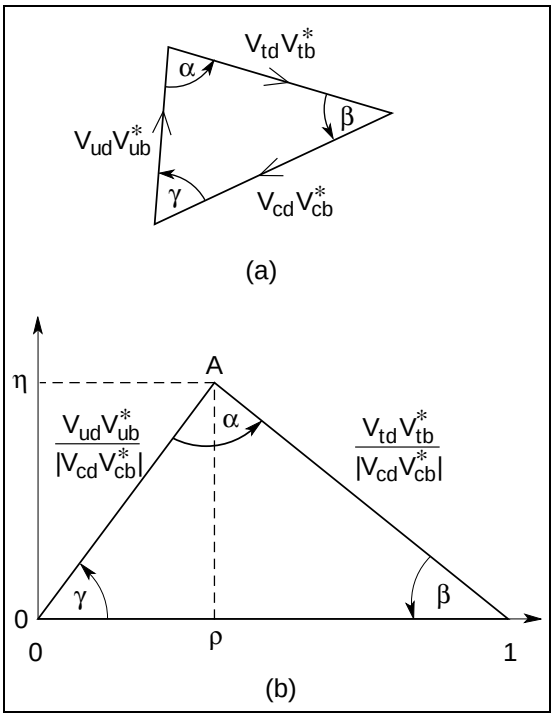

Figure 2.1: *The representation of the unitarity triangle both before and after rescaling with* $|V_{cd}V_{cb}^*|$

is real thus making 2 vertices lie on the real axis at $(0,0)$ and $(1,0)$. The angles of the triangle are named α, β, γ and are given by

$$\alpha = \arg\left(-\frac{V_{td}V_{tb}^*}{V_{ud}V_{ub}^*}\right) \tag{2.57}$$

$$\beta = \arg\left(-\frac{V_{cd}V_{cb}^*}{V_{td}V_{tb}^*}\right) \tag{2.58}$$

$$\gamma = \arg\left(-\frac{V_{ud}V_{ub}^*}{V_{cd}V_{cb}^*}\right) \tag{2.59}$$

From the Wolfenstein parameterisation as shown in equation 2.54 there are 4 parameters. Two of them are well measured, $\lambda = |V_{us}|$ and $A = |V_{cb}| / |V_{us}|^2$. The 2 parameters ρ and η are also the coordinates of the top vertex of the unitarity triangle . Figure 2.2 shows these in graphical form. Constraints from earlier apply the following conditions to ρ and η [17].

$$0.27 < \sqrt{\rho^2 + \eta^2} < 0.45$$
$$0.79 < \sqrt{(1-\rho)^2 + \eta^2} < 1.18$$
$$0.36 < \eta\,(1.29 - \rho) < 0.53$$

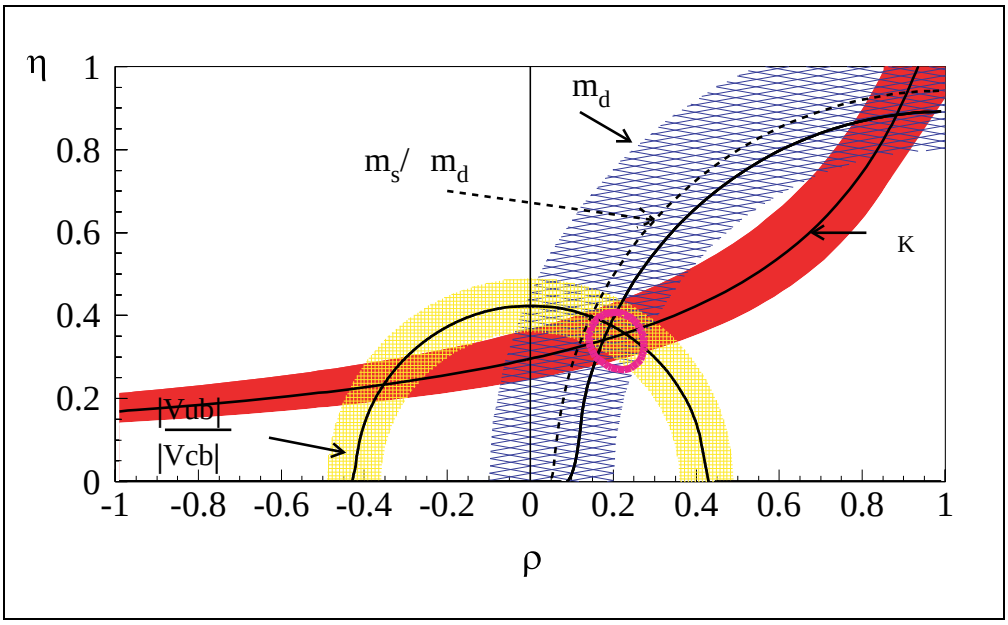

Figure 2.2: *The current experimental constraints on ρ and η*

2.5.2 Methods of Measuring the angles of the Unitarity Triangle

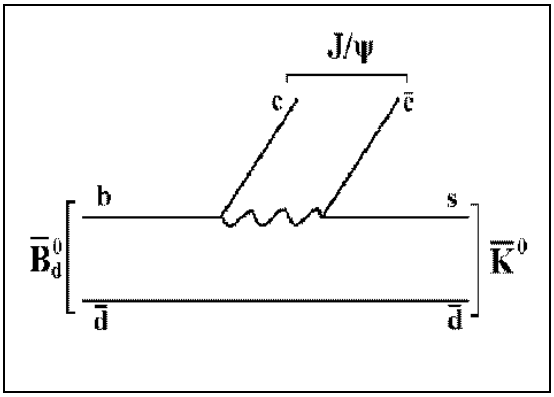

Figure 2.3: *A colour suppressed $\bar{B}^0_d \to J/\psi \bar{K}^0_s$ decay*

Within this section a description of the way that the decay $B \to J/\psi K^0_s$ can be used to find the angle β will be done. Further information above and beyond that covered here may be found in the *BABAR* Physics Book[18] and [19]. Since this decay is colour suppressed then the tree level contributions are expected to be dominant. This is shown in figure 2.3. However the dominant penguin contribution also has the same weak phase as the tree level process, with the only mode with different weak phase

heavily Cabibbo suppressed by $\mathcal{O}(\lambda^2)$. Since this channel also includes the K_s^0 then it must also be taken into account and hence:

$$\lambda = \left(\frac{q}{p}\right)\left(\frac{\bar{A}}{A}\right)\left(\frac{q}{p}\right)_K \tag{2.60}$$

where the first term comes from $B_d^0\bar{B}_d^0$ mixing, the second from the amplitude ratio of $\frac{\bar{A}(f)}{A(f)}$ and the third from the $K^0\bar{K}^0$ mixing. Therefore:

$$\lambda\left(B_d^0 \to J/\psi K_S^0\right) = -\left(\frac{V_{tb}^* V_{td}}{V_{tb} V_{td}^*}\right)\left(\frac{V_{cs}^* V_{cb}}{V_{cs} V_{cb}^*}\right)\left(\frac{V_{cd}^* V_{cs}}{V_{cd} V_{cs}^*}\right) \tag{2.61}$$

From equation 2.58 this leads us to the following conclusion:

$$Im(\lambda) = \sin 2\beta \tag{2.62}$$

For the actual experimental measurement of β we must consider the only possible measurable difference between the 2 CP eigenstates is the difference in their lifetimes. This physically manifests itself within the *BABAR* experiment as a difference in vertex position in z where Δz is described in equation 2.63.

$$\Delta z = z_{CP} - z_{tag} = \gamma\beta c\Delta t \tag{2.63}$$

Neglecting measurement errors the distribution of Δz will be of the form:

$$\Delta z = Ne^{-\Gamma_z|\Delta z|}\left[1 + a_f(\Delta z)\right] \tag{2.64}$$

where $a_f(\Delta z) = C_f \cos\Delta m\Delta z + S_f \sin\Delta m\Delta z$. In this case for $B \to J/\psi K_s^0$ then $C_f = 0$ and $S_f = \sin 2\beta$. From this it can be seen that the extraction of $\sin 2\beta$ comes from the fitting of the Δz distribution for S_f with appropriate smearing occurring of the result due to experimental resolution. The error on the measurement is given by:

$$\sigma_{\sin 2\beta} = \frac{\sigma\left(\sin 2\beta, \Delta m/\Gamma, \sigma_z\right)}{\sqrt{N_s}\sqrt{\epsilon_{tag}\left(1-2w\right)^2}} \frac{\sqrt{1 + \frac{N_B}{N_S}}}{1 + \left(\frac{A_B}{A_S}\right)\left(\frac{N_B}{N_S}\right)} \tag{2.65}$$

Experimentally it will be necessary to include the following systematic errors in any calculation of β:

- Reconstruction Uncertainties
  - Vertexing and tracking efficiencies
  - Vertex and drift chamber resolution
  - Particle Identification efficiencies and mis-id fractions

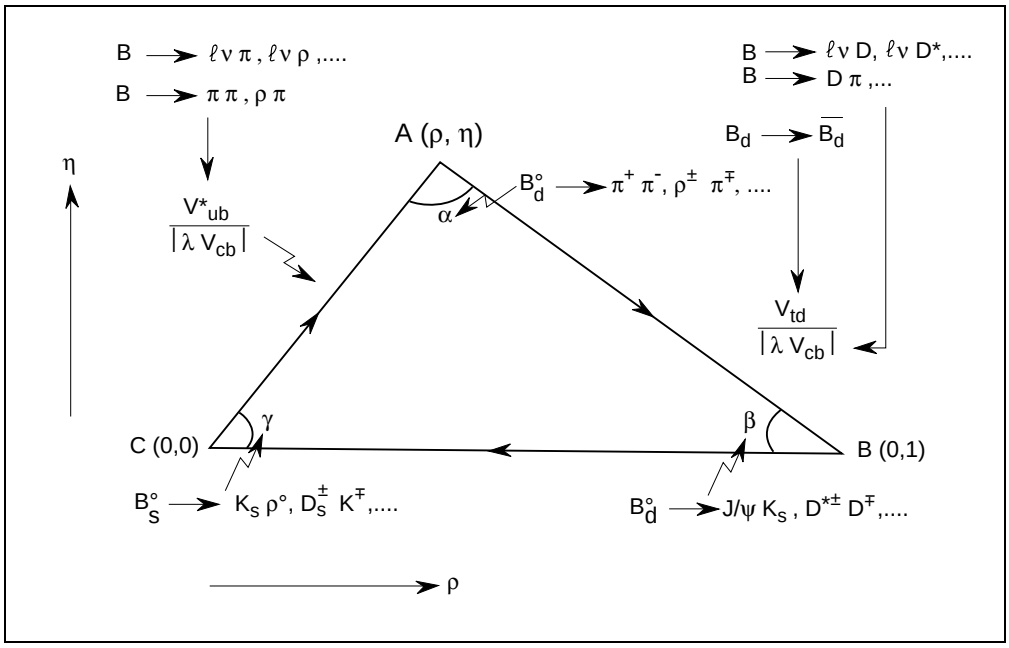

Figure 2.4: *The representation of the unitarity triangle showing decays used for the calculation of α, β and γ*

  - Uncertainties in the B flavour tagging efficiencies

- Detector Performance Uncertainties
  - Tracking asymmetries in charge
  - Detector resolutions
  - Overlapping tracks

- Backgrounds
  - Amount of background
  - Time distribution of background

- Experimental Parameter Uncertainties
  - B lifetime, τ_B
  - B mixing, Δm_d

The golden decay mode can be studied in two major ways dependant on the decay mode of the K_s^0 that you wish to use. By far the easiest is the charged decay producing a pair of oppositely charged πs. This accounts for nearly 70% of the K_s^0 decays. The other and more complicated since it depends almost entirely on the resolution of the

calorimeter and its reconstruction code is through the production of a pair of π^0. Since this makes up over 30% of the K_s^0 decay then it is essential that this neutral mode reconstruction is included in any complete study of the $B^0 \rightarrow J/\Psi K_s^0$ decay channel for a measurement of $\sin 2\beta$. The possibility of this analysis being used within the overall context of *BABAR* producing a conclusive measurement of this was the reason behind my choice of physics analysis.

For completeness the methods of finding the remaining two angles of the unitarity triangle will also be discussed briefly here. For finding the angle α the decay $B_d \rightarrow \pi^+\pi^-$ is used. Though there may be loop process contributions these are expected to be small enough that only the tree level processes can be considered.

$$\lambda\left(B_d^0 \rightarrow \pi^+\pi^-\right) = \left(\frac{V_{td}V_{tb}^*}{V_{td}^*V_{tb}}\right)\left(\frac{V_{ub}V_{ud}^*}{V_{ub}^*V_{ud}}\right) \tag{2.66}$$

This leads to the following conclusion:

$$Im(\lambda) = \sin 2(\pi - \beta - \gamma) = \sin 2\alpha \tag{2.67}$$

For γ the process $B_d^0 \rightarrow \rho K_S^0$ is used. Again the mixing of the decay product K_S^0 must be taken into account.

$$\lambda\left(B_d^0 \rightarrow \rho K_S^0\right) = \left(\frac{V_{ts}V_{tb}^*}{V_{ts}^*V_{tb}}\right)\left(\frac{V_{ub}V_{ud}^*}{V_{ub}^*V_{ud}}\right)\left(\frac{V_{cs}V_{cd}^*}{V_{cs}^*V_{cd}}\right) \tag{2.68}$$

which leads to:

$$\lambda\left(B_d^0 \rightarrow \rho K_S^0\right) = \frac{V_{cb}^*V_{ud}^*V_{ub}V_{cd}}{V_{cb}^*V_{ud}V_{ub}^*V_{cd}} \tag{2.69}$$

$\Rightarrow$

$$Im(\lambda) = -\sin 2\gamma \tag{2.70}$$

Experimentally the calculation of γ is the most difficult since it involves modes with particularly small branching ratios or the use of $K\pi$ modes but have to rely on isospin and SU(3) (U-spin) symmetries which currently have much larger theoretical uncertainties.

2.6 Summary

Within this section the basis of *CP* violation and mixing has been discussed along with the way that the first observations of *CP* violation were made in the Kaon system and the mechanisms behind it. Also the 3 types of *CP* violation exhibited within

theoretical models of the B meson system have been shown. The idea of the CKM matrix has also been introduced with a brief discussion on the current constraints of the elements and with it the idea of the unitarity triangle as a tool for measuring the complex phases which indicate CP violation. Methods for measuring the angles of the unitarity triangle were also discussed with particular attention paid to β. The ideas here will be used as a basis for the analysis in following chapters.

Chapter 3

The *BABAR* Detector and PEP-II Storage Ring

3.1 Introduction

The *BABAR* detector is situated on the PEP-II storage ring. With the small branching ratios of B$\rightarrow$ f_{CP} $\mathcal{O}(10^{-4})$ (where f_{CP} is any CP eigenstate) it is crucial that the collider must deliver unprecedented *integrated* luminosity. To measure *CP* violation it is necessary to measure the difference in decay lengths between the two B mesons. Since this distance in the rest frame is very small, asymmetric beam energies are used to boost the CM frame. This boost now makes the decay times of the B^0 mesons easily measurable using current technologies. The detector performance is optimised for the physics being studied, in particular the vertex resolution and particle identification system (especially K/π separation) as well as high quality tracking and calorimetry to provide separation of important final states.

This chapter will first describe the linear accelerator injection system and PEP-II storage ring and then move on to the *BABAR* detector.

3.2 PEP-II A new idea for a new problem

The PEP-II storage ring is a state of the art asymmetric e^+e^-collider. It has been designed to operate at the $\Upsilon(4s)$ resonance i.e. with a CM energy of 10.58 GeV which has been shown to produce the maximum number of $B\bar{B}$ pairs.

The selection of an e^+e^- over hadron collider brings the following benefits[20]:

- High signal to background ratio
- Clean events with average charge multiplicity of 11.

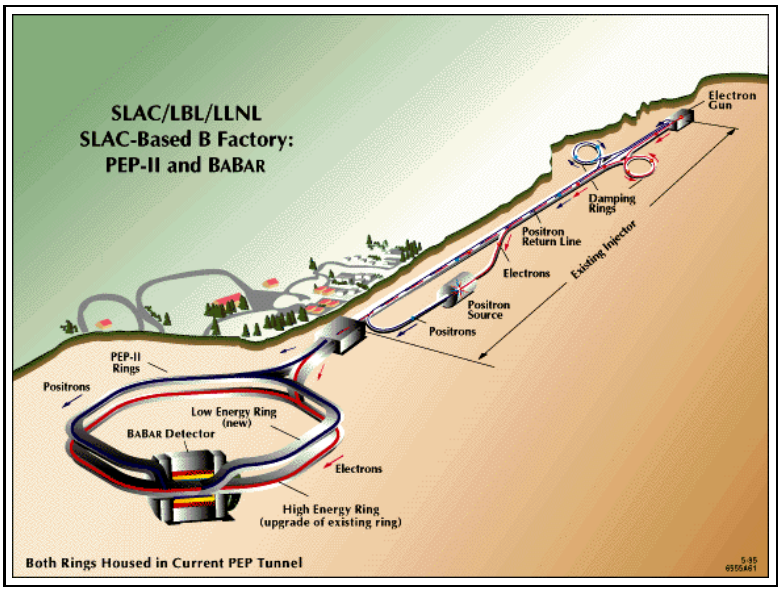

Figure 3.1: *A computer simulated aerial view of the new PEP-II storage ring also showing the linac and detector position*

- Low interaction rate ($\tilde{1}$0 Hz physics rate).
- Easier reconstruction of final states containing π^0 and photons, thus enabling many more channels to be studied.
- Easy and straightforward extrapolation from existing experiments.

3.2.1 The Linac and Injection

The main injector for the PEP-II storage ring is the SLAC linac operating in a 2-cycle mode. The first cycle accelerates a bunch of electrons and injects them into PEP-II. A second bunch is meanwhile stored in one of the linac damping rings. The next cycle accelerates a positron bunch and skims them off at the appropriate energy into a bypass transmission line. The second electron bunch is then accelerated to high energy (≈30 GeV) and is used to create the next positron bunch which is then stored in the other damping ring. The pulse rate for this is 60Hz. The physical design is shown in figure 3.2. Due to beam lifetimes a top-up will be required every hour and luminosity considerations dictate that this occurs within 3 minutes. Each pulse must therefore contain $0.3\text{x}10^{10} e^{\pm}$, compared to $3\text{x}10^{10} e^{\pm}$ regularly delivered to the SLC collider. The injection scheme itself is a vertical one to reduce the number of parasitic beam crossings due to synchrotron oscillations of off momenta particles. The location for injection is chosen to be at large β_y and this combined with the momentum

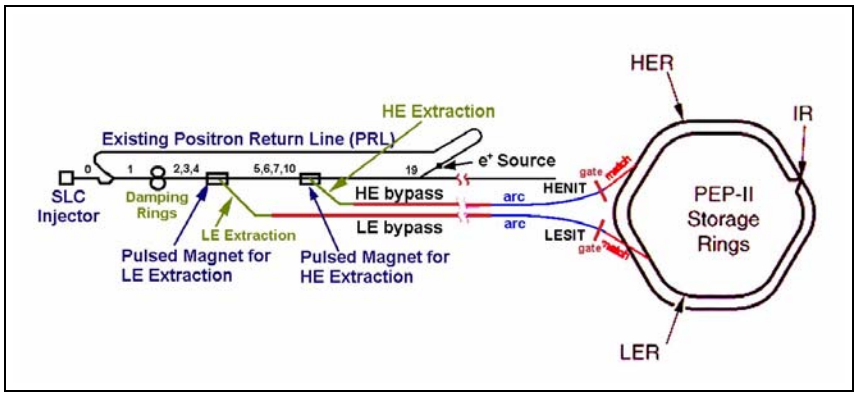

Figure 3.2: *Diagram showing the SLAC linac and injection mechanism into PEP-II*

resolution of 0.7% (FWHM) gives the maximum acceptance of the injected particles into the circulating beams.

3.2.2 The Storage Ring

The e^+e^- cross section for $B\bar{B}$ at the $\Upsilon(4s)$ is approximately 1.1 nb on a background of 2.5 nb ($c\bar{c}, s\bar{s}, u\bar{u}, d\bar{d}$ and lepton pair production). To produce the required 3x10^7 B mesons per year, a luminosity of 3x10^{33} $cm^{-2}\,s^{-1}$ is needed. The parameters chosen to achieve these requirements are shown in table 3.1.

An asymmetric collider can provide adequate time resolution to study *CP* violation at the $\Upsilon(4s)$and it has been shown that the optimal asymmetry is in the region of 1 : 3[21]. This leads to beam energies of 3.1 GeV (positrons), Low Energy Ring (LER) and 9.0 GeV (electrons), High Energy Ring (HER) giving a $\beta\gamma$ to the $\Upsilon(4s)$ of 0.56, giving a mean separation of the decay points of the two B^0 s of 250 μm. This is well within the current vertex detector performance. The main PEP-II parameters are listed in table 3.1.

3.2.3 The Interaction Region

The asymmetry and high luminosity of PEP-II pose particular difficulties in the interaction region (IP). The components in the IP are shown in fig 3.3. The focusing of the LER is achieved using a pair of quadrupoles (QD1,QF2), with QD1 used for the vertical focusing and QF2 for the horizontal some 2.5m away from the IP. QD1 also achieves some focusing of the HER though this is mainly done using QD4 for the horizontal and QF5 for the vertical. These are 4 and 7m away from the IP respectively. A small dipole is situated at 3.7 m from the IP to ensure that the synchrotron radiation

	Low energy ring	High energy ring
Energy (GeV)	3.1	9.0
Circumference (m)	2199.32	2199.32
IP spot size, x/y (μm)	155/6.2	155/6.2
Emittance at IP $\varepsilon_x/\varepsilon_y$ (nm rad)	64.3/2.6	48.2/1.9
Beta function at IP β_x^*/β_y^* (cm)	37.5/1.5	50.0/2.0
Beam-beam tune shift $\xi_{0,x}/\xi_{0,y}$	0.03/0.03	0.03/0.03
RF frequency (MHz)	476	476
RF voltage (MV)	5.9	18.5
Bunch length (cm)	1.0	1.0
Number of bunches	1658	1658
Bunch separation (m)	1.26	1.26
Total current (A)	2.14	0.99

Table 3.1: *Parameters of the PEP-II asymmetric storage ring.*

generated by the focusing quadrupoles does not shine on the IP. Within the IP region itself are a pair of dipoles (B1) which are used to give a horizontal separation to the beams. Within the IP region, these have a significant impact, limiting the acceptance of the *BABAR* detector to $|\cos\theta_{lab}| < 0.955$.

After leaving the IP the LER continues to undergo horizontal separation, reaching a maximum distance of 2.8 m from the HER at 40 m from the IP, where more dipoles return it to the same horizontal position as the HER. Between 22 m and 60 m, the LER is also separated vertically from the HER by 1 m, which allows the two to be at the same radius for the rest of the ring. The QD1 quadrupole, being off axis w.r.t the low energy beam, and the B1 separation dipoles are the principal sources of synchrotron radiation at the IP.

3.2.4 Backgrounds

To enable meaningful physics results to be achieved the background levels must be similar to those of existing e^+e^- machines with beam currents a factor of ten higher than currently employed at CESR[22]. Backgrounds were considered to be the largest problem during design and construction. There are three principal sources of machine background to be considered with PEP-II:

- Lost beam particles due to Bremsstrahlung or Coulomb scattering off residual gas molecules.

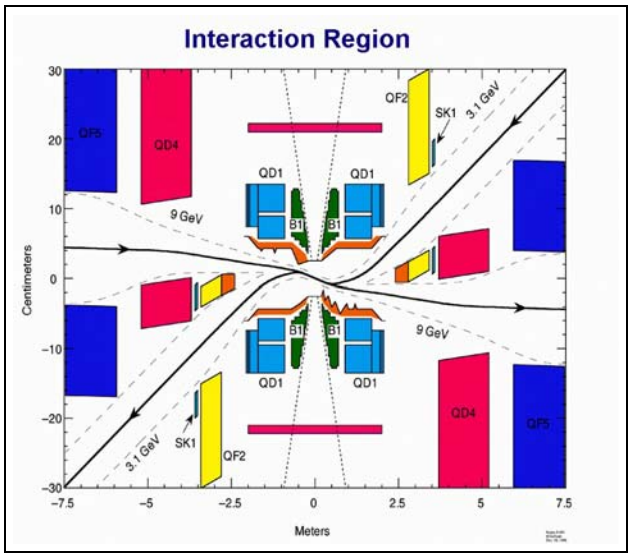

Figure 3.3: *The PEP-II interaction region showing essential components*

- Synchrotron radiation photons produced in the machine bending magnets.
- Beam-beam Bremsstrahlung at the interaction point where enough energy is radiated from beam particles to be bent into machine components by B1 or Q1.

Acceptable background levels have been calculated [23] for each of the detector components and are shown in table 3.2. Detector performance can be adversely impacted either by too high component occupancy levels or radiation damage.

		Occupancy		Rad. dose (yr)	
		Nominal	Limit	Nominal	Limit
Silicon Vertex	Average	1.3%	20%	33 krad	1500 krad
	Inner Layer	3.3%	20%	82 krad	1500 krad
Drift Chamber	Average	0.05%	10%	4×10^{-4} C/ cm	0.1 C/ cm
	Inner Layer	0.5%	10%	4.5×10^{-3} C/ cm	0.1 C/ cm
DIRC		0.015%	2%		
Calorimeter	Photons	1.1/ μs	20/ μs	1.5 krad	100 krad

Table 3.2: *Occupancy rates and radiation doses from lost beam particle backgrounds in the four innermost sections of the BABAR experiment.*

3.2.4.1 Lost Beam Particle Interaction

A significant part of the background for *BABAR* is a result of Bremsstrahlung and Coulomb scattering caused by lost beam particles. These are caused when beam particles strike residual beam-gas particles and lose enough energy to fall out of the momentum range of the storage ring. They then strike the beam-pipe and cause an electromagnetic shower. The rate of this occurrence has been simulated[23]. It has been found that the rate of these interactions from Bremsstrahlung are approximately ten times those from Coulomb scattering. This makes it imperative that the pressure within the interaction region straight section is kept as low as possible.

3.2.4.2 Synchrotron Radiation

There are two types of synchrotron radiation, quadrupole and fan. These are caused by:

- Quadrupole: Off-axis particles passing through an on-axis quadrupole or sextupole (generally at least 3σ from the nominal beam position).
- Fan: Beam passing through a dipole magnet or an offset quadrupole magnet, in which all particles radiate in a fan shape projecting forwards from the beam.

Studies have shown [23] that the quadrupole contributes less than 1% of the synchrotron radiation rate at PEP-II, and so only fan will be considered. Further, the dominant contribution to the synchrotron radiation rates near the IP are the dipole bending magnets B1, described in section 3.2.3, and the first focusing quadrupole which, whilst the high energy beam passes through a field-free region of this magnet, deposits significant radiation in the same region due to the low energy ring.

3.2.4.3 Beam-Beam

Beam-beam backgrounds are produced from three sources at *BABAR*, enhanced beam-gas interactions in the HER, due to low-energy ring IP synchrotron radiation impinging onto the incoming HER beam pipe, photons and low-energy $e^{+/-}$ from radiative-Bhabha scattering hitting nearby vacuum components; and tails generated by the beam-beam interaction and/or by the electron-cloud-induced blowup of the low-energy beam.

3.3 *BABAR*

In order to fully achieve the physics goal of the experiment the following criteria will have to be met[24]:

- Maximum acceptance in the CM system,
- Accommodate the necessary beam components near the interaction point. This is necessary due to the high luminosities as discussed in section 3.2.3 as well as the asymmetric design of PEP-II.
- Excellent vertex resolution (better than 80 μm).
- Near perfect tracking for $\sim$60 MeV $<$ p_t $<$ $\sim$4 GeV
- Ability to identify correctly e, μ, K, p & neutral hadrons over a wide kinematic range.
- Photon and π^0 identification over 20 MeV $<$ E $<$ 5 GeV.

In table 3.3 some of the *BABAR* design parameters are given.

There are 5 principal detector components, a vertex detector, tracking chamber, crystal electromagnetic calorimeter, particle identification system and an instrumented flux return. All but the flux return are located within a 1.5T magnetic field. In the following pages both the physical structure of each detector component and its associated readout system will be described. The core online system will also be discussed.

Parameter	Value
Tracking coverage ($/4\pi$)	0.92
$\sigma_(p_t)/p_t$(%)(1 GeV pions at 90^o)	0.36
$\sigma_{z0}(\mu$m)(1 GeV pions at 90^o)	52
Calorimetry coverage ($/4\pi$)	0.90
X_O in front of Calorimeter (at 90^o)	0.25
σ_E/E (%)(1 GeV γ at all angles)	1.8
γ efficiency within acceptance (at 100 MeV)	0.92
Charged hadron ID coverage($/4\pi$)	0.84

Table 3.3: *Detector performance parameters*

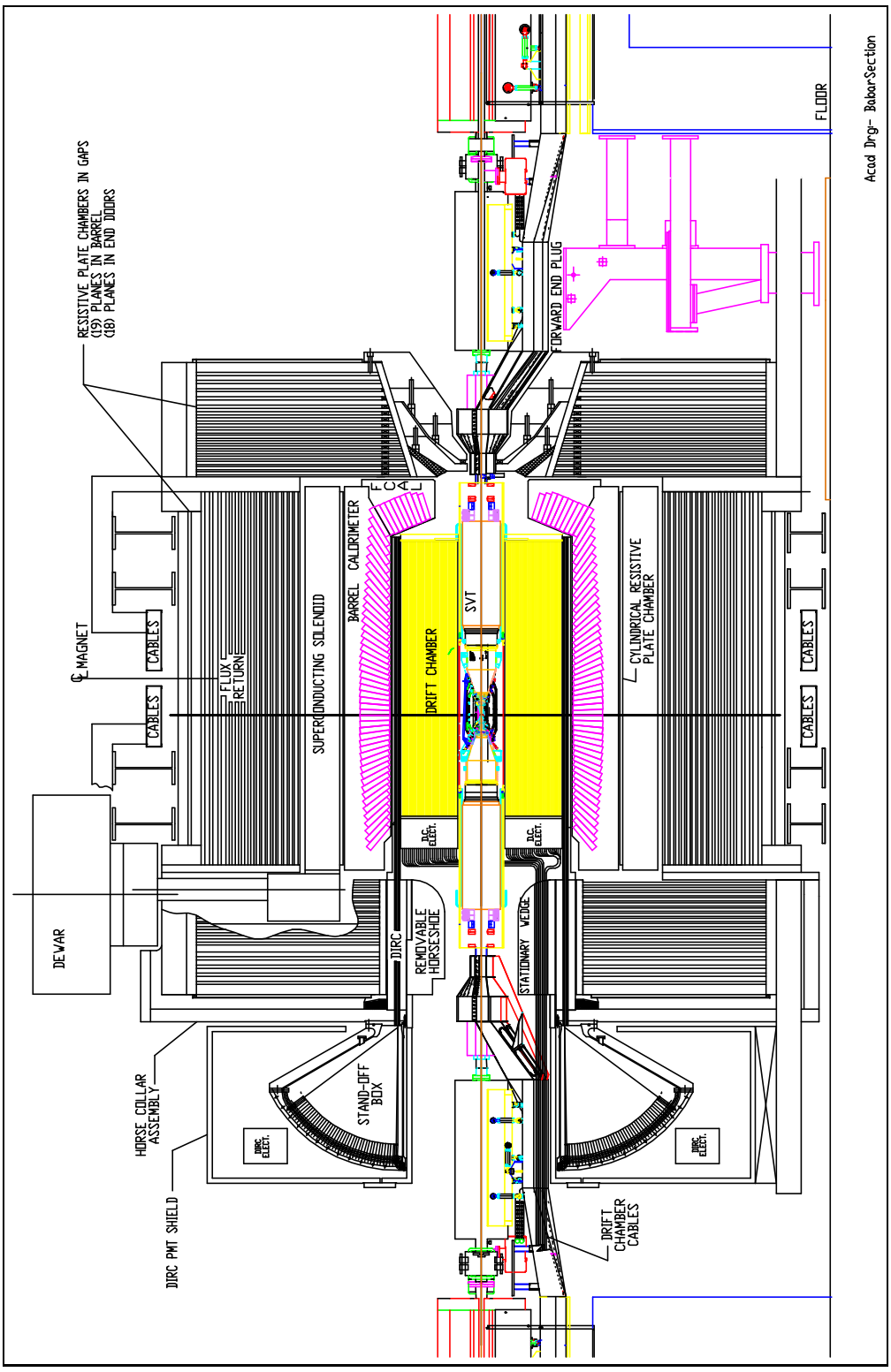

Figure 3.4: *A cross-section through the BABAR detector showing all major components*

3.3.1 The Silicon Vertex Tracker

3.3.1.1 Detector Design

The main purpose of the Silicon Vertex Tracker (SVT) is to accurately reconstruct both of the B decay vertices. A vertex resolution of better than 80 μm is needed, corresponding to a single point resolution of 15μm. This is achieved using a silicon micro strip detector[26]. Using the multi layer design a single point resolution of 10 - 15 μm has been achieved.

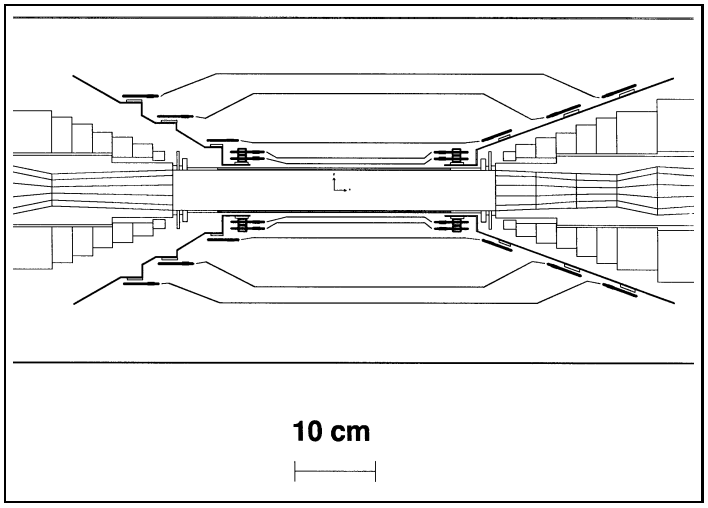

Figure 3.5: *Projection of the SVT showing all layers in z*

As with all collider experiments it is important to cover as much of the solid angle as possible though this has been limited in BaBar by beam components. Thus the maximum acceptance is 17.2^o in both the forward and backward directions. Due to the SVTs proximity to the interaction point it must also be radiation hard with an expected dose of 240 krad/yr to the inner layers and 110 krad/yr to the outer layers. The detector itself has been designed to be able to stand more that 10 times that dosage over the whole 10 years of BaBars operation. It is very important that as many redundancies as possible are built into the system since any invasive work would require a long shutdown due to the location of the SVT.

As can be seen in fig 3.5 and 3.6 the design is cylindrical with 5 layers of silicon micro strip detectors arranged so that 3 are very close to the beam pipe with a further 2 approximately 5cm further away. There are 6 modules per inner layer and 16 and 18 for the outer 2 layers. These outer layers are electrically separated into a forward and backward part. The inner surface has the strips arranged perpendicular to the

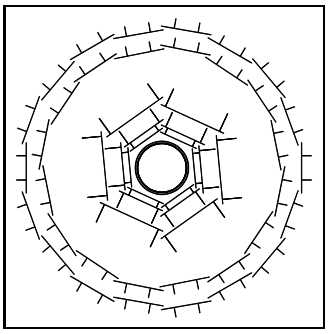

Figure 3.6: *Projection in the xy plane through the SVT showing all layers*

beam axis for accurate measurement of z. The outer surface has the strips arranged parallel in order to measure ϕ as accurately as possible. All the detectors are mounted on Kevlar ribs which are then mounted on a Kevlar cone at either end. These cones support the readout electronics as well as provide the mounting onto the innermost beam steering magnets.

In total there are 340 separate detectors with a total number of $\sim$150000 readout channels. To ensure capacitive decoupling some of the detector micro-strips are biased but not actually readout. These are known as floating strips. This improves the spatial resolution of the detector as a whole and prevents ghosting i.e. strips firing because their neighbour has, when in fact they have not received a hit. The full performance of the SVT is shown in table 3.4.

3.3.1.2 The Readout System

The front-end electronics (FEE) for the SVT are constructed from radiation hard CMOS integrated circuits mounted on a hybrid circuit board[27]. These distribute power and data signals and provide a thermal interface to the cooling system. The output signals from each of the detectors is then amplified, shaped and then compared to a configurable threshold. The length of time that the signal exceeds the threshold has an approximately logarithmic relationship to the current produced. This method is known as Time Over Threshold (TOT). This has one major advantage for a system that has this number of readout channels. Due to the logarithmic relationship the number of bits used in the digitisation is greatly reduced which in turn greatly reduces the data volume needed to be read out. From the FEE the signals are then fed out of BaBar into another board that is used to convert the electrical signals into optical output for transport to the readout modules mounted in 7 logical crates within the electronics hut.

	Layer						
	1	2	3	4		5	
				a	b	a	b
Radius (mm)	32	40	54	124	127	140	144
Modules/Layer	6	6	6	8	8	9	9
Wafers/Module	4	4	6	7	7	8	8
Readout Pitch (μm)							
ϕ	55	55	55	80 - 100		80 - 100	
z	100	100	100	210		210	
Floating Strips							
ϕ	-	-	-	1		1	
z	1	1	1	1		1	
Intrinsic Resol.(μm)							
ϕ	10	10	10	10 - 12		10 - 12	
z	12	12	12	25		25	

Table 3.4: *Design parameters of the SVT system*

3.3.2 The Drift Chamber

3.3.2.1 Detector Design

The Drift Chamber (DCH) is the main tracking component of the BaBar detector. In the $R-\phi$ plane a resolution of greater than 140μm is needed. It is also possible to do particle identification using dE/dx measurements. A dE/dx resolution of 7% is achievable when all 40 tracking points contribute to the measurement. In general for a track with $p_t > 1$ GeV/c, $\sigma p_t \approx 0.3\% \times p_t$. The angular acceptance of the DCH is designed to cover the region completely down to the limitations imposed by beamline components (i.e. 300mrad in both forward and backward directions). The low p_t resolution is limited by multiple scattering from the SVT and inner surface of the chamber. For electron multiplication a mixture of helium and isobutane is used in the ratio 80:20. This was chosen due to its ability to promote good spatial and dE/dx resolution and a very short drift time within the chamber.

Mechanically the DCH is 2.8m long with an inner radius of 23.6cm and outer radius of 80.1cm[28]. Fig 3.7 shows the DCH in z projection. The inner cylinder is made of beryllium and the outer surface of Kevlar with a Nomex core, limiting the amount of material in the detectable volume. Both of these together contribute less than 2%

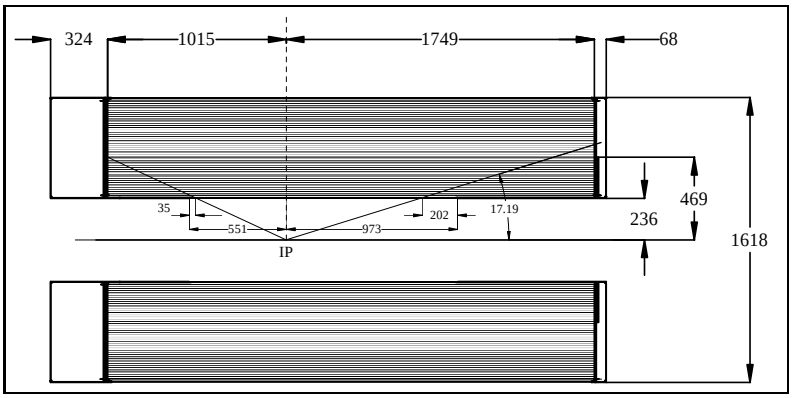

Figure 3.7: *Z-projection through the Drift Chamber*

of a radiation length of material in the active volume. Due to the boost inherent in the BaBar detector it is important that the amount of material in the forward end is kept to a minimum. To this end the aluminium DCH end plates are of different thicknesses. The forward end is 12mm thick whilst the backward is 16mm. Also all of the front end electronics (FEE) are mounted on the backward end of the detector.

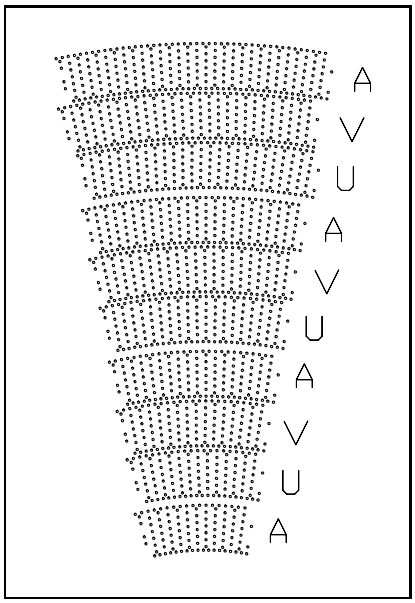

Figure 3.8: *The wire layout of one of the 16 sectors in the Drift Chamber*

The stringing of the DCH has been arranged radially in 10 superlayers of 4 drift cell thickness each, with each drift cell having dimensions of 1.2 $\times$ 1.8 cm^2. The superlayers are arranged in the following order: an axial layer (A) and alternating

stereo layers (U & V). This is best shown in fig 3.8. The stereo angle varies from 40 mrad for the innermost stereo layer to 70 mrad in the outermost stereo layer. The chambers' sense wires are constructed of 20μm gold plated tungsten-rubidium whilst the field wires are 120μm and 80μm gold plated aluminium.

3.3.2.2 The Readout System

To readout the signals from the chamber and for detecting the drift time (t_d), the leading edge of the signal from the sense wire is detected and digitised with a resolution of 1ns. For dE/dx measurements the total charge from a pulse is needed. To achieve this a slow shaper is used and then digitised at 15MHz using a 6-bit Fast Analogue to Digital Converter (FADC)[29]. Due to the total number of channels (7104) and their density it was necessary to use a 4-channel amplifier/discriminator integrated circuit with two of these components feeding into an 8-channel Time to Digital Converter (TDC)/FADC. The event information is then passed into 12μs latency buffers to allow for the trigger decision to be made. If a Level-1 accept is detected then the information is passed into one of four event buffers. Since the DCH is one of the principal suppliers of information to generate the Level-1 accept, the information from all 7104 channels must be passed to the Level-1 trigger system. This is done at a sampling frequency of 3.74MHz on 24 *BABAR* standard optical links. The expected single cell efficiency of the DCH is >95%.

3.3.3 The Detector of Internally Reflected light (DIRC)

3.3.3.1 Detector Design

In the BaBar detector the particle I.D. system must be able to fulfil the following design requirements:

- Kaon identification up to 2 GeV/c
- Separation of K and π from 2 body processes such as $B^0 \rightarrow \pi^+\pi^-$ & $B^0 \rightarrow K^+K^-$ for momentum up to 4 GeV/c at large forward angles.

The DIRC system was chosen over the more conventional RICH due to the following factors:

- The same amount of material would be contained within the active detector volume (14% of X_0 for a particle travelling perpendicular from the I.P.) as with other techniques such as RICH.

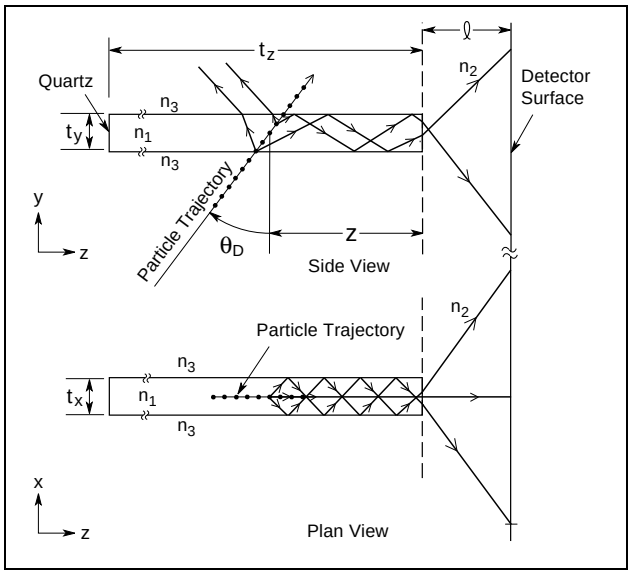

Figure 3.9: *The concept behind the DIRC System*

- Including support structure the system is only 8cm thick allowing as large as possible Drift chamber radius whilst keeping the calorimeter volume as small as possible (so as to ensure minimum impact on energy resolution and also minimising extra costs).
- The soft photon efficiency is maintained since the bar boxes are mounted as close as possible to the ends of the calorimeter crystals. This is also assisted by the physically small thickness of the quartz crystals.
- The photon output is enhanced for particles that are incident at as steep an entry angle as possible which perfectly suits the conditions that will be found in the *BABAR* detector.
- It is a very robust design using conventional photo detectors and very well known materials.

The basic idea behind the DIRC is shown in fig 3.9. For each particle the Cherenkov radiation is emitted at a specific angle given by

$$\cos\theta_c = (\beta n)^{-1}$$

where β is the velocity of the incoming particle over c and n is the refractive index of the material. The Cherenkov photons are then trapped within the radiator due to total internal reflection[30]. The Cherenkov angle is also more highly preserved in a high refractive index material. To this end *BABAR* has chosen quartz ($n = 1.474$) though the following factors also facilitated the decision:

- Long radiation length (11.7 cm)
- Long absorption length for the emitted UV light
- Ease of finishing to an optical quality surface

A computer model of the DIRC system design is shown in fig 3.10. The physical layout of the quartz bars is 12 per bar box with 12 bar boxes arranged to cover the entire ϕ range along the barrel. These bar boxes extend through the backward end flux return to the Standoff Box. This structure contains 6 m^3 of purified water to act as a light guide to the photodetectors. The water was chosen due to its similar refractive index to quartz. The instrumented area of the Standoff Box is kept to a minimum by the addition of trapezoid quartz blocks. These reflect half the image generated back upon the other. The photodetection is done through 11000 photo-multiplier tubes arranged in a close packed linearly focused array. Those photons travelling forward are reflected at the forward end of the bar box by a mirror. Due to the large volume of the Standoff Box and solid angle coverage afforded by it the errors due to the finite size of the quartz bars and PM tubes are approximately equal to those due to the achromicity of the quartz itself. To ensure constant performance over the solid angle covered by the Standoff Box the distance from the end of a PM tube to the end of the nearest bar box has been maintained evenly at 1.2m.

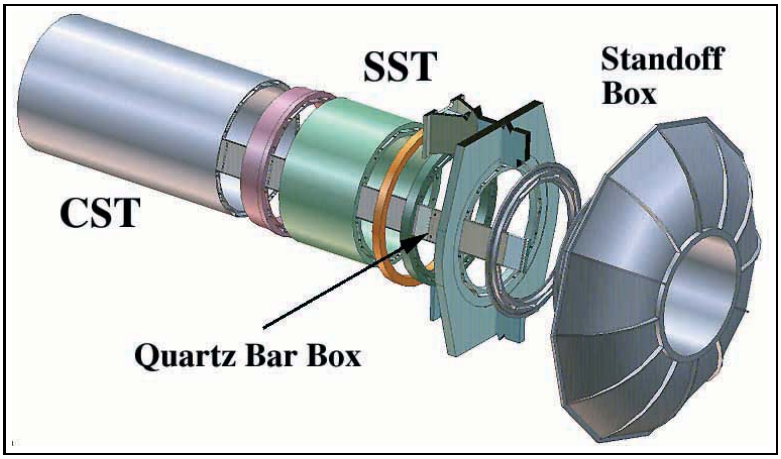

Figure 3.10: *The DIRC System*

The total acceptance of the DIRC system is limited by the 1.5T magnetic field and 80cm radius of the DCH to particles with $p_t > 250$ MeV/c (when produced at the IP). The bar boxes extend 178cm forward of the I.P. (60^o in dip angle). This ensures that 87% of the polar solid angle in the centre of mass frame is covered. The total

coverage in the ϕ plane is limited to 97% due to the gaps between the 12 bar boxes.

The only worry with the system is the low photoelectron yield. This is dependent on the transparency of the quartz, water and glues, reflectiveness of mirrors and light collectors and most importantly of all the quality of the polishing of the quartz bars.

3.3.3.2 The Readout System

The DIRC system has to be able to process input signals up to a rate of 100 kHz. The contributions to this can be separated out as follows. 1 khz from electronic noise from the PMT tubes themselves, 30 kHz from PEP-II backgrounds with the rest being signal. To ensure the required single electron sensitivity of the DIRC system and to save cables the front end electronics is mounted very close to the detector. Therefore it has been designed in a highly integrated way using CMOS technology as much as possible. This is housed in 192 DIRC front-end boards (DFB)[18]. These are housed in 12 front end crates, which are in turn connected using the *BABAR* standard 1.2Gbit/s optical fibre links to 6 Read Out Modules. These are mounted in one logical VME crate.

Each DFB receives as input the signals from 64 PMT tubes. The board houses 8 analogue chips first amplifying and applying a threshold to the inputs and then shaping the pulse. Using a zero-cross discriminator a digital output pulse is generated in time with the peak of the input pulse as well as a Gaussian pulse with an 80 ns peaking time. This has been chosen to allow the multiplexing system to selectively pass the analogue outputs onto the 8-bit Flash ADC (FADC) of which there are 1 per DFB. Since a timing resolution of better than 1 ns is needed a single hysteresis comparator is chosen instead of the more normal 2 discriminators. The hysteresis chosen is equal to the threshold that is applied which means that a leading edge exceeding threshold fires off the discriminator which is then cleared once the differentiated input level crosses the ground level. The trailing edge of the output signal is therefore synchronous with the maximum of the input pulse. This is then sent to the TDC chip for conversion. The TDC chip chosen uses 500 ps bins with a full range of 32 ns. This was chosen to allow for the 12μs latency of the Level-1 trigger system. The collective output of both chips is then passed into the event buffers for passing onto the readout modules on receipt of a Level-1 accept signal. The other components on the board are used to calibrate the system from a simulated PMT input to the analogue chips through to pattern generation to test the ADCs. To calibrate the whole chain from PMT through to the DAQ crates there is also a chain of LEDs mounted within the Stand-Off Box to simulate Cherenkov rings within the detector.For each front-end crate there is a DIRC

Crate Controller (DCC). This interfaces with the G-link optical signals coming from the DRC DAQ VME crate, passing the standard *BABAR* runtime commands (such as L1Accept and Cal-strobe) onto the DFB.

3.3.4 The Electromagnetic Calorimeter

3.3.4.1 Particle showers and Calorimeters

The development of an electromagnetic shower occurs through the Bremsstrahlung and pair production processes. Bremsstrahlung occurs when a high energy particle moves within a short distance of a nucleus and emits a photon. The average energy of this photon is proportional to the energy of the incident particle. Pair production again occurs within a short distance of the nucleus but this time a photon is converted into an electron-positron pair and so for this to occur the energy of the photon must be a least twice the rest mass of the electron. Therefore the electromagnetic shower develops by producing many photons and e^+e^- pairs until the energy of the shower drops below a critical energy E_0. From this point onwards the shower dies away slowly until the particles at the end of the shower do not have enough energy to initiate either of the previously mentioned processes. The number of particles produced in the shower increase with the energy of the incident particle whilst the length is an approximately logarithmic relationship. The development of the shower is best shown using the number of particles contained within the shower as a function of the thickness of the absorber. This is shown in figure 3.11.

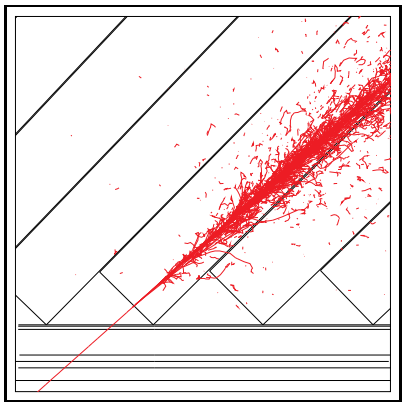

Figure 3.11: *The development of an electromagnetic shower within an absorber shown using the Geant 4 simulation*

An electromagnetic shower also develops transversely due to multiple Coulomb scattering within the material. Approximately 90% of the energy of the shower being

Radiation length (X_0/cm)	1.85
Molière Radius (cm)	3.8
Absorption length for 5 GeV Pions (cm)	41.7
Density (g/cm^3)	4.5
dE/dx_{mip} (MeV/cm)	5.6
Light Yield (Photons/MeV x 10^3)	40 - 50
Light Yield Temperature Coef. (%/ ^{o}C)	0.1
Peak emission (nm)	565 nm
Refractive Index at Emission Maximum	1.79
Decay Time (ns)	940
Hygroscopic	slight
Radiation Hardness (rad)	10^3-10^4

Table 3.5: *Fundamental properties of CsI(Tl)*

contained within a cylinder whose radius R_M is known as the Molière radius. This is given by equation 3.1.

$$R_M = X_0 \frac{E_s}{E_c} \tag{3.1}$$

where X_0 is the radiation length for the particle within an absorber, E_s is the scale energy ($\approx$ 21 MeV for electrons) and E_c is the critical energy which is defined as the energy at which the ionisation loss per radiation length is equal to the particle's energy.

3.3.4.2 Detector Design

The goals of the BaBar experiment led to the Electromagnetic Calorimeter being a homogeneous cesium iodide crystal design[31]. Caesium Iodide was chosen as the scintillator due to its high light output and short decay time, as well as the principal wave length of its scintillation light being well within the range acceptable to silicon photodiodes. The full properties of CsI(Tl)are shown in table 3.5. The main problem with CsI is its hygroscopic nature meaning that the crystals must be maintained within a very well controlled environment. It is also a plastic material and so cannot be considered as any part of the structure of the detector. The calorimeter was also the most expensive component of the detector to construct.

The calorimeter covers the solid angle from -0.775$\leq$ cosθ $\leq$0.962 in the laboratory frame (-0.916$\leq$ cosθ $\leq$0.895 in centre of mass). The scintillation light is collected by

photodiodes mounted on the rear face of the crystals. This was necessary since the calorimeter is mounted within the B-field which makes photo multipliers unusable. A cross-section through the calorimeter is shown in fig 3.12. There are 5760 crystals in the barrel section, mounted in 48 polar angle rows of differing crystal lengths. The rear most sections of the barrel have crystals of length $16.1X_0$; moving toward the forward end the crystal length increases by $0.5X_0$ each seven crystals up to a length of $17.6X_0$in the most forward region, with 120 crystals in each ϕ ring.

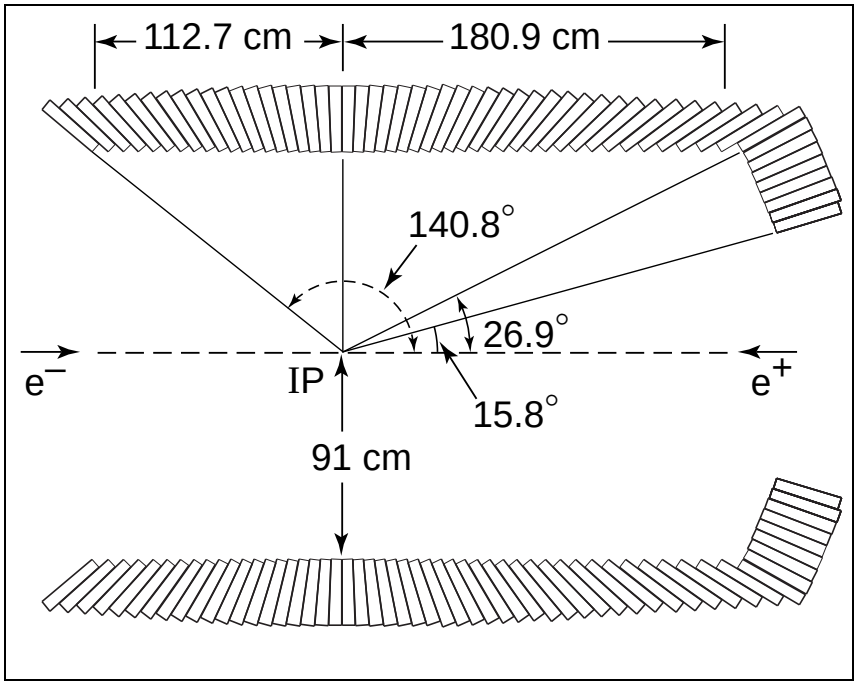

Figure 3.12: *Projection of the Electromagnetic Calorimeter in Z*

The barrel construction is done using modules. These are made of 300μm carbon fibre to reduce the material in front of the crystals. These contain 21 crystals each arranged in a 7 x 3 matrix in θ and ϕ respectively, covering a solid angle corresponding to -0.775 $\leq \cos\theta \leq$ 0.892 in the lab (-0.916 $\leq \cos\theta \leq$ 0.715 in the centre of mass). The strong mount is done from the back plate, which also contains all the services for the modules as well as the readout electronics. The only additional calorimeter material in front of the crystals is the radioactive source calibration system pipe work. This will be discussed later.

The End-Cap of the EMC is constructed slightly differently. It has 20 modules arranged in ϕ. They are of conic section with a minimum gap between the end of the barrel and the outer radius of the end-cap of 2mm. There are 820 crystals arranged

in 8 rows, these crystals are all $17.6X_0$ in length. There is a ninth row, though this is currently filled with lead shielding blocks. The total coverage by the endcap is $0.893 \leq \cos\theta \leq 0.962$ in the lab frame ($0.718 \leq \cos\theta \leq 0.895$ in the centre of mass frame). Due to the construction of the modules for the end-cap there is unequal ϕ segmentation in the endcap with 120 crystals in the 3 outer most rings, 100 in the next 3 and 80 in the last 3 rings. This means that the contribution of each part of an endcap module to the readout system is complicated somewhat.

A cross-section through a single crystal is shown in fig 3.13. Here you can see the mylar wrapping as well as the location of the photodiodes used for readout.

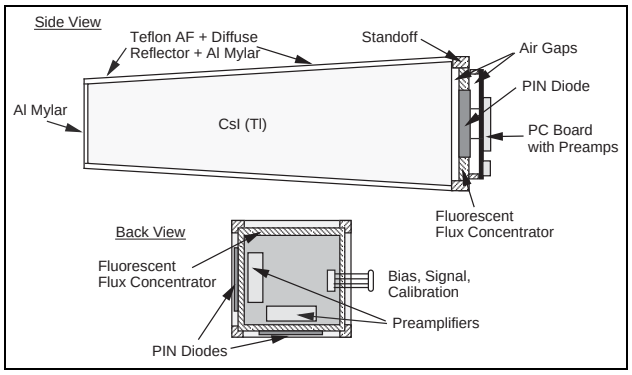

Figure 3.13: *The structure of a crystal in the EMC*

The target photon energy resolution at a polar angle of 90^0 to the IP is given by equation 3.2.

$$\frac{\sigma_E}{E} = \frac{1\%}{\sqrt{E(GeV)}} \oplus 1.2\% \tag{3.2}$$

With the constant term made up of the following, front and rear leakage ($\leq$0.5%), inter-calibration errors (0.25%) and light collection non-uniformity ($\leq$ 0.5%). This expression though does not include electronic noise or inter-beam backgrounds. The energy resolution is degraded at each end of the barrel due to the staggered arrangement of the crystals and large amounts of inactive material in front of the crystals.

3.3.4.3 The Readout System

Unlike all other major detector components, the EMC system digitisation of event information occurs within the front-end electronics with all event buffering and signal shaping done off detector in the *BABAR* electronics house. The crystal readout follows the chain described below[32].

Photodiode → PreAmplifier → ADB → IOB → UPC

On each crystal there are 2 photodiodes directly attached to the rear surface of the CsI crystal. Also mounted on this subassembly are the preamplifier chips and the input fibres for the Light Pulser system. The readout system has a different architecture in the barrel and endcap and these will be described separately here.

For the barrel each fanout board connects to 12 crystals arranged in a 3 (ϕ) by 4 (θ) matrix. Six fanout boards cover half a crystal subassembly strong-back. Each fanout board connects directly to an analogue to digital converter card (ADB). The joint between fanout and ADB occurs across a bulkhead introduced to improve gas tightness of the barrel modules for cooling as well as allowing ADB servicing without disturbing the connections from fanout to crystal sub-assemblies. Six of these fanout/ADB combinations are connected to each input/output board (IOB). These are used to interface between the electrical signals that are produced from the ADBs and the optical signals that are passed into the *BABAR* electronics house to the untriggered readout modules (UPC). On each IOB are 3 Finisar transmitters with the output from 1 IOB corresponding to 1 UPC. In the barrel there are therefore 40 UPC's in ϕ by 2 in θ. This corresponds to 8 logical DAQ crates for the barrel with a total of 80 UPC modules.

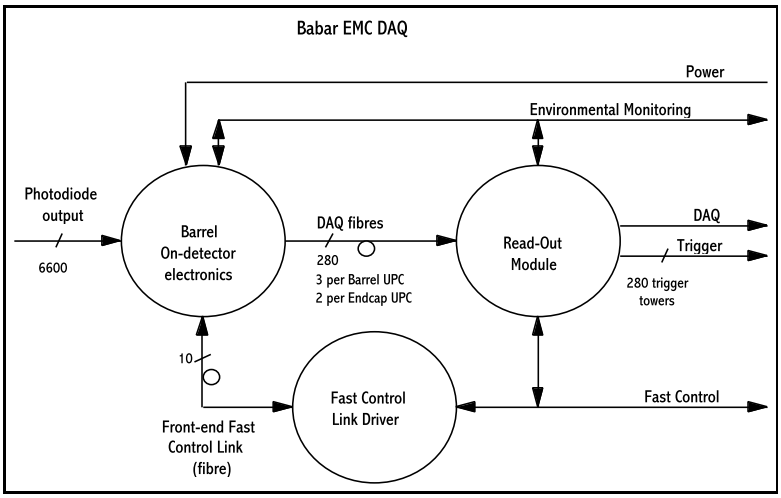

Figure 3.14: *Block diagram of the EMC readout electronics*

In the endcap each fanout board connects to all crystals in a module (45 crystals). To each of these fanout boards 4 ADB cards are connected which are then in turn connected to 1 IOB per endcap module. This arrangement has necessitated physically different designs for a lot of the electronics in the endcap from that in the barrel.

One consequence of this is that each endcap IOB has only 2 Finisar transmitters and correspondingly the UPC boards are different for the barrel and endcaps with only 2 optical fibre inputs in the endcap boards.

The above sections deal with the readout of data from the detector but it is also necessary to be able to communicate with the on-detector electronics from the DAQ crates. This is to allow the passing of the 59.5 MHz clock for system alignment both to and from the IOBs and the relaying of fast control commands to the IOBs. For this each DAQ crate has a normal triggered readout module connected to a transition board (TRB). This has a normal *BABAR* standard C-link and D-link arrangement (described in more detail within section 4.3.1). The return of the clock signal from the IOB to TRB means that the system will be self-aligning, thereby reducing the chance of data transmission errors. The system also has monitoring of all environmental conditions such as crystal temperature, module humidity and electrical voltages on detector.

3.3.4.4 Calibrations

It is important to know the behaviour of the calorimeter over the whole energy range of BaBar. Of particular importance is the monitoring for the effects of radiation damage both in the short and long term[33]. The calibration and monitoring system for the EMC consists of the following components:

- A charge injection system to linearise the electronic response over the 4 ADC ranges to better than 0.1%
- A radioactive source using 6.1 MeV photons from the ^{16}N β - γ cascade for setting the initial energy scale per crystal to better than 0.5%
- A light pulser system for conveniently tracking short term changes in the system behaviour to better than 0.5%
- Using physics processes with known behaviour to determine individual crystal energy scales to better than 0.5%

The electronic calibration uses known charge deposits in each preamp to determine the linearity of behaviour of each of the four ranges on the ADC chips so as to track behaviour in the important switching regions between ranges. This also gives a measure of the electronic noise level.

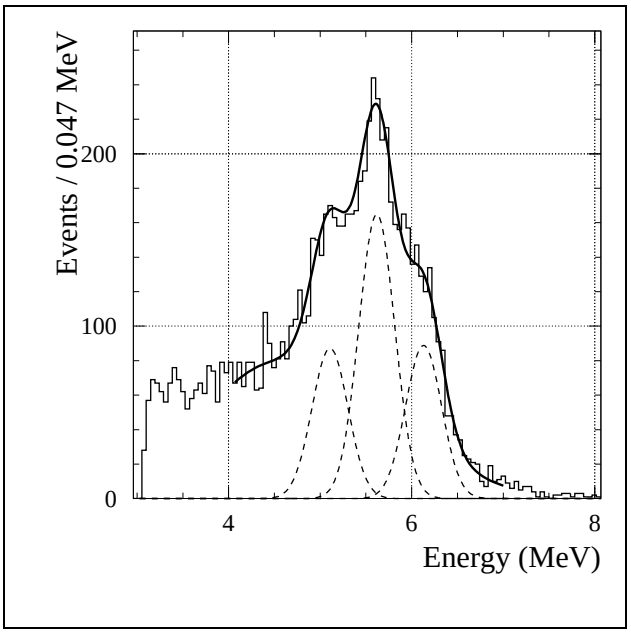

Figure 3.15: *The energy spectrum from the source calibration system*

The main use of the radioactive source calibration is to determine initial single-crystal calibration constants and to monitor changes in the light collection efficiency due to radiation damage and optical decoupling. The main advantage of this system is that it gives a completely known and stable photon-energy deposit in a single crystal. The energy peaks from the source calibration system at 6.13 MeV with peaks at 511 and 1022 eV lower are shown in fig 3.15. This is used as the initial point in the response curve for each crystal and as such is used to establish the Bhabha calibration procedure. In combination with the Bhabha procedure it will provide continuing calibration of the energy dependence of single crystal response which is a necessity in the harsh PEP-II environment. This is particularly true for those crystals that are not hit by coincident Bhabha events i.e. those perpendicular to the IP. For these a more detailed knowledge of crystal behaviour at lower energies is needed to calculate the energy deposit in each from a Bhabha that is not incident directly on a single crystal.

The main purpose of the light pulser calibration system is for monitoring the relative crystal responses and also to provide a convenient and flexible diagnostic tool for the complete readout chain from light collection through to DAQ. The amount of energy deposited in each crystal is equal and can be altered in intensity. The advantage of this system is that it can run at a very low rate during datataking or for short periods during top-off of the storage ring to provide quick feedback on problems. The system itself consists of 5 Xenon lamps which feed light into the rear face of each crystal

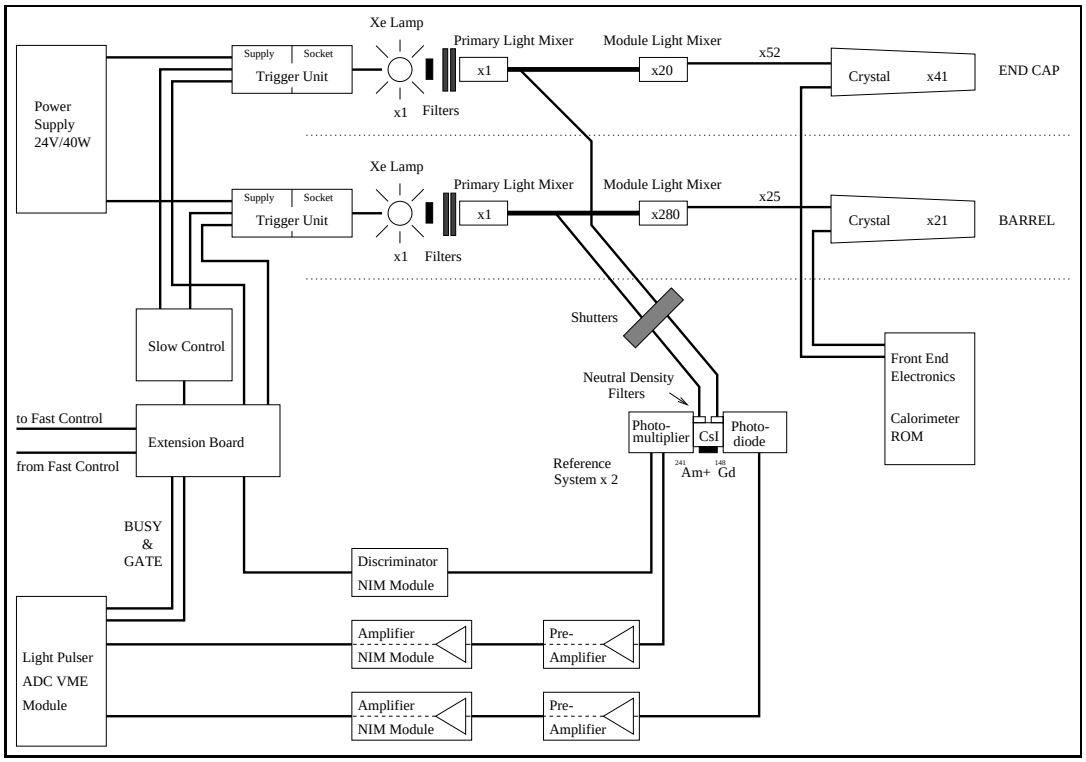

Figure 3.16: *The design of the light pulser calibration system for the EMC*

through an arrangement of filters, primary and secondary fibres, and light mixing bars. A diagram of this setup is shown in fig 3.16. The light pulser system has been designed to maintain light stability for approximately 1 week and any changes over a longer period will be taken into account by cross-calibration with earlier taken data. The light output from the system is adjusted to match as closely as possible the scintillation spectrum of the CsI crystals. More details may be found in [34].

The usage of Bhabha events to calibrate a calorimeter has been used many times for example the Crystal Ball and CLEO experiments, though the kinematics of Bhabha events are not as simple as those at a symmetric e^+e^-collider. In general, calibration of the crystal energy is given by $E = \Sigma c_i \epsilon_i$ where c_i is the crystal calibration constant, ϵ_i is the energy measured in the crystal and i is the crystal number.

Initially the performance of the calorimeter was limited by higher than expected electronic noise from the FEE. This was traced to the CARE amplifier chip which it was found would go into saturation upon switching from one amplification range to another. This non-linearity of behaviour is best shown in figure 3.17(left). This also shows the corresponding curve after the ADB's and grounding and shielding scheme

were altered to reduce crosstalk and had a slight change to the overall design implemented. This was an example where the light pulser system was able to directly diagnose and check that the solution had actually worked.

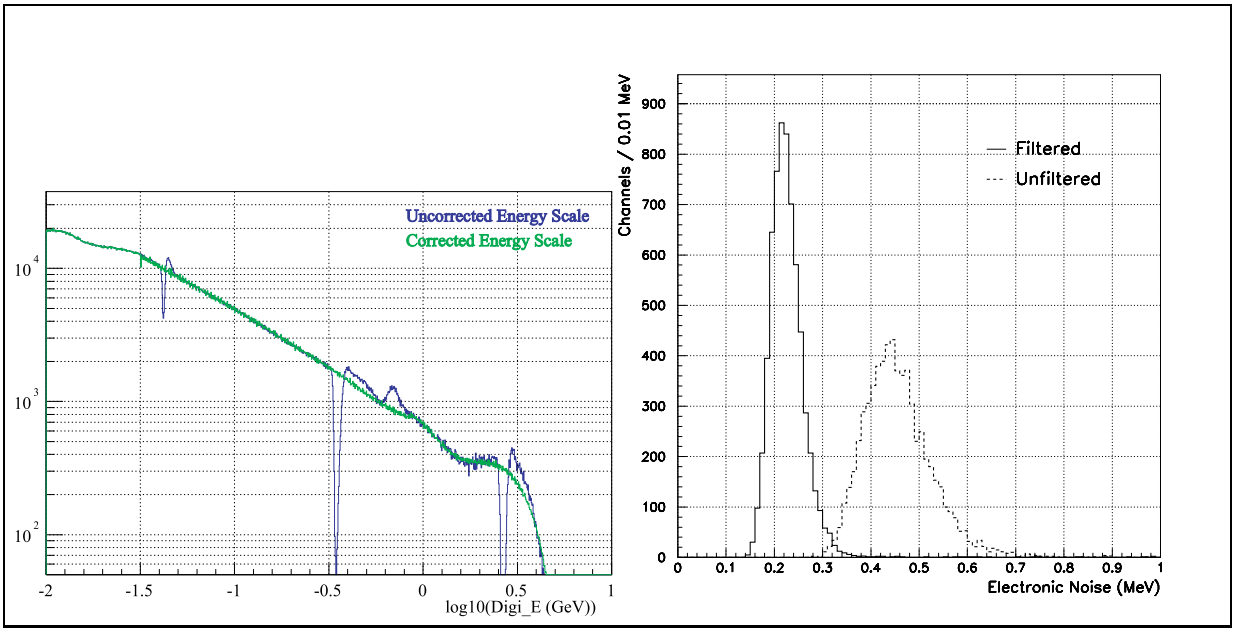

Figure 3.17: *(left) The linearity of the energy deposits with respect to the digi energy and (right) The electronic noise present in the EMC system before and after digital filtering*

The contribution of electronic noise within the readout chain is measured as the RMS of the pedestal energy applied to each crystal. Figure 3.17(right) shows the distribution of electronic noise for all channels with and without digital filtering implemented with an average of 230(440) keV with (without) filtering. Measuring the autocorrelation functions of the digital filter weights shows that the changes to the grounding scheme have reduced coherent noise present in the system to a negligible level when compared to incoherent noise.

The energy resolution of the calorimeter is measured using a combination of the 6.13 MeV radioactive source, $\pi^0$and η decays to $\gamma\gamma$ at energies of less than 1 GeV and electrons from Bhabha scattering at greater energies. This yields the results shown in figure 3.18(left). An addition point in the curve may be found using the decay $\chi_{c1} \rightarrow J/\psi\gamma$ at 500 MeV. This is compared with the Monte Carlo predictions including electronic noise and beam backgrounds. Angular resolution is measured again using the $\pi^0$and η decays to $\gamma\gamma$ due to the properties of the two decay products having

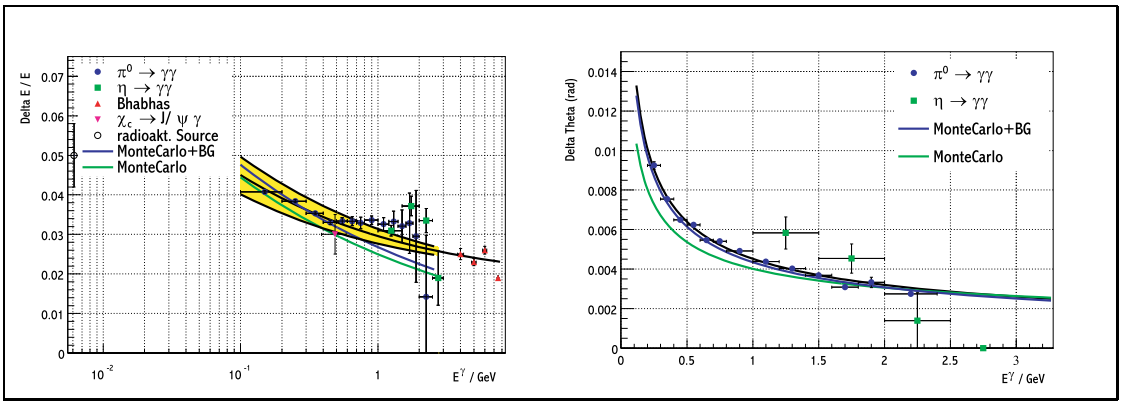

Figure 3.18: *(left) The energy resolution of the EMC over the complete energy range, (right) The angular resolution of the EMC*

approximately equal energy and a known angular structure. The curve produced shows a variation between 12 mrad at low energies and 3 mrad at high energies.

3.3.5 The Instrumented Flux Return

3.3.5.1 Detector Design

The magnet yoke is segmented using a plate structure separated by Resistive Plate Counters (RPC's) between each plate in the system. This is intended for muon and (in conjunction with the EMC) neutral hadron identification. The basic structure of the detector is a hexagonal barrel with endcaps covering the forward and backward regions (See fig 3.19). The solid angle coverage of the detector is -0.921$\leq \cos\theta \leq$0.955 in the lab frame and -0.825$\leq \cos\theta \leq$0.983 in centre of mass. Each section of the detector is segmented into 18 iron plate layers with a graduated thickness ranging from 2cm for the inner plates to 5cm for the outermost. This was as a result of Monte Carlo studies showing K_L^0 and μ identification efficiency increasing the thinner the absorber[31]. The total thickness of the plate layers is 65cm for the barrel and 60cm for the endcap doors. These are vertically divided so that they can be rolled out of the way for maintenance of the inner detector components

Within the barrel sextants there are 21 layers of RPC's. They start with a double layer of cylindrical RPC's between the EMC and magnet and then planar RPC's are interleaved with the iron layers. This gives a total detection area in the barrel of $\approx$ 1000 m^2. The endcap doors are also segmented horizontally into 3 sections. The spacers that are used must be very strong to withstand the 1.5 T field returning through them and also totally electrically isolating. For safety reasons an argon -

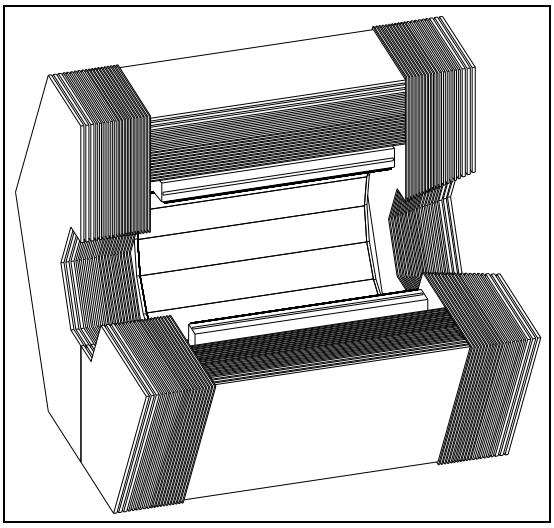

Figure 3.19: *The Structure of the IFR Detector showing also the position of the superconducting coil*

freon ($C_2H_2F_4$) mix was chosen with 4.5% isobutane. This enables the chambers to operate in streamer mode which both improves efficiency and lifetime. The current average hit efficiency is ≈82%. The losses are due to problems with dark currents (the current that the RPC draws when not operating) causing the detector to warm and the gaps between sextants and the barrel - endcap.

3.3.5.2 The Readout System

The Resistive plate chamber (RPC) principles of operation are given in [36] with the system being used in many previous experiments [37]. Fig 3.20 shows a cross-section through an RPC as used in the *BABAR* detector. Positional information is generated by the orthogonal layout of the readout strips on each side of the RPC as well as its known position within the IFR structure.

The IFR readout system is relatively simple using custom Front End Readout Cards (FEC) to readout the RPC information, this is then passed into TDC circuits to allow a 1 ns resolution on the timing information for each hit. Due to the number of channels each FEC reads out 16 channels. To ensure reliability a strip in an RPC is connected to 2 different FEC cards. The output from the FEC is then fed into a custom interface card which produces digital optical output for transfer to the Readout Modules located in the counting house.

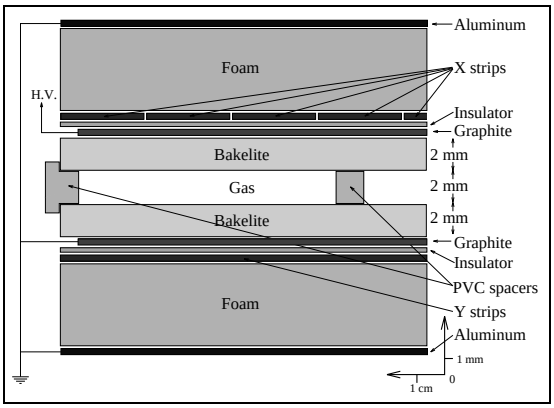

Figure 3.20: *A cross-section through an RPC as used in the BABAR IFR*

3.3.6 The Magnet

The *BABAR* superconducting solenoid produces a central magnetic field of 1.5 T. The field uniformity is $\pm 2\%$ within the tracking volume ($r < 80\,\text{cm}, -1.17\,\text{m} < z < 1.91\,\text{m}$). The superconducting windings consist of 20 Rutherford NbTi/Cu wires embedded in a pure aluminium matrix, using a coextrusion process. The windings are cooled to an operating temperature of 4.5 K by liquid helium. They are directly wound inside an aluminium support cylinder and impregnated with epoxy. To meet the requirements for field uniformity the current density has to be higher at the ends than in the central region. Therefore there are two different winding types, thinner windings at each end (3.6 mm) with thicker ones in the central region (6.2 mm). In total there are 735 turns made up by 315 turns in the central region and 210 turns in each of the end regions. The superconducting solenoid is surrounded by a cryostat consisting of a tubular vacuum vessel containing the cold mass and thermal shielding held at 87K. The solenoid is located outside the calorimeter, between the inner cylindrical RPC and the IFR see figure 3.19. The operating current is 6830 A and the peak field at the windings is 2.5 T. For the full system description see [38].

3.3.7 The DAQ and Trigger System

The Level-1 Trigger system receives continuous information from both the Drift Chamber and Electromagnetic Calorimeter. This information is processed in hardware and Level-1 Accept signals are then generated and distributed to the rest of the DAQ system. Since no event information is available from fast detector elements the Level-1 trigger must identify interesting beamcrossings and also determine the time that such events occurred. As can be seen in fig 3.21 the trigger system interacts in a significant way with 6 different parts of the BaBar electronics system:

- Drift Chamber FEE
- Calorimeter Readout Modules
- Instrumented Flux Return FEE
- Fast Control System
- DAQ
- Slow Controls and Monitoring

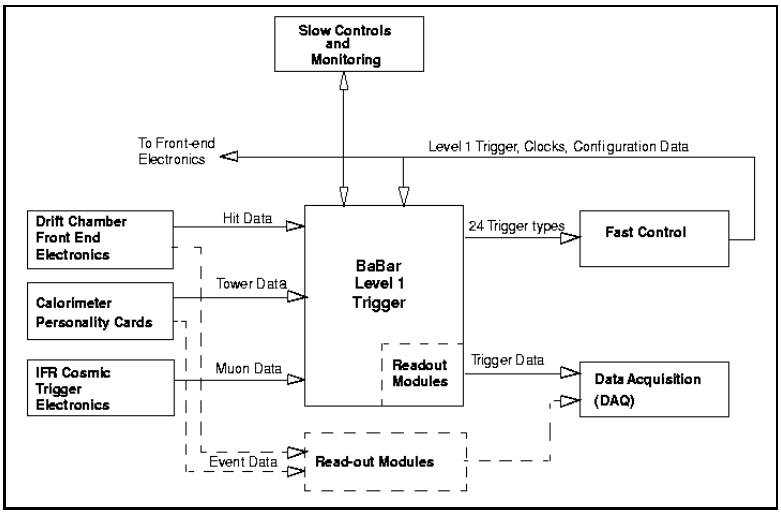

Figure 3.21: *Overall Context of the Level-1 Trigger*

The entire DAQ and trigger system is described in much greater detail within chapter 4.

3.4 Summary

In this chapter a description of the mechanics of the PEP-II storage ring as well as key elements of the *BABAR* detector have been given. These components allow the precision measurement of *CP* violation using a state of the art particle physics facility.

Since *BABAR* has now been running for over a year it is appropriate to include some comparisons between the Technical Design Report performance goals and the current results from actual data taking. This is summarised in table 3.6.

Detector	Parameter	TDR Value	Current Performance
PEP-II	Luminosity	3×10^{33} cm^{-2} s^{-1}	3.1×10^{33} cm^{-2} s^{-1}
	No. of Bunches	1658	692
	LER current	2140mA	2140mA
	HER current	610mA	920mA
SVT	Hit Resolution	15μm	12μm
DCH	Hit Resolution	140μm	125μm
	dE/dx Resolution	7%	7.5%
DIRC	Cherenkov AngleResolution	2mrad	2.8mrad
EMC	$\frac{\sigma_E}{E}$(Stochastic Term)	1%	(1.33±0.16)%
	$\frac{\sigma_E}{E}$(Constant Term)	1.2%	(2.1±0.06)%
	σ_θ	2.4mrad	3mrad
IFR	RPC hit Efficiency	97%	78%(Barrel) 84%(EndCaps)
TRG	$B\bar{B}$ efficiency	99.9%	99.9%
	Latency	12μs	11μs
DAQ	L1Accept Rate	2kHz	≈750Hz
	L3 Logging Rate	100Hz	≈85Hz

Table 3.6: *Current Detector performance compared with TDR*

As can be seen the majority of PEP-II and *BABAR* detector components are performing to at least design specification. The only exceptions to this are:

- The DIRC whose Cherenkov angle resolution is slightly below specification. This is due to light yield from the quartz radiators not being as prolific as originally expected due to the quality of the polishing of the bars.

- The EMC energy resolution is also slightly below original specification though this is being recalculated due to many improvements in the FEE of the system to remove most of the coherent electronic noise that was present during run-1. The angular resolution is currently being studied to find the cause of the slight performance deficiency.

- The IFR performance is the greatest concern since this is due to intrinsic problems in the design. This is due to underestimating the heat dissipation properties of the iron segments of the detector. This has led to large portions of the detector having to be switched off due to runaway dark currents as the RPCs warm. To partially cure this the external faces of all surfaces of the IFR have been lined with cooling pipes to try to keep the iron as cool as possible. Further

investigation of these problems is underway to find permanent solutions as soon as possible.

Chapter 4

The *BABAR* Trigger, Online and DAQ System

4.1 Introduction

This chapter will give an introduction to the *BABAR* trigger system. Both Level 1 and Level 3 will be discussed as well as the underlying data acquisition system. The beam-crossing rate of 237 MHz and the high luminosity of PEP-II proved to be a major challenge to the trigger and DAQ systems. To this end it was decided that the primary event selection would be implemented in hardware with further selection made in software. In the initial design the possibility for inclusion for a software Level 2 trigger was included should backgrounds be high enough that the two stage trigger was unable to cope. For simplicity the readout control hardware should also be as generic as possible.

4.2 The Trigger System

4.2.1 Design Requirements

Though the primary objective of the *BABAR* detector is to study *CP* violation, the PEP-II storage ring also offers a new environment in which to study other B-physics phenomenology as well as τ pair and $\gamma\gamma$ physics. During the initial design of the trigger a set of physics considerations were proposed as shown in table 4.1 [39].
It was important though that the definition of the trigger system not be such that it would effectively define what physics analyses could be performed. To this end the design was chosen that gave maximum flexibility though maintained strict quality control measures. The trigger must also be able to cope with the study of channels having extremely small branching ratios such as some of the charmless decays, while still rejecting background below the level that reduces data acquisition system performance to such an extent that unnecessary deadtime is introduced.

Physics Data Samples	ϵ	$d\epsilon$	f
$B\bar{B}$ from the Υ(4s): *CP* Channels	99%	0.5%	1
$B\bar{B}$ from the Υ(4s): Non-*CP* Channels	99%	0.5%	1
B Physics at the Υ*(5s)*	99%	0.5%	1
Charm Physics	95%	2%	1
Continuum $q\bar{q}$(u,d,s)	95%	2%	5
τ Physics: Rare Decays	90%	10%	1
τ Physics: Lorentz Structure	95%	1%	5
τ Physics: Branching Ratios	95%	0.1%	10
$\gamma\gamma$ Physics: Exclusive Meson Pairs	90%	4%	5
$\gamma\gamma$ Physics: All Neutrals	80%	4%	5
$\gamma\gamma$ Physics: Exotic Resonances	90%	4%	1
$\gamma\gamma$ Physics: Tagged	90%	4%	1

Table 4.1: *Principal Trigger Efficiency Requirements for each Physics Data Sample. Listed are the minimum efficiency goal, maximum tolerable uncertainty in efficiency and maximum allowable prescale factor*

There are also physics requirements that are needed, not for process study, but for detector/accelerator monitoring and calibration. These are primarily the Bhabha events, 1 and 2 prongs, radiative and non-radiative. Principally these are used for luminosity determination and energy scale determination of the calorimeter (as described in section 3.3.4.4). These processes are recorded at a predetermined prescaled rate.

The detection of different types of events in the Level-1 trigger is made generally using the number of tracks that an event has as a first indicator for events such as the multi-hadrons; these type of events encompass the channels such as $B^0 \rightarrow J/\Psi K^0_s$ that are used for the easiest measurement of *CP* violation, though this type of event will also leave many deposits in the calorimeter which means that the most efficient method is the combination of drift chamber and calorimeter trigger primitives and either two tracks or two deposits in the calorimeter of varying energy for either the Bhabha, $\gamma\gamma$ or $\tau\tau$ events. This forms the basis of the experimental event selection.

Beam crossings at PEP-II occur every 4.2 ns, which in terms of readout of an electronic system can be considered as essentially continuous. To still be able to investigate CP violation within this environment a very precise trigger is necessary causing the trigger

system to be constructed within very tight design restrictions [39]. The main design requirements are described below:

- Provide a platform wide strobe signal (Level-1 Accept) to initiate feature extraction in all detector component readout electronics.
- Have a fixed maximum latency between signal generation in the detector and trigger decision (Level-1 Accept) output of 12μs with a maximum jitter of 1μs due to the fixed event buffer length of all detector component readout systems.
- Initiate collection of all data associated with an event from all detector components (Event building)

Due to the small latency requirement it is necessary that initial processing be performed in hardware on a minimised subset of available data (trigger primitives)[40]. In the Electromagnetic Calorimeter Trigger (EMT) the trigger primitives are a preprocessed section of the calorimeter data which will be from here on described as towers, whereas the Drift Chamber Trigger DCT receives a minimised set of drift chamber information known as cells. Due to restrictions in the overall capability of the DAQ system to cope with a data transfer rate off-detector for the major subsystems the maximum Level-1 Accept rate is set at 2 kHz.

To achieve the design goals for the trigger not only in its operation but also for studying its behaviour, the following criteria were decided upon.

- Orthogonal event selection criteria
- Redundant event selection for each orthogonal selection
- Recording of all trigger primitives for selected events, in the case of the EMT energy sums and tower bit maps
- Sharp efficiency turn-on
- Straightforward to model in simulation
- Sufficient monitoring, calibration and diagnostic testing to ensure reliability of trigger decisions

The use of orthogonal but still redundant event selection ensures that any degradation of one of the primary trigger supplying detectors should have little or no effect on the overall performance of the system. This also enables easy study of the system performance. This is further enhanced by the recording of all system input and output

data and supply of these to the offline system for recording, as well as the design of the system to allow easy modelling in Monte Carlo for comparison.

During operation it is also necessary to be able to monitor the system operation based not only on its outputs but also the actual process of constructing the trigger primitives. To this end the systems were designed to enable a software model to be run on the system at the same time in real-time receiving the same inputs as the hardware algorithms. This system is defined as the 'Spy' and is used to flag errors in processing. Constructing a trigger with high efficiencies for Υ and $c\bar{c}$ events is relatively straightforward due to their high multiplicity, though the ability of the system to also have high and measurable efficiencies for the low multiplicity events such as $\tau^+\tau^-$ at the same time is significant.
Operationally the system must operate with a dead-time of less than 1% with all software interfaces adhering to the *BABAR* standards of online and offline coding. This ensures smooth system maintenance hand-over as new personnel come into the experiment. The interface to the calorimeter must also ensure that for each of the 3.7 MHz samples sent from the UPCs, trigger towers are created using a configurable threshold applied to crystals added to the tower sums. They must also have a large enough dynamic range to ensure that saturation occurs at full scale, preferably corresponding to an energy range that is far outside the operational ranges of the PEP-II accelerator.

4.2.2 The Level-1 Trigger

The Level-1 trigger system can be split up into 3 major components that will be described in the following sections. The functionality of the Level-3 trigger will also be discussed.

4.2.2.1 The Level-1 Electromagnetic Calorimeter Trigger (EMT)

Since the EMT was Bristols' responsibility, and most of the hardware work concerning the trigger was done on the EMT, more details can be found in chapter 5. Here follows a brief description:

The calorimeter is split into 40 ϕ strips, with each containing 7 θ segments. These make up 280 input towers. The basic trigger primitives of the system are as follows. The first 3 are active over a whole strip in ϕ whereas the last 2 are positional triggers for veto and clear selection of certain types of interactions: (this is shown in fig 4.1). When the trigger fires it is an indication that an energy deposit has been found within the ϕ strip with an energy greater than a certain threshold. They are as follows:

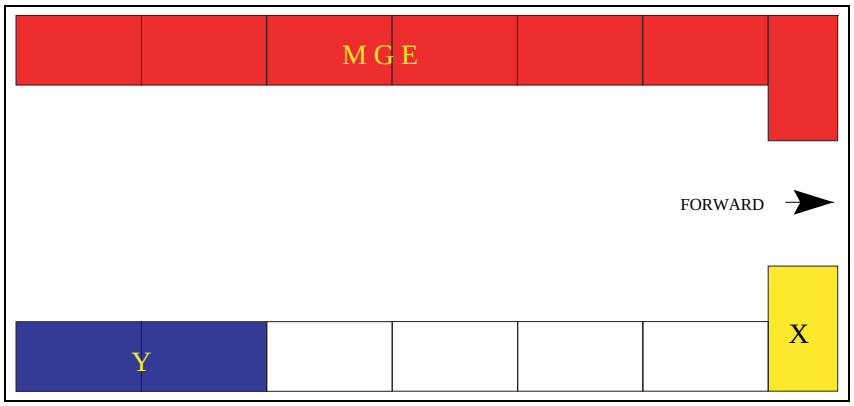

Figure 4.1: *A Schematic representation of the tower layout in the L1EMT System using a longitudinal slice through the EMC*

M 108MeV This is intended to catch minimum ionising particles as they pass through the calorimeter.

G 500MeV This is intended to pick up Gamma radiation in the calorimeter.

E 1GeV This is primarily to detect high energy Electrons.

The 2 positional triggers:

X 108MeV If a deposit is seen in the forward endcap then the X trigger line fires. This is intended to be used to reduce the background and as such operate as a veto for low energy beam gas interaction particles.

Y 2GeV The calorimeter is further separated with the 2 most rearward towers for each ϕ strip contributing to the Y trigger primitive. This has a very high independent threshold and is intended to be used to filter out Bhabha events which at design luminosity will have a very high rate and could swamp the DAQ system.

4.2.2.2 The Level-1 Drift Chamber Trigger (DCT)

The Drift Chamber Trigger (DCT) actually consists of three different types of module each performing one part of the trigger object generation process. They are the Track Segment Finder (TSF), Binary Link Tracker (BLT) and P_t Discriminator (PTD)[41]. The path of data into the system from the Drift Chamber Front End Electronics is shown in fig 4.2.

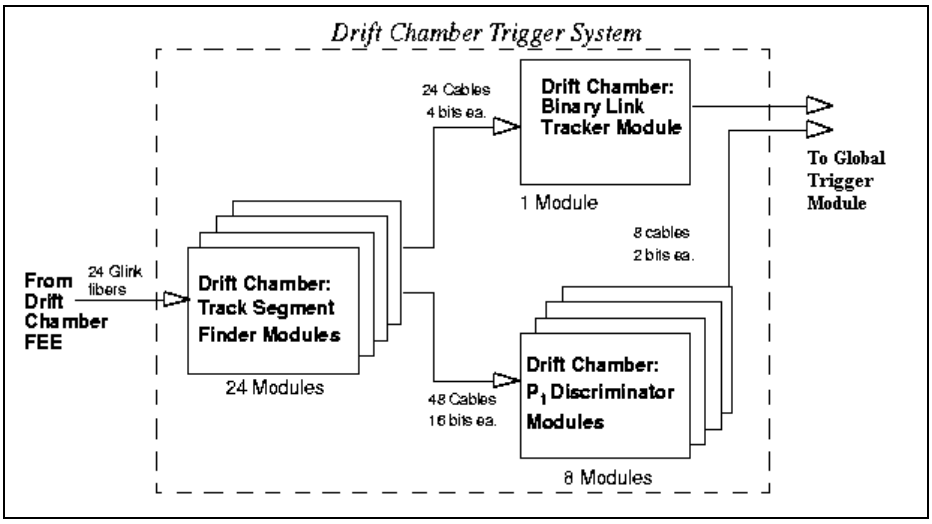

Figure 4.2: *The L1 DCT System Showing Inputs and Outputs*

Track Segment Finder (TSF) These modules receive inputs from the 7104 cells of the Drift Chamber. There are 2 different types of TSF, the TSFX which monitors super layers 1 - 4 and 8 - 10. and TSFY which monitors layers 5 -7.

Each of the DCH cells have a separate TSF "Engine" chip. The search for a track segment is organised in terms of pivot cells. These are the third layer of each super-layer. Each pivot cell and its surrounding cells constitute a pivot group. This is illustrated in fig 4.3. Even though some of the surrounding cells are shared with other pivot groups there is only ever one pivot cell per pivot group.

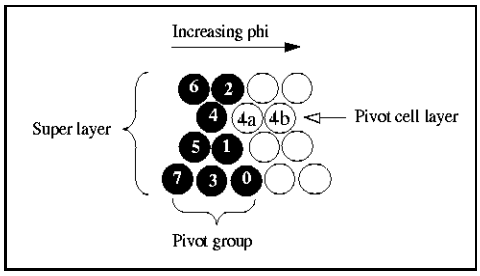

Figure 4.3: *The Arrangement of a Pivot Group as used in the TSF*

The outputs from the TSF boards are dependent on the quality of the track segments found. There are 2 different outputs that can be given.

- 2-bit output to a data volume reduction chip mounted on the board. This signifies the weight of the track segment found.

- If the segment is associated with a track that has had a hit in the outermost super-layer then an output is also sent to the P_t data reduction chip. This data output also contains the same weight information that was sent to the BLT data reducer. The cell ϕ positions are the remaining parts of this information.

Criteria for Valid TSF segments: a valid TSF segment typically consists of hits close together in time on at least 3 or 4 layers of the pivot group. The criteria are listed below:

1. Passes through the pivot cell.
2. Also passes through cells which represent at least 2 other layers (preferably 3) of the super-layer. Track segments that have 4 hits in them are called 4/4, those with 3 layers are 3/4.
3. If there are three hits in the super-layer not including the pivot cell then a 4/4 is made up by artificially including the pivot cell.
4. Any hits that fit the criteria of the above 3 must occur within a time interval of 807 ns.
5. The azimuthal angle must be within a predetermined configurable limit.

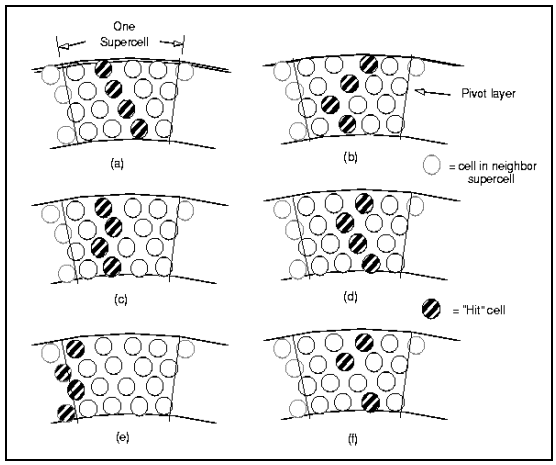

Figure 4.4: *Examples of valid track segments. The supercell shown contains four cells in each layer. Sketches (a) - (d) show four basic segment-finder patterns with the same pivot cell; (e) illustrates a boundary track; (f) illustrates a valid 3/4 track segment.*

These criteria are illustrated in fig 4.4.

Binary Link Tracker (BLT) This module takes as inputs the track segments from the 24 TSF modules. It starts a search for continuous tracks in the DCH. A

continuous track is one that has hits in every super-layer. It also makes the decision on whether a track found is an A or B track. The definition of these are below:

- A Track: This is a track that exit the DCH through the outermost super-layer 10.
- B Track: This signifies a track that has passed through at least super-layer 5.

Since it would be quite possible for a track to not cause hits in every super-layer (due to inefficiencies, dead sectors etc.) it is necessary that the criteria for passing a track be loosened so that it can have up to 2 layers in the path of the track missing. Several criteria must be satisfied if these missing segments are not to alter the efficiency of the system though and are described below:

1. Either or both layers 5 and 6 must have been hit.
2. Only one of layers 1, 2, 3, 4, and 5 may be missing a hit.
3. Only one of layers 6, 7, 8, 9, and 10 may be missing a hit.
4. (a) Either or (b) both of criteria 2 and 3 are allowed for a given track.

The output from the BLT is passed straight to the Global Trigger.

P_t Discriminator (PTD) The output from the TSF modules is also passed straight to the PTD. This uses layers 7 or 10 as seeds and searches within a predetermined set of cells per super-layer according to a lookup table that is loaded during configuration. The P_t threshold is also loaded at this time. Since it is quite possible that a track will be bordering cells then it essential that neighbour information is available. If the PTD passes a track then another trigger object is flagged this is an A'.

4.2.2.3 The Level-1 Instrumented Flux Return Trigger (IFT)

The last of the trigger subsystems to provide input to the Global trigger is the Instrumented Flux Return Trigger[42]. This is primarily used for cosmic ray rejection, though later requirements introduced included a 1 muon trigger object for the backward endcap so as to help in the calibration of the backward end of the EMC. The IFR system is divided up into 10 independent sectors (6 in the barrel and 2 in each of the endcaps). As can be seen in fig 4.6, the outputs from 8 of the 19 RPC layers in the IFR are connected to the IFT. The output from each layer in either a sextant or half door is then fed into the Majority Logic Boards that generate one of the 3

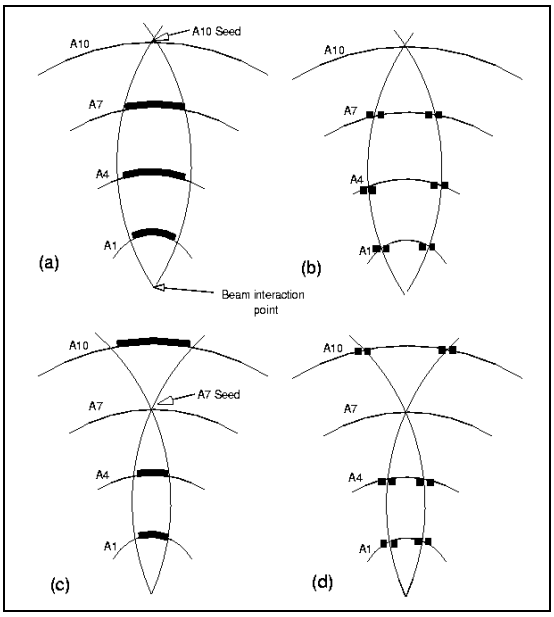

Figure 4.5: *Limits of tracks with P_t > minimum: (a) & (b) for layer 10 seed, (c) & (d) for layer 7 seed*

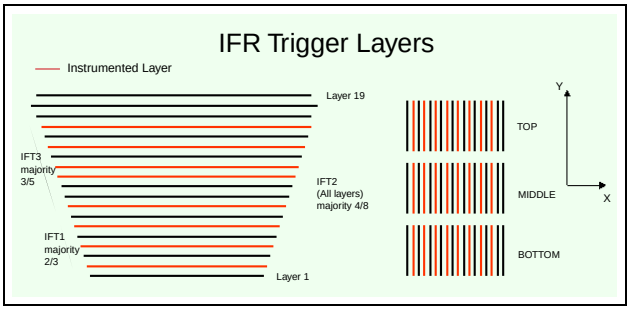

Figure 4.6: *The layers used by the IFT to generate trigger bits*

IFT trigger objects, IFT1, IFT2 and IFT3. These each have a weighting associated with the momentum of an incident particle that would be necessary to generate the particular object with IFT1 having the lowest priority and IFT3 the highest. Only the highest priority object per sector is created. The IFT1 objects have a background rate that prohibits their use exclusively for trigger bit generation, though they are used to study the overlap regions between barrel and endcaps. The output from the majority logic boards are 3 bits for each sector of the detector and so 30 bits in total are passed into the Interface and Synch board. The main functionality of this board is:

- Input signal alignment

- Composite object construction
- Clock synchronisation
- Trigger output word generation
- Latency adjustment

An illustration of the complete IFR → IFT → Global Trigger chain is shown in fig 4.7.

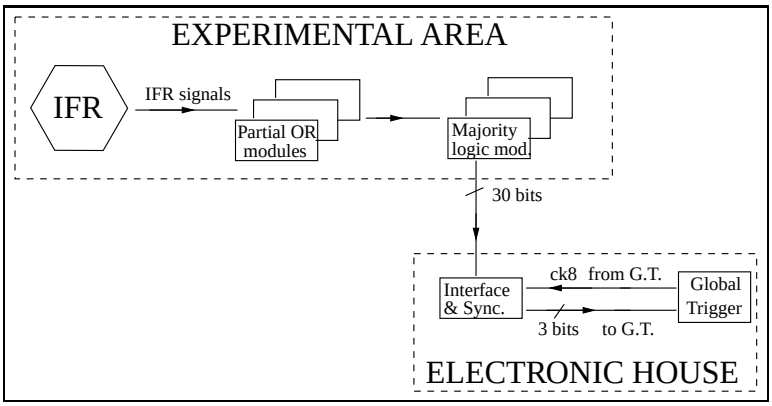

Figure 4.7: *An overview of the IFT system showing data path from detector to Global Trigger module*

The most unusual thing about the IFT in general is that, unlike all other systems in *BABAR*, it does not use the normal DAQ crate configuration with separate fast control electronics. Instead it is physically mounted in the same crate as the Global Trigger module. Since the Interface and Synch board is unable to be configured by software, all the IFT trigger logic is held in lookup tables and Programmable Logic Devices. The IFT may be defined as an untriggered system since it constantly reads the output from the IFR and passes this along to the GLT as a 3 bit stream through the backplane. The bit pattern definitions are shown in table 4.2. Since the readout from the RPC's in the IFR and the functionality of the IFT boards are very fast (≈400– 500 ns) the Interface and Synch board must also have a large delay capability to bring its latency budget within the scope of the other trigger systems. This amounts to approximately $8\mu s$. To allow for configuration of this value there is a maximum $134ns$ adjustment which can be made using 'jumpers' on the board.

4.2.2.4 The Level-1 Global Trigger

The Level-1 Global Trigger (GLT) consists of only one board which receives the input from all 3 of the previously stated systems at a rate of 7.44 MHz[41]. The information

Bit Pattern	Description
000	No Trigger
001	1 IFT3 in backward endcap
010	1 IFT3 in barrel or forward endcap
011	2 back-to-back IFT3
100	1 IFT2
101	2 IFT2
110	> = 2 IFT3 or IFT2
111	Not Used

Table 4.2: *IFT trigger bits as passed to the input stage of the Global Trigger module*

that the GLT receives has been summarised in table 4.3. [1] From these inputs the

Name	No. Bits (ϕ resolution)	Description	Origin
From Drift Chamber Trigger			
A	16	Track that exited layer A10	BLTM
B	16	Track that passed layer U5	BLTM
A'	16	A Track satisfying p_t cuts	PTDM
From Calorimeter Trigger			
M	20	E> 130MeV	TPB
G	20	E> 325MeV	TPB
E	20	E> 810MeV	TPB
X	20	E> 110MeV in Forward End Cap	TPB
Y	10	E> 975MeV in Backward 1/3 of Barrel	TPB
From the Instrumented Flux Return			
U	3	Muon Track Data	IFTB

Table 4.3: *Trigger Objects received by the Global Trigger Processor*

GLT generates 24 trigger outputs that can be configured to match particular physics demands. These are passed directly into the Fast Control System for distribution to other parts of the *BABAR* electronics system. As shown in fig 4.8 the functionality of the Global Trigger module can be divided up into 4 major blocks:

- Delay, Match and Combine:

[1] The values for the EMT thresholds are correct as of 12/10/00. These may have since changed to account for tuning

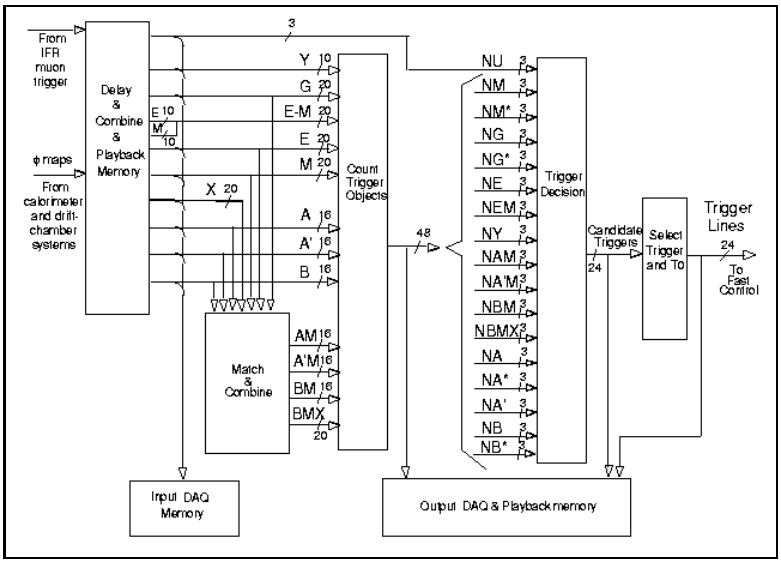

Figure 4.8: *The Internal Data and Memory path within the GLT showing the 4 functional blocks*

Since the space on the GLT module VME card is limited, the signals from the 3 systems providing trigger objects must all be received on a "back of crate" card. This receives the 10 cables from the calorimeter trigger system, 10 cables for the Drift Chamber trigger BLT(2) and PTD(8) modules and 1 cable for the IFT. These are then fed into the Delay, Match and Combine block.

Since the detectors that the separate parts of the trigger system are connected to each use a very different method of particle detection they take widely differing times to construct the trigger primitives. The latency of the different trigger systems is also not equal and the GLT board must have configurable delays for each input line to synchronise all trigger bits within an event. Within the Match and Combine unit there are 5 sets of correlations made between the input trigger objects. The simplest combinations are those between 1 DCT object such as A and 1 EMT object such as M. As can be seen from table 4.3 the number of divisions in ϕ for the DCT and EMT are different. Due to this a special method of adding for combinational trigger lines must be used. This must be able to take into account not only geometric considerations but also that due to the momentum of the incident particle, the curvature of the track will cause an output from the DCT which will cause the GLT to search within a wider region in ϕ for a matching EMT object. To circumvent this problem the GLT makes use of the fact that a single DCT ϕ sector will be subtended by several EMT sectors. A logical OR is made of all possible EMT sectors that could match with

the DCT sector, the output from this is then AND-ed with the DCT information to create the matched object. This is repeated for each of the 16 DCT ϕ bins.

The trigger combination BMX nearly replicates this method of logic construction though the definition necessitates a slightly different approach. This can be thought of as an M cluster map where any M cluster that has an associated X cluster (i.e. a hit in the forward endcap of the calorimeter) which itself doesn't have an associated B track is discounted. Here a range of DCT sectors are scanned for the presence of a short track (B) using a calorimeter ϕ sector containing both an M and X object as a seed. As for the simple combinations this is repeated, though in this instance 20 times (1 for every EMT ϕ bin).

The final combination that this module handles is the combination of 1 high energy EMT object with another back to back low energy object, EM. This is done through ORing neighbouring M objects and its associated E object (if it has one). This produces a 10 fold map. The outputs from these are then combined into one word for later use. The range of bins that can be used in any combinational trigger object is controlled through software which is downloaded onto the boards though the DAQ system. The method of doing this is described in more detail in section 4.3.2.2. For both the simple combinations and BMX the allowable ranges for matching are between 2 and 6 ϕ bins in both DCT and EMT sectors.

- Trigger Object Count:

  The combinational objects as well as the single trigger objects are then passed into the trigger counting block. During each clock8 (1/8th of system 59.9 MHz clock) cycle the number of trigger objects passed to it are counted. To ensure double counting doesn't occur a number of objects within a configurable ϕ range are counted as one object. This allows for particles that have deposited their energy over several sectors due either to their angle or position of entry. This also assists in producing physics cuts to separate background from physics events.

  One input stream will be considered in this example. The input can be represented as a binary stream representing the object ϕ map. The count is first zeroed and then a search for the longest string of continuous zeros is made. After encountering the first 1, the counter is incremented. To avoid double counting a number of ϕ bins after the first one are ignored (N, effectively a $\Delta\phi$ cut), this value is a configurable parameter. This would be set to 2 during normal running conditions though it can be increased in the presence of heavy background. Continue looking for ones immediately after the N bins and again increment the

counter when the next 1 is found. This process is then repeated for the entire ϕ range of 16 bins for the DCT inputs and 20 for the EMT.

To create the trigger objects that use back to back considerations in their construction a variation of the counting method is used, though the value of N will be very large. An example that could be used for this is the E-M line. Here the starting point of the count is indicated by the placement of the E cluster. The corresponding M cluster in ϕ is then found and a count made of the number of M clusters that fall outside the large value of N. The result of this then passed into the trigger decision block. This value of N was set initially to 150^o, though it was later lowered to 120^o.

- Trigger Decision:

  The input to the trigger decision block consists of 17 3-bit primary and composite objects: nM, nM*, nG, nG*, nE, nEM, nY, nA, nA*, nB, nB*, nA', nAM, nBM, nA'M, nBMX & nU (Where the * indicates a back to back condition). The actual decision is made by comparing the count of each trigger object with a configurable look up table. This is done using 24 separate and independent circuits implemented using FPGA's, one for each of the output lines. Each of these receives all 17 of the 3-bit words of trigger objects and does a 2-bit compare to produce simple binary operations such as no cut, $\geq$, = or <. The definitions of these are shown in table 4.4. The outputs from these are then fed into a single AND gate to produce the output trigger lines which are passed onto the Trigger Select and T0 block.

Oper(i,j)	Definition
00	Pass(i,j)=.true.
01	Pass(i,j)=N(i)$\geq$Cut(i,j)
10	Pass(i,j)=N(i)=Cut(i,j)
11	Pass(i,j)=N(i)<Cut(i,j)

Table 4.4: *The definition of the inputs to the 2-bit compare module*

- Trigger Select and T0:

  The function of this block within the GLT is to select the highest priority line from an event and use it to find the event T0 (trigger time). Once the highest priority line has been found then a search is made of the other 24 configurable lines to find those open during the gated window of the selected line. This

functionality is also used to block trigger lines that are constantly on and would cause a steady stream of triggers. This is particularly important for those lines with the highest priority. The actual assignment of the priority of the trigger lines is done using the configuration file with the written ordering of this defining the priority with line 1 the highest and line 24 the lowest. Since the latency of the whole trigger system is predefined it is very useful to be able to use all of the available time. To enable this each line is given a delay value since some are much quicker to fire, e.g. for the IFT input lines. The trailing edge of the signal from each line is then aligned using differing delays for each line. Using this method the total latency budget is used most effectively.

The other main function is to gate the raw output trigger lines. Due to the unknown nature of the backgrounds of the PEP-II system the GLT has been designed so that the 24 trigger lines that it can output to the Fast Control and Timing System (FCTS) are configurable. Each of the lines may have its output prescaled to ensure the Level-1 output rate does not exceed 2kHz. An example of these are the 1M and 1B lines, which have an individual rate far above that acceptable for the DAQ system, though they are of great use for background monitoring.

4.2.3 The Level-3 Trigger

Since it would be currently impossible to log and then process data from the *BABAR* experiment at the L1 trigger output rate of 2kHz, it is necessary to reduce the rate through the introduction of a Level-3 trigger. Running within the Online Framework (described fully in section 4.3.3) this is a purely software based trigger which classifies the events as either physics or background which the Online Event Processing (OEP) system then logs at the maximum rate possible of 100Hz. In the *BABAR* system there are 32 instances of the L3 program running in parallel, one for each node of the OEP farm. As the Level-3 trigger code is the final stage within the deadtime domain of the online system it must run extremely quickly and reliably. It is also the first system that receives fully assembled events so all subsystem data must be available to it. Being built purely in software, hooks have been left for a Level-2 trigger to be inserted should background levels be such that the output from Level-3 is greater than 100Hz.
The Level-3 trigger software is based upon the idea of *input lines, filters and output lines*. This is show in figure 4.9. As can be seen from this the inputs are made up of the outputs from previous modules, each of which are called tools. Between, scripts

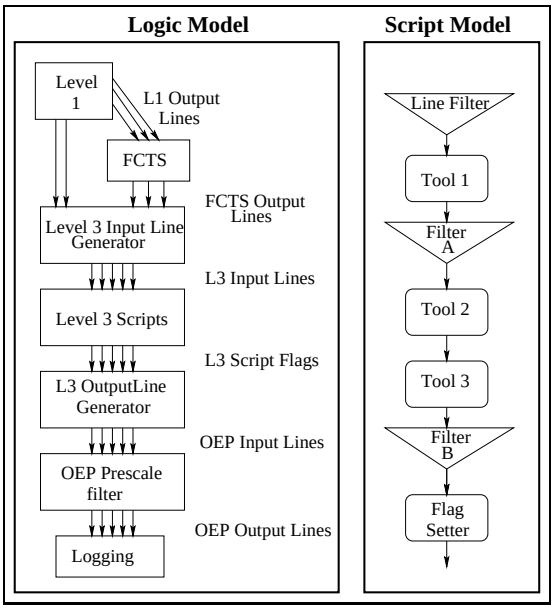

Figure 4.9: *The conceptual model behind the Level-3 Trigger design*

are layered to gate the output from the previous tools. This has the effect of gaining efficiency since the modules further downstream only look at events that have passed previous cuts. In this case the first tool that the Level-3 system sees is the Level-1 system. The output lines from the GLT system and the Fast Control and Timing System (FCTS) are then used to gate the inputs to the Level-3. These are passed into the Input Lines Generator for Level-3. For example there is a wide difference between the multiple charged tracks seen in a B-decay event to the 2 tracks generated by a Bhabha event. As such a script can be made to recognise the output from the tools to categorise these 2 track events. Also due to the asymmetric nature of PEP-II many of the Bhabha events will in fact only have 1 track within detector acceptance. For this another script can be construction to look only for these. Grouped together then these can be used for generic Bhabha event selection. As was shown in section 3.3.4.4 these events are used for EMC calibration and luminosity determination. In general the scripts may be thought of as an easily configurable way of changing the outputs of sets of tools.

Consider the example of sorting Bhabha events from B-events, using the trigger scheme as outlined in fig 4.10. There are 2 input line generators InputSafe2 and Input1Y. The input line Input1Y is used to identify high energy deposits in the back 1/3 of the EMC barrel intended to be used to identify 1-prong Bhabhas. The Input line filters are represented by the "bow-tie" symbols and the scripts as the ovals. The scripts used are the L3Dch, L3Emt and Matcher, looking for tracks in the DCH, clus-

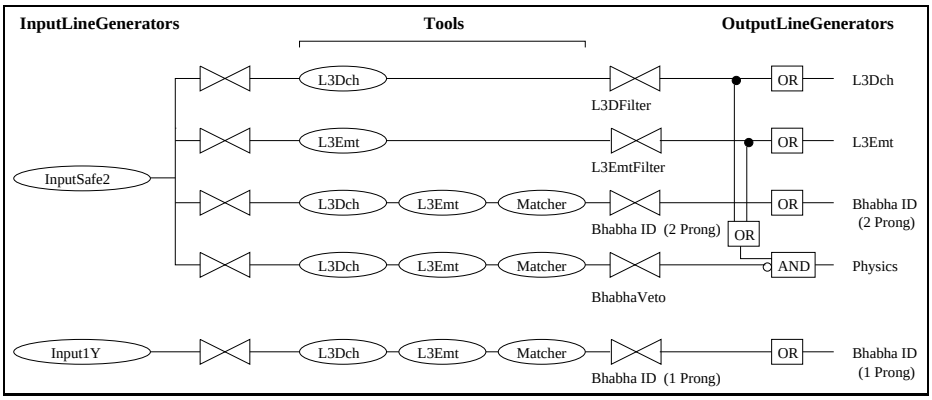

Figure 4.10: *A simple model of the usage of tools and scripts for the construction of the Level-3 Trigger Software*

ters in the EMC and matches between the 2 respectively. Even though there are many instances of each of the tools, the method of coding means that each tool will never run more than once. This means that the diagram shown is a great over-simplification of the form of the interconnection between each tool.
The top 2 lines are looking for physics whilst the other 3 are for firstly counting and then either collecting a sample of or vetoing Bhabha events. There are 2 scripts, both taking the same L3DCH, L3EMT and Matching tools as inputs, operating for 2 prong Bhabhas. The filter labelled as Bhabha ID has a looser set of criteria for calibration. The other is used as an input for the physics line to leave a clean sample of physics events. In order to collect all the Bhabha events there is also the Input1Y line that is used to collect the 1-prong Bhabhas.
In the whole Level-3 trigger system there are 32 input lines from the L1 trigger that are then passed through the first level of scripts. Currently the configuration of the Level-3 trigger has Tools for event selection based on DCH and EMC data using information such as the closeness of the track starting points to the IP and the most energetic deposit in the EMC, as well as specific filters used for the following tasks:

- Hadronic Event selection
- $\gamma\gamma$ final state selection
- μ pair event selection
- Bhabha Accept
- Bhabha Veto
- Luminosity Measurement Online

Each of these tools have their own scripts to operate them though special mention should be made of the way that the selection of important physics channels such as the

hadronic and Bhabha event selection is done in multiple ways. The hadronic selection follows 2 separate paths so that efficiencies can be measured and minimised. The Bhabha veto selection is done in 2 different ways to ensure that both 1 and 2 prong events are removed as cleanly as possible. There is also a script designed to allow a low frequency of raw Level-1 selected events through for trigger studies. Another

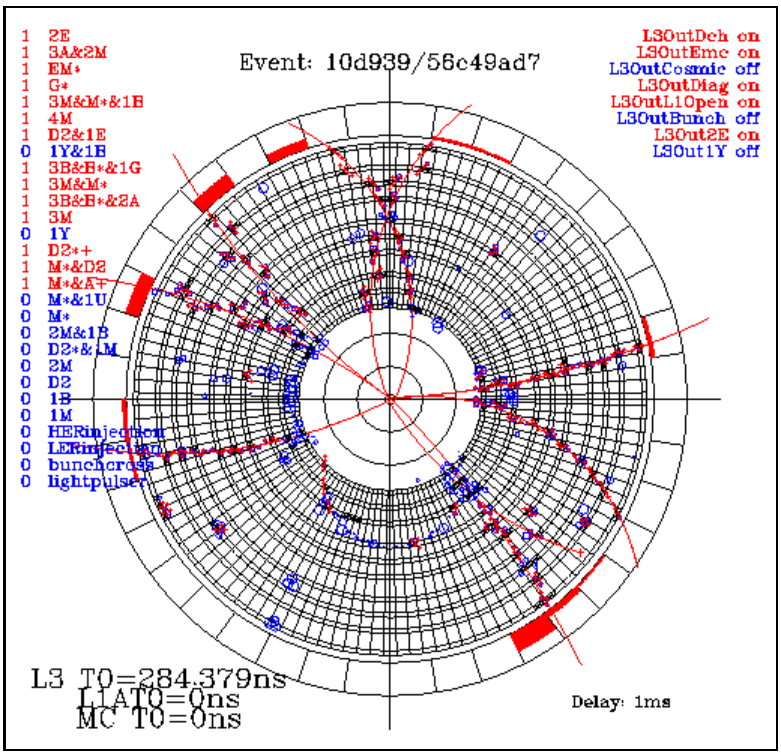

Figure 4.11: *A multi-hadron event as seen on the Level-3 Event Display*

functionality stated in the requirements was for a fully functional event display showing input and output lines for the Level-3 trigger. An example of this can be seen in fig 4.11.

4.3 Online and DAQ System

The *BABAR* data acquisition system is based around a common VME interface to all detector elements. Each systems data is read using a custom personality card into commercial VME processors in which the subsystem feature extraction code is run. Data is then read out over a TCP/IP network to a farm of Sun^{TM} computers. The system is capable of sustaining a Level-1 rate of 2 kHz with an event size of 1.2 Mbytes leading to a data rate of 2.35 Gbytes/sec from the entire IR-2 system.
The DAQ system is an intimate partnership between both hardware and software

systems which can be viewed as the hardware system augmenting functionality of the software system. Here the hardware will be referred to as the *Dataflow Platform* (DFP) and the software as *DataFlow* generically together called the *Data Acquisition Platform* (DAP), together with other systems such as Online Event Processing (OEP) and Calibration they are the *Data Acquisition System* (DAS)[44]. The generic advantage of this type of system is that each subdetector is able to develop concurrently, test and calibrate on a separate system that behaves in exactly the same way as the final system. Each separate partition:

- Can consist of any subset of slave crates.
- Represents a copy of the whole BaBar DAP (The only caveat to this is that a slave crate may only be in one partition at a time).
- Allows the subset of slave crates to be calibrated using their own specific trigger signals without interfering with other partitions.

An example of the entire *BABAR* DAP separated into 3 separate partitions is shown in fig 4.12.

4.3.1 DAQ Hardware

4.3.1.1 DAQ Crates

The DAQ system can be separated into 2 sections on a hardware level. Firstly the Master Crate which is in overall control of all the DAQ system and Slave crates which operate in response to signals sent to them from the master crate (See fig 4.13 for photographs of both).
The Master crate houses the specific Fast Control and Timing System (FCTS) modules that will enable it to control up to 32 slave crates simultaneously. In addition it holds an additional module to interface *BABAR* to the accelerator timing system. Each platform may only have one Master Crate. Following is a description of each of the modules that make up the platform (except the Read Out Module (ROM) for which a full description can be found in section 4.3.1.2) also stating their location within the DAP :

- Fast Control Timing Module (FCTM): This receives the PEP-II clock and phases the *BABAR* timing to it. By definition this is located only in the Master Crate.
- Fast Control Gate Module (FCGM): This receives the Level-1 Trigger word, distributes and scales it as well as the auxiliary trigger signals and calibration system start signals. Located only in the Master Crate.

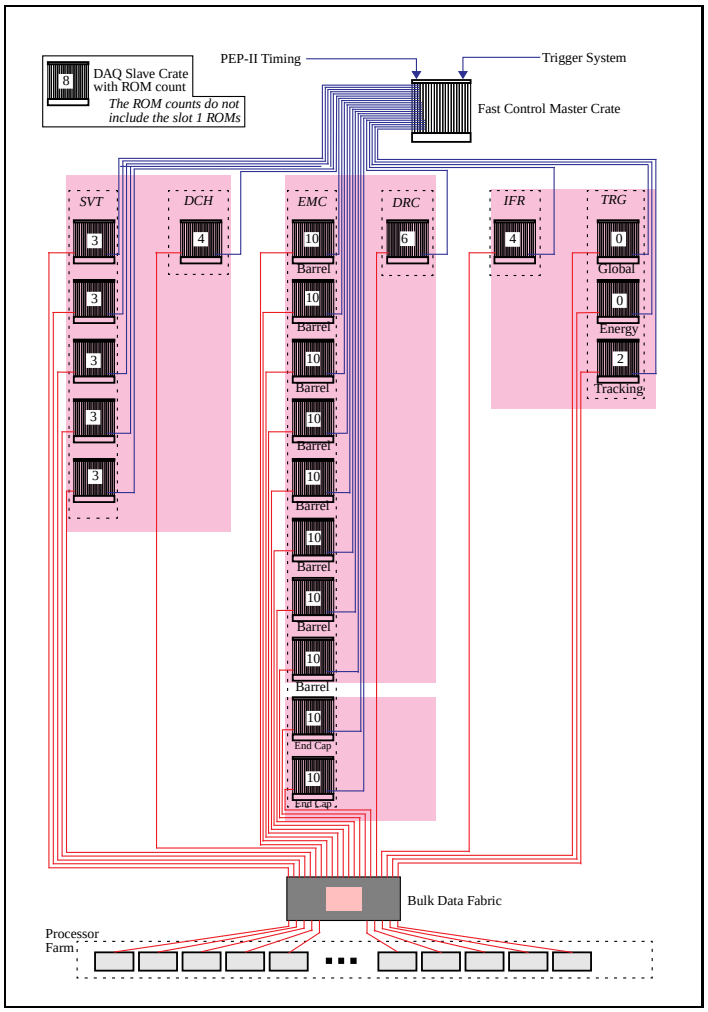

Figure 4.12: *An example of 3 different partitions in the BaBar DAQ System*

- Fast Control Partition Master (FCPM): This takes input from the Trigger system and FCDM to construct *L1Accepts*. It resides in the Master Crate.
- Fast Control Partition Router (FCPR): Fans out FCTS command packets and the system clock (*sysclk*) to and receives *full/available* from FCDM modules located in slave crates. Each has the capability of connecting to 8 slave FCDM modules. Sits in the Master Crate.
- Fast Control Distribution Module (FCDM): Receives *sysclk* and FCTS command packets and redistributes to the Read Out Modules located in the slave crate. It also transmits the *full/available* signals from its ROMs onto the Master Crate. This module only resides in a slave crate.

The fully populated Master Crate has 2 ReadOut Modules, 1 FCTM, 1 FCGM, 4 FCPR and 12 FCPM whilst a slave crate has between 1 and 6 ROMs and 1 FCDM.

Figure 4.13: *(left)A fully populated Master Crate, (right) A Slave Crate showing DAQ system hardware installed*

The backplane on the slave crate has the availability for also inserting 1 FCPM. This allows a slave crate to operate as its own Master and allow for test-stand setups without having to go through the extra expense of having multiple Master crates.

4.3.1.2 The Readout Module

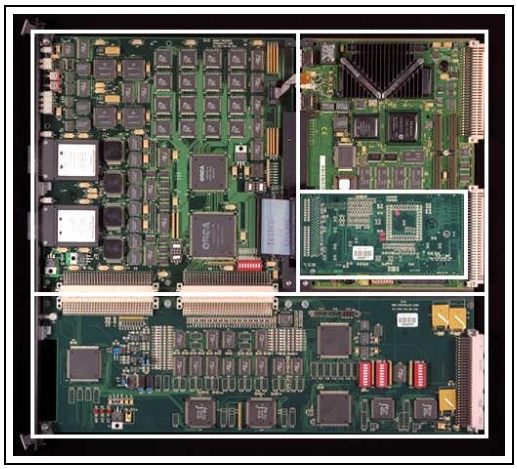

Figure 4.14: *A Photograph of a TPC based Read Out Module, Personality card top left, Motorola CPU (with i960EMC mezzanine card on it) top right & Controller Card bottom*

Each Readout Module can be considered to be made up of 4 separate parts, here their

function will be described as well as their methods of interfacing with each other.

Single Board Computer (SBC) This is a commercially available Motorola MVME-2306 Power PC Module[46] VME standard module stripped of its front panel. It runs a 300MHz processor with 32Mbytes of RAM. Within this board the subsystem dependent *Feature Extraction* code runs and management of communication within the platform, either over 100 base-T ethernet or VME is done.

i960PMC Card (i960PMC) On this mezzanine board which is mounted on the SBC is an i960 Risk processor and 1Mbytes of memory. This is the interface between the personality cards event store and the SBC. It also allows the movement of FCTS commands from the Controller Card to the SBC. This is done through interfacing the PCI bus on the SBC with the i960 bus on the Controller card and Personality Card.

Personality Card (PC) This is the part of the readout module that interfaces with the detector front end elements. It uses a *BABAR* standard protocol to read data from the front ends into the intermediate store. The controller card initiates readout from the intermediate store and the result is forwarded to the i960PMC. Since the rate of flow of data into the PC may not be constant, the intermediate store is made up to a set number of discretely partioned memory spaces.

The PC comes in 2 flavours. Either triggered (TPC) or untriggered (UPC). The trigger PC moves data from the event store in the front end elements to the intermediate store upon receipt of a *L1Accept*, whereas the UPC is used exclusively in the readout of the electromagnetic calorimeter and receives a constant stream of data from the FEE in effect having the event buffer queue within the PC itself.

Controller Card (CC) This is the part of the ROM that the FCTS interfaces with receiving both *sysclk* and command packets. The CC then strips off the FCTS specific part of each packet and forwards the rest to the detector front end elements. It also forwards via the i960PMC the entire packet back to DataFlow for error checking.

Upon receiving a *L1Accept* from the FCTS the CC then manages the movement of the event data from the PC to the SBC. The CC also manages flow control within the platform asserting *full* if all event buffers are used up in the system. Using this method, back pressure and trigger regulation ensure no events are lost during inter-system transport, though this does contribute to the deadtime of the experiment.

4.3.2 The DAQ Software

The DataFlow code may be thought of as having different functionality for each type of system that it is designed to run with. In the case of *BABAR* this is SunOS5[47] and VxWorks[48]. There are 5 different levels at which the code can be built. Each level is designed to only run on one of the 2 platforms. The data path runs down from control through to the event levels and then back up to form a loop. These levels are:

- Control
- Source
- Segment
- Fragment
- Event

Each level performs different functions, some of which are hidden from the user.

Control As its name suggests this level is used to issue all commands which are then passed down onto the Slot 1 ReadOut Module(ROM) which is in each DAQ slave crate. This is also used to fill the sequencer that will be mentioned later when discussing calibrations. There are several different functions that can be performed by the sequencer. They are *L1Accept, StartPlayback, CalStrobe* and *NoOp*. Of these the most important are *L1Accept* and *StartPlayback* since they are used within nearly all calibrations. NoOp is generally used to adjust the spacing between 2 other commands within the sequencer. This code runs on the host machine i.e. the SunOS5 architecture.

Source This really is the base of the DataFlow code and as such is transparent to the user. It acts as an interface between the control level running on the host machine and the VxWorks running on the Single Board Computer mounted on the ROM.

Segment The segment level is where all the user code runs to control all the Front End Electronics (FEE). This is run on the user ROMs and runs the commands that have been passed down from control level. This operates the FEE and reads the data from each of the elements. This is then collected into tagged containers for each event[45]. These are the normal method of data transport within the Dataflow system. This then passes the tagged containers that contain all the data up to the next level.

Fragment Fragment level code is run from within the Slot 1 (controller) ROM for each slave crate. It is used to accumulate all the information that the user ROMs have generated for each event and then collates it into a consistent entity and passes it up to the final level.

Event Running on the Sun hosts, the event level code collects all the information that has been passed to it in the form of tagged containers from each systems slot 1 ROM. It is then assigned a 32bit timestamp and the trigger bit information from the FCTS Master crate. This information could then be called an event. From here it is then run through Level-3 trigger and onto data storage.

4.3.2.1 The Finite State Machine

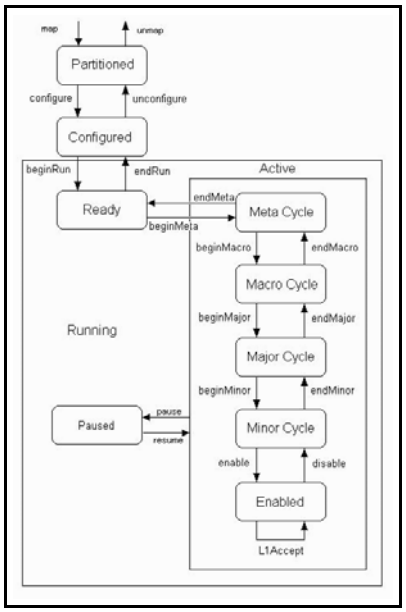

Figure 4.15: *A diagrammatic representation of the DataFlow finite state machine*

To ensure that the changes of the system state are well known and consistent there must be a fixed network of steps. To this end DataFlow have constructed a finite state machine in which transitions are only allowed from one state to either the next or previous. A graphical representation of the FSM is shown in figure 4.15. Actions must be defined for each of the steps from *configure* through to *L1Accept*.

4.3.2.2 Reverse Dataflow

Though the majority of the data moves from detector to mass storage there is a small amount such as configuration constants that must flow in the opposite direction. This

is called Reverse DataFlow and is almost a separate system[49]. It is completely data driven in as much as the request for information is made by the system itself, not through an explicit call by the user. This is shown in figure 4.16. It is important that it is well known what constants are downloaded to the electronics at any one time. To this end each subsystem makes an internal copy of its downloaded data for validation before running starts.

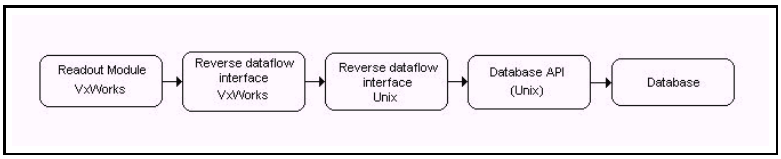

Figure 4.16: *The path of accessing the database from the ROM in a data driven system*

These constants must be encapsulated in a tagged container to enable the data to be moved within the DataFlow framework. They are then added to the configuration key that is used by the control level application such as Run Control or the Dataflow GUI. A representation of the format of the configuration key and map structure is given in fig 4.17. Since the information held within the configuration database is persistent,

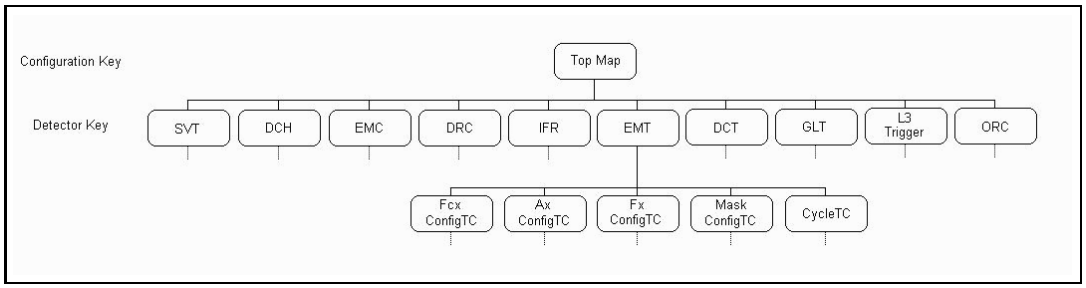

Figure 4.17: *The Configuration Map Tree*

the configuration key will change for the top map every time any one of the Detector map key values change. This is a disadvantage for things that change very frequently.

4.3.3 Online Event Processing

The Online Event Processing system (OEP) is a collection of tools that run within a common framework. It carries out all primary processing on fully built events short of full reconstruction. The OEP system has clients running within it, the most important being the Level-3 trigger, but also Fast Monitoring and high level calibrations. Since it receives all of the events that the DataFlow system generates upon receipt of a *L1Accept* this also means that it can possibly cause deadtime. The design maximum

for this is 1%. Overall control of its operation is done through the Run Control process. The OEP framework is designed to control the operation of processing units called *modules*, though unlike the offline framework it is important that the system can guarantee in which order these are run (In fact essential since Level-3 relies on this)[50]. Fig 4.18 shows the context of the OEP system and other systems with which it communicates. Within the central OEP box is also the Level-3 algorithm. In the *BABAR* interaction hall system there are 32 instances of the framework running on commercial Sun Ultra 5's each connected to the Dataflow Platform via a high performance data switch.

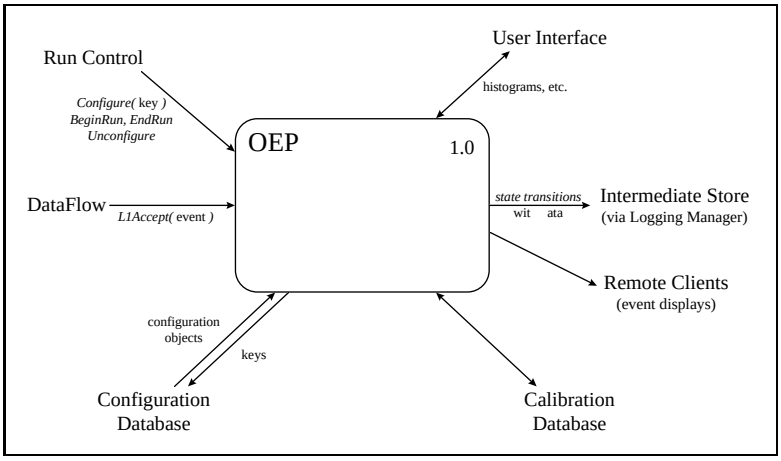

Figure 4.18: *The OEP system in context showing all data input and output paths*

The design of the OEP system was dictated firstly by the data access that it would need to be able to provide. There are three levels of access allowed;

Modify This has the option of being able to permanently modify any data that it sees, both data already present in the event and data to be added. Since this is the highest level of access it is envisaged that the only process given this ability will be the DataFlow Event Builder.

Append All data already present within the event cannot be changed though new data can be added. It is intended that there be only one such instance of a process per occurrence of the framework, the Level-3 trigger processor.

Read-Only This is the level at which all other applications are designed to be run such as Fast Monitoring and online event displays. Also most importantly the event logging manager will also only have this level of access.

The access to the input datastream from DataFlow is also closely controlled since this can directly affect the DAP deadtime. There are 2 types of *event* access, **Privileged**

which is guaranteed every event that is output from DataFlow. The only processes with this level of access are the Logging Manager for transfer of data to the intermediate store and the Level-3 trigger. All other clients will have **Sampled** access. Here the process that is requesting the event will only receive the next once it has finished processing the previous. In this way there should be little danger of data loss and deadtime. There are also handles available for access to the data stream in read-only sampling mode for other systems should they become necessary. One example envisaged is the Calorimeter for its Bhabha calibration since the nominal rate of Bhabha events intended to be included in the main output stream will be too low. Another output stream may therefore be connected in parallel for recording.
The output from Level-3 is passed directly to OEP as a set of 'output lines' where the trigger decision has been asserted for the event. Within OEP the actual logging decision is made and prescales are given to each of the output lines. This mechanism is shown in fig 4.19. This output is then made available to the Data Logging Manager. This method of data control also allows other systems to create OEP input lines. Though since these process will necessarily have to have **Append, Privileged** access they must satisfy the same strict dead time minimisation procedures as Level-3 and as such are discouraged. After being passed to the logging manager the data is passed

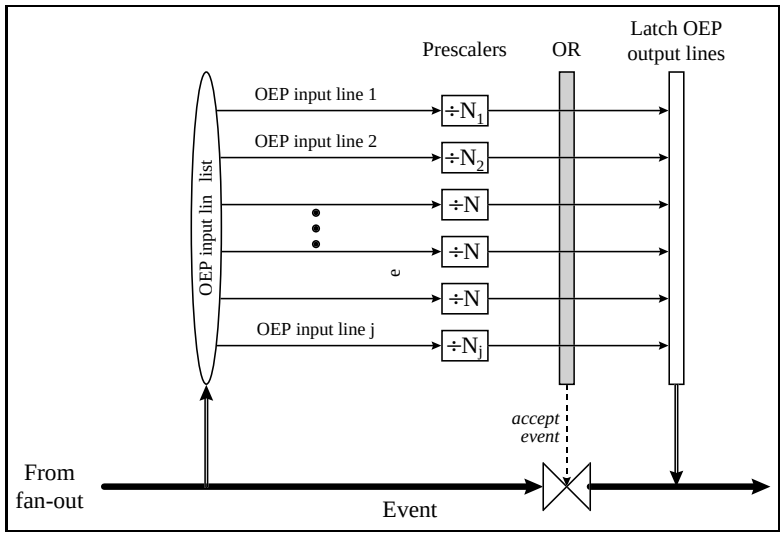

Figure 4.19: *The output prescale stage of OEP showing data is streamed in parallel through the OEP filter and onto storage dependent on the filter decision*

into the intermediate store. Originally envisaged to be an object orientated database the current design uses binary files (*xtc*) written to disk since it was decided that this would be a safer baseline considering the currently unsatisfactory performance of the database.

4.4 Performance

Now that the system has been in operation for the first year it is appropriate to include some data on current performance.

4.4.1 L1Trigger

The Level-1 system performance discussed here will focus mainly on the major system components, i.e. the DCT and GLT (The EMT performance is dealt with in section 5.5). The latency of the system is within its 12 μs budget by a significant margin (2μs) and so the full delay capability of the system has had to be employed. In the following sections the efficiency of both will be considered seperately.

4.4.1.1 DCT Performance

The DCT system performance is studied using events that are classified as Level-1 pass throughs. These are recorded since the Level-3 system allows a prescaled factor of Level-1 events through all its filters even if they would have been rejected normally. These events are then checked to see which Level-1 component caused the highest priority trigger. For the DCT this must be the EMT system with either a 2E trigger, i.e. two high energy deposits in the calorimeter. The number of DCT events that also trigger is then measured. These results are given in figure 4.20. These are compared with Monte Carlo, designed to give a true indicator of detector performance using hit removal and also reflecting the lowering of the drift voltage within the DCH.

4.4.1.2 GLT Performance

The GLT performance can really only be considered in as much as does it work. The performance of the hardware is unquestioned since we are using all available functionality to provide the Level-1 trigger signals to the fast control system. The system has been completely reliable since installation requiring no intervention since installation except to fine tune boot time loaded lookup tables.

One of the most stringent requirements of the Level-1 trigger system was that the trigger rate should not exceed 2kHz when running at design luminosity. This was considered one of the hardest constraints within the trigger designers especially since there was very little know about possible background levels at this luminosity.

Figure 4.21 shows the contributions to the overall Level-1 trigger rate as passed to the whole DAQ system from each individual trigger line. As can be seen the differences

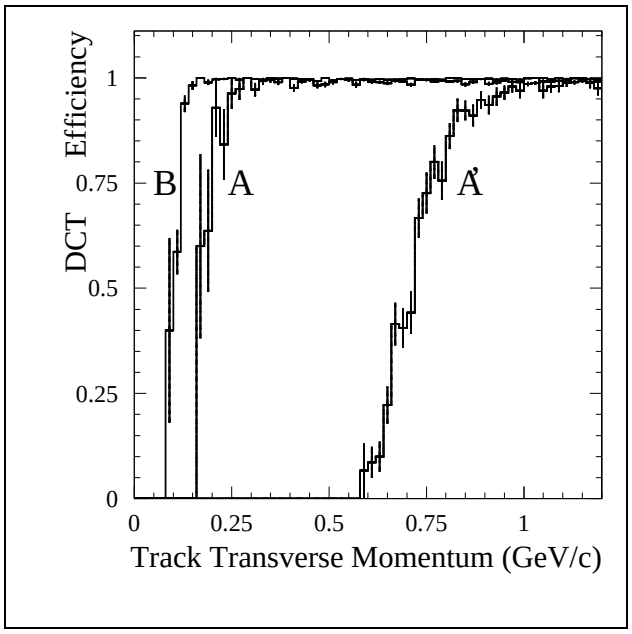

Figure 4.20: *The efficiency of the DCT against momentum for B, A and A' triggers*

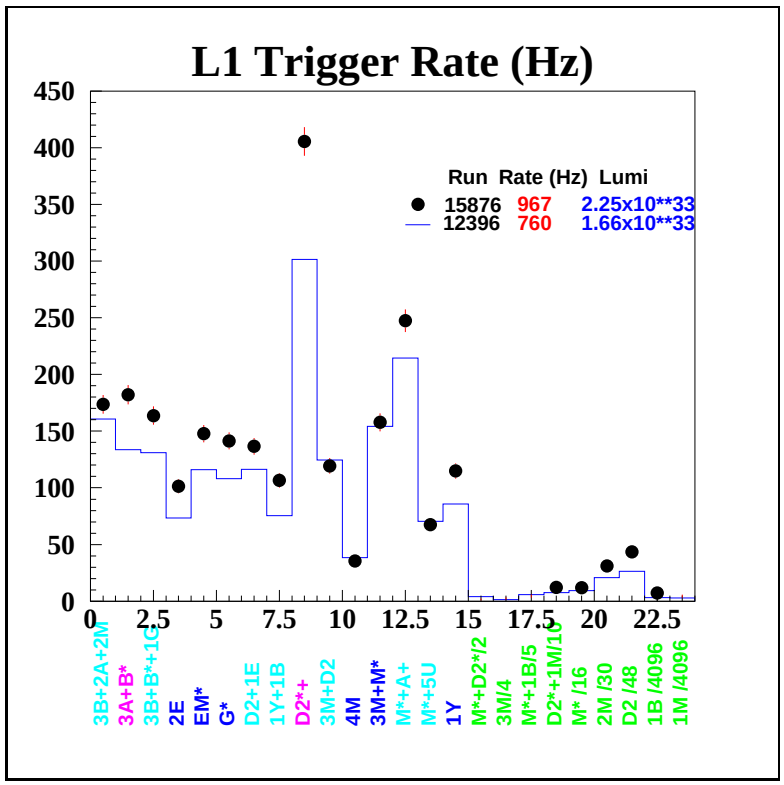

Figure 4.21: *The Level-1 trigger rate showing a comparison between runs taken early on in the BABAR development and then when nearing factory operation*

between the two runs, one taken at a luminosity of 1.66 $\times 10^{33}\text{cm}^{-2}\text{s}^{-1}$ and the other at 2.25 $\times 10^{33}\text{cm}^{-2}\text{s}^{-1}$ shows that the system has plenty of headroom for luminosity increase without nearing the systems' hard limit.

4.4.2 L3Trigger

One method that the Level-3 trigger uses to further reduce the trigger rate to a level that would be suitable to write to tape is to measure the position of the event vertex with relation to the measured beam-crossing point. The results of this are shown in figure 4.22.

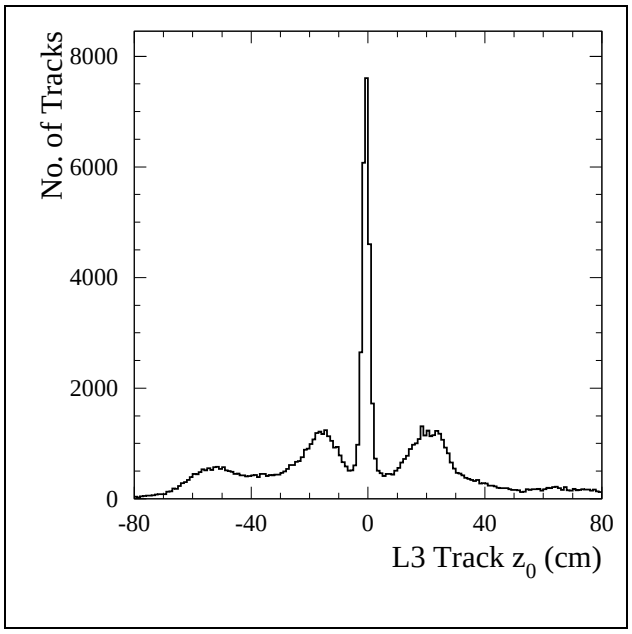

Figure 4.22: *The measured position of the event vertex with respect to the beam-crossing point as measured offline*

This plot shows the distribution of tracks in z as passed by all filters and bypass selections. These include the Level-1 passthroughs and random selections. The two peaks to either side of z0 are the two closest quadrupoles B1 and B2 with each of them causing background as discussed in section 3.2.4.

4.4.3 Dataflow and OEP

This system is the most difficult to give direct performance measurements on since the only true way of saying whether the system design has been a success or failure

is whether it works or not. In section 3.4 it is shown that the overall performance as described in the TDR has been exceeded in terms of rate capability. There is also a limitation on the system dead-time that is currently matched. Since these are really the only measures of the Dataflow system then I will elaborate more on the work that was done to achieve this current performance and some of the currently inherent limitations.

4.4.3.1 Overall Event Rate

The most pressing limitation on the overall event rate is the limitation on the event size. This is currently hardwired in the system at 32 kbytes. Since the dataflow system can be considered as many parallel "assembly lines", the system is only able to work as quickly as the slowest worker. The current model of the system has produced the following results for each subsystem. This information was used to produce table 4.5.

	SVT	DCH	DIRC	EMC	IFR
G-Link	11.4	26.0	9.7	0.0	16.0
I960	29.0	48.3	63.2	50.5	61.2
PCI-n	5.2	21.8	14.7	45.5	19.2
MPC-n	3.3	12.0	8.3	22.9	10.2
CPU-n	40.0	83.2	110.5	270.0	100.8
VME	44.4	36.4	60.0	100.0	48.0
PCI-0	8.3	9.0	11.3	7.5	9.0
MPC-0	10.4	11.3	14.1	9.4	11.3
CPU-0	231.8	235.6	253.6	234.0	238.0
Network	111.0	120.0	150.0	100.0	120.0
Total	445.9	603.6	695.4	839.8	633.7

Table 4.5: *The current subsystem processing times in μs. XXX-n indicates slot n ROMs whilst XXX-0 indicates slot-0 ROM processing*

As can be seen the slot-n ROM functionality is vastly different from subsystem to subsystem though careful optimisation of the feature extraction code for the DIRC, EMC and IFR should reduce their CPU times. The VME times are a function of the number of slave ROM's in each system, causing contention on the VME bus. This is most clearly demonstrated by the EMC which has 10 slot-n ROM's per VME crate, by far the largest in the platform. The most significant piece of information is the time taken for processing in the slot-0 ROM, since this not only does the crate man-

agement but also all the event building from the slave ROM's. The flat nature of the time taken across the whole platform though indicates that an underlying dataflow process is taking most of the CPU time. This is currently under investigation. The other flat distribution across the platform is the network time.

To reduce the network time the most obvious solution is to upgrade the network link between all the VME crates and the Level-3 farm. This would involve the upgrading of the back of crate network cards and the switch from their current 100Mb/s specification to a gigabyte link. Since this is relatively simple to do then this is most probably the area where most performance increase can be found.

4.4.4 Deadtime

A minimised deadtime is very important to an experiment that wishes to perform analysis on channels with very small branching fractions. To this end the *BABAR* system has been designed to minimise this. Running with design luminosity the deadtime was measured at 1.2% during normal background conditions just after storage ring top-up. This is the period during which background is greatest due to slight beam tuning that must occur to reduce instabilities during introduced.

4.5 Summary

Currently the *BABAR* DAP is operating with a *L1Accept* rate of 1.9 - 2.0 kHz with minimal deadtime. Data is continually logged at less than 70Hz as per the original design brief with currents of 516 (943) mA in the HER (LER). Within this chapter a detailed description of the trigger system for *BABAR* has been given, showing all the steps of the processes controlling the flow of data from detector to storage. The mechanism for monitoring its quality and displaying online results has also been shown. This chapter will also provide a basis to Chapter 5.

Chapter 5

The Level 1 Electromagnetic Calorimeter Trigger System

5.1 Introduction

The Level-1 ElectroMagnetic Trigger (EMT) is one of the two major suppliers of the trigger primitives for the generation of Level-1 trigger objects. As with previous calorimeter triggers it is designed to fire when an incident particle deposits enough energy in the calorimeter that an applied threshold is passed. The *BABAR* EMT also generates positional information in θ and ϕ using the segmentation of the input and then combinations of this to generate the hit map. The system was a collaboration of four UK institutions, University of Bristol, Rutherford Appleton Laboratory (RAL), Royal Holloway and Bedford New College (RHNBC) and Imperial College (IC). The responsibilities for the project were divided up into the management and electronic design conducted by RAL and IC, with the software for both system control and data analysis by the other institutions.

The EMT has been designed to receive digital data from the EMC. A threshold is then applied so as to remove low level noise from the input to the trigger. The trigger system then condenses this data to give information on the energy and ϕ position of energy deposits in the EMC. The system itself makes no event selection but passes trigger objects formed from this data onto the GLT. As such the EMT is an untriggered, stateless, free running system that will generate objects as long as it is supplied with input. The whole system is controlled by a CPU which plays no actual part in the decision process but monitors the output not only in real-time but also by passing the input and output data for offline analysis. See [51] for further details of the system requirements.
The calorimeter has an approximate 40 fold symmetry as dictated by the configuration

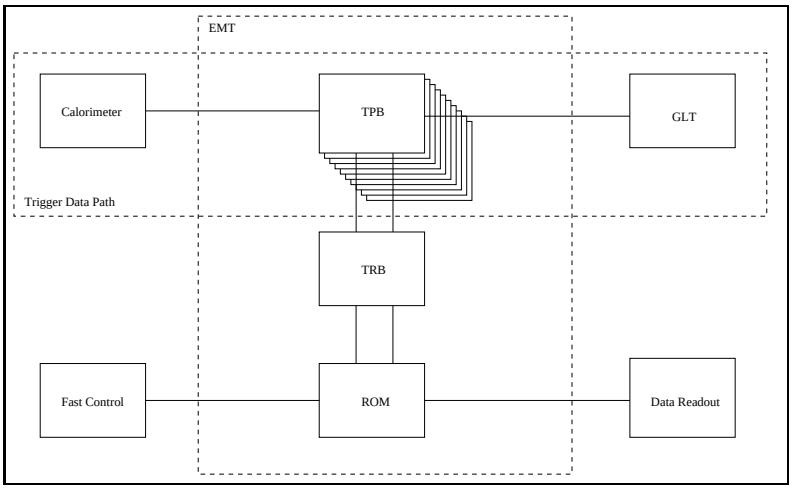

Figure 5.1: *The Overall EMT system showing connections to other systems*

of the EMC readout system. Within each 9^o segment in ϕ all the crystals are summed and then added to their neighbours in ϕ. This provides a 20-fold output map to the GLT system. This method was primarily chosen since it turns the 2 dimensional space of the EMC into a 1-dimensional system which eases the combinational logic involved to process the data.

Along with all the requirements given in section 4.2.1 there are also many that are specific to the EMT system. These are mainly concerned with the electronic operation of the system. The EMT receives its data from the EMC at a word rate of 3.4MHz as a sum of 24 crystal front end electronics outputs which is then condensed into a 16-bit word. This operation is used to reduce the input data volume from 6600 crystals to 280 input units. This data compression is the physical realisation of the read-out from an 8x3 array of crystals in θ & ϕ. The main reason for choosing this format was that it exactly corresponds to the input from one of the EMC optical fibres from the FEE to the UPCs. The data is received in digital format having no channel to channel variations removed. The algorithm design must therefore be robust to this. The data arrives at a bit rate of 59.5MHz with a framing bit to allow for synchronisation between systems. Each cable running between the EMC and EMT carries 3 data lines, 1 frame line and a clock line in the barrel with the endcap readout only having 2 data lines. This is illustrated in figure 5.2. The input from each ϕ sector is processed separately. The algorithm creates 3 energy dependent trigger objects M, G & E as well as 2 positional triggers, X and Y. These were described in section 4.2.2.1 but will be repeated below for completeness.

M 108MeV This is intended to catch minimum ionising particles as they pass through the calorimeter.

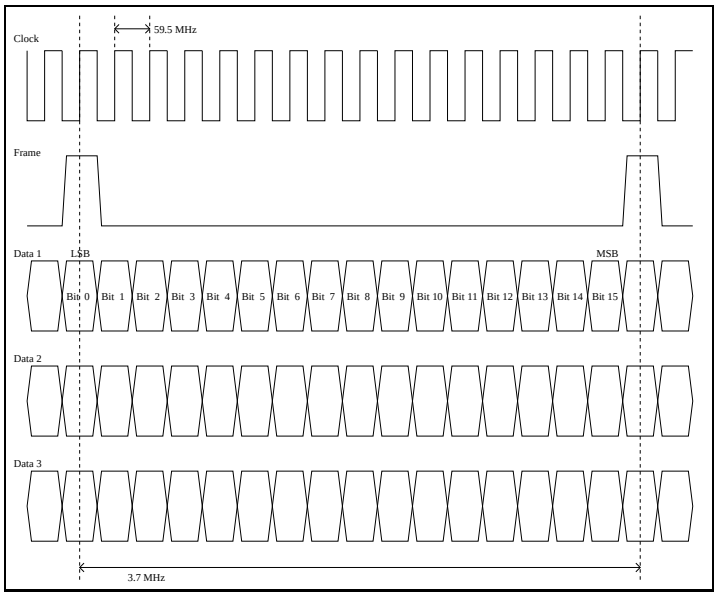

Figure 5.2: *A diagrammatic representation of the individual data lines within an interconnecting cable between the EMC & EMT*

G 500MeV This is intended to pick up γ radiation in the calorimeter.

E 1GeV This is primarily to detect high energy electrons.

The 2 positional triggers:

X If a deposit is seen in the forward endcap then the X trigger line fires. This is intended to be used as a veto for low energy beam gas interaction particles and as such to reduce background.

Y The calorimeter is further separated with the 2 most rearward towers for each ϕ strip contributing to the Y trigger primitive. This has a very high independent threshold and is intended to be used to filter out Bhabha events which at design luminosity will have a very high rate and could swamp the DAQ system. The concept of operation of the EMT trigger is shown in figure 5.3.

The summation of the separate towers into a whole ϕ strip follows equation 5.1 for M, G, E, equation 5.2 for Y and equation 5.3 for X, with j=0,39 for all. [1]

$$\phi = \sum_{\theta=0}^{7} T_{\theta,j} + T_{\theta,j+1} \tag{5.1}$$

[1]The design for the EMT included the possibility for *BABAR* to be constructed with a backward endcap. Currently this has not been implemented and so θ_6 is the most rearward tower.

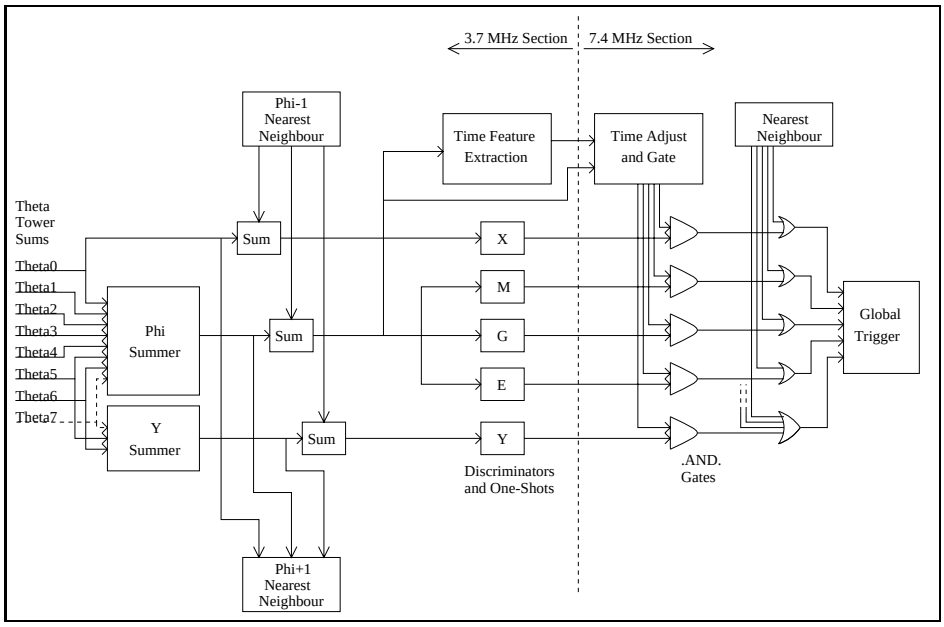

Figure 5.3: *The conceptual design of operation of the EMT system*

$$\mathrm{Y} = \sum_{\theta=5}^{7} T_{\theta,j} + T_{\theta,j+1} \tag{5.2}$$

$$\mathrm{X} = T_{\theta_0,j} + T_{\theta_0,j+1} \tag{5.3}$$

When the tower sums are received from the EMC UPC's they will undoubtedly be skewed with respect to other inputs and as such must first be aligned. At this point it is important that the input to any tower sum can be selectively turned off and discarded from the tower sum so as to allow operation to continue in the event of a malfunction of the EMC FEE for this tower. The input from the ϕ strip is then summed with its nearest neighbour. This is important since it is possible that a cluster could cross more than one ϕ strip. These sums are made for the whole ϕ strip as well as the X and Y regions. The sums are then passed into a Finite Impulse Response (FIR) filter to determine the event/trigger time as well as to a discriminator to generate the 3 different ϕ objects. The output from one of the algorithm chips must then be summed with its partner to allow the generation of the output map that is passed as output.

The interface from the EMT to the GLT operates on an even more reduced data volume. From the output of the algorithm the data is then summed with its positive neighbour to produce a 20-fold output map for the M, G, E & X objects with 10-fold map for Y. This has been determined to be sufficient granularity to allow the GLT to

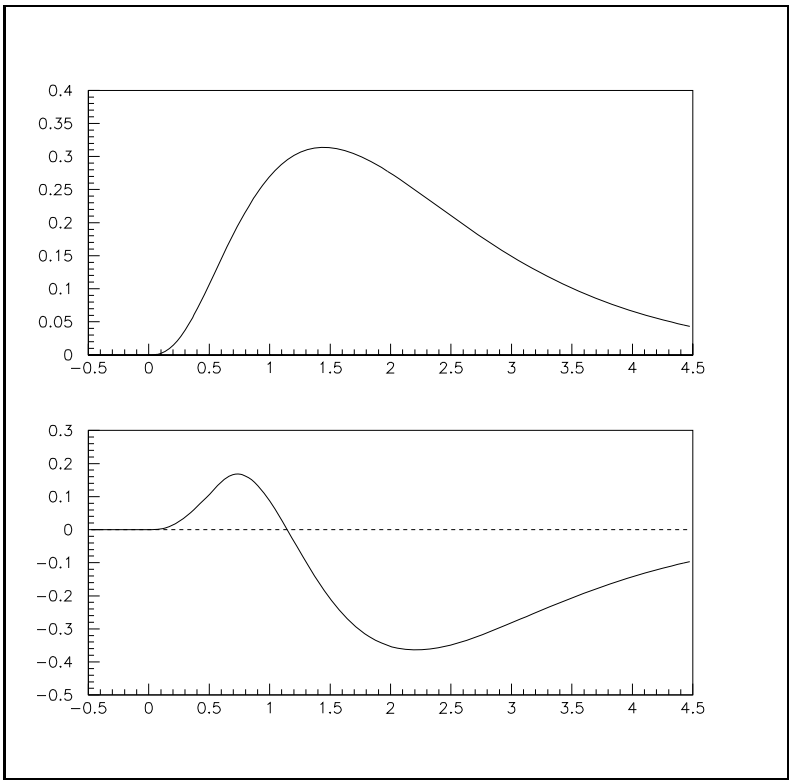

Figure 5.4: *Output from the FIR filter(bottom) for an ideal input calorimeter signal(top) showing the determination of the trigger time using the zero-crossing. The current filter weights used constrain this to occur 1.2μs after the arrival of the input signal*

be able to make meaningful decisions without degrading performance. This output though runs at twice the frequency of the input side to allow finer selection of trigger timing and finer adjustment for latency. To allow the GLT time to align the input data from all the input systems the overall latency for the whole of the EMT from input to output has been fixed at 8μs. Any saving on this time will be taken up by delays within the GLT. The physical transport between the EMT and GLT are 10 cables working on ECL differential logic, with the output from 2 processor boards being sent along each cable.

Since the EMT system, as with all others, must interface with the FC control system it must be able to respond to the accepted set of fast control commands. To do this an interface board was built to allow this communication. This was interfaced with the *BABAR* standard ROM using optical fibres. The system though must be able to know if a command has been sent at an inappropriate time and if so flag an error which will be displayed during the next readout. If a command is sent which is correctly timed but not applicable the system must stay in a known state and if necessary ignore this

command. The most important command that is sent other than those associated with the reading out of data is the *Synch*. This command must initiate a resetting of all clocks and buffer timings, synchronising the system with the rest of the *BABAR* DAQ system.
As a final check on the operation of the EMT it must be possible to load a predetermined set of data into buffers on the boards and feed this data through the algorithm. Its outputs are then checked against the known response to this data. The algorithm should be unable to tell the path by which the data has come to make this test as fair as possible.
The optical fibre is also the path along which all configuration data is sent. This is the fundamental information which the hardware needs to be able to function. This is down-loaded from a persistent database that will allow offline analysis to also read this information. It must also be able to be read back at any moment when the system isn't running to verify that the information has been loaded correctly into the system.
The information that is read out after receipt of a Level-1 accept must be such that it can be used for offline trigger analysis to study efficiency of the trigger system and to find errors in the synchronisation of the system and the EMC/GLT. This is essential to the factory mode that *BABAR* must operate in. There is also the possibility of a Level 2 trigger should the background levels be too high at full luminosity. The EMT could be the only system that could be used to trigger efficiently on neutral objects and as such all possible input data should be read out. The solution to the above design criteria is shown in the next section along with solutions to problems that arose in the design and prototyping process.

5.2 The Hardware

The system hardware consists of the following:

- 10 Trigger Processor Boards (TPB)
- 1 Trigger Carrier Board (TCB)
- 1 Triggered Personality Card Read Out Module (TPC ROM)
- 1 Fast Control Distribution Module (FCDM)

All of these components are mounted within a custom 9U crate that supplies all electrical power as well as managing communication between the TPC and external networks as well as the FCDM & TPBs. The crate is also used to mount the patch panel for the 100 cables carrying information from the calorimeter UPC boards. The crate is shown in figure 5.5.

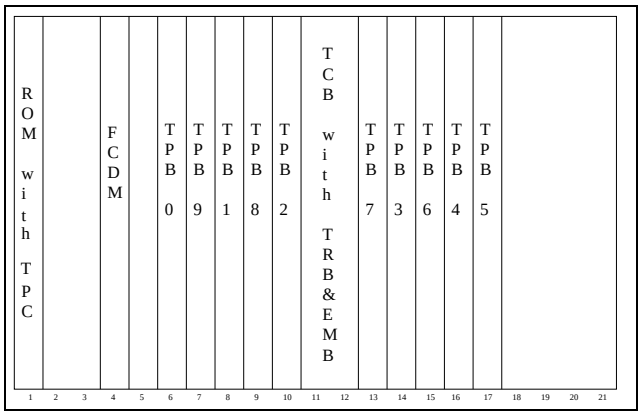

Figure 5.5: *The arrangement of boards within the EMT crate*

5.2.1 The Trigger Processor Board

The process of receiving the incoming data from the EMC, looking for deposits within the calorimeter and producing appropriate trigger primitives is done with the Trigger Processor Board (See figure 5.6)[52]. These each handle 4 of the 40 ϕ strips. A single ϕ strip has its own digital processing chip which receives the data from 3 UPCs in the EMC, one in the endcap, one in the forward barrel and one in the backward barrel. Each of the 7 segments in θ have a 1 to 1 relation with a fibre input from the FEE into the UPC. Each TPB has 4 different types of Xilinx Field Programmable Gate Arrays (FPGA) to fulfil the following functionality:

- Algorithm Xilinx (AX). Processes data received from the calorimeter, constructs the trigger primitives to be passed onto the global trigger and pass the input data onto the latency buffers. See section 5.2.2

- Fast Control Xilinx (FCX). This chip interprets the fast control systems global commands as passed from the readout module as well as subsystem specific commands. It also passes configuration information to various parts of the board and it controls the readout of various buffers on the board that are used for data transfer and diagnostics.[55]

- Formatter Xilinx (FX). Controls the passing of data stored in the latency buffer into the event buffers on receipt of a Level-1 Accept signal and the readout from these buffers on occurrence of a *readevent*. It also controls the number of time slices of data that are passed out during a Level-1 Accept.[56]

- VME Control Xilinx (VX) This controls all VME functionality on the board as well as decodes VME address to ensure communication between the readout module and the correct TPB.[57]

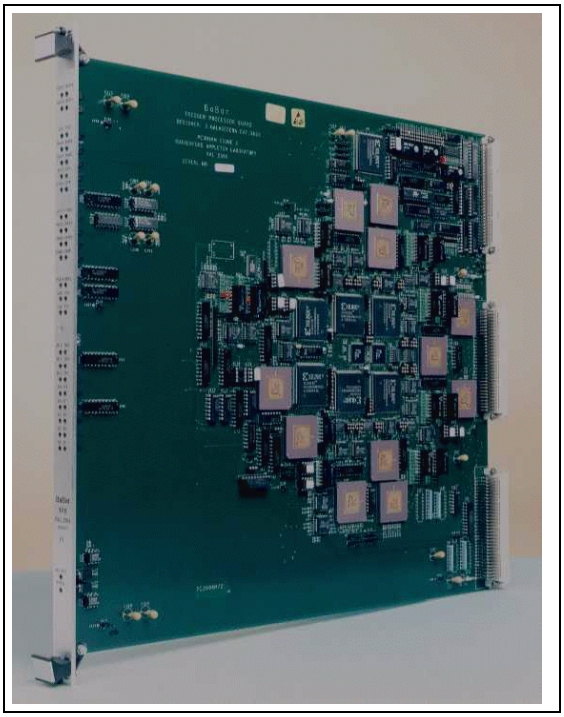

Figure 5.6: *A Production Trigger Processor Board*

The operation of the TPB can be represented as in figure 5.7. Data is received in a continuous stream from the EMC. This is passed through the AX which looks for a peak in the data stream input. This is done using a finite input response filter which differentiates the input waveform so that the energy peak appears as a zero-crossing (this is detailed more thoroughly in section 5.2.2). This generates a trigger primitive and the appropriate bits are set and sent to the global trigger board. In parallel the data is also passed into a circular buffer of fixed length. This must be equal to or greater than the time taken for a trigger decision to be made. When a Level-1 Accept arrives the event for which the decision has been made is then passed into an event buffer. Each TPB has 4 event buffers. On the issue of a ReadEvent command from the Master crate the oldest data in one of the event buffers is passed to the Level 3 trigger. This is shown in figure 5.8.

5.2.2 The Trigger Algorithm Design

The design of the algorithm must fulfil the following tasks most of which follow from the overall EMT requirements.

- Receive skewed tower sum inputs from the EMC.
- Synchronise these inputs.

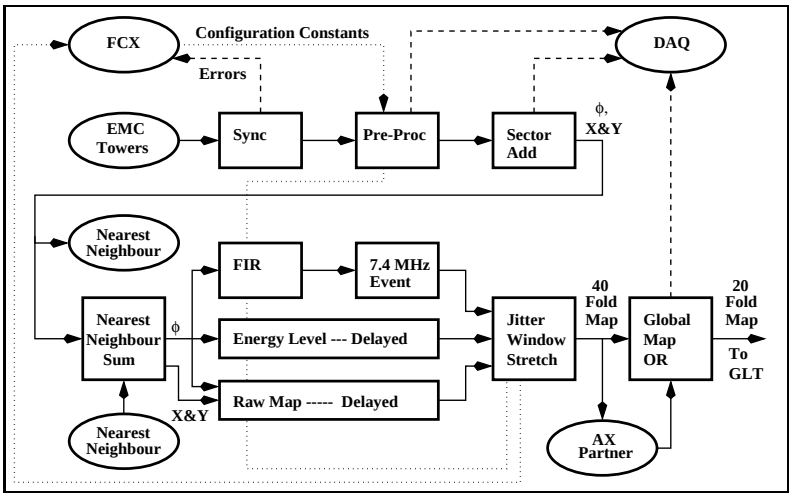

Figure 5.7: *Internal operation of the Trigger Processor Board (TPB)*

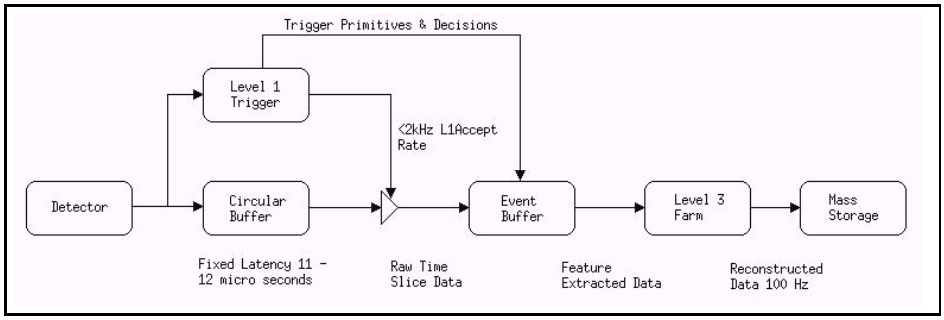

Figure 5.8: *The Data and trigger decision path from Detector to Mass storage*

- Apply selective control in which tower inputs are used in the trigger object generation.
- Sum the input towers over nearest neighbours to create ϕ, X & Y objects.
- Process ϕ sums through the Finite Input Response (FIR) filter to determine trigger time.
- Discriminate ϕ, X & Y objects to filter noise for X & Y and generate the M, G & E objects in ϕ.
- Select appropriate jitter window dependent on energy of ϕ sum.
- Generate 40-fold global Map from event time, 5 discriminator outputs and selected jitter window.
- OR with partner to generate 20-fold map for output to the GLT.
- Output 5 lines to the DAQ system

  - Tower sum bitmaps
  - ϕ, X & Y sums before nearest neighbours
  - 20 fold Global map

- Output to Spy
  - Synchronised tower inputs
  - Selected feature extracted and discriminated data
  - ϕ, X & Y after nearest neighbour & DAQ output
  - Nearest neighbour inputs
  - 5 spare lines

- Complete all the above operations within a time window of 5μs

The actual implementation has been done using a Xilinx FPGA [53]. The coding for this was done using the Viewlogic[54] program. The operation of the final design can be broken down into logical blocks as shown in figure 5.9:

- Input Data Processing

  The data received must first be synchronised through all towers. This is done by firstly grouping the inputs into θ_0, θ_{1-3} & θ_{4-6}. In case it is decided that a backward endcap is necessary on the EMC the inputs for θ_7 are also included.

  All the data signals are fed into a dual port memory with the clock supplied by each cable being used to synchronise writing into the memory. The internal board clock is then used to initiate readout. The frame bits sent down the 5th line in the cable are used to ensure that the memory is not being written and read at the same time, as well as produce a check on the physical connection of the cables. This signal is OR'd over all input cables to produce the results for a status bit within the CSER as well as an LED on the front panel of the board.

  The synchronised data is then fed into the next module which performs initial preprocessing of tower sum data. The principal operation carried out here is the masking out of particular towers from the strip sums. This is done using configuration data loaded into the board. A situation where this would be used is for example a failure of one of the EMC front end modules causing 'high energy' noise. This would give the possibility of large noise levels within the system with the consequence of high deadtime. Each algorithm chip receives the mask information through an 8-bit word. These are then loaded into a shift register and AND'd with the input data stream to remove malfunctioning towers. This module is also used to generate the θ bitmap which is passed directly into the

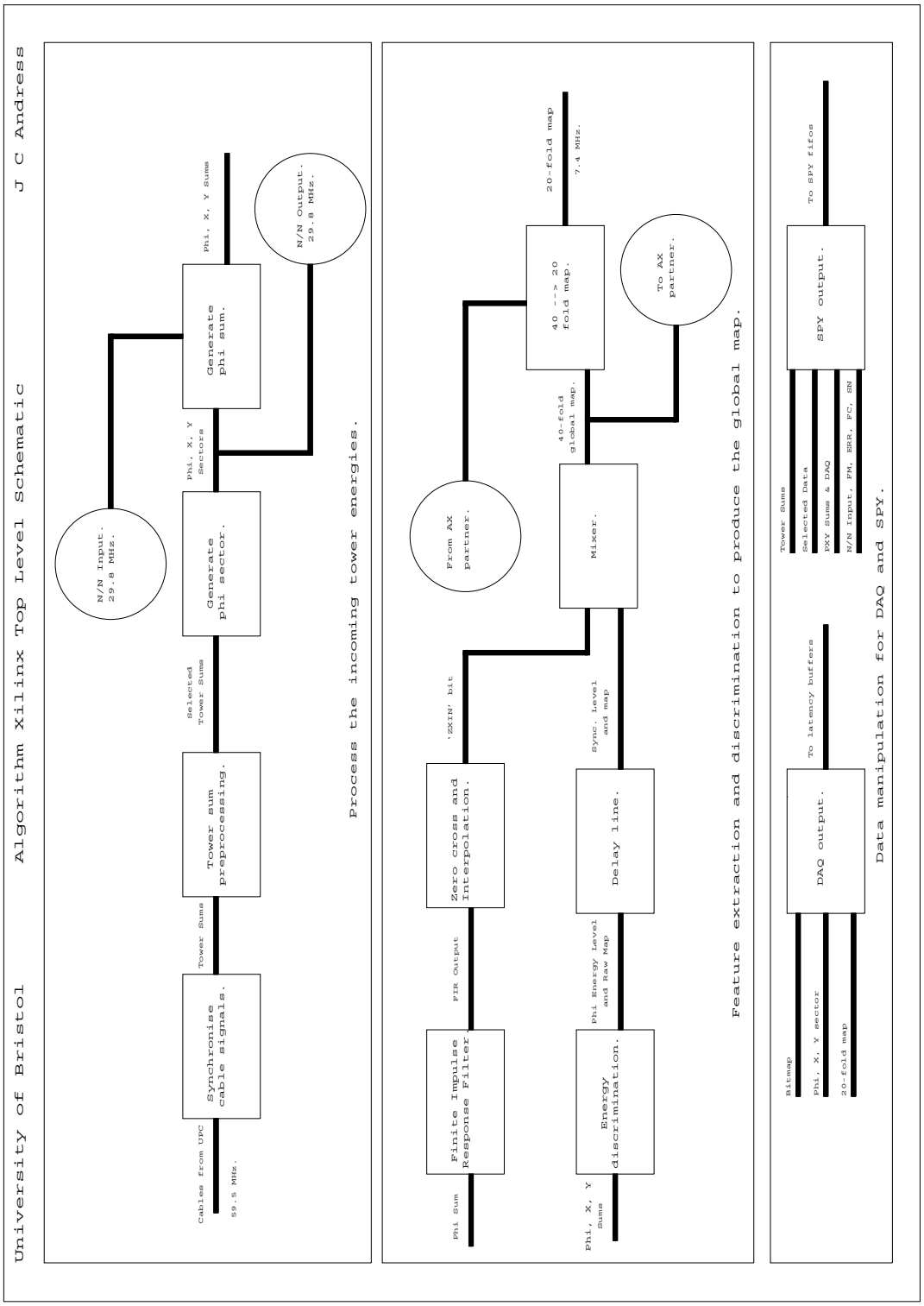

Figure 5.9: *The functional blocks within the final Algorithm chip design,* **Top** *Input Data Processing,* **Middle** *Feature Extraction & Discrimination to Produce Global Map,* **Bottom** *Output to DAQ & Spy*

latency buffers. The other operations carried out within the function block are comparisons to determine the tower with highest energy deposit. This is done by comparing the following blocks of tower objects.

1) θ 0>1
2) θ 2>3
3) θ 0|1>2|3
4) θ 4>5
5) θ 4|5>6
6) θ (0|1>2|3)>(4|5>6)

Not all of the energy from an EM shower is likely to be nicely contained within the physical boundaries of the ϕ structure. It is therefore necessary to have a way of adding neighbouring strips to produce a more complete picture of the energy deposits. Initially the total ϕ sum is made over all values of θ for that ϕ strip. The tower ϕ sum from the lower numerical ϕ strip are then added to it. At the same time the pre-added value of the ϕ strip is also passed to its next most positive neighbour. The ϕ sums resulting from this addition are then passed into the feature extraction part of the algorithm to generate the trigger objects.

- Feature Extraction and Discrimination to Produce the Global Map. Within this functional block 2 operations are performed on the ϕ sums received. The ϕ data only is passed into the FIR filter, whilst all information is passed into the energy discrimination block. The energy discrimination process will be described first since this is the easiest block to visualise.

  The trigger objects that are passed to the GLT system to create the Level 1 triggers are M, G, E, X and Y. Firstly X or Y are created by splitting off the data from towers θ_0 and θ_{5-6} respectively. The whole ϕ strip is then compared against a ladder of ascending threshold values. The X and Y sums are discriminated against their own threshold. All these are loaded during configuration. An associated feature of the EMC preamplifiers is that they have an energy dependent timing uncertainty (or jitter). Another effect due to the adding of the outputs from many preamps is the alteration of the pulse shape. To counter this the ϕ sum is compared against a preset set of threshold steps. When the signal has exceeded threshold the address of the passed threshold is converted into a 3-bit address which is compared with a lookup table (LUT) loaded at

configuration time to fetch the jitter window length. This sets the length of time that the trigger object will be switched on for when passed to the GLT.

The other part of the ϕ data path running concurrently with the discrimination is the Finite Input Response Filter and zero crossing/trigger time determination. The FIR design as included in the EMT algorithm uses an 8-tap time skew buffer with 2 distributed arithmetic LUTs and a shift and load accumulator. During configuration, the 7-bit Half Partial Product Sums (HPPS) are injected into the look up table serially, entering MSB first and then winding down the LUT one bit per clock pulse. To ensure instant operation of the filter when the constants are read back the ϕ inputs are closed temporarily and then flushed through with zeros. The input stream is tapped of equivalent positional bits from either successive unsigned energy input words. These are held in 8 individual RAM modules. These eight are then split into 2 separate 4-bit address words to be sent to the 2 LUT's to access the signed HPPS. The outputs from these 2 are then added together to give the partial product sum for that clock tick. The 16 results of this are then passed through a parallel shift and accumulate module to give a signed, 24-bit final sum of products. Since the output is constrained to be a 16-bit word then this must be passed through a reducer. Here small words (i.e. low value) are left but those that are larger than the allowed are firstly identified using the 8 most significant bits. If the result is large then an overflow condition is created, 0x7FFF for a positive number & 0x8000 for a negative number. Otherwise the sign bit is then merged with the low fifteen bits to produce the 16-bit FIR output word.

The input received by the Zero-Cross and Interpolate module is in the form of a 16-bit bipolar waveform. The time at which the zero crossing occurs is taken as the peak energy time. Since the input to the TPB runs at 3.4MHz but the output runs at twice this frequency, the determination of the trigger time can be done to twice the accuracy by interpolation of the FIR output waveform between successive outputs spanning the zero-crossing. In actual terms this is done using 2 successive positive and negative words, using binary addition and then by checking the carry bit to determine in which half of the frame the trigger occurred. For example if the carry bit is 0 since the crossing led from a large positive value to a small negative value then the zero cross occurred in the second half of the frame. The output from this module is one 134ns (7.4MHz) bit.

- Output to DAQ & Spy

  The output from the EMT at this stage would be a 40-fold map. The interface

between the EMT and GLT is designed for a 20-fold map. Therefore each output must be summed with its respective 'AX partner'. A simple ORing method is used and since each AX partner is contained on the same TPB all summing occurs on board. It is necessary to further reduce the Y output object to a 10-fold map.

The data is sent separately to the DAQ system and Spy. This enables error checking both online within the EMT crate in the case of the Spy and offline for efficiency studies etc in the case of the DAQ data. All of the output sent to the GLT is also automatically sent to the latency buffers mounted on the TPB as well as the individual tower inputs. Upon receipt of a Level-1 Accept this is then transfered to an event buffer for later readout.

As defined within the specification a limited set of data is also written out to the Spy buffers. In this case it comprises of the input data, intermediate data after summing and at various stages of the algorithm as well as the final output to the GLT.

- Latency

  The latency budget is particularly stringent due to the long preshaping time of the signal within the EMC front-end electronics. All the above operations must be completed within 5μs. During the design stages a copy of the AX was loaded into the Elchecker program to complete a full simulation. When the design was finished and found to be working correctly an oscilloscope with probes mounted after the input multiplexers and before the output multiplexers was used. A realistic pulse was then loaded into the frontend playbacks so as to get an actual physical value. It was found that the total latency for operations was 4.7μs. The output is displayed in figure 5.10.

5.2.3 The Rest of the EMT Crate

5.2.3.1 The Trigger Carrier Board

To enable communication between the single Readout Module and the 10 TPBs the Trigger Carrier Board (TCB) is used. This is a single 9U PCB that interfaces the optical connection with the electrical input and output from the individual TPB's. On this board are the Trigger Receiver Board (TRB) and the E-link Monitoring Board (EMB)[58]. The layout of these two boards on the main carrier board are shown in figure 5.11. This method was chosen since the TRB is a standard EMC piece of hardware that is used to interface with the FC system and as such requires little

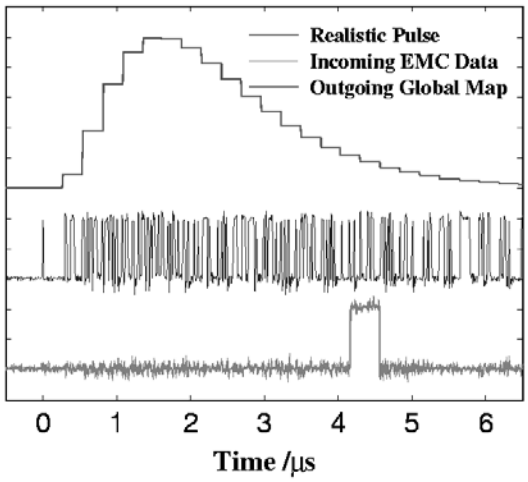

Figure 5.10: *Latency through the Algorithm Xilinx design as tested using a realistic pulse(top), the digital input EMC data(middle) and output trigger primitive(bottom)*

development work. The TRB receives the serial input data stream from the Gbyte optical link. This carries the driver chips for the Finisar transceiver as well as the fan out multiplexing chips to communicate individually with each TPB. This board also carries the CAEN interface to the Environmental Monitoring Board for output of TRB status to the slow control system. This is again an EMC standard board.
The data coming from the ROM via the C-link is 16-bits at the *BABAR* standard 59.5MHz as well as the system clock. Within the EMT, 12 of these bits are forwarded directly to the back plane with 10 connected directly to the TPB's and 2 as spare. The clock is also multiplexed and sent separately to each.
The output from the TCB along the D-link is the logical reverse with the first 10 bits of the 16 containing the data from each TPB in logical sequence. A block diagram of the internal operation of the TRB is shown in figure 5.11(right). Both the C & D links are physically interfaced through the custom J3 backplane (this is further described in section 5.2.3.2), whilst the optical and EMB connections are made through the front panel.

5.2.3.2 Custom Backplane & Patch Panel

The requirement of interfacing the C/D-link signals from the TCB to each TPB and the nearest neighbour connections between boards forced the design of a custom VME backplane from the trigger crate[59]. The full back plane layout in the crate is shown in figure 5.12. This shows the commercial J1 (top row) used for VME communication along the whole crate as well as the *BABAR* specfic J2 & J3 (middle & bottom rows

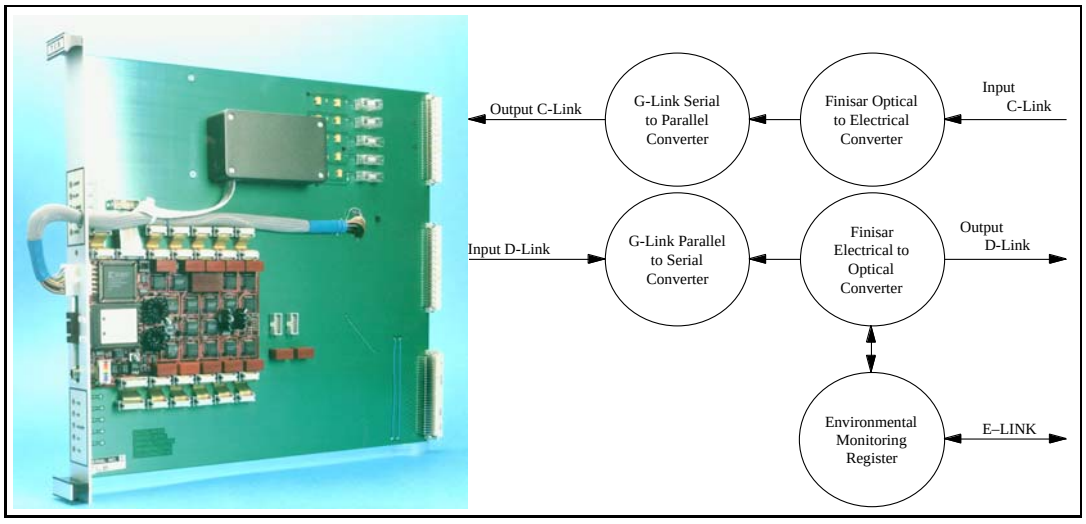

Figure 5.11: *A production Trigger Carrier Board showing positioning of the TRB and front panel(left) and Representation of the operation of the TRB(right)*

respectively) for the first 5 slots. The J3 is designed so that certain FC boards can only fit into their correct slots. The first 3 rows allow readout modules with the possibility of a FCPM in the 4th(to allow for standalone testing) and an FCDM in the 5th. The back of this section of the crate is also kept clear to allow the fixing of backplane network cards to the ROM's. The J2/J3 for the rest of the crate is completely EMT specific with 10 slots for the TPB's and one for the TCB. To prevent the boards from being inserted in the wrong slots these connections are intentionally different. The layout of the TCB – TPB connections is shown in figure 5.12. The layout of the boards within the crate was chosen to minimise the incurred delay during nearest neighbour transmission.

The physical distribution of the input signals from the cables through to the J2 inputs of the TPB's is achieved using a custom patch-panel design. This also enables all connections to be logically laid out with the TPB numbers running from 0 – 9 and the input θ towers logically 0 – 6. The layout of the connectors is shown in figure 5.13. Each patch-panel contains connectors for 24 input cables from the EMC system as well as the connectors for the cables out to the GLT system. Each EMT – GLT cable transmits 2 ϕ object outputs per cable and 1 Y object.

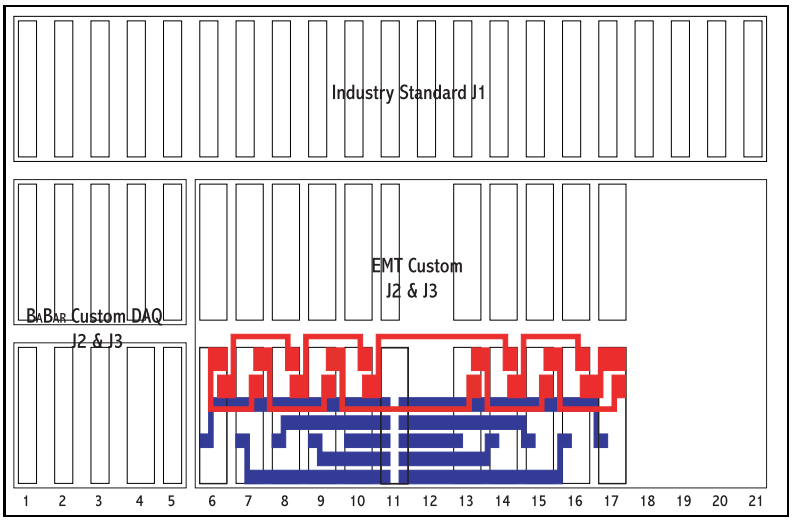

Figure 5.12: *The layout of the backplane of the EMT crate showing BaBar & EMT specific parts, The interconnections between the TCB & TPB's(dark blue) and the nearest neighbour connections(light red) are also shown*

5.3 The Software

The software for running the EMT system consists of 5 packages that are built within the online software environment. As with all *BaBar* programming code they are written in C++ using an object orientated design philosophy[60]. They are:

- L1EmtOnline
- L1EmtCalOnline
- L1EmtOdf
- L1EmtCalOdf
- L1EmtSpy

These 5 packages are built in such a way that they only create object libraries which are then loaded into the ROM. They are dynamically linked and package dependencies control the order of loading. Figure 5.14 shows the dependencies between each of the EMT packages as well as the Core Dataflow, Reverse Dataflow and Calibration packages. This is discussed further in [62]. The basic functionality of each package will be discussed. Core class descriptions are located in Appendix A.

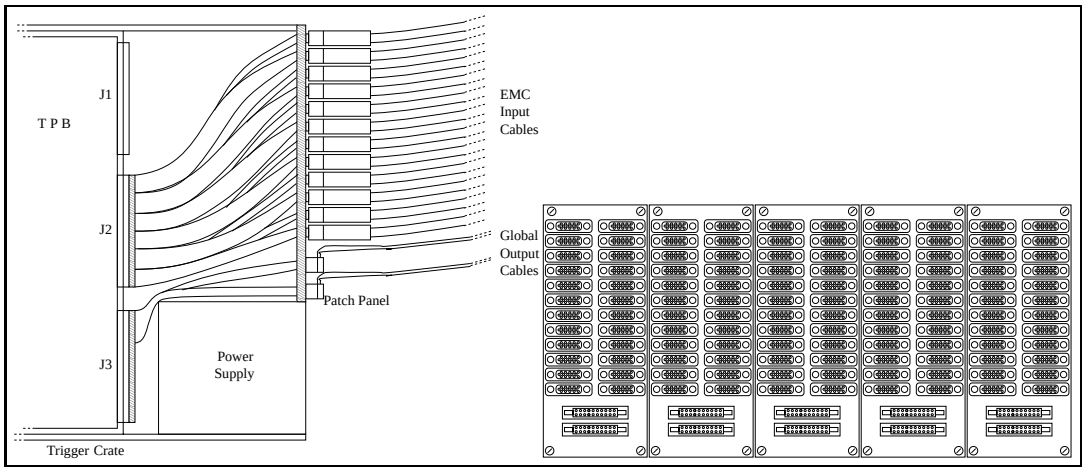

Figure 5.13: *The physical connection between the patch-panel and the crate backplane (left) and the layout of the patch panel as seen from the rear (right)*

5.3.1 L1EmtOnline

This package is used for managing the data transfer both into the ROMs for configuration and then out of the system for the event data. As described in chapter 4 any data movement within the Dataflow platform must be done using a tagged container (TC). This package therefore contains the EMT specific derivatives of the core tagged containers. For configuration a complete software model of the system is built within the ROM memory space. This is done through first constructing a C++ singleton object labelled a crate. The singleton was used since it is impossible for there to be more than one physical crate in the system and this also creates memory security. Within the crate object a number of TPB objects are then created as defined by the VME read during the boot phase of the system startup. For each TPB there are six different types of configurable objects, the Xilinx chips, playback buffers and the Control, Status and Error Register(CSER). Within the software model these are replicated. This is best shown in figure 5.15. The configuration data is stored within a 'rawdata' class and during initialisation these are filled with default values. For system integrity the hardcoded values are not physically sensible, so that should configuration fail it will be immediately noticeable to the *BABAR* shift crew. For each type of configuration data a separate class exists containing all accessor functions. These classes also contain methods for choosing the source of configuration data. This can either be from a flat ASCII file or a binary TC. This was done in preparation for reading the data from persistent storage within an Objectivity database[61]. The contents of each type of configuration data is described within Appendix A.
The TC classes have exactly the same available methods as the ROM accessor classes.

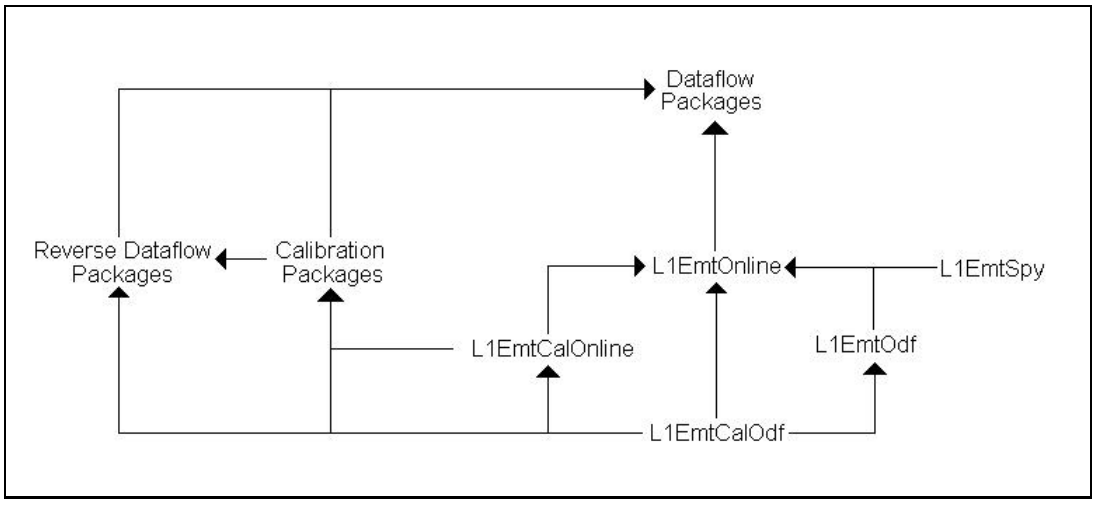

Figure 5.14: *The Class Dependencies for The EMT Software packages*

It is necessary to have a compiled program that is dedicated to constructing these files that are written in a binary format. Each type of Xilinx data has its own TC construction program. Once the files have been transfered to the database and added to a specific configuration key, changing the contents of any part of the Run Control Key requires a change to the database entry. This is currently a cumbersome and time consuming operation. As such it was decided that for a limited period of time the EMT mask section of the AX data will be read from a flat file, which is much easier to change.
Apart from configuration the other main functionality of this package is to transmit the event data from the TPBs through to final data storage. There are 2 distinct classes which are used L1EmtSlotTC and L1EmtChannelTC. A ChannelTC contains the event information from each TPB. These are in turn contained in one SlotTC which collects all TPB's output as well as the Global Map output. As such an iterator class is required. During the development of the system the format of these containers changed and to ensure that any data that had been written before the change could still be read it was necessary to create classes to act as an interpreter between the two versions. The information that is read out for each event is as follows:

- SlotTC
  - Control Status & Error Register.
  - Number of Channel TCs contained.
  - Number of time samples for each piece of information in a channel TC.
  - The beam crossing time.

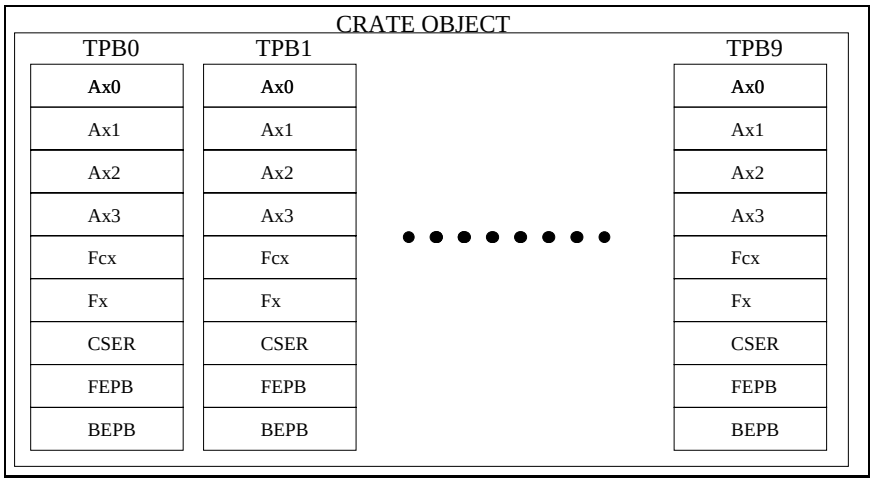

Figure 5.15: *The software model of the EMT physical system used for storage of configuration information*

  - The information as passed out to the Global Trigger
  - ChannelTCs themselves.

- ChannelTC
  - Channel Number: (0 to 39)
  - Data bitmap: This the energy information for that channel
  - ϕ, θ information
  - X Information: Energy deposited in that X region
  - Y Information: Energy deposited in that Y region

Within the online software system it is necessary that any TC objects are given their own unique identifier. These are allotted on a subsystem basis though within the allocated range of values the subsystem is given complete freedom of usage. As such a separate class was also needed to manage this allocation.

5.3.2 L1EmtCalOnline

This dual-use package contains code that is used for data collection and analysis as well as the code used for the creation of the CycleTCs. These are used to define which type of calibration run cycles the finite state machine will operate. For each step of the finite state machine a separate class is created with each constructor having to have the following list of arguments.

- OdfArena, This is the memory space allocated for the complete CycleTC tree.

- Type ID, any TC working within the dataflow platform must have a specific identification number associated with its type.
- Transmission flag, this controls whether data that is being analysed within the calibration framework will be transmitted further down the tree.

As with other packages that are built using the online makefile system it is necessary to declare any templates within the package classes. This was determined to be due to a bug in the C++ precompiler for the VxWorks operating system. Also contained are the files that produce the executables for the production of CycleTC files. There is one of these files per type of calibration run that can be done. Their internal structure is as follows.

1. Initially an OdfArena is created in memory space. This is used to hold all the CycleTCs before they are written to file.
2. A TopTC is then created on which the subsystem specific CycleTC's are appended.
3. The ConfigCycleTC is then constructed with the calibration specific *Calchoice* and *CSERChoice* variables as constructor arguments. This is then appended to the topTC. Within this part of the code is also a variable to determine the number of subclass meta cycles that will be attached.
4. Next the number of Metacycles is iterated through. Within each Meta cycle is a variable to determine the number of Macro cycles per Meta cycle, Major per Macro and Minor per Major. This is best illustrated within figure 4.17.
5. Within Each Minor Cycle a dataflow command can be issued such as Level 1 Accept. The number issued can also be controlled.

The order of operation for a configuration TC is to perform all the operations for the 1st of each type of FSM level first and then iterate back up the configuration tree to perform the next iteration of the previous level.
The final group of classes within this package are those to store and process the data collected from the Frame Clash calibration[63]. This calibration is described in more detail in section 5.3.4. The classes contained here are used to collect the data from each different TPB frame offset and EMC frame offset combination for later analysis.

5.3.3 L1EmtOdf

This package forms the primary interface between the EMT software and the core dataflow code. It has been written to conform to the *BABAR* Dataflow API as described

in [64]. Any operation that involves core dataflow software will depend on a class defined here. The specialised read and write classes for all status registers as well as playback buffers are located here. This package initially held the classes that were used to run the system on the prototype teststand at SLAC using the version 1 (or alpha) release of the dataflow software. This involved no use of the finite state machine but instead just defined the interfaces that would need to be designed against for all interactions between ROMs and front-end systems.
One of the crucial parts of the initial design brief for the EMT system was a method of real time error checking using the processing power of the ROM to maintain a software model of the algorithm to be able to compare results. The analytical code for this is in the package L1EmtSpy (See section 5.3.5). Since it is important that this functionality does not interfere with either the readout of the data from the system through the ROM or further propagation onto persistent storage, this process must be run as a VxWorks background task. All the code for maintaining this relationship is also based within this package. They are described below:

5.3.3.1 DAQ Words

The format of the command and control words that the DAQ system is designed to handle is such that very much the same format is used for reading and writing. Here the read side will be described. Each word read from the ROM contains a 4 byte header. This is to ensure correct flow of the data. The headers structure is as follows:

- 1-bit Start bit, always 1
- 1-bit Event data flag, always 1 for event data
- 5-bit Trigger tag, Checked by the dataflow software to ensure all data is from the same event.
- 1-bit (Reserved for byte alignment)
- 5-bit Trigger counter, holds the event time stamp.
- 2-bit Event buffer number
- 1-bit (Reserved for byte alignment)
- 16-bits for the Control, Status & Error Register for all boards. This includes mode, G-link & i/o memory status.
- Padding to ensure correct length since different subsystems will produce different length data.

The event data then follows the header. For the EMT system this is as shown in table 5.1 at maximum capacity. This leads to each TPB producing 296 bytes and therefore the whole system producing a maximum of 3040 bytes including header.

	bytes/sector	sectors/board	Ticks	bytes/event
ϕ	2	4	16	128
X	2	4	6	48
Y	2	4	6	48
ϕ Map 1	1	4	6	24
ϕ Map 2	1	4	6	24
GLT	1	4	6	24

Table 5.1: *The maximum possible event size produced by the EMT system*

5.3.4 L1EmtCalOdf

This package contains all the finite state machine actions for all the different modes of operation of the system for data collection, calibrations and interface tests. These can be grouped in 2 different ways. Firstly are the action classes that are automatically attached to the finite state machine independent of the calibration type chosen and then those that are only attached for their specific calibration. The *Reset, Configure, Begin Run* and *Begin Meta* are all the first type of classes. When an action is attached to the FSM then an entry is made in the state table so that the software knows to run that action for a specific transition within the FSM.

When the system is turned on and the boot process for the ROM automatically starts, the FSM is initialised and then the *Reset* action attached. This initialisation also creates the system software model within the ROM memory space. Defined within each action class is a method called *fire*. This contains the precise definition of what functionality the class will perform. Once the boot sequence has started then the fire method for this action is called and all memory buffers on the TPB are zeroed and the TPB's internal clock is then synchronised with the system clock. This action also attaches the *Configure* action onto the FSM. Within this action the decision is made over which type of CSER will be downloaded on to the boards and configuration constants are to be downloaded firstly into the software model (as described in section 5.3.1) and then into the TPB. The *Begin Run* transition reads the registers from each of the Xilinx chips and checks the contents against the software model for errors during download of constants. Within the *Begin Meta* transition the decision of which calibration will be run is made and the appropriate next transition is added to the FSM. The inherent operation of classes for the specific calibrations will be detailed later.

Each action inherits from 2 separate base classes. One is the dataflow action base-class which holds all necessary functionality to attach an action to the FSM. The other is

an EMT specific class used to contain functions that are needed within many of the actions. It contains functions that are used for reading and writing of configuration data from the TPB as well as the software model contained in ROM memory space. Currently this class also contains the interface between the EMT software and reverse dataflow.
As outlined in section 4.3.2.1 the calibration of the system must be consistently known and matched to recorded data. To allow this a persistent *Calibration Database* has been created which contains configuration constants and the definitions of what the system will do at each stage of the FSM. This system makes calibrations quick and easy to both define and perform. Examples of calibrations that are performed on the EMT system are below.

1. Feature Extraction: This is described in section 5.3.4.1. [1]
2. FrameClash Calibration:
3. Tower Calibration:
4. FCX Calibration:
5. Phi Calibration:
6. Front-End Playback Calibration:
7. Back-end Playback Calibration:

These calibration can be grouped into different types. The most prevalent are those that change one or more configuration values then collect data (be it normal DAQ data or the contents of the CSER). The FSM is then backed-down a number of states and the configuration data is changed and more data collected. The Tower, FCX and Phi calibrations all change the tower input mask.
The most important of these is the Tower calibration. This allows the physical interconnection with the EMC to be checked using either the set serial number pattern output of the EMC UPC's or system noise when reading directly from the front end electronics. The idea behind the latter is to alert the expert to any channels that are misbehaving and would need to be masked out when collecting real event data.
The FCX calibration was to monitor the system response to a change in the *synchDelay* variable within the FCX configuration data to ensure that the EMT latency budget was used as efficiently as possible. There are 16 possible values for this, equally shared

[1] Even though it is listed as a calibration 'Feature Extraction' is used for collecting real data. This is a consequence of the construction of the calibration system

between the first and second half of the 7.4MHz output signal. Therefore, though 16 different values of this can be set, the effect is the same if you have values 0 & 8, 1 & 9 ... 7 & 15.
The Phi calibration is used to check the connection between the EMT & GLT. With the overall trigger mask set to take triggers resulting from the EMT system then the output of the GLT should exactly match the input mask loaded. The synchronised systems then collect a set number of Level-1 accepts after which the ϕ sectors that are unmasked are changed and more data is then collected. This continues for a complete rotation of the calorimeter ϕ sectors.
The FrameClash calibration is used to synchronise the EMC and EMT systems interconnection. The data from the EMC system is fed into a dual port memory buffer, i.e. it can be read and written to at the same time. When exactly the same 'bit' is being written at exactly the moment when it is read, this can cause data corruption. With the data a frame bit is sent down a separate twisted pair. This must not occur on the same clock pulse as the TPB frame bit. The operation of this calibration is slightly different to the rest since one of the values that are being altered are actually in the EMC UPC configuration data for the EMC frame offset.
As described in section 5.4.1 for the development of the prototype TPBs there were many diagnostic tests developed to run from the VxWorks command line. The Board Test calibration was developed to allow these to again be run but from within the dataflow finite state machine. This was done to automate the process of hardware failure detection. The operation of each of these tests is given in more detail in section 5.4.1.
During the software development it became clear that the format of the DAQ SlotTC and ChannelTC objects would need to be changed slightly. To test this a new calibration was designed to write the DAQ data read simultaneously into a new version of the output TCs as well as the known older version. The results could then be checked offline for data corruption.

5.3.4.1 Feature Extraction

During feature extraction of the stored data in an event buffer there are 2 operations performed on the data:

- Reformatting
- Zero-suppression

Reformatting is necessary since the format of the data as it is written into the event buffers is not necessarily the most efficient way of persistently storing the data. During

an average high background event only 15% of the calorimeter will contain data above the crystal threshold that qualifies it to be added to a tower. Zero suppression has the possibility to reduce the event size from the maximum possible of 2240 bytes of data to 500 bytes. The only part of the event data read out to the DAQ system, that is not suppressed is the ϕ map. Therefore the average event size actually read out is 1360 bytes.

5.3.5 L1EmtSpy

This package contains the code that is used to sample the input data fed into the boards and apply a software simulation of the algorithm design to it to generate its own set of outputs. These are then periodically checked during runtime. Currently this requires an expert to view the error-logs created to check for inconsistencies between the algorithm and the software model.

5.4 System Commissioning and Operation

As described in section 4.2.1 the EMT system must have significant methods of fault finding, both in the hardware and software to be able to completely rely on the trigger decisions made. This is especially true when the system is in the prototyping stage. To this end it was necessary to design software that would be able to test the inherent behaviour of the system during design and construction as well as when in use during running.

5.4.1 Prototype Testing

After the acceptance of the Preliminary Design Report for the system it became necessary to construct and test a prototype of the TPB. The construction of the board was done at the Rutherford Appleton Labs where the PCB design was done. Since it was not possible to duplicate the entire *BABAR* dataflow platform it was necessary to construct as close a system as possible. This was done using a custom optical transceiver board the RAL 2301 controlled by a proprietary Motorola single board computer. These boards were arranged in the standard VME crate as shown in figure 5.16. As with the final system the SBC runs the VxWorks operating system. The only specific software needed was a mock up of the core dataflow code.This was written in the same way as the final system, to achieve sufficient portability. The TPBs were then run through their operation at each stage of the design to ensure complicity with the requirements. The tests that were performed are grouped into sections below. The full results from these tests may be found in [65].

- Input from J2 connection from UPC through to the input to the algorithm chip

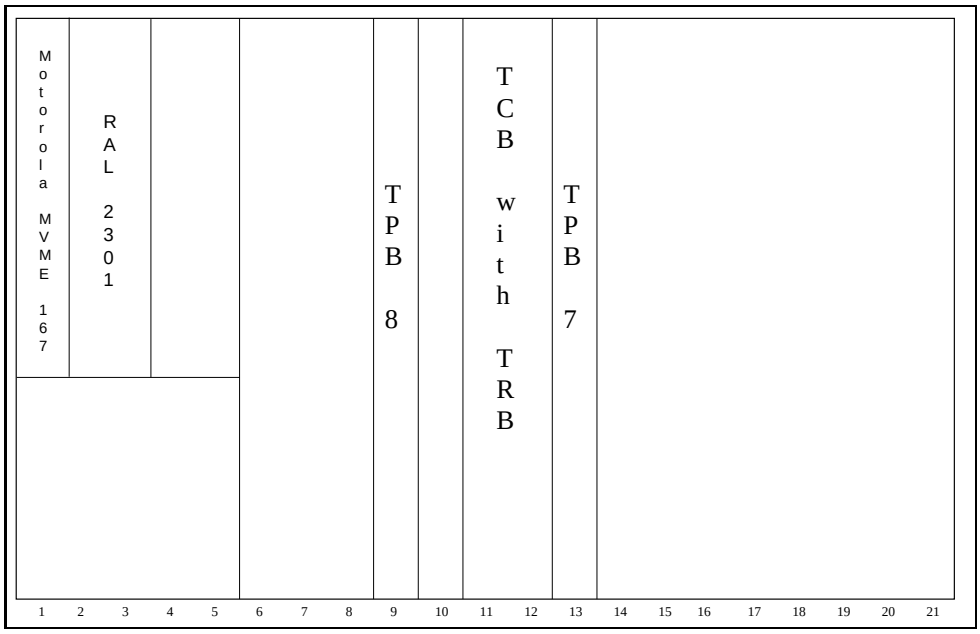

Figure 5.16: *The arrangement of boards within the EMT prototype crate*

  - To test the input stages on board the RAL 2301 board can be loaded with many bits of simulated data which are then transfered into the Front End Playback buffers. The design of the board is such that the algorithm is insensitive to the path along which the supplied data is fed.

- Algorithm
  - During construction of both the Algorithm chip design and the TPBs it was important that development could continue in parallel. To this end initially the AX was replaced with a design that piped the inputs received straight through to the output stages for transmission through the VME interface. As each stage of the design of the algorithm progressed then it became possible to test it independently using a known input pattern loaded into the front-end playbacks and then processed and compared with know outputs. The design for a the algorithm was also heavily simulated using the Viewlogic chip design software.

- GLT outputs
  - Testing the path of data completely, from the backplane interface to the GLT outputs could only be done using a logic analyser. To this end as simple a dataword as possible was used to simulate input and then the output is written through the complete board into the logic analyser.

- Fast control interface (Fast Control Xilinx)
  - The RAL 2301 output buffers were loaded with a sequence of Fast Control Words which were then written through the C-link. Checks were then

performed by writing the *Control, Status and Error Register* contents out through the VME interface for comparison against the known inputs. Most of the other tests made use of fast control commands so we were able to combine many of these tests.

- Formatter Xilinx
  - Testing of this component was done by loading a known pattern into the Event buffers which was then read back a number of times with a different mask loaded at configuration time to the Fx. This also tests the writing and reading of the on board memory within the chip. This was also done in a controlled way when testing the prototype algorithm designs.
- Spy & playback FIFOs
  - These are very crucial initially since testing of various other components on the TPB requires known patterns being loaded. These are then passed through the board in the case of the Playback FIFOs to check other components. The Spy FIFOs are used to record information passed through the board which can then be read out through the VME interface. The various functionality of control for stopping the Spy buffer cycle such as "Stop On L1Accept" or "Stop On Full" was tested as part of other system tests.
- Event & Latency buffers
  - For the latency buffers various patterns are loaded into the TPB Front Playbacks and then passed through the Algorithm. The latency buffer operation is tested using differing latency buffer configuration lengths and a logic analyser. For the Event buffer tests the correct operation must be observed for the following Fast Control commands, L1Accept, Clear Readout and Read Event. This was done with data being read in from the Front playback FIFOs and then all commands were injected using the RAL 2301. The operation was then monitored using a logic analyser initially and software once this had been developed.
- VME interface
  - Many of the tests depend upon the VME interface. To ensure complete reliability many small tests were devised to exercise all aspects of its functionality. These were initially to ensure that the result of a VME read for each of the boards was completely reliable. This was done using a sent configuration that was easy to check, configuration mode on the boards with all other bits in the control word set to 0. The board is then cycled through from configuration to run mode, each time having the VME read after state transition. This enabled the test to be run over many iterations.

5.4.2 Diagnostics

Initially all the tests that were used for the validation of the prototype TPB were grouped together using a VxWorks executable script. The operation of this enabled the system to be run through the tests with all output being written to file for later analysis. It became apparent that only the higher level checks would be needed to run within the calibration system framework. Alterations were therefore needed to port the code to the new framework. This enabled quick and easy checking of any boards that had apparent problems, before they were moved from the *BABAR* platform into the teststand.

5.4.3 Calibration

Obviously one of the most important aspects of the system calibration is ensuring the correct connection between the EMT and GLT. The method of checking this is described below.

- EMC connection. This connection is also needed to ensure the validation of the input tower mask for data taking. There is a dedicated calibration sequence for this within the L1EmtCalOdf package. The EMC UPCs can be configured to output various test pulses that are loaded into the intermediate store. The other output needed for the connection verification is that all the cables are plugged into the correct location. The UPC was designed to allow this by outputting the unique serial number from each board with an associated tower label. These calibrations are set up in the following manner.

- GLT Connection. As above this is tested by loading a set pattern and then playing this through the system starting at a known time. In this case it is possible to control completely the patterns being played through loading them into either the front or back playback buffers. The analysis software must also know what pattern has been loaded. Initially this involved hardcoding this into several different classes that were chosen by TCL, but eventually the software would read the output DAQ data from the EMT and then attempt a match with the GLT data.

5.4.4 Fast Monitoring

Eventually the experiment should be run by 2 - 3 people. This will be the Shiftleader, Data Acquisition Expert and Data Quality Monitor (DQM). To ensure that this can be done all relevant parts of the detector and its data must be checked. The Data Quality Monitor can view the incoming data using histograms on a Java interface (JAS) on a local World Wide Web page (more information may be found on JAS at [66]). As the run is progressing the information in the histograms is updated live via a trickle stream (i.e. only a small fraction of the data that is passing through is copied into this stream). For the trigger system as a whole the fast monitoring for the Global trigger, Drift Chamber Trigger and EMT has been grouped together. A screen capture of this is shown in figure 5.17. Since this is the first stage in maintaining the health

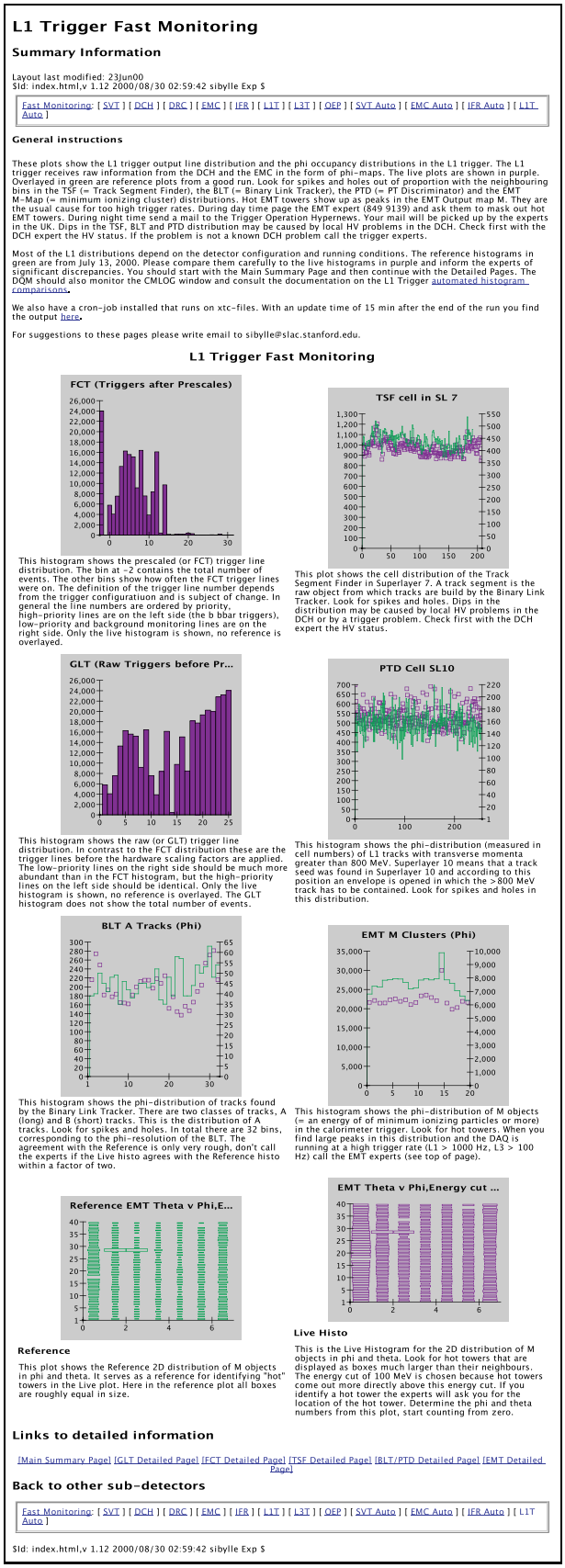

L1 Trigger Fast Monitoring

Summary Information

Layout last modified: 23Jun00
$Id: index.html,v 1.12 2000/08/30 02:59:42 sibylle Exp $

Fast Monitoring: [SVT] [DCH] [DRC] [EMC] [IFR] [L1T] [L3T] [OEP] [SVT Auto] [EMC Auto] [IFR Auto] [L1T Auto]

General instructions

These plots show the L1 trigger output line distribution and the phi occupancy distributions in the L1 trigger. The L1 trigger receives raw information from the DCH and the EMC in the form of phi-maps. The live plots are shown in purple. Overlayed in green are reference plots from a good run. Look for spikes and holes out of proportion with the neighbouring bins in the TSF (= Track Segment Finder), the BLT (= Binary Link Tracker), the PTD (= PT Discriminator) and the EMT M-Map (= minimum ionizing cluster) distributions. Hot EMT towers show up as peaks in the EMT Output map M. They are the usual cause for too high trigger rates. During day time page the EMT expert (849 9139) and ask them to mask out hot EMT towers. During night time send a mail to the Trigger Operation Hypernews. Your mail will be picked up by the experts in the UK. Dips in the TSF, BLT and PTD distribution may be caused by local HV problems in the DCH. Check first with the DCH expert the HV status. If the problem is not a known DCH problem call the trigger experts.

Most of the L1 distributions depend on the detector configuration and running conditions. The reference histograms in green are from July 13, 2000. Please compare them carefully to the live histograms in purple and inform the experts of significant discrepancies. You should start with the Main Summary Page and then continue with the Detailed Pages. The DQM should also monitor the CMLOG window and consult the documentation on the L1 Trigger automated histogram comparisons.

We also have a cron-job installed that runs on xtc-files. With an update time of 15 min after the end of the run you find the output here.

For suggestions to these pages please write email to sibylle@slac.stanford.edu.

L1 Trigger Fast Monitoring

FCT (Triggers after Prescales)

This histogram shows the prescaled (or FCT) trigger line distribution. The bin at -2 contains the total number of events. The other bins show how often the FCT trigger lines were on. The definition of the trigger line number depends from the trigger configuratiuon and is subject of change. In general the line numbers are ordered by priority, high-priority lines are on the left side (the b bbar triggers), low-priority and background monitoring lines are on the right side. Only the live histogram is shown, no reference is overlayed.

TSF cell in SL 7

This plot shows the cell distribution of the Track Segment Finder in Superlayer 7. A track segment is the raw object from which tracks are build by the Binary Link Tracker. Look for spikes and holes. Dips in the distribution may be caused by local HV problems in the DCH or by a trigger problem. Check first with the DCH expert the HV status.

GLT (Raw Triggers before Pr...

This histogram shows the raw (or GLT) trigger line distribution. In contrast to the FCT distribution these are the trigger lines before the hardware scaling factors are applied. The low-priority lines on the right side should be much more abundant than in the FCT histogram, but the high-priority lines on the left side should be identical. Only the live histogram is shown, no reference is overlayed. The GLT histogram does not show the total number of events.

PTD Cell SL10

This histogram shows the phi-distribution (measured in cell numbers) of L1 tracks with transverse momenta greater than 800 MeV. Superlayer 10 means that a track seed was found in Superlayer 10 and according to this position an envelope is opened in which the >800 MeV track has to be contained. Look for spikes and holes in this distribution.

BLT A Tracks (Phi)

This histogram shows the phi-distribution of tracks found by the Binary Link Tracker. There are two classes of tracks, A (long) and B (short) tracks. This is the distribution of A tracks. Look for spikes and holes. In total there are 32 bins, corresponding to the phi-resolution of the BLT. The agreement with the Reference is only very rough, don't call the experts if the Live histo agrees with the Reference histo within a factor of two.

EMT M Clusters (Phi)

This histogram shows the phi-distribution of M objects (= an energy of of minimum ionizing particles or more) in the calorimeter trigger. Look for hot towers. When you find large peaks in this distribution and the DAQ is running at a high trigger rate (L1 > 1000 Hz, L3 > 100 Hz) call the EMT experts (see top of page).

Reference EMT Theta v Phi,E...

Reference

This plot shows the Reference 2D distribution of M objects in phi and theta. It serves as a reference for identifying "hot" towers in the Live plot. Here in the reference plot all boxes are roughly equal in size.

EMT Theta v Phi,Energy cut ...

Live Histo

This is the Live Histogram for the 2D distribution of M objects in phi and theta. Look for hot towers that are displayed as boxes much larger than their neighbours. The energy cut of 100 MeV is chosen because hot towers come out more directly above this energy cut. If you identify a hot tower the experts will ask you for the location of the hot tower. Determine the phi and theta numbers from this plot, start counting from zero.

Links to detailed information

[Main Summary Page] [GLT Detailed Page] [FCT Detailed Page] [TSF Detailed Page] [BLT/PTD Detailed Page] [EMT Detailed Page]

Back to other sub-detectors

Fast Monitoring: [SVT] [DCH] [DRC] [EMC] [IFR] [L1T] [L3T] [OEP] [SVT Auto] [EMC Auto] [IFR Auto] [L1T Auto]

$Id: index.html,v 1.12 2000/08/30 02:59:42 sibylle Exp $

Figure 5.17: *Example screen capture of JAS Level 1 trigger Fast monitoring, showing the GLT/FCTS plot top and middle left, DCT top and middle right and EMT bottom*

of the system, it is important that the plots that are used are as clear as possible. Therefore a set of recent 'reference plots' is kept with which the output from the current run is compared. For the EMT the histograms chosen will both change shape dramatically if there is a problem in the system. As a WWW link from this page a set of more detailed plots are available. These were chosen so that a non-EMT expert could look at them and get a good idea on the state of the system. Some duplication from the previous page was necessary to give an overall picture of the system state in one page. A screen shot of these is shown in fig 5.18. These are:

Phi map of M trigger objects Using this it is very easy to identify when noisy channels appear. This can push the L1Accept rate up to an unacceptable level very quickly. This also features on the general trigger page.

EMT time of trigger outputs to the GLT If a problem develops with one of the Trigger Processor boards then it is more than likely that it would show up as either a solid band indicating triggers constantly going off or as a dead region since no triggers are being fired by that ϕ strip.

A Hit map of all trigger objects giving their θ/ϕ reference This is very useful once the presence of a hot region has been established for telling the trigger expert where it is so that they can quickly and easily mask it off.

The above plot with an Energy cut at the MIP energy This can remove a lot of noise that is generate by electronics and shows where the EMT should have fired for any event.

In parallel with the WWW based fast monitoring the original method of monitoring is still run. The method of implementation was using a separate executable that was run using an automated process to produce a postscript file that can be viewed later. This also had the advantage that it can be viewed by the "on-call" expert easily from home should a system problem arise. It was also necessary to construct some form of 'expert' monitoring that could be used by an EMT expert. To achieve this a TCL parameter was introduced *emtexpert*. This would be left switched off. The other subsystems monitoring is independent and so may be left at the non-expert level to ensure that the speed of event processing isn't too slow and the output file is not unmanageably large.
The histograms that are included from this are below:

Output maps in ϕ for all 5 trigger objects M, G, E, X and Y Quickly identify regions that are not behaving correctly.

Timing against ϕ plots for all 5 objects These ensure that there is no energy dependence in the timing of the trigger primitives.

Weighted maps for all the trigger objects These are profile plots of the above scatter plots.

Peak energy in each ϕ strip, X and Y region for all 40ϕ strips A noisy tower will show up very quickly in one of these plots depending on its position.

BaBar L1 Trigger EMT

Detailed Information

Layout last modified: 23Jun00

Fast Monitoring: [SVT] [DCH] [DRC] [EMC] [IFR] [L1T] [L3T] [QEP]

Back to main L1 Trigger page

This page helps you to find "hot" EMT towers. If you notice a high trigger rate (L1 > 1000 Hz, L3 > 100 Hz) check out this page whether it is caused by hot EMT towers. In case you can identify large peaks follow instructions on main trigger page and notify the EMT experts.

L1-EMT Trigger Fast Monitoring

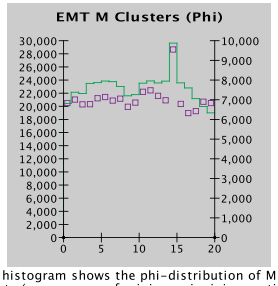

This histogram shows the phi-distribution of M objects (= an energy of minimum ionizing particles or more) in the calorimeter trigger. Look for large peaks in this distribution (= hot towers).

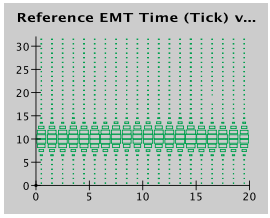

Reference

This is the Reference 2D-histogram of the Output Map M versus time. It is a timing plot of the M objects. The peak is centered around tick 10 and all ticks line up.

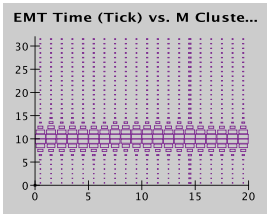

Live Histo

This 2D-histogram shows the Live Output Map M versus time. The peak should be centered around tick 10. They should all line up. In the region of hot towers the time ticks outside of the peak are also populated and the peak appears to be less pronounced as in the neighbor bins.

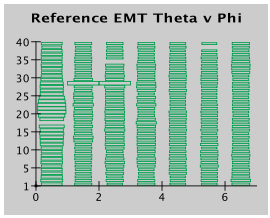

Reference

This plot shows the Reference 2D distribution of M objects in phi and theta. It serves as a reference for identifying "hot" towers in the Live plot.

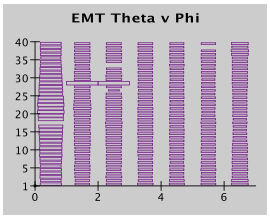

Live Histo

This plot shows the 2D distribution of M objects in phi and theta. It is good for showing "hot" towers. These are displayed as boxes much larger than their neighbours.

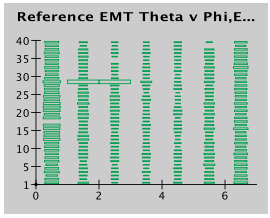

Reference

Reference histogram as in upper row, but with an energy cut of 100 MeV.

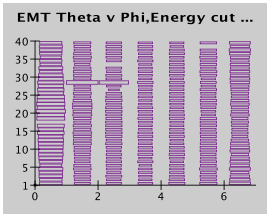

Live Histo

Live histogram as in upper row, but with an energy cut of 100 MeV. Typically hot towers come out more directly here. The difference to the neighbour towers is more pronounced. If you identify hot towers the experts will ask you for the location of the hot tower. Determine the phi and theta numbers from this plot, start counting from zero.

Links to detailed information

[Main Summary Page] [GLT Detailed Page] [FCT Detailed Page] [TSF Detailed Page] [BLT/PTD Detailed Page] [EMT Detailed Page]

Back to other sub-detectors

Fast Monitoring: [SVT] [DCH] [DRC] [EMC] [IFR] [L1T] [L3T] [___]

Figure 5.18: *The EMT specific page of the JAS Fast Monitoring*

The θ bits in each ϕ strip for the whole run These show the location of all hits in the strip.

Energy plots for all energies for ϕ, X and Y This can indicate a problem with the input to the system from the EMC frontend electronics and help to easily pinpoint it.

This gives a total of 588 histograms that can be used to totally check the health of the EMT system.

5.5 Performance Studies

5.5.1 Efficiency

As was described in the requirements of the trigger system, the efficiency for the EMT must be not only high but also precisely known. To this end there have been many studies to determine exact efficiency figures for the system. The most crucial features of a trigger system that employs thresholds to create different objects is the threshold turn-on rate. A structure was created to study this.

The method chosen uses events selected from the Level-3 output line 'L1PassThrough' which produces events that are purely selected by the Level-1 trigger and then written directly to storage. These are then further parsed so that the events used for efficiency calculations are triggered only using the DCT to generate the primary trigger line for the event. A geometrical constraint is then applied to account for the EMC geometrical coverage. The EMC information contained in an event is then checked and a match attempted for the corresponding θ,ϕ position in the EMT system. This is done for all of the trigger objects over all ranges of P_t. Since the data that is used to create the efficiency curves has been taken with varying input masks set, EMC data from towers that have been masked off have been ignored in the input.
As can be seen in figure 5.19 the peak efficiency when the system has reached the efficiency plateau is greater than 99%. These plots have been produced from run number 10323 in the beginning of January 2000. It can be seen that there is particularly good agreement for the lower energy thresholds but this decreases for the high energy in particular Y. This problem is made worse by the low statistics. This problem is due to the Monte Carlo simulation being too efficient and not totally modelling the high energy behaviour. Further analysis of these results has also lead to the discovery of a tiny fraction of events that are not correctly triggering[67]. There are 2 possible scenarios. In the first the EMT fires when no new calorimeter pulse has been seen. This has been tracked to a situation where a pulse has been detected by the calorimeter and then during the decay part of the pulse there is a small fluctuation in the background noise which results in another out of time local maximum in the energy spectrum producing a spurious trigger. The second case is where the EMT fails to fire. This is thought to be caused by the peak time in the EMC pulse to be outside the feature extraction window.

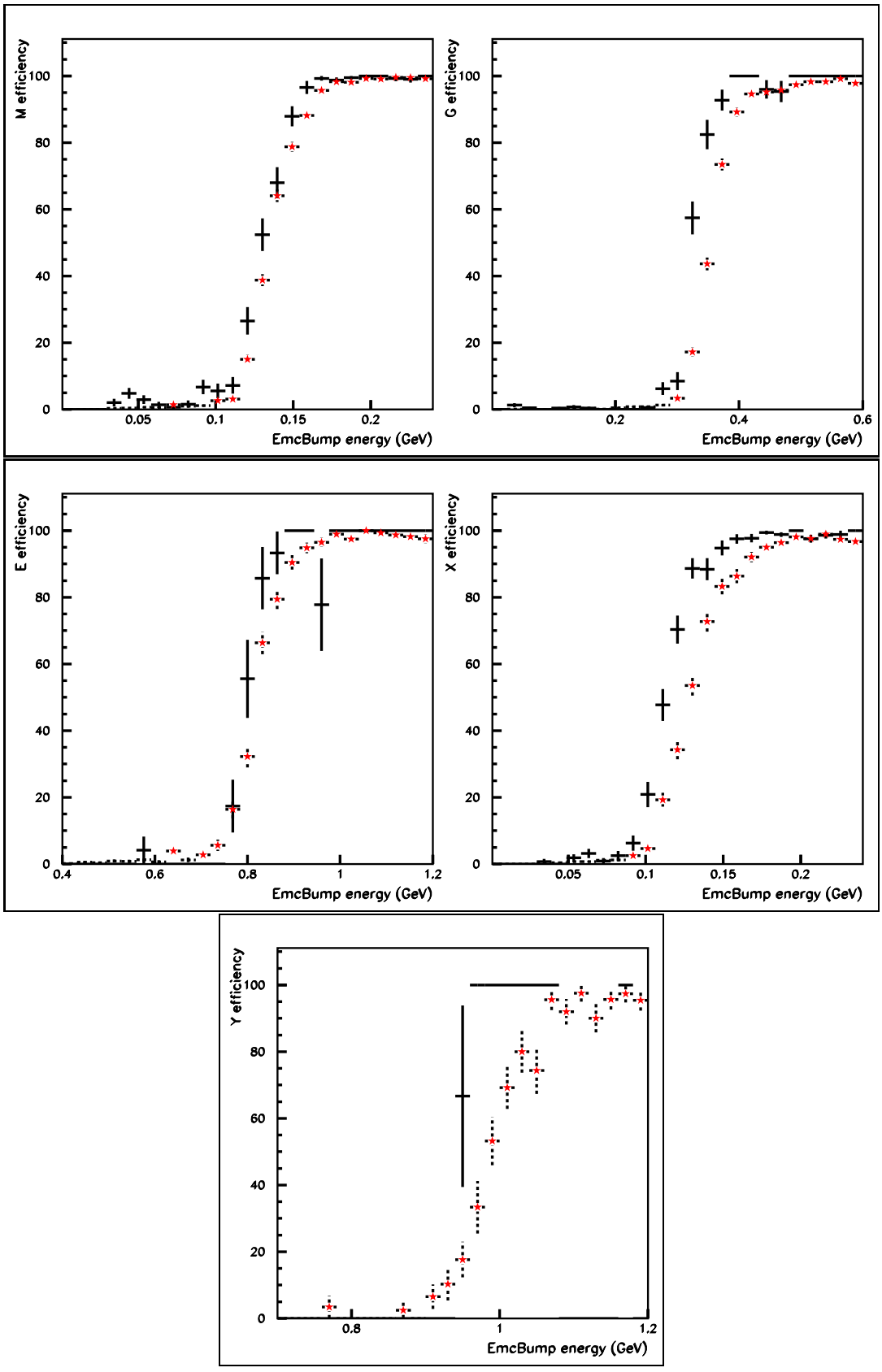

Figure 5.19: *Comparison of the data and Monte Carlo efficiency of the EMT system for the 5 basic trigger objects with Monte Carlo(solid black) and data(dashed red)*

During development of the system it was necessary to observe the triggering of events within the EMT system itself and so the plots in figure 5.20 were developed. These show the incoming energy peak from the EMC for all phi strips on the right and the resulting output from the EMT in the form of trigger primitives on the left. The top pair shows a 2M event with both incoming peaks crossing the threshold whereas the lower pair show a 1M event since the smaller of the two input energy peaks fails to cross threshold. A feature to note is in the top right plot. On the trailing edge of the energy peak is one time slice whose energy is far out of step with its neighbours. The cause of this was found to be a fault in the EMC ADB design during switches between ranges. This is a good illustration of the EMT monitoring being able to assist in the diagnosing of EMC problems. The GLT systems monitoring also produces an event display which is shown in figure 5.21. These events were recorded due to the following Level-1 trigger lines being satisfied, a 2G (top left), EM (top right and bottom left) and a 2E (bottom right). These events would only have been recorded due to the EMT firing since none of the criteria for the DCT recording the event have been met since none of the tracks pass through layer 1 of the DCH.

5.5.2 Reliability

Since the inclusion of the EMT system within the IR-2 DAQ platform there has been one hardware failure. This was a TRB board mounted on the TCB which had a failure within the Finisar optical transceiver driver chip. This was caused by the fixing for the mounted heatsink failing. The only other hardware problem has resulted from the construction of the cables connecting the EMC to the EMT. The main problem has been with the connectors mounted at each end of the cable. The plastic housing for the pins becomes significantly weakened if the pins are reinserted due to initial misplacing. These are currently being replaced.

5.6 Summary

Within this chapter a full description of the design of the Electromagnetic Calorimeter Trigger and its operation for the first year in *BABAR* has been given. The system has operated reliably through the entire period with only minor glitches due to the frailties of the EMC-EMT connection. The monitoring setup for the system both during running and later offline analysis has been fully implemented and is currently in regular use. During the first year of operation the system has had to be able to cope with the rapidly changing PEP-II environment with high levels of background whilst still performing to specification with near perfect efficiency for multi-hadronic B events.

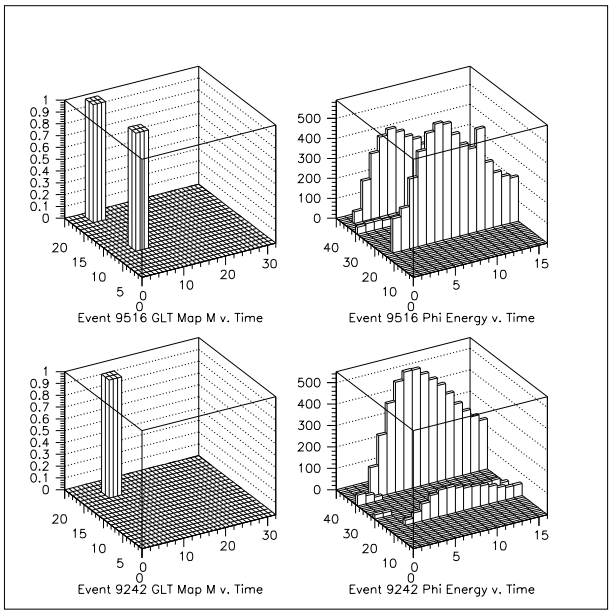

Figure 5.20: *The EMT event display showing on the right for two separate events the input EMC energy peak and on the left the resultant EMT trigger output object*

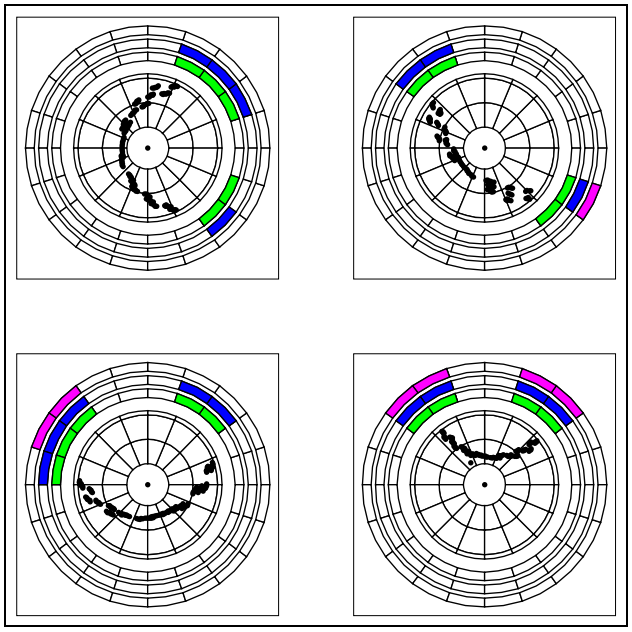

Figure 5.21: *The GLT event display showing events during the cosmic integration run that have been triggered only by the EMT since they fulfil none of the criteria for the DCT*

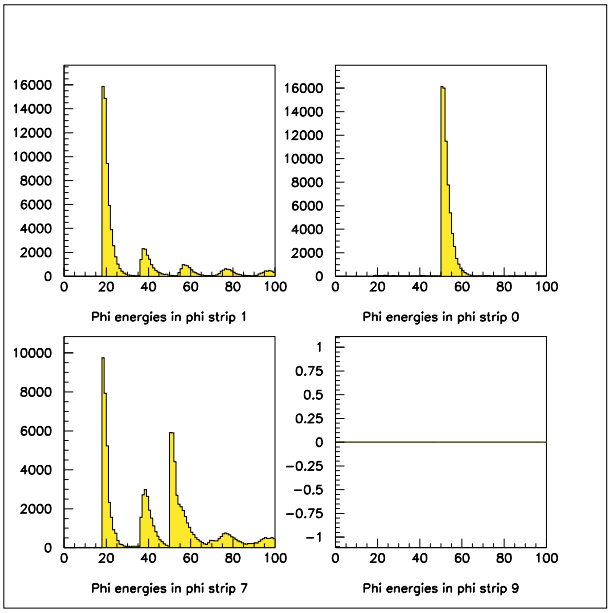

Figure 5.22: *Four plots showing the effect of the trigger summer output threshold in different scenarios as seen by the EMT*

Chapter 6

The Reconstruction of Neutral Objects at *BABAR*

6.1 Introduction

Many channels within the scope of the *BABAR* analysis include a large number of neutral objects. The successful reconstruction of π^0's is one of the essential ingredients for hadronic final state reconstruction in *BABAR*. One of the most important of these is $B^0 \rightarrow J/\Psi K^0_s$ where 33% of the K^0_s decay to two π^0's. To contribute effectively to the sin2β analysis, the K^0_s must be fully reconstructed. This chapter will firstly outline the reconstruction method of the raw calorimeter objects, moving onto the creation of gamma candidates and their use to construct π^0 candidates. A description is made of the method used to create a composite K^0_s candidate from the π^0's.

6.2 Electromagnetic Calorimeter Reconstruction

The reconstruction of objects within the calorimeter is done on two distinct levels which will be explained here. Information is received from the calorimeter in the form of digitised packets representing the energy deposited and its position. To prevent the readout system from being swamped with background a threshold of 5 MeV is applied. The TDR[31] value for this is 0.5 MeV, though this had to be raised due to high levels of incoherent noise in the EMC readout electronics. Below this level the crystal output information will not be digitised but ignored at the hardware level. This makes the performance of the calibrations as described in section 3.3.4.4 even more critical. In previous experiments such as CLEO[68], a cluster is a predetermined set of crystals (usually a 3x3 or 5x5 matrix). The *BABAR* endcap geometry precludes this and a more flexible approach must be taken. In *BABAR* a cluster is defined as a contiguous region of crystals which are all above threshold.

The algorithm to produce clusters works by first searching through the calorimeter raw data to find the crystal with the highest energy locally. This is then used as a seed. In a effort to reduce background this "seed crystal" has an independent threshold applied to it. All the neighbouring crystals to the seed are then added to a list of prospective crystals for inclusion to the cluster. These are then parsed to check if they independently pass another threshold. Those that don't are removed from the

list. The neighbouring crystals to these are then added to the list and again parsed with the same threshold. This continues until no more crystals can be included. The list of crystals then have their energy summed and compared to an overall crystal energy threshold. Only after passing this is the cluster added to the list within the event. This process is more easily described with the aid of fig 6.1.

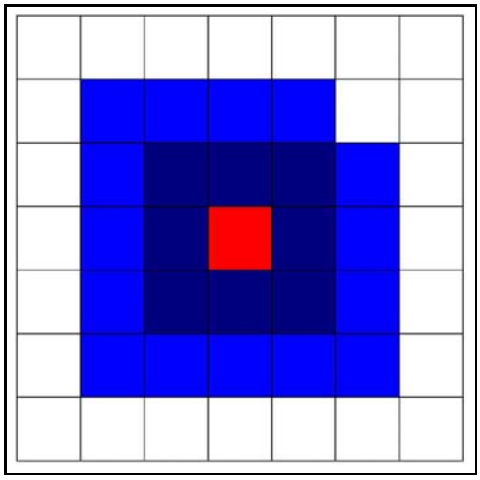

Figure 6.1: *Schematic representation of a cluster within the EMC showing the seed crystal in red (centre), crystals added to the cluster at each successive pass in lighter blues*

Due to the granularity of the calorimeter it is possible for 2 incident particles to impact with a small enough separation that the clustering algorithm will treat them as a single cluster. To separate these a lower level of granularity of reconstructed objects is needed. Within each cluster local maxima are found and then separated. Consider the example in fig 6.2.
Though this is a very much simplified view the basic principles can be easily shown. In this case one cluster would be formed by the algorithm. The process of splitting this up follows the following pattern:

1. Find the local maxima within the cluster boundaries (*Red crystals*).
2. Divide the energy contained within crystals shared by both local maxima (*single row of light blue between the 2 bumps*).

Each of these objects is called a bump and in the case of this analysis is most important when trying to find merged π^0's. This will be discussed more fully in section 6.4.

6.3 Neutral Reconstruction and Fitting

The reconstruction of neutral objects is understandably harder than their charged cousins. The specification of the *BABAR* calorimeter is extremely stringent with a

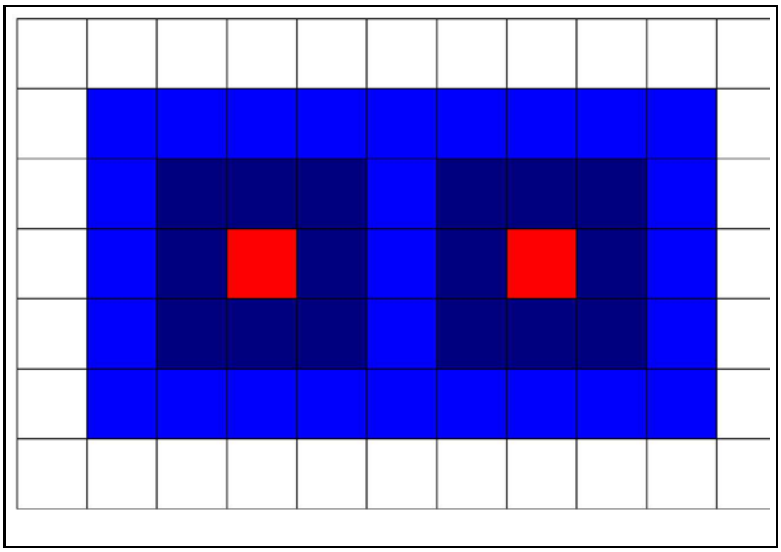

Figure 6.2: *Schematic representation of a merged 2 bump cluster within the EMC (coloured as before)*

minimum detectable energy of 10 - 20 MeV and an efficiency of greater than 85% (Full specifications are given in table 3.6). From the raw bump lists it is necessary to do track matching first to remove those objects that are caused by charged particles such as electrons. The method used within *BABAR* is by matching a track to a cluster. There are many factors that can make the association between these ambiguous, so it was decided that a method using a confidence level approach would be designed. Scattering in the DIRC can cause the hit position in the EMC to be different from that predicted by the track leaving the DCH. Hadronic showers can, due to their wide spatial distribution, cause the centre of the cluster to be widely displaced from the track impact point and bremsstrahlung from electrons causes inaccurate tracking parameters. It was decided that one method of compensating for this would be to have an associator for both matching tracks to clusters and also the same operation in reverse, averaging the confidence level for each match to produce the final result. The exact details of these algorithms can be found in [69]. After those clusters that have been successfully matched to a track have been removed from consideration then the remainder can be considered as neutral.

It is at this point that PID comes into operation to separate these classes of objects. The inclusion of the IFR data is used in much the same way as the track-cluster matching to separate π^0, γ and K_L^0. The K_L^0 is selected using the following selection criteria:

- Raw energy of the cluster > 0.1GeV
- Number of IFR layers hit ≥ 2
- IFR first layer hit is the cylindrical RPC

Additional selection is then made using the shape of the electro-magnetic shower in the EMC. To remove these from the neutral object list the result is inverted to act as a veto. The photon ID used relies on the shape of the electromagnetic shower as the primary discriminating variable that is then fed into a custom identifier module. This returns a consistency for the photon hypothesis. A cut is based on this. The photon selector efficiency has been measured at 91% with 87% purity.[70]

6.4 π^0 Reconstruction

Initially let us consider the generic π^0 and how it is reconstructed. We consider two possible methods of reconstruction, composite objects where the γ daughters are clearly in separate clusters and the case where both of the γ are incident in the calorimeter with a small enough separation that they both fall within a single cluster. These can either be still far enough apart that they can be easily separated into separate bumps or be in the tricky situation where they are indistinguishable as separate objects.

The composite π^0 is the easiest to reconstruct with the starting point being a list of photons that have already had an energy cut of 30 MeV applied to them as well as a cut on the lateral moment of less than 0.8. This is designed as a further way of removing K_L from the input list[70]. The lateral moment of a cluster is defined in equation 6.1:

$$\mathrm{LAT} = \frac{\sum_{i=3}^{n} \mathrm{E}_i \mathrm{r}_i^2}{\sum_{i=3}^{n} \mathrm{E}_i \mathrm{r}_i^2 + \mathrm{E}_1 \mathrm{R}_0^2 + \mathrm{E}_2 \mathrm{R}_0^2} \tag{6.1}$$

Where E_i and r_i are the *ith* crystals' energy and distance from the cluster center of gravity, i is the crystal index number within the cluster in descending energy order, E_1 & E_2 are the energies of the two most energetic crystals in the cluster and R_0 is the average distance between two crystals ($\approx$ 5 cm in *BABAR*), these are shown in figure 6.3. The lateral moment may be thought of as a method of determining the distribution of energy within the cluster.

The process of making the π^0 is to select the first γ in the input photon list and then, using 4-vector addition, sum it with the next in the list. To calculate the mass and other properties of the composite object the two candidate photons have a mass constrained fit done on them. The fitter used considers both geometric and kinematic properties when making the fit. The mass of the fitted object is then checked to see if it falls within a window of 110 MeV - 155 MeV and that its energy is greater than 200 MeV. If both selections are passed then the π^0 is added to the output list. The selector then passes to the next γ in the list and the process is again repeated. Further details of this may be found in [71].

For the case of 2-bump clusters we must consider the relationship between the energy of the π^0 and the cluster/bump separation as shown in figure 6.4. The barrel and

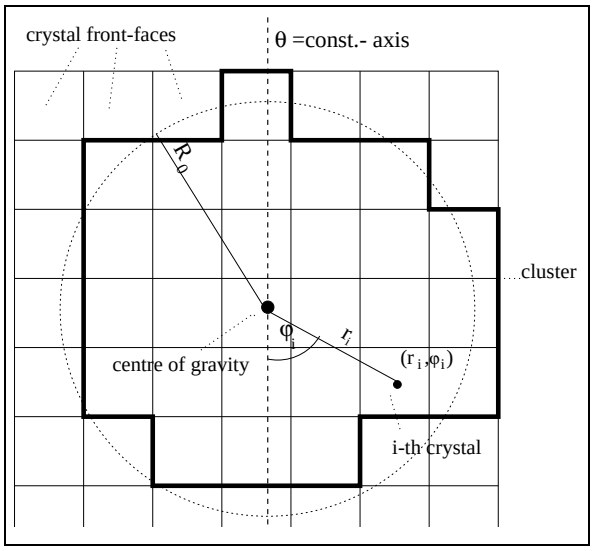

Figure 6.3: *Definition of the variables used in equation 6.1*

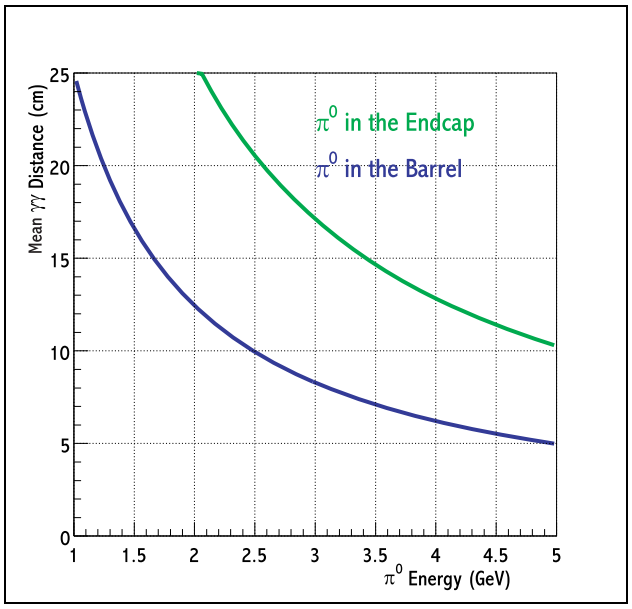

Figure 6.4: *The relationship between π^0 energy and bump separation*

endcap are treated separately due to their differing geometries. Due to the granularity of the EMC it is likely that should the photons be incident closer than 25cm apart then they will be reconstructed as a single cluster though two bumps will still be discernible. In the barrel though at π^0 energies of greater than 2.5GeV the γ separation is less than two crystal widths which results in only 1-bump being produced within the cluster. π^0's where the γ pair are both reconstructed within the same cluster are known as merged.

The merged π^0s fall into two distinct categories either 1 or 2-bump clusters. The division of the 2-bump clusters is completely driven by the EMC geometry since there is a slight θ dependence on the ratio of merged/unmerged π^0.

The identification of 2-bump clusters follows the scheme described previously with the resulting 2 separate objects being treated as with the composite objects. The 1-bump clusters are slightly more difficult, though a method has been developed which depends on the raw energy of the cluster E, and the cluster second moment, S: [72]

$$\mathrm{m} = \mathrm{E}\sqrt{\mathrm{S} - \mathrm{c}} \tag{6.2}$$

From simulation studies it has been found that c = 0.0009945, m can be considered as the mass of the merged π^0 and as such has the same cuts applied to it as the composite object. The cluster Second Moment is defined as:

$$\mathrm{S} = \frac{\sum_{i=0}^{i=n} E_i(\Delta\theta_i)^2}{\sum_{i=0}^{i=n} E_i} \tag{6.3}$$

where $\Delta\theta_i$ is defined as:

$$\Delta\theta_i = \begin{pmatrix} \theta_{clus} - \theta_i \\ \phi_{clus} - \phi_i \end{pmatrix} \tag{6.4}$$

and:

$$\theta_{clus} = \frac{\sum_{i=0}^{i=n} E_i\theta_i}{\sum_{i=0}^{i=n} E_i} \tag{6.5}$$

This moment can be considered as a way of measuring the cluster regularity. This is most effective for medium to high energies and is most suitable for discriminating between merged π^0s and high energy photons. Thereafter a merged π^0 also has to pass the following criteria for 1 (2) bump clusters:

- Raw Energy $\geq$2.1(0.9) GeV
- Charged track to calorimeter cluster match consistency ≤ 0.01.
- merged π^0 consistency ≥ 0.001 [73]

The track to cluster consistency measurement is made using the following method. Since the distance between the DCH track exit point from the calorimeter to the energy centre of the EMC cluster is dependent on the momentum of the particle due to the angle of entry into the EMC we must consider $\Delta\mathrm{r}\phi$, this distance. This is shown in figure 6.5. The distribution is flat across Δz due to the nature of the internal B field. A normalised distance for $\Delta\mathrm{r}\phi$ is then calculated using equation 6.6 producing a Gaussian for each value of the momentum.The letters v and w are the coefficients of the linear and logarithmic terms of the lin-log fits to the gaussians.

$$< \Delta r\phi >= \frac{1}{p}v - \frac{1}{p}w\ln\frac{1}{|p|} \tag{6.6}$$

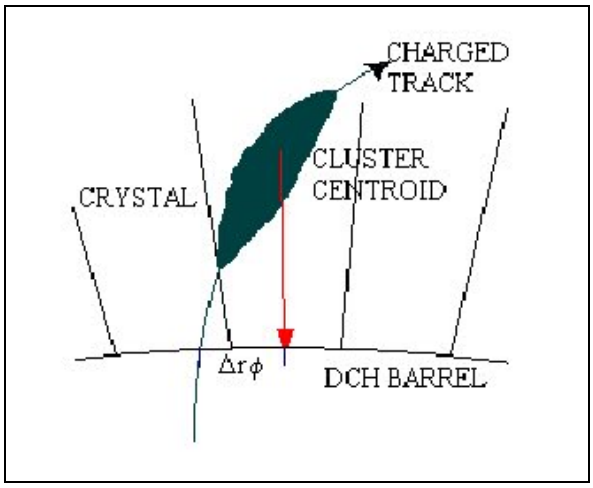

Figure 6.5: *An illustration of the distance between the DCH exit point and EMC cluster energy centroid*

The consistency is then measured by subtracting the area of the Gaussian outside the ± value of the track-cluster candidate's distance from the centre of the peak from the whole area. From this then the overall consistence is measured using equation 6.7.

$$C_{tot} = C_{r\phi}C_z(1 - ln(C_{r\phi}C_z)) \tag{6.7}$$

Another method to discriminate the γ from the merged π^0 can be made using the value of m, since for 99% of photons it is less than 0.05 GeV.

The combining of the lists of merged and composite π^0 must be done with great care to ensure that the γ used within the events are not double counted and as such contribute a π^0 to both lists. To ensure this doesn't happen a special 'merger' has been developed that checks the γ content of each π^0 in both lists and ensures they are different.

6.4.1 π^0 Masses

Using generic Monte Carlo simulated data processed with the latest version of the reconstruction software and including background mixing the simulated π^0 mass was measured as 135.2 MeV (this is shown in figure 6.6(left), with a width of 6.4 MeV. Collision data from runs 13345-13358 onpeak and 13263-13286 offpeak running over all events collected, yields a mass of 134.4±0.4 MeV with a width of 6.8±0.3 MeV as shown in figure 6.6(right). These are consistent with the PDG value.

6.4.2 π^0 Selector Efficiency

The efficiency of the selector was found by running over Monte Carlo data and comparing the true momentum distribution of the π^0 to the reconstructed distribution.

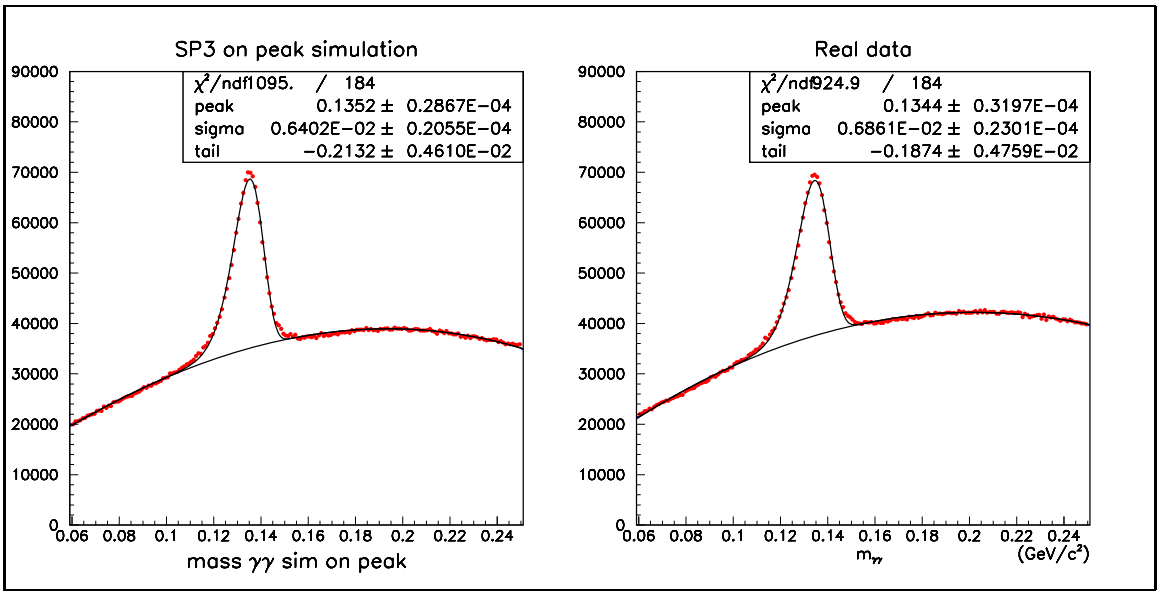

Figure 6.6: *The π^0mass as found from combined photon pairs in Monte-Carlo(left) and data(right)*

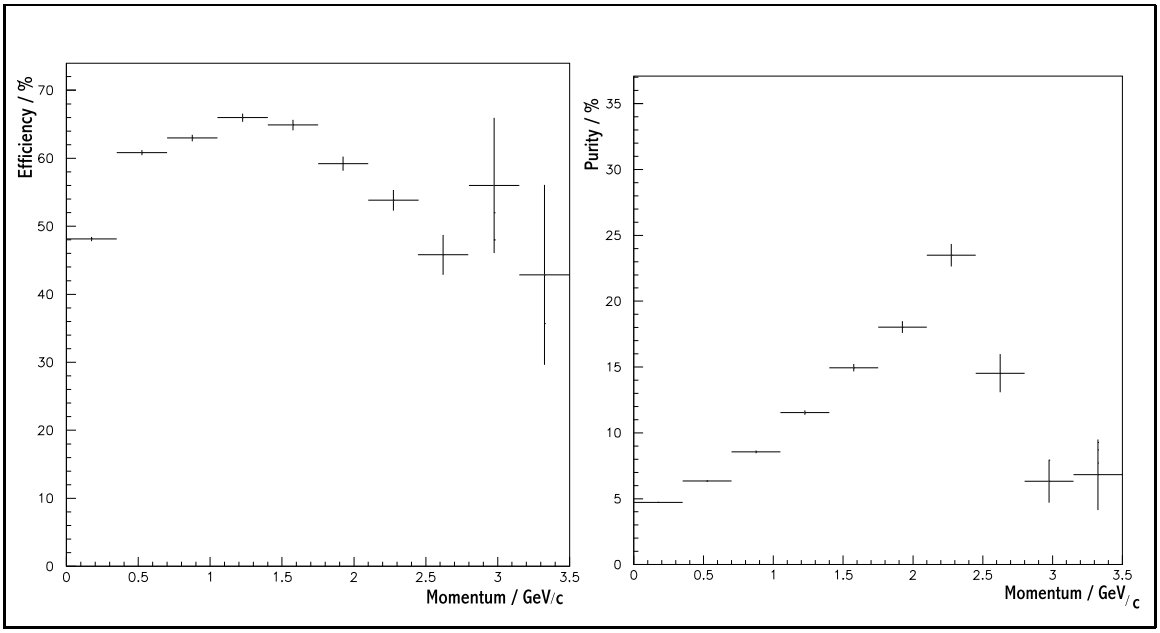

Figure 6.7: *The π^0 selector efficiency and purity as a function of momentum in data*

An energy cut of 30 MeV for photons and 300 MeV for $\pi^0$was introduced to remove as much background as possible, and a 3σ cut around the π^0 mass so as to remove spurious data. As can be seen in figure 6.7 there is a sharp rise from very low efficiency at low energies to the peak efficiency at around 1 - 1.5 GeV. The drop off at high energies though can be attributed to the increasing number of merged π^0s that are present as well as the γ energy spectrum drops off very steeply to give very few

candidates. The overall efficiency of the selector is ≈56%, with a maximum purity of ≈ 24%. The purity of the selector is calculated using a Monte Carlo sample of π^0, charged π and leptons. The momentum distrubution of the selector is then compared with the momentum distribution with an addition selection that the selected candidates must have the Monte Carlo truth identification number of the π^0.

6.5 K_s^0 Reconstruction

The K_s^0 reconstruction described here is for the purely neutral $K_s^0 \rightarrow \pi^0\pi^0$. As with the composite case of the π^0 the K_s^0 selector receives as input an uncorrelated list of π^0s. The initial composition of the K_s^0 is then done in the same way as the composite π^0s. The determination of the K_s^0 vertex though is done though a custom fitter. This will now be described.

6.5.1 The K_s^0 Fitter

To produce a fully fitted K_s^0 there are several steps that must first be done. Upon receiving the input list of π^0 the same process of 4-vector addition as for the construction of the π^0 is done. Before this, certain constraints must be applied. For the *BABAR* standard Geometric and Kinematic fitter the momentum and mass of the daughter objects must be given. The composite K_s^0 is then created to perform the addition. Then a mass constraint of the composite object is given and a vertex position in order for the fitter to work.

The composite object is then passed into the fitter. For the purely neutral channel described here a special fitter had to be developed so as to optimise the K_s^0 decay vertex. Since the fitter requires a vertex being passed to it, the most accurate starting point not only improves the accuracy of the fit but also reduces processing time. We illustrate the dependence of the fit quality on the initial starting point using a "pull" plot.

$$\text{pull} = \frac{\mathrm{E}_{Reco} - \mathrm{E}_{True}}{\sigma_{\mathrm{E}_{Reco}}} \tag{6.8}$$

$$\text{effective pull} = \frac{\mathrm{E}_{Reco} - \mathrm{E}_{True}}{\mathrm{E}_{True}} \tag{6.9}$$

These measure the change in reconstructed energy before and after the fit with reference to the uncertainty in the reconstructed energy after fitting, according to equation 6.8. The pull plot for this fit is shown in figure 6.8(left). This contains the unfitted peak, peak from the fit at the best K_s^0 vertex and an illustrative fit at the J/ψ vertex. As can be seen the original peak is centred around zero with a width of 1.76. The optimised vertex position peak is also centred though its width has increased to 2.34. In contrast the peak produced by the fit at the J/ψ vertex has been shifted away from zero to 1.85 and its width has increased still further to 2.75. This shift away from

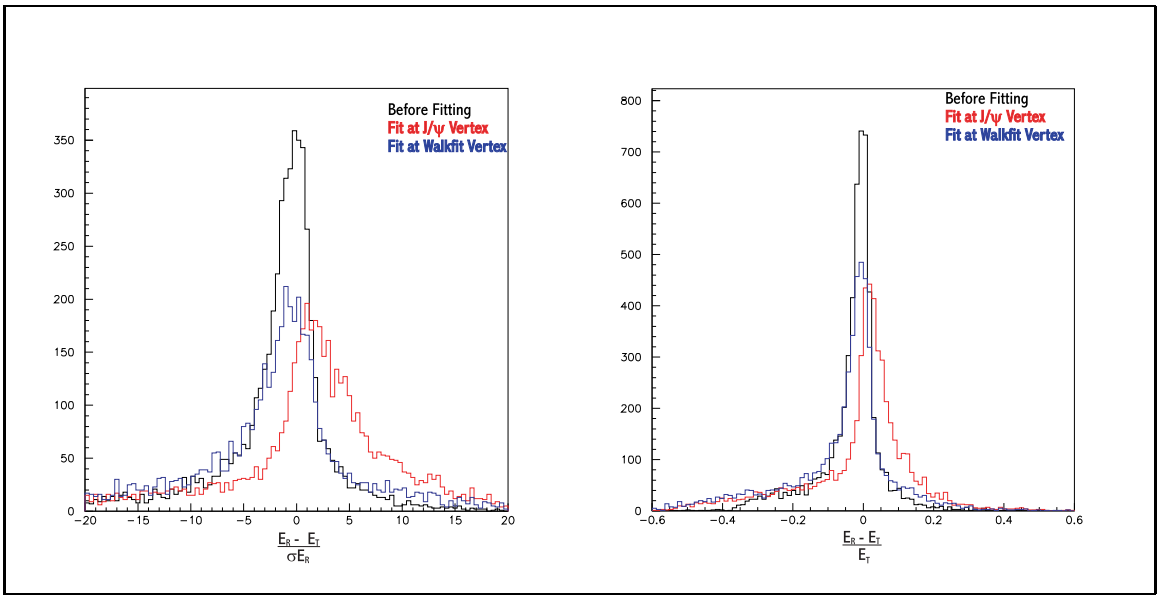

Figure 6.8: *K^0_s pull plot(left) and effective pull plot(right) using reconstructed data*

zero for the J/ψ vertex peak is an indication that the energy of the fitted K^0_s is being artificially increased to compensate for the inaccurate vertex position being passed as its starting point. The broadening of the peak is due to the minimisation of σE_R after fitting. To illustrate this, the plot in figure 6.8(right) is produced using equation 6.9. This shows a stable peak width before and after fitting though still displays the peak shifting for the fit using the inaccurate vertex position. The results of this study led to the development of a specific tool to try to optimise the K^0_s vertex as given to the fitter[75].

When the composite K^0_s is constructed the momentum direction is found and recorded. An imaginary line is then drawn from the event primary vertex along this direction. The fitter is then used to find the χ^2 and number of degrees of freedom of the fit from which the probability of the fit is calculated. This is then recorded. The fitter starting point is iterated a small distance along the K^0_s line of flight. Here the earlier fit is first invalidated and then redone. The fit parameters are then compared with the earlier fit results and if they show an improvement in the fit probability then the new result is recorded in place of the old. This continues until a probability maximum is found at which point the candidate K^0_s is then copied into the output list for use elsewhere. The process of this walking fit is illustrated in figure 6.9. For speed of operation it was found that the optimal step distance was 2 cm since the fitter is capable of moving the vertex position within this limit so as to obtain the best fit possible.

6.5.2 K^0_s Efficiency, mis-id and backgrounds

The efficiencies of this selector are shown in figure 6.10. To calculate this all Monte-Carlo K^0_s were recorded and then compared with those found using the selector. As

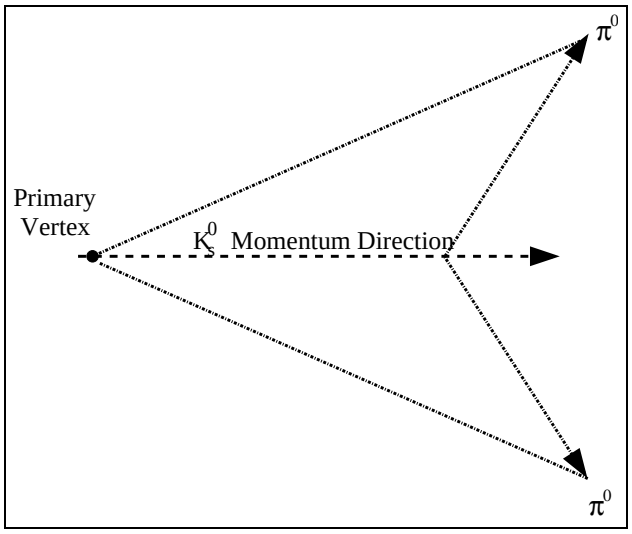

Figure 6.9: *Diagrammatic representation of the operation of the Walk fitter*

is seen in fig 6.10 the selector in its raw output form has an overall efficiency of 35%. The purity is also very low over all ranges of momentum at 10%. To improve this additional selection options were used as detailed below.

- Energy of the π^0s > 0.3 GeV
- θ of π^0s > 0.41 rad
- cos of the angle between the 2 π^0s > 0.6
- Energy of the photons used to compose the π^0s > 0.2 GeV
- θ of the photons used to compose the π^0s > 0.41 rad
- cos of the angle between the 2 photons for each $\pi^0 > 0.6$
- θ of the $K^0_s > 0.41$ rad
- Position of the K^0_s vertex more than 1.5 cm from the Primary vertex
- Probability of the K^0_s fit > 0.05

The addition of these cuts decreased the overall efficiency to 21% with a peak efficiency of 29%. The effect on the purity though was most dramatic with a peak in the 2.5GeV/c^2 bin at 69% and an average value of 35% over all momentum bins. These figures are constructed using the method as for figure 6.7.

6.5.3 Mass and Lifetime

The mass of the resultant output list of reconstructed objects is then plotted. Figure 6.11(left) shows the raw selector output, with the output from the new selector

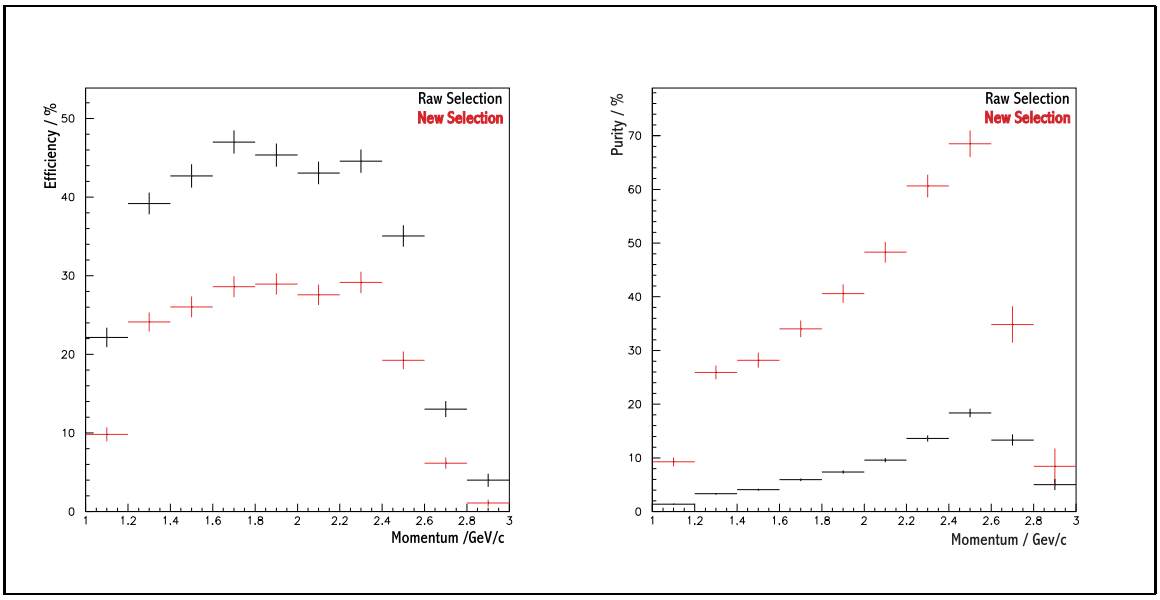

Figure 6.10: *The K^0_s selector efficiency and purity as a function of momentum, no cuts(black), added cuts(red)*

right. As can be seen the background in the raw output is large enough to obscure the signal. With the additional cuts as described previously the mass peak becomes clear. Fitting this leads to a reconstructed K^0_s mass of 472.0±6.3 MeV with a width

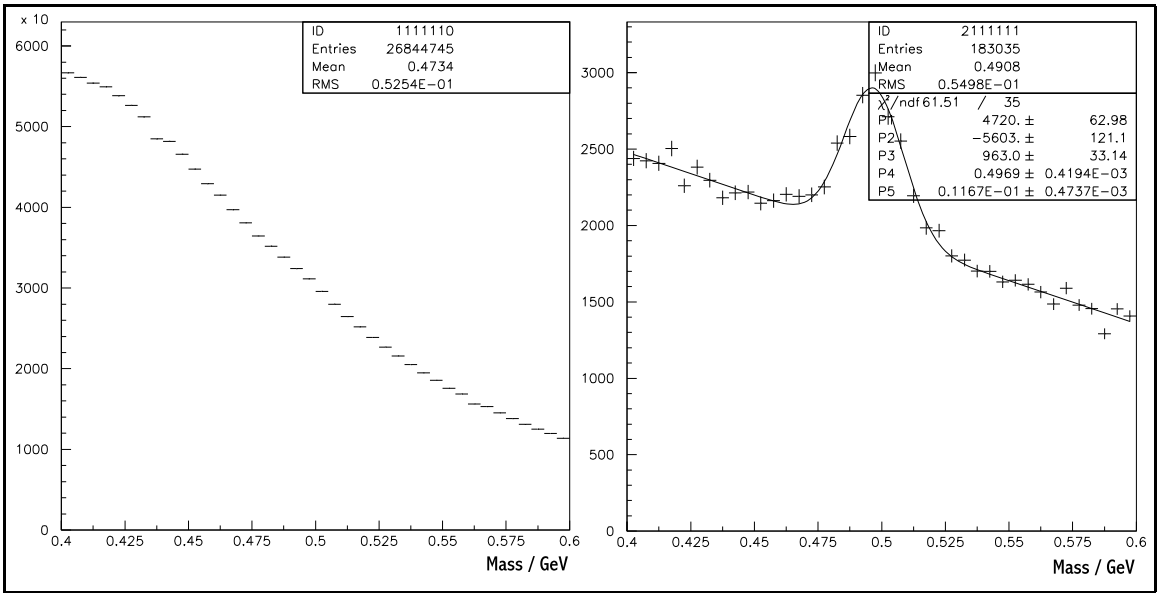

Figure 6.11: *K^0_s mass from raw selector output(left) and with additional cuts(right)*

of 96.3±3.3 MeV. This is consistent with the PDG[13] value.
The K^0_s lifetime is well known, though within the scope of this analysis it will provide a verification that the background levels of the selector are within tolerable limits.

Initially to check the Monte Carlo a plot is made of the true K_s^0 lifetime to simply verify that this is set correctly (see figure 6.12).
Equation 6.11 is used:

$$c\tau = \left(\left(\frac{p_x}{m}\right)\left(\frac{\sigma^2_{c\tau}}{\sigma^2_{\Delta x}}\right)(x_d - x_p)\right) + \left(\left(\frac{p_y}{m}\right)\left(\frac{\sigma^2_{c\tau}}{\sigma^2_{\Delta y}}\right)(y_d - y_p)\right) + \left(\left(\frac{p_z}{\mathrm{m}}\right)\left(\frac{\sigma^2_{c\tau}}{\sigma^2_{\Delta z}}\right)(z_d - z_p)\right) \tag{6.10}$$

where:

$$\sigma^2_{c\tau} = \frac{1}{\left(\left(\left(\frac{p_x^2}{m^2}\right)/\sigma^2_{\Delta x}\right) + \left(\left(\frac{p_y^2}{m^2}\right)/\sigma^2_{\Delta y}\right) + \left(\left(\frac{p_z^2}{m^2}\right)/\sigma^2_{\Delta z}\right)\right)} \tag{6.11}$$

and:

$$\sigma^2_{\Delta x} = \sigma^2_{x_p} + \sigma^2_{x_d} \tag{6.12}$$

Within these equations m is the mass of the particle, p_x, p_y, p_z are the momentum

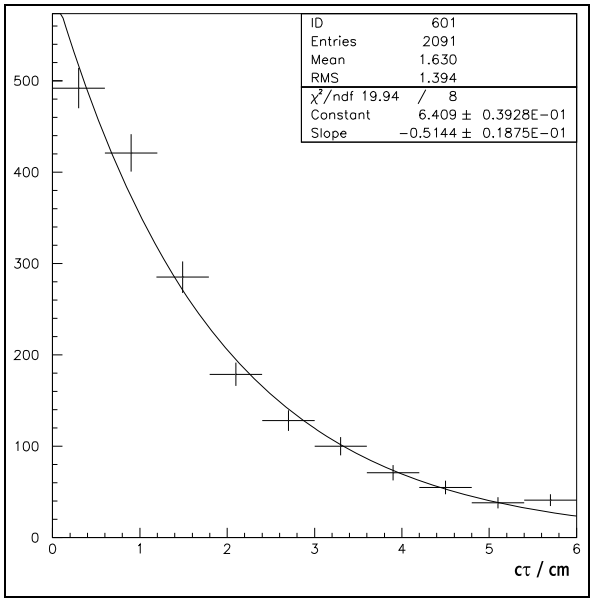

Figure 6.12: *K_s^0 lifetime from Monte Carlo truth*

contributions in the x, y, z directions with the p and d subscripts indicating production and decay points in the three directions.

In an effort to reduce background contamination an extra momentum cut of 1 GeV/c^2 has been added on the K_s^0 to cope with the selector inefficiency below this. The efficiency of the selector over all momentum bins is now only 20% but the purity has

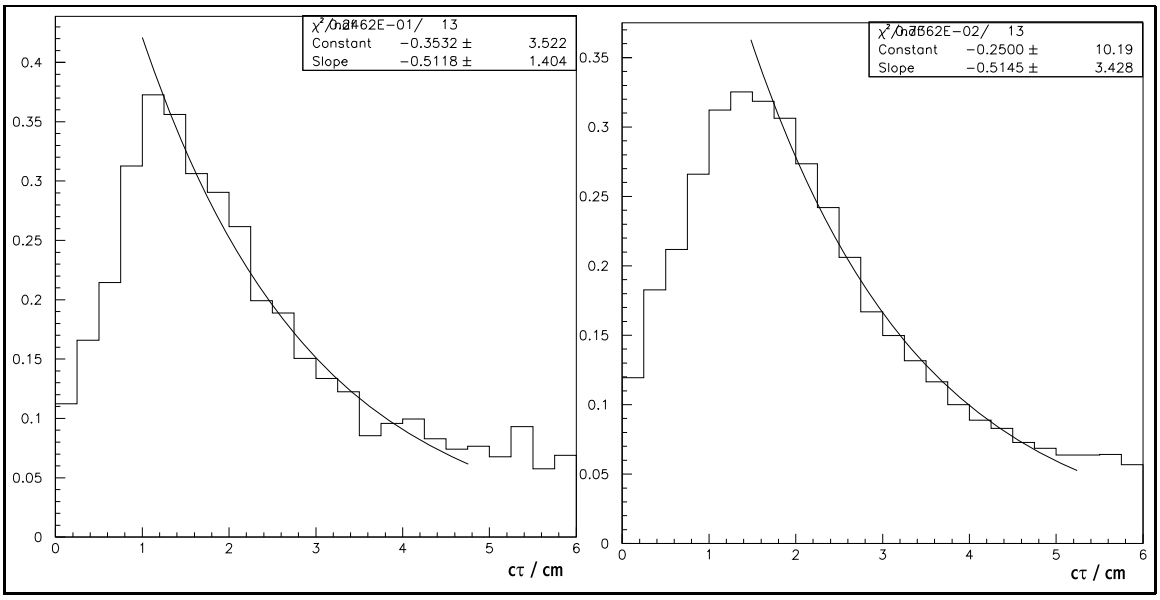

Figure 6.13: *K^0_s lifetime from Reconstructed Monte Carlo(left) and data(right)*

increased to 39%. As can be seen in figure 6.11 the signal to background ratio is still quite high. To reduce the contaminating effects of this on the lifetime plots the mass sidebands were used to do background subtraction. A lifetime measurement was taken using 3 bins above and below the K^0_s peak and this was then subtracted from the lifetime plot produced by using the 10 bins of the peak only. Therefore the first 2 bins in the lifetime plots are ignored, the effect of leaving this uncut is to artificially lower the value of $c\tau$. The Monte-Carlo Truth value for the lifetime is calculated to be 2.7±0.5 cm. This is within the PDG[13] reference value of 2.6762 cm. The actual value of the lifetime from the reconstructed data and Monte Carlo is shown in figure 6.13. This shows good agreement between both the Monte Carlo and data as well as the correct value when the slope of the exponential fit to the trailing edge of the peak is made. The finally calculated values of $c\tau$ are shown in table 6.1.

Reconstructed Monte Carlo	2.7 ± 0.5 cm
Data	2.7 ± 0.4 cm
PDG value	2.678 ± 0.003 cm

Table 6.1: *Calculated values for $c\tau$ compared with the PDG value*

6.6 Summary

The output list of K^0_s candidates is to be used for the analysis contained within the next chapter. Here the selection of K^0_s is further improved by also looking for a matching

J/ψ. This chapter has given an overview of the methods used to produce neutral calorimeter objects. These are then used to construct firstly π^0 and then in turn K^0_s. The operations of various fitters which are used within the following analysis are also explained. These are used to calculate the efficiency and purity of the selectors. This culminated with a measurement of the K^0_s lifetime to verify the selector performance.

Chapter 7

The decay channel $B^0 \rightarrow J/\Psi K^0_s \rightarrow l^+l^-\pi^0\pi^0$, calculating its branching ratio

7.1 Introduction

In this chapter I will describe the measurement of the branching ratio of $B^0 \rightarrow J/\Psi K^0_s$ with the K^0_s decaying via two π^0's. This is a validation analysis for the initial results that were given at the 2000 ICHEP meeting in Osaka [76].
First the reconstruction of the J/Ψ is described. Then comes the combination of the reconstructed J/Ψ with the K^0_s, (the reconstruction of which has been described in chapter 6) to create the B meson.

7.2 The Data Set and Primary Event Selection

The data set used for this analysis was collected between 22nd October 1999 and 28th October 2000. This amounts to 22.41fb^{-1} of data with 19.95fb^{-1} collected at the Υ(4s) resonance (or 'on-peak') and 2.46fb^{-1} 'off-peak'. The data was processed using the 8.8.0 or higher version of the prompt reconstruction software. The first stage of the analysis is to create a skim of events that are most likely to contain a $B^0 \rightarrow J/\Psi K^0_s$ decay, this is defined as:

- BGFMultiHadron (See below)
- Number of good tracks (within $0.41 < \theta_{lab} < 2.54$) >=4
- R2 (as described in chapter 6) < 0.7
- aJpsiCand (See below)

The BGFMultiHadron flag is raised during processing before the skim is made. It is defined as:

- Charged Tracks > 2
- R2 < 0.98

For an event containing a J/ψ the criteria will be implicitly met due to the decaying l^+l^- pair that is produced as well as the decay of the other B-meson produced in the $B\bar{B}$ pair.

The θ cuts introduced on the tracks are to allow easier comparison of the Monte Carlo and real data since the region outside of this is not well described in the simulation due to the presence of the inner steering magnets and the SVT support structure. The variable R2 is the ratio of the second to the zeroth Fox Wolfram moments for the tracks within an event.

The Fox Wolfram Moment is another event shape variable. It is defined as the momentum distribution between the decay products of a reaction. The are many moments that can be calculated using equation 7.1.

$$H_l = \sum_{i,j}^{l} \frac{|p_i|\,|p_j|}{E_{VIS}^2} P_l(cos\theta_{i,j}) \tag{7.1}$$

(By energy conservation $H_0 = 1$). R2 is especially good for continuum rejection since this ratio tends to 1 whereas $B^0\bar{B}^0$ events tend to 0.

The tag selection of *aJpsiCand* is flagged when the event has at least one pair of oppositely charged tracks with an invariant mass of between 2.5 and 3.2 GeV. This selector receives as input the *GoodTracksLoose* list which confines the origin of the tracks used to within 1.5cm in X-Y and 10cm in X or the origin. They must each also have at least 20 hits in the Drift Chamber associated with them and a momentum of at least 100MeV/c. The tag selector itself requires no actual additional vertexing requirement.

To calculate the efficiency of selection variables, Monte Carlo, containing the latest version of corrections matching the inefficiency of the model to that of the data, is used. This is especially true for the Drift Chamber since the tracking efficiency is lower than design due to the lowering of the drift voltage to cope with damage having a larger than expected effect on the chambers overall gas gain. The progression of the number of events that pass each stage of the anaysis from raw number of B$\bar{\text{B}}$ pairs to finally selected candidates may be seen in table 7.2.

7.3 Reconstruction of the J/Ψ

The reconstruction of the J/Ψ's is done by the combination of a sub-set of lists that each contain one of the possible lepton decays, ie. J/$\Psi\rightarrow \mu^+\mu^-$ and J/$\Psi\rightarrow e^+e^-$[77]. The selections of these are done as below.

J/$\Psi\rightarrow e^+e^-$ The selection proceeds by first receiving a list of Bremsstrahlung corrected electrons. These have passed the Loose electron selector. The invariant mass condition from the *aJpsiLoose* tag is also maintained. The two tracks from the leptons are then vertexed using a geometric and kinematic fitter though no

actual convergence of the fit is required. If the vertexer fails to converge then simple 4-vector addition is used.

J/$\Psi \rightarrow \mu^+\mu^-$ The selection of these events is slightly harder since they receive as input the raw *GoodTracksLoose* list and each member is then assigned the μ mass. The selection then proceeds as per the electron case.

The combining of these two lists then proceeds by first checking if a single candidate has passed both selection criteria so as to be included in both the ee and $\mu\mu$ cases. If this occurs then the electron case is preferred since this has had particle identification applied to it.

Now that a single list of J/Ψ candidates has been assembled then further selection criteria are applied. The invariant mass cut is tightened to 2.95 GeV$< M_{J/\psi} <$3.14 GeV and 3.06 GeV$< M_{J/\psi} <$3.14 GeV for the electron and muon cases respectively. When completing this study the electron selection is tightened so that at least one of the electrons must also pass the *Tight* selection or if no calorimeter cluster may be associated with the track then the requirement 550 MeV/m$< \frac{dE}{dx} <$850 MeV/m. For the μ case at least one of the tracks must then pass the Loose Muon selector. The other must deposit less than 400 MeV in the calorimeter to qualify as a minimum ionising particle.

7.3.1 Lepton Identification Methods and Efficiencies

The selectors that have been described in the previous section will now be discussed in greater detail.

Electron Selectors The loose and tight electron selectors have as their base the following set of criteria. This is what is known as a cut-based selector.[78]

- Initially the main discriminating variable for electron identification is the ratio of the energy of the incident candidate with its momentum. For the loose electron selector, this cut has been placed so that only those candidates with E/p greater than 0.5 are passed. For the tight selection this has been altered so that only a window of E/p is allowed between 0.75 and 1.3.
- The number of crystals that contribute to a cluster in the calorimeter is also important. For all selectors this cut is placed at a minimum of 3 crystals contributing.
- The rate of energy loss for the candidate is used within these selectors with a minimum of 500 MeV/m and maximum of 1000 MeV/m.

The *Tight* and *Very Tight* selectors make use of additional variables as described below.

- The Lateral moment of the shower is used to differentiate between pions and electrons as described in section 6.4. Here the cut is for the LAT to

be below 0.6 to remove the π contamination. For the *Very Tight* selection the LAT must also be greater than 0.1. This is shown in figure 7.1.

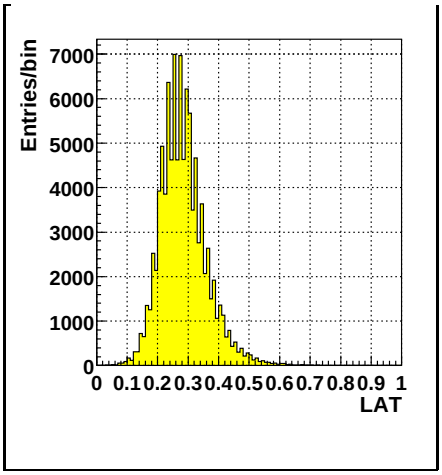

Figure 7.1: *The Lateral moment distribution for electrons [78]*

- For the *Very Tight* selector only an additional variable is introduced, the Zernicke moments, A_{nm}. These are used to define the energy leakage from a circular region about the centre of gravity of the cluster. They are calculated using equation 7.2. This is shown in fig 7.2

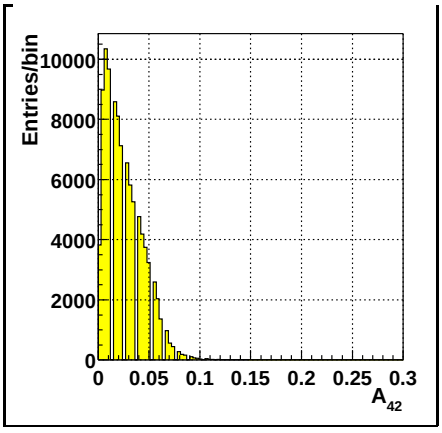

Figure 7.2: *The Zernicke moment distribution for electrons [78]*

$$A_{nm} = \sum_{r_i \leq R_0}^{n} \frac{E_i}{E} f_{nm}\left(\frac{r_i}{R_0}\right) .e^{-im\phi_i} \tag{7.2}$$

With n, m ≥ 0 integers, n $-$ m even and m$\leq$n. ϕ_i is the angle from the fixed event axis. In the case of *BABAR* this is taken to be parallel to the beam axis in the forward direction. E_i is the energy of the *ith* crystal with

r_i its radius from the cluster centre of gravity. E is the energy of the cluster and f_{nm} is defined in equation 7.3.

$$f_{nm} = \sum_{s=0}^{(n-m)/2} \frac{(-1)^s (n-s)! \rho^{n-2s}}{s!((n+m)/2-s)!((n-m)/2-s)!} \tag{7.3}$$

The variable used is the ratio of the 2nd and 4th Zernicke moments used to again describe the shape of the electromagnetic shower within the EMC. The EM shower will have A_{42} close to zero whilst hadronic showers have much larger values. For electrons this cut is set so that only candidates with A_{42} less than 0.1 pass.

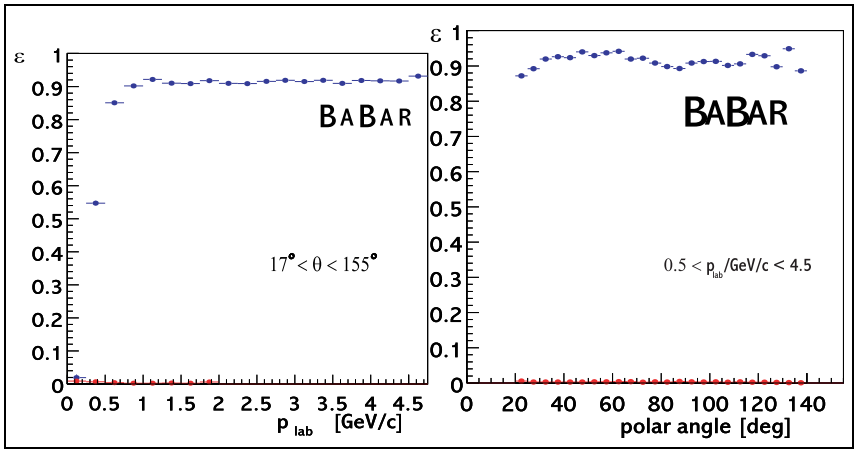

Figure 7.3: *The efficiency and mis-id rate of the Tight electron selector. (The mis-id rate is shown very close to the x-axis)*

The efficiency and mis-id rates of the *Tight* selector against momentum and θ are shown in figure 7.3. The *BABAR* standard electron control samples used are from Bhabhas, conversions and $\gamma\gamma \rightarrow 4e$ and the π's from K_s. These give the average selector efficiency of 91.5% for electrons above 1 GeV/c with a pion mis-id of around 0.13%.

Muon Selectors The muon identification is done using a combination of information from the EMC, DCH and IFR. The basis of the selector is described below.[79]

- Energy deposited in the calorimeter less than 0.5GeV, though this cut can only be included if the candidate has associated EMC information. It is ignored if it is missing.
- The number of hit layers in the IFR to be greater than 1 since a cluster in the IFR is always required.
- The number of interaction lengths within the iron the candidate will penetrate in the IFR can be simulated dependent on the energy of the incident candidate. A cut is introduced on the difference between this calculated

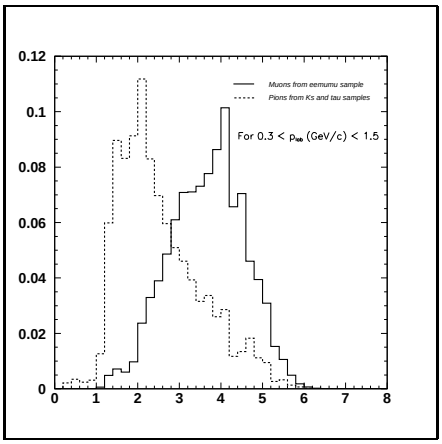

Figure 7.4: *The number of interaction lengths traversed by muons and pions from the BABAR control samples, the cut on this is set at 2*

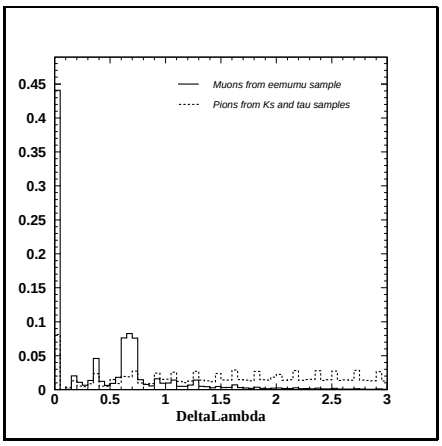

Figure 7.5: *Difference between the measured number of interaction lengths traversed and the simulated swum number of interaction lengths for muons and pions from the BABAR control samples*

value and the actual number of interaction lengths that the candidate traverses of less than ± 1.

- The χ^2 of the fit to the track that results from using a swimming track matcher to be less than 7.
- The ratio of the χ^2 of the track from a polynomial fit to the number of layers within the IFR that contributed to the track can also be used for discrimination of candidates. The initial cut is set at less than 4.
- A plain cut on the measured interaction length is also used for discrimination. The value of the cut used is set so that the candidate must have traversed more than 2 interaction lengths in the IFR.
- Due to the segmentation of the IFR into barrel and endcap segments, high pion fake rates in the gaps between these segments are seen. The

track-continuity has been designed to compensate for this and is defined as follows: L_T Total number of IFR Layers Hit
L_B Number of Layers hit in Barrel
L_E Number of Layers hit in the Endcap

I With hit in the Inner layer of the IFR

$$Track\ Continuity = \frac{L_T}{L_B - L_E}$$

II Without hit in the Inner layer of the IFR

$$TrackContinuity = \frac{L_T}{L_B - L_E + 1}$$

It was shown [79] that a cut at Track Continuity greater than 0.3 gave the best discriminating power.

- The multiplicity of a track is used in two ways within *BABAR*, the average multiplicity and the sigma of the multiplicity. The two definitions are:
S_T: Total number of RPC strips hit
S_i: Number of RPC strips hit in the layer i
S_a: Average number of strips hit per layer

$$Average\ Multiplicity = \frac{S_T}{L_T}$$

$$\sigma Multiplicity = \sqrt{\Sigma_i \frac{(S_i - S_a)^2}{L_T}}$$

The cut on the Average StripMultiplicity is set at less than 8, whilst the Sigma of the Multiplicity is set at less than 4.

In order to study and assesses the performance of the Muon selector several control samples were used. To provide an unbiased set of muons in the complete range of the *BABAR* experiment the channel $e^+e^- \rightarrow \mu^+\mu^-\gamma$ is used as well as $e^+e^- \rightarrow e^+e^-\mu^+\mu^-$. To study pion contaminiation the pions extractd from $K^0_s \rightarrow \pi^+\pi^-$ are used as well as from $e^+e^- \rightarrow \tau^+\tau^-$ where one τ decays into a lepton and the other into 3π. These cover the entire momentum range of *BABAR*. The *Tight* muon selector performance may be summarised as an overall efficiency for muons between 1.5 and 3 GeV/c of 74% with a π mis-id rate of 2.7%. The distributions with respect to momentum and θ are shown in figure 7.6.

7.3.2 J/Ψ Mass

The invariant mass of the 2 different selections for the J/Ψ decay gives the following results.

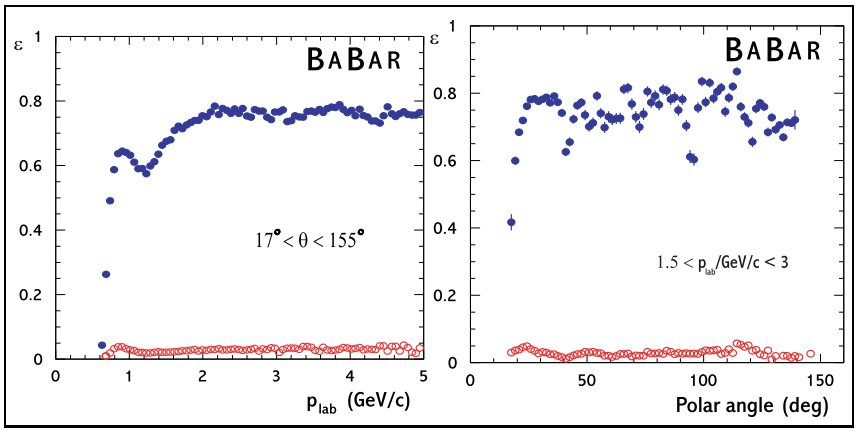

Figure 7.6: *The efficiency and mis-id rate of the Tight muon selector*

J/$\Psi \rightarrow \mu^+\mu^-$ 3.0934±0.0064GeV with a width of 15MeV

J/$\Psi \rightarrow e^+e^-$ 3.090±0.001GeV with a width of 14MeV

The Monte Carlo produces a mass of 3.098±0.001GeV with a width of 10±1MeV. The mass plots from data are shown in figures 7.7.

The method of selection of the J/Ψ events within the charmonium skim is such that it is almost guaranteed to only produce a single candidate per event. The K^0_s though can generate many candidates per event as shown in fig 7.8.

7.4 The B^0

7.4.1 Methods of Reconstruction

Now that the list of J/Ψ and K^0_s candidates has been made, it is possible to reconstruct the B^0. The process of producing the fully reconstructed B^0 is as follows.

The input lists of J/Ψ and K^0_s candidates are supplied and checked first to see if they both have a length of greater than 0. If not then this event is passed over and the processing continues to the next event. If both lists are present then the J/Ψ list is processed first. The first J/Ψ in the list is checked for the number of daughters, if this is equal to two and they have both been identified as leptons then further checking is done on the daughter leptons such that they must both pass an energy cut of 0.5 GeV. The mass of the candidate J/Ψ is also constrained to lie between 2.5 and 3.5 GeV. A selection is also made using the event R2 set at 0.5 though this should have been passed by the criteria set within the J/Ψ list creation module. At this stage if any of the cuts are not passed then that J/Ψ candidate is discarded and the process proceeds to the next in the list.

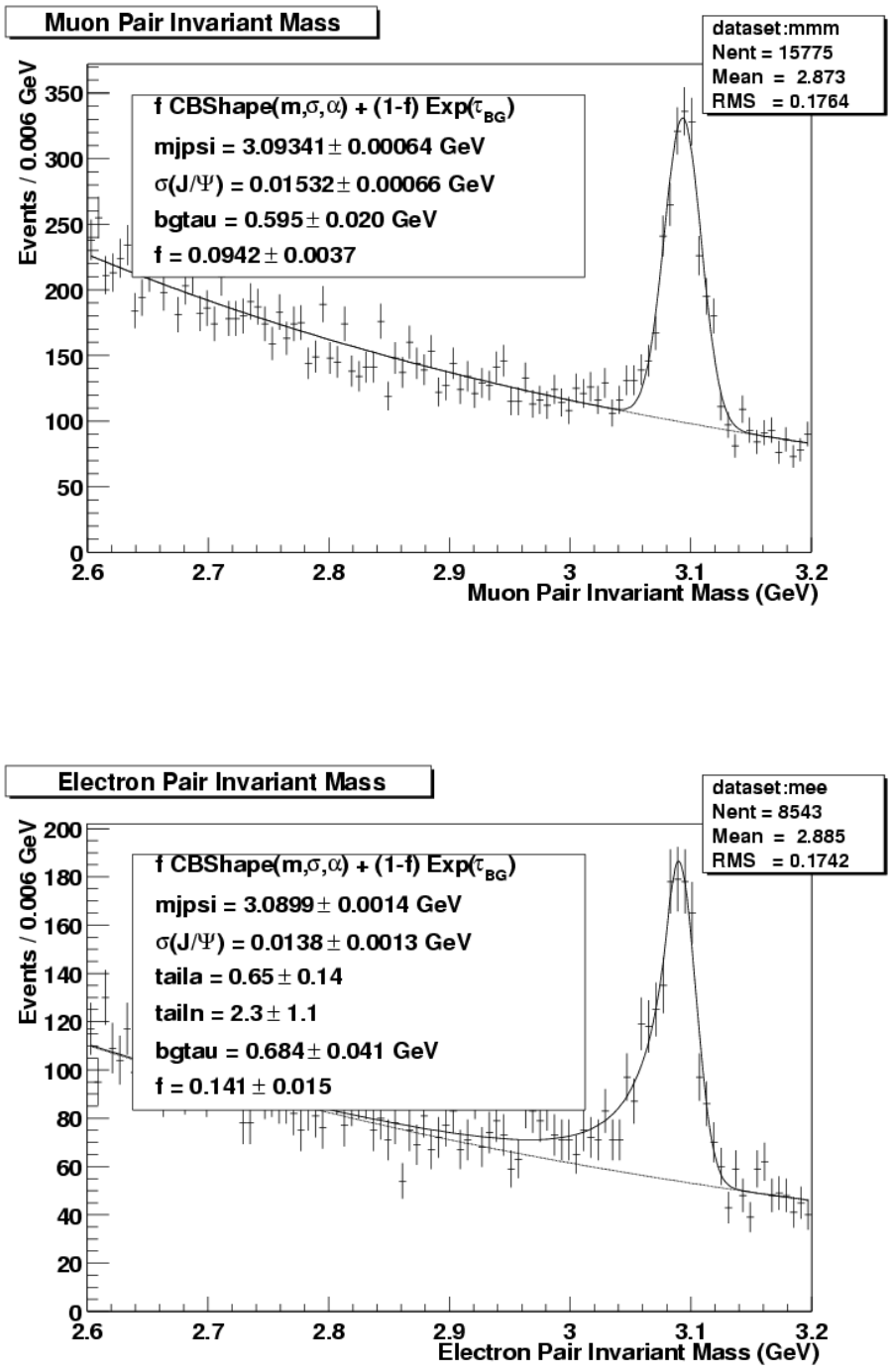

Figure 7.7: *The invariant mass from the $J/\Psi \rightarrow l^+l^-$ using the μ selection (top) and e selection (bottom)*

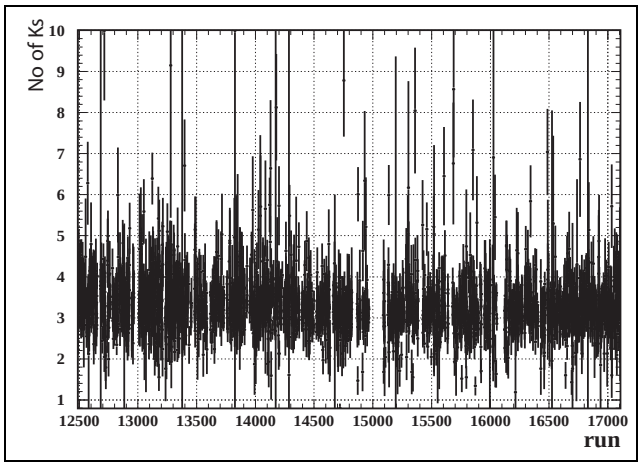

Figure 7.8: *The number of K^0_s as a function of runnumber within the dataset used*

If the prospective J/Ψ passes all these cuts then it is combined with the first K^0_s in the candidate list. It is at this point that the beam constrained mass and ΔE of the B^0 candidate are calculated. The constructed B^0 then has several cuts applied to it, a minimum and maximum mass, transverse momentum and ΔE. If the B^0 passes these then it is added to the B^0 list. Since it is most unlikely that the wrong combination of J/Ψ and K^0_s will fulfil all these criteria the same J/Ψ is then allowed to be used again to try to create another B^0. Once all the K^0_s candidates in the list have been iterated over then the operation is repeated with the next J/Ψ in the list.

Once all candidates in both the J/Ψ and K^0_s list have been iterated over then the resultant list of B^0's is checked. Initially for convenience the list is first reordered in ascending ΔE. The candidate with the best ΔE is then checked to see if the mass of the J/Ψ used in the composition is within five percent of the PDG[13] value for the J/Ψ mass. If it is then that B^0 is removed from this candidate list and added to the final B^0 list.

If the B^0 and J/Ψ pass the above checks then the raw B^0 candidate is split into its daughter candidates. These are then given their PDG Lund identification numbers for reference later. These are then again further dissected into their daughters. The result from this is six candidates, one for each of the particles making the full decay of the B^0 into the lepton and π^0 pairs. First the two leptons are again passed into the *BABAR* standard geometric and kinematic fitter to improve the vertex resolution of the J/Ψ candidate. The same operation is then repeated for the π^0 pair though this time the same fitter as described in section 6.5.1 is used before passing the output from this again into the standard *BABAR* fitter[80]. For both of these fits we use the fitters ability to refit not only the composite particle but also its daughters to improve the energy resolution of these.

Once both the J/Ψ and K^0_s have been refitted they are both passed to the decay tree

creator to create the B^0 again. Again the Geometric and kinematic fitter is used with the beamspot being used as the starting point of the fit. The resultant B^0 from this fit is then used to recalculate the ΔE and the beam constrained mass. To calculate the helicity of the event the K^0_s is boosted into the J/Ψ rest frame and the cosine of the angle between the J/Ψ and K^0_s calculated. This process is repeated for the π^0 and lepton pairs. The candidate information from the complete decay tree is then passed into a PAW ntuple for storage and later analysis.

Apart from the candidate information several pieces of total event information are also stored. These are described below:

- Beamspot position and error
- Event time
- Total energy of all reconstructed candidates in the event
- Total number of tracks in the event
- Event primary vertex and its uncertainty
- Event sphericity and Fox Wolfram Moments from tracks within the fiducial volume.

7.4.2 Calculating the Branching Ratio of $B^0 \rightarrow J/\Psi K^0_s$

7.4.2.1 B-Counting at *BABAR*

The total number of $B^0\bar{B}^0$ pairs created is obviously one of the most important factors when trying to determine the branching fraction of a B meson decay channel. Details of the counting technique may be found in BAD 134[81].

The starting point for any B^0 counting is to determine a method for calculating the number of multi-hadron events within the data sample and then applying further cuts. The hadronic selection should be done whilst still optimising the following factors.

- Minimise systematic errors. This involves minimising the effect on the selection to small changes in the selection as well as minimising such factors as beam gas interactions and varying beam conditions.
- Well understood and high efficiency: The high efficiency minimises branching ratio corrections needed and improves statistical significance. The well understood nature restricts us to using variables that are well described by Monte Carlo.
- Suppress non $B^0\bar{B}^0$ events such as Bhabhas and tau pairs which can generate fake J/Ψ's.

In order to fulfil the 'well known efficiency of the selection criterion' a decision was made on the precise tracking volume that *BABAR* can cover which is well represented within the Monte Carlo. This covers the fiducial volume $0.41 < \theta_{Lab} < 2.54$ for charged tracks since this excludes the SVT front-end electronics and support structure which is not well modelled within the Monte Carlo. For the track selection the list 'ChargedTrack' is used, which has a pion mass hypothesis attached to each track. For neutral objects a slightly different fiducial volume is considered, $0.41 < \theta_{Lab} < 2.409$ The first selection is made on the event tag done using the Level 3 trigger output lines for an event called BGFMultiHadron. This is an intrinsic filter used within the software trigger system (Filters are discussed in section 4.3.3). In order to further reject leptonic events such as tau pairs and Bhabhas a cut on the number of tracks present in the event at ≥ 4 and an additional cut on R2 is made. This is illustrated in figure 7.9

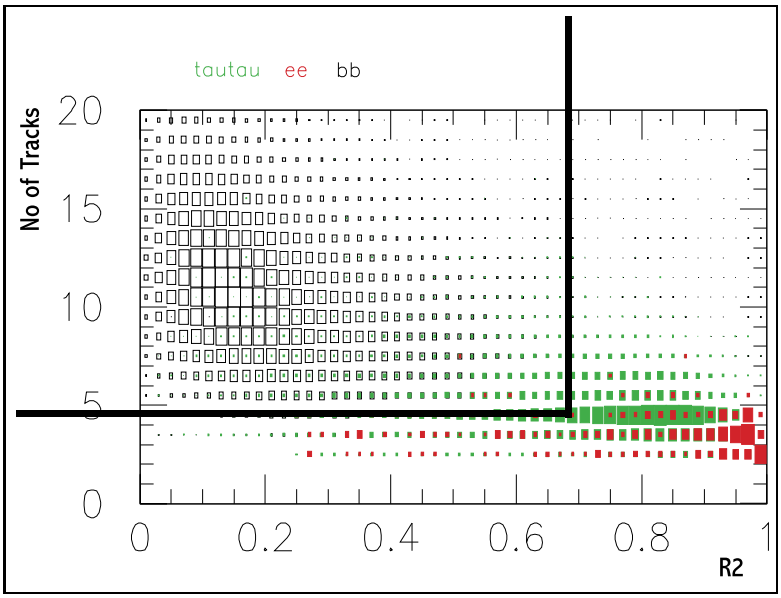

Figure 7.9: *The distribution of number of Tracks within the fiducial volume against R2 for $B^0\bar{B}^0$(white boxes), τ pairs(light green) and Bhabhas(dark red)*

In order to remove a significant fraction of beam-gas events from the sample additional cuts must be introduced. The most effective of those tested is a cut on the total energy of the event candidates in the lab frame set at >5 GeV. This is shown in figure 7.10 with the top figure showing the off-resonance 'background' removed by this cuts from the sample. A cut on the primary vertex of the event is also used since a beam-gas event may have this several cm's from the beam-spot. This has been set at 0.5 cm in the xy-plane though no cut is made in the z-position. Therefore within *BABAR* the hadronic event selection is made using the following cuts:

- Level 3 trigger filter BGFMultiHadron
- nTracks ≥ 4

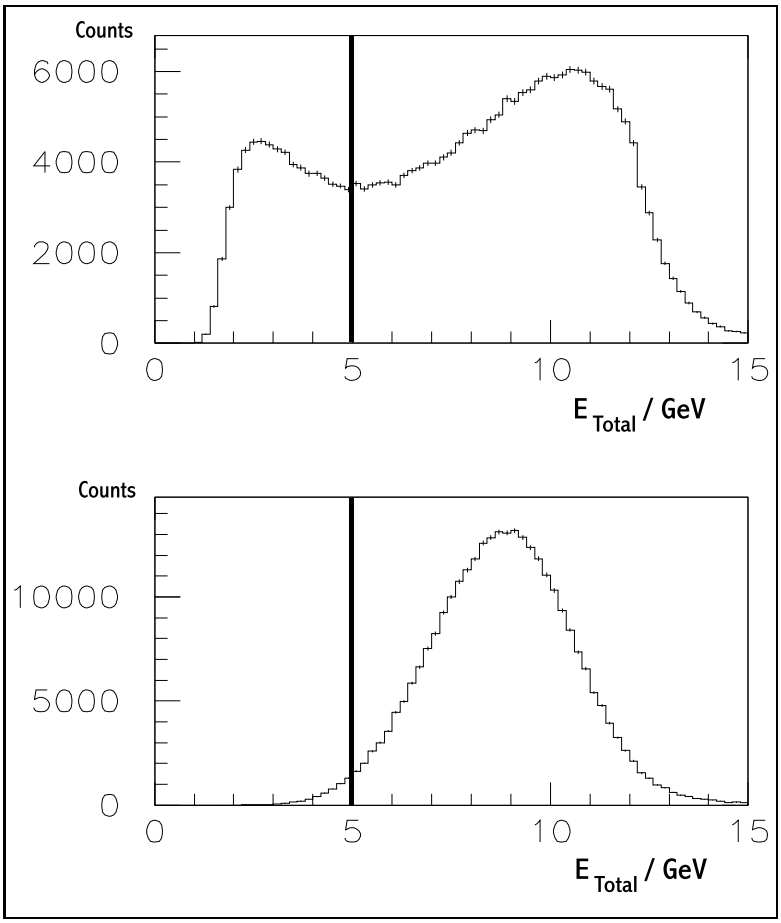

Figure 7.10: *The energy distribution of off-resonance Monte Carlo(top) and on-resonance $B^0\bar{B}^0$(bottom) after both have been scaled by the number of μ pairs in each and had cuts on the number of tracks and R2 applied*

- R2 < 0.7
- eTotal > 5 GeV
- Primary vertex < 0.5 cm from beam-spot in xy plane

Once a list of events that have passed the hadronic selection has been made then this can then be used to calculate the number of $B^0\bar{B}^0$ in a sample. The method chosen within *BABAR* is defined as:

$$N_{B^0\bar{B}^0} = N_{MH}^{On} - N_X^{On} \tag{7.4}$$

where N_{MH}^{On} is the number of events within the on-resonance sample that passed the Multi-hadron selector and N_X^{On} the number of non-$B^0\bar{B}^0$ events that passed the selection. We can write the number of non-$B^0\bar{B}^0$ events as a function of the efficiency to pass the selector, production cross section and the luminosity.

Therefore, since the luminosity may be calculated using the number of muon pairs produced, equation 7.4 can be rewritten as:

$$N_{B^0\bar{B}^0} = N_{MH}^{On} - \sigma_X(s_0)\cdot\varepsilon_X(s_0)\cdot N_{\mu\mu}^{On}/\sigma_{\mu\mu}(s_0)\cdot\varepsilon_{\mu\mu}(s_0) \tag{7.5}$$

s_0 is used to indicate the centre-of-mass energy squared when on-resonance which is set in *BABAR* at $(10.58\ \text{GeV})^2$. The method used to calculate the number of non-$B^0\bar{B}^0$ events is to run the storage ring off resonance (10.54 GeV). A similar equation can be written to find the number of multi-hadrons within this sample.

$$N_{MH}^{Off} = \sigma_X(s_1)\cdot\varepsilon_X(s_1)\cdot N_{\mu\mu}^{Off}/\sigma_{\mu\mu}(s_1)\cdot\varepsilon_{\mu\mu}(s_1) \tag{7.6}$$

Combining the last two equations gives the number of $B^0\bar{B}^0$ events satisfying the selection criteria.

$$N_{B^0\bar{B}^0} = N_{MH}^{On} - N_{\mu\mu}^{On}\cdot R_{off}\cdot\kappa \tag{7.7}$$

Where R_{off} is the ratio of hadronic events to muon pairs when running off resonance and κ is given by equation 7.8:

$$\kappa = \frac{\sigma_{\mu\mu}(s_1)}{\sigma_{\mu\mu}(s_0)}\frac{\varepsilon_{\mu\mu}(s_1)}{\varepsilon_{\mu\mu}(s_0)}\frac{\sigma_X(s_1)}{\sigma_X(s_0)}\frac{\varepsilon_X(s_1)}{\varepsilon_X(s_0)} \tag{7.8}$$

Using equation 7.7, the Run-1 dataset has been found to contain 2.27×10^7 $B^0\bar{B}^0$ decays with an uncertainty of 1.6%.

7.4.2.2 Method of Calculating the Branching Ratio

A branching ratio is defined as the ratio between the number of possible decays of a particle (ie the number of mother particles present) to the number that you actually find after corrections to efficiencies and detector acceptances. Therefore you start with the raw (ie uncorrected) number of daughter particles found in the data sample. A correction is then applied to account for the efficiency of selection of the daughter particles. Since this analysis is calculating the branching ratio for a channel using only one of the many possible final decay states then another correction is then needed to account for this branching fraction. For this the value is given by the PDG. With $B^0\bar{B}^0$ decays the resultant $\text{B}^0 \rightarrow \text{J}/\Psi\text{K}_s^0$ decay can come from either and so the result must be divided by two. This gives the final branching ratio.
The branching ratio is calculated using :

$$B.R. = \frac{N_T - N_{Bkg}}{2.N_{BB}} \tag{7.9}$$

where N_T is the total number of events in a 3σ window in ΔE and m_B, N_{Bkg} is the number of background events that are included in the window, N_{BB} is the number of produced $B^0\bar{B}^0$ events in the data sample used.

Since the decay of the $\text{B}^0 \rightarrow \text{J}/\Psi\text{K}_s^0 \rightarrow l^+l^-\pi^0\pi^0$ is just one of the many that can occur and we are only considering lepton pair decays of the J/Ψ corrections must be

Secondary Decay Channel	Branching Ratio/%
$J/\Psi \rightarrow e^+e^-$	(6.02±0.19)
$J/\Psi \rightarrow \mu^+\mu^-$	(6.01±0.19)
$K_s^0 \rightarrow \pi^0\pi^0$	(31.39±0.28)

Table 7.1: *The PDG quoted branching ratios for the secondary decays from* $B^0 \rightarrow J/\Psi K_s^0$

made for these to get the overall $B^0 \rightarrow J/\Psi K_s^0$ branching ratio. The PDG value of the branching ratios of these is used to ascertain the correction factor needed. These are summarised in table 7.1

Therefore equation 7.9 becomes:

$$B.R. = \frac{N_T - N_{Bkg}}{N_{BB}.\Sigma_i \epsilon_i f_i} \tag{7.10}$$

where i sums over all secondary decays considered and ϵ and f are the efficiencies and branching fractions of the secondary decays(as shown in table 7.1).

The statistical error for the branching ratio is calculated using equation 7.11 below.

$$B.R. = \frac{\sqrt{N_T - (N_{Bkg})^2}}{N_{BB}.\Sigma_i \epsilon_i f_i} \tag{7.11}$$

7.4.2.3 Final Event Selection

For the final selection of the $B^0 \rightarrow J/\Psi K_s^0$ channel further cuts are necessary for the processing of the recorded ntuple described in section 7.4.1. Initially checks must be made to ensure that all candidates J/Ψ daughters have passed the tight lepton cuts and then that all tracks used to construct the leptons and π^0 are from within the well understood fiducial volume. In order to remove as much background as possible a selection is then made dependent on the mass of the B^0 being greater than 5.2GeV. The J/Ψ mass is further cut to a window of $3.06 < M_{J/\Psi} < 3.14$ GeV and $2.95 < M_{J/\Psi} < 3.14$ for the $\mu^+\mu^-$ and e^+e^- J/Ψ decay channels respectively. A cut on the cosine of the J/Ψ helicity was also used: a maximum of 0.8 and 0.7 for the $\mu^+\mu^-$ and e^+e^- respectively. The helicity distribution of the skimmed data sample is shown in comparison with the final selection in figure 7.11 (both to an arbitrary scale).

For the K_s^0 the invariant mass range was also tightened to $470 < M_{K_s^0} < 550$ MeV with the π^0 mass also being used as a selection variable with a window of $110 < M_{\pi^0} < 155$ MeV. A further additional cut was made on the flight length of the K_s^0 from the reconstructed J/Ψ vertex with a minimum of 1cm.

7.4.2.4 Efficiency Calculation and Systematics

The efficiency of the selection is determined using the following method:

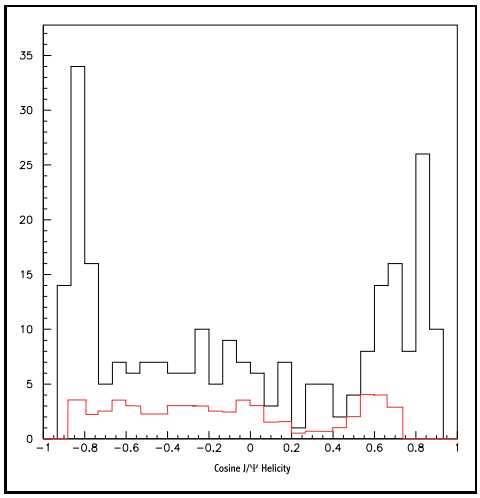

Figure 7.11: *The cosine of the J/Ψ helicity for the raw skimmed data sample(black) and selected $B^0 \rightarrow J/\Psi K^0_s$ events (to an arbitrary scale)*

- Initially using Monte Carlo generated $B^0 \rightarrow J/\Psi K^0_s$ containing B^0, $\bar{B}^0$ and mixing, using the latest version of all reconstruction code and including all possible corrections and the inclusion of the latest version of the *BABAR* track finding software.

- To account fully for the efficiency of the particle identification(PID) methods, a technique of PID killing is applied to reconstructed Monte-Carlo data using efficiency tables for extracted tracks. This takes the form of a statistical removal of reconstructed tracks from within the Drift Chamber to account for the lowering of the drift voltage to prevent damage from a vacuum leak.

- The replication of the efficiency for data of the neutral particle detection in real data. There is also a need to smear the energy of the reconstructed photons in the Monte-Carlo as well as apply random killing of calorimeter clusters to mimic the behaviour of the real EMC system.

The efficiency and purity of the selected sample in Monte Carlo can then be checked using simple counting of real $B^0 \rightarrow J/\Psi K^0_s$ events selected against those in the sample. Since there are slightly different efficiencies for the $e^+e^-$and $\mu\mu$ channels of the J/Ψ decay then these must be taken into account. A check was made on the whole sample and it was found that the overall efficiency for both J/Ψ decay channels was 15.67±2.73%. The final results are shown in table 7.3.

7.4.2.5 Backgrounds and Systematics

The signal region within the 2-dimensional ΔE against Beam constrained mass plots was described as being:

$$|\Delta E| \leq 3\sigma$$

Selection	Number of Events Selectedfrom Data Sample		
	e^+e^-	$\mu\mu$	Total
All			$22.74 \pm 0.36 \times 10^6$
Raw	1086	1035	2121
Particle ID Selection Passed	670	608	1278
Tracks within Fiducial Volume	481	541	1022
B Mass	258	318	576
π^0 Mass	236	275	505
K_s^0 Mass	201	262	463
J/Ψ Mass	101	74	174
K_s^0 Fight Length	85	69	154
Cosine J/Ψ Helicity	45	47	92
Inside Signal Window	30	34	64

Table 7.2: *The number of events raw from the skim showing the effect on event numbers of each cut*

J/Ψ decay channel	Overall efficiency %
e^+e^-	14.50±2.11
$\mu^+\mu^-$	16.83±3.54
l^+l^-	15.67±2.73

Table 7.3: *Overall efficiencies of the selection of* $B^0 \rightarrow J/\Psi K_s^0$, $K_s^0 \rightarrow \pi^0\pi^0$

Where σ is defined as the ΔE resolution.
The background within this region can come from two sources. Firstly from continuum events which can be modelled using an Argus function, with the magnitude of this being determined using off-peak data and an appropriate mixture of u,d,s and $c\bar{c}$ Monte-Carlo. Other B$\rightarrow$J/ΨX events also contribute to background and also have a mass peak present at the B mass. These backgrounds are both measured and using the selection described previously have shown a contamination within the final event sample of less than 3%, with a total number of events of 7.3$\pm$2.9 for J/$\Psi\rightarrow \mu^+\mu^-$ and 4.9$\pm$2.3 for J/$\Psi\rightarrow$e$^+$e$^-$events.

The systematic effects acting on the measurement of the branching ratio can be summarised as below:

- 1.9% systematic error on the total number of B$\bar{\text{B}}$ events counted.
- The uncertainty in the branching fractions of the secondary decays. The values as given by the PDG are used.
- Uncertainties in the tracking and lepton identification efficiencies. The uncertainty in the tracking efficiency has been measured to be 1.2% per *GoodTrackLoose* track from the analysis in [82] and using slow pions from the ψ(2s) $\rightarrow$J/Ψ 2% per track. The dependence of track efficiency on the applied drift voltage is shown in figure 7.12 showing the large drop in efficiency with only a slight drop in the drift voltage.

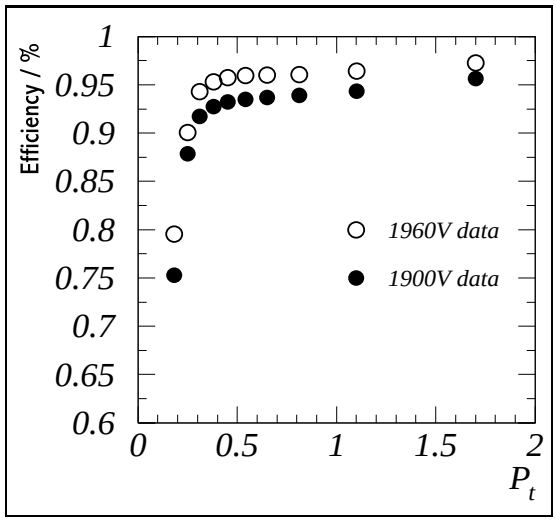

Figure 7.12: *The dependence of tracking efficiency on the DCH drift voltage*

- A discrepancy between Monte Carlo and data descriptions of the alignment between the SVT and DCH. Also differences between the Monte Carlo and data descriptions of the errors in the magnetic field as well as a not totally accurate description of the materials present in the detector. These all lead to

an uncertainty in the measurement of δE. This has been shown in the analysis in [83].

- Incorrect description of the EMC efficiency in the Monte-Carlo allowing the efficiency of the neutral particle detection to be wrong. Studies using τ, D and D^* as well as the result in Chapter 6 have shown that in general the simulation gives a good description of the neutral efficiency and resolution. To determine the systematic error a method to smear the photon energies , shift the π^0 energy peak dependent on energy and randomly kill photon clusters within the Monte Carlo has been developed. The dependence of π^0 mass to energy is shown in figure 7.13.

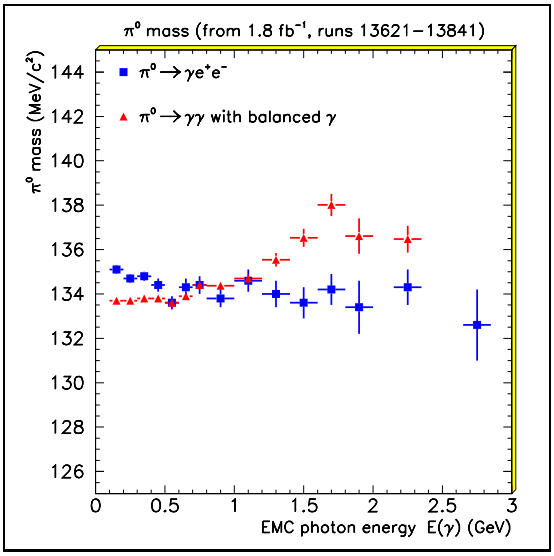

Figure 7.13: *The dependence on γ energy of the π^0 mass*

- Uncertainty in the Argus fit of background due to the extremely low statistics in the ΔE sidebands. In the default fit all parameters are allowed to float but for the signal region this is redone fixing the parameters determined by the fit to the sideband, except for the normalisation. The difference is determined to be the systematic error.

- Possible slight differences in the distributions of the cut variables between the Monte-Carlo and data. To allow for this the cuts are altered by the amounts shown in table 7.4 one by one and the calculation of the yield redone. The differences in the yields are then assigned as the systematic error.

The systematic effects are summarised in table 7.5.

7.4.3 Results

The yields for the individual $B^0 \rightarrow J/\Psi K^0_s$ $J/\Psi \rightarrow \mu^+\mu^-$ and $J/\Psi \rightarrow e^+e^-$, combined l^+l^- and branching fractions for the same are summarised in table 7.6.

Cut	Variation
J/Ψ Mass	$\pm 1\sigma$
K_s^0 Mass	$\pm 0.5\sigma$
π^0 Mass	± 4 MeV
Helicity	± 0.05
K_s^0 Flight Length	Remove Cut

Table 7.4: *Cut variations to assess systematic impact*

Parameter	J/Ψ Daughter Decay		
	J/$\Psi \to e^+e^-$	J/$\Psi \to \mu^+\mu^-$	J/$\Psi \to l^+l^-$
NBB	± 1.6	± 1.6	± 1.6
PID	± 0.1	± 0.5	± 0.5
ϵ(Trk)	± 2.4	± 2.4	± 2.4
ϵ(gamma)	± 4.3	± 4.3	± 4.3
Backgrounds	± 2.1	± 1.9	± 2.0
Cuts	$^{+1.83}_{-5.33}$	$^{+2.65}_{-4.17}$	$^{+3.30}_{-6.73}$
Total	$^{+5.88}_{-6.57}$	$^{+6.14}_{-6.93}$	$^{+6.47}_{-8.74}$

Table 7.5: *The Systematic effects of cuts on the selection of* $B^0 \to J/\Psi K_s^0$, $K_s^0 \to \pi^0\pi^0$

J/ΨDaughter Decay	Number of Candidate Events	Number of Calculated Background Events	Branching Fraction (with systematic errors)
e^+e^-	30	4.28	$8.27^{+0.57}_{-1.66} \times 10^{-4}$
$\mu^+\mu^-$	34	4.57	$8.17^{+0.74}_{-1.16} \times 10^{-4}$
l^+l^-	64	8.85	$8.65^{+0.48}_{-0.99} \times 10^{-4}$

Table 7.6: *The number of events found and branching fractions for* $B^0 \to J/\Psi K_s^0$

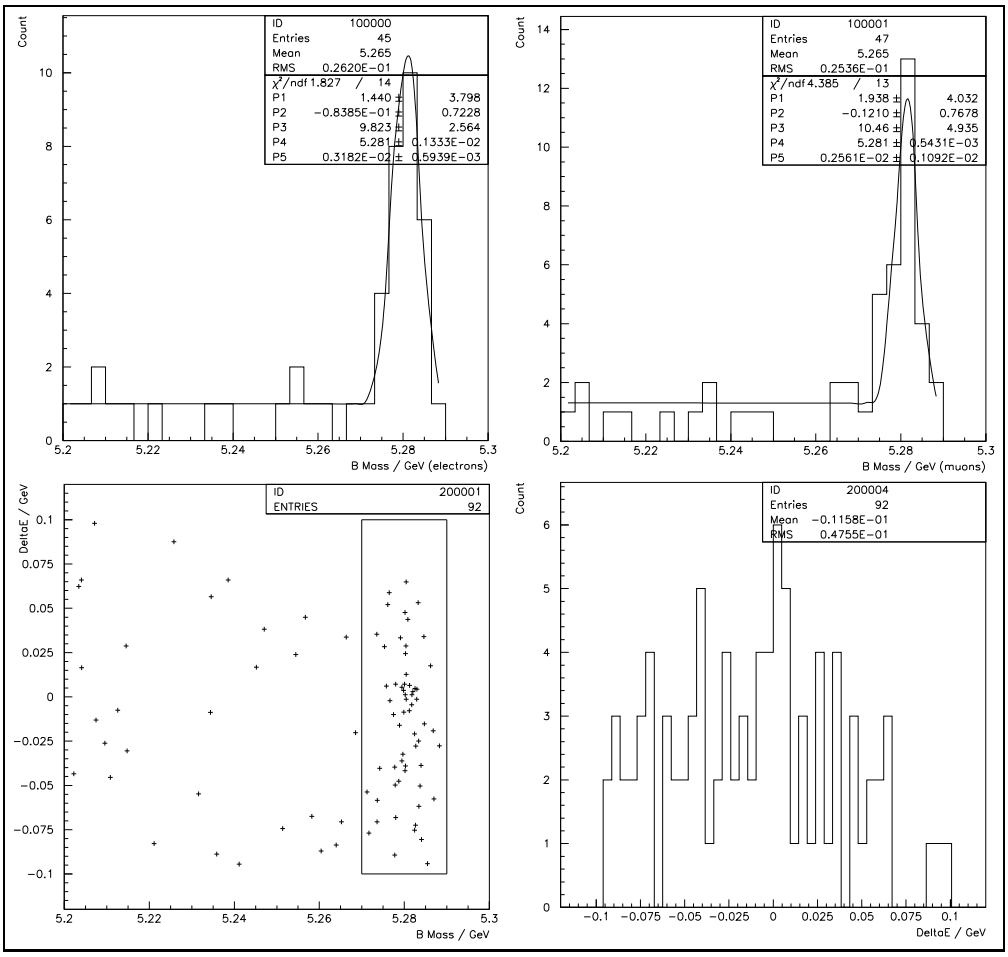

Figure 7.14: *Beam constrained B Mass from J/Ψ→e^+e^-(top left), J/Ψ→ $\mu^+\mu^-$(top right), Beam constrained B Mass against ΔE from J/Ψ→l^+l^- with the signal region contained within the box (bottom left) and ΔE(bottom right)*

7.5 Summary

The method of firstly selecting $B^0 \rightarrow J/\Psi K^0_s$ events has been described as well as the other techniques necessary to produce a measurement of the branching ratio for the neutral K^0_s decay mode. The systematic errors have been ascertained and included in the final result for the branching ratio of the neutral mode of $B^0 \rightarrow J/\Psi K^0_s$ ($K^0_s \rightarrow \pi^0\pi^0$). As a cross-check the measurement for the branching ratio of the charged mode $B^0 \rightarrow J/\Psi K^0_s$ ($K^0_s \rightarrow \pi^+\pi^-$) has been used. This has been measured many times with the result below being calculated by the *BABAR* charmonium working group[83]. (A correction has also been applied to this to account for the K^0_s branching ratio)

$$\text{B.R.}\left(\frac{B^0 \rightarrow J/\psi K^0_s}{B^0 \rightarrow X}\right), K^0_s \rightarrow \pi^+\pi^- = 8.3 \pm 0.6(\text{Stat}) \pm 0.5(\text{Sys}) \times 10^{-4}$$

$$\text{B.R.}\left(\frac{B^0 \rightarrow J/\psi K^0_s}{B^0 \rightarrow X}\right), K^0_s \rightarrow \pi^0\pi^0 = 8.65 \pm 0.6(\text{Stat})^{+0.48}_{-0.99}(\text{Sys}) \times 10^{-4}$$

As can be seen the results for the charged and neutral K_s^0 decay mode from the $B^0 \rightarrow J/\Psi K_s^0$ channel agree showing that the analysis and reconstruction of B mesons is operating correctly as expected.

Chapter 8

Conclusion

The *BABAR* experiment has now been operating for over a year with the Run-1 event sample being the largest single dataset of B mesons ever collected. Figure 8.1 shows the total integrated luminosity collected by *BABAR*. By the end of Run-1 PEP-II also surpassed many of its design goals for peak luminosity and integrated luminosity delivered to the *BABAR* experiment. As well as the branching ratio measurement

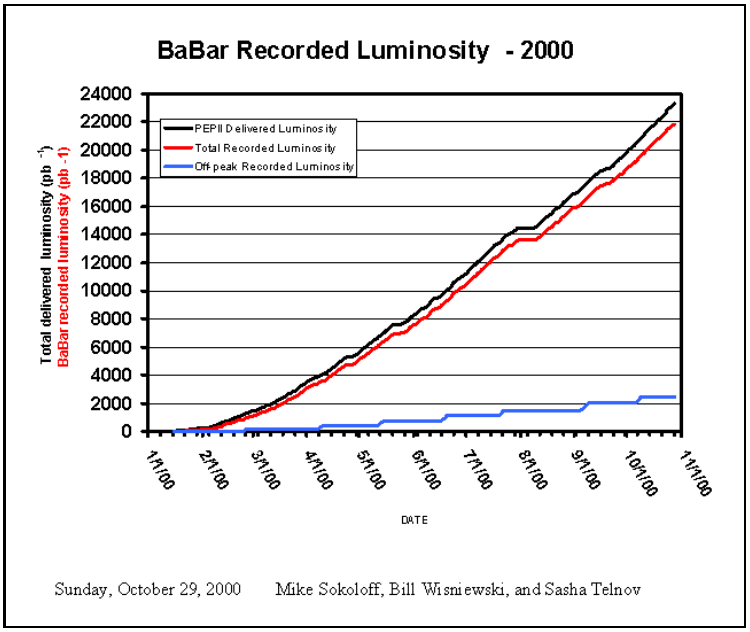

Figure 8.1: *Total integrated luminosity collected by BABAR until end of Run 1*

presented here there has also been a measurement made of sin2β using both the charged and neutral modes of the K^0_s decay. This result was presented in a paper submitted for publication in PRL.

The Level 1 Calorimeter Trigger has been operating smoothly from the first day of operation with only very minor problems mostly in the interconnections between the Calorimeter front-end electronics and the trigger system. The EMT has shown itself to be robust to the extremely high backgrounds that are present within the system.

During the minor upgrade to the detector in preparation for Run-2 it has been decided that it was unnecessary to change the EMT and it is looking very likely that this will be the case also when PEP-II is upgraded to provide $10^{34}\mathrm{cm}^{-2}\mathrm{s}^{-1}$ luminosity.
The analysis of neutral objects in *BABAR* has been shown to be reliable and produces accurate measurements of the masses of the π^0 and K^0_s. The π^0 mass is calculated to be 134.4±0.4 MeV with a width of 6.8±0.3 MeV. From the neutral decay mode of the K^0_s the mass is determined to be 472.0±6.3 MeV with a width of 96.3±3.3 MeV. The lifetime of the K^0_s has also been determined at 2.7±0.4 cm which is in line with the PDG value.
For the measurement of sin2β the inclusion of the neutral decay mode of the K^0_s from $\mathrm{B}^0 \rightarrow \mathrm{J}/\Psi\mathrm{K}^0_s$ is necessary both to provide extra statistics and as a cross-check on the charged mode. The branching ratio has been calculated as:

$$\mathrm{B.R.}\left(\frac{\mathrm{B}^0 \rightarrow \mathrm{J}/\psi\mathrm{K}^0_s}{\mathrm{B}^0 \rightarrow \mathrm{X}}\right), \mathrm{K}^0_s \rightarrow \pi^0\pi^0 = 8.65 \pm 0.6(\mathrm{Stat})^{+0.48}_{-0.99}(\mathrm{Sys}) \times 10^{-4}$$

which is in line with both the charged mode calculation by the *BABAR* collaboration and the PDG value.
BABAR will start running again for Run 2 at the beginning of April with a projected target of $40\mathrm{fb}^{-1}$ data to be collected. This will boost the total number of B mesons collected by *BABAR* to a projected 60M $\mathrm{B\bar{B}}$ pairs. After this it may be necessary to perform some preventative maintenance on the detector before an accelerator upgrade but it should prove strong and reliable for many years to come, giving us hopefully that much needed further glimpse into the origins of the Universe.

Appendix A

Class Structure of the EMT Software

The full description of the operation of the packages used to run the online side of the EMT system is located in chapter 5. Within this appendix a complete description of the individual classes as well as register addresses will be given

A.1 L1EmtOnline

- *L1EmtTpbCrate:* This class is arranged as a singleton. It is arranged so that a complete model of the configuration data is loaded onto the TPB's. This class has accessors to allow the contained data to be read & set. Each TPB contains 4 Ax, 1 FcX, 1 Fx and 1 CSER. There are also the individual serial numbers and slot addresses for the TPB's. This class has the function 'set' overloaded with each type of contents, Ax, FcX etc. to allow the filling of each TPB object with its data.

- *L1EmtTpbRawData:* This class actually contains the arrays holding the TPB's Raw Data. As such this contains the accessor and set functions.

- *L1EmtAx, L1EmtFcx, L1EmtFx, L1EmtCser:* This class contains all accessor functions for all parts of the configuration data for the Algorithm Xilinx. These consist of the functions required to firstly set all the types of data as defined in the RawData class. The data can be read either from a simple text file or a binary file that is created using binary executables created within this package at build time. Functions are also within these classes to create an output text file as well as fill a tagged container of the appropriate type.

- *L1EmtAxRawData, L1EmtFcxRawData, L1EmtFxRawData, L1EmtCserRawData:* These classes contain arrays to hold all types of configuration data. Initially when constructed there are default values for each. Each of the RawData classes data is described on the next page.

- Ax
  - JitterWindows
  - TimeAlignment
  - GlobalThresholds
  - JitterThresholds
  - CfdProducts
  - BitmapThresholds
  - CableMask
  - TowerMask
- Fcx
  - GlobalDelay
  - MapDelay
  - xyDelay
  - PhiDelay
  - nIoPbWords
  - ReadDelay
  - synchDelay
  - nPbWords
  - ReadPhase
  - nSpyWords
- Fx
  - Mask
- CSER
  - bufferStatus
  - spyStatus
  - syncStatus
  - playbackStatus
  - paulsSecret
  - spyStart
  - spyStop
  - playbackCycle
  - playbackPosition
  - playbackEnable
  - tpbMode
  - cableErrors
  - serialNumber
  - geomAddress
  - unsynchronised

    * anyAxError
    * badSubAddress
    * badOpCode

- *L1EmtAxTC, L1EmtFcxTC, L1EmtFxTC:* These classes contain containers that are used for persistent storage of the configuration data for the TPB's. For the persistent versions of this data it was decided to separate the functions needed for writing the tagged container for these objects so as to reduce confusion with the already present classes for handling the objects on ROM. To this end the configurationTC variants of the configuration data were developed. This also dovetailed nicely with the initial usage of reverse dataflow (the process of recovering data from persistent storage is described in section 4.3.2.2).

- *axCreateConfig, fcxCreateConfig, fxCreateConfig:*
  Though not strictly classes the functionality of these files should be mentioned. Each of these is used to create a binary xtc file containing the information written in appropriate flat files. These were designed to allow the editing of configuration information from off-site though as described below this was not always successful.

To transmit the event data from the TPBs through to final data storage there are 2 distinct classes which are used L1EmtSlotTC and L1EmtChannelTC. During the development of the system the format of these containers changed and to ensure that any data that had been written before the change could still be read it was necessary to create Version1 examples of these classes.

- *L1EmtSlotTC:*One Slot TC collects all TPB's output in the form of a ChannelTC for each as well as the Global Map output. As such it represents the total data output from the EMT system.
  - Control Status & Error Register.
  - Number of Channel TCs contained.
  - Number of time samples for each piece of information in a channel TC.
  - The beam crossing time.
  - The information as passed out to the Global Trigger
  - Channel Tagged Containers themselves.

- *L1EmtChannelTC:* A Channel tagged container contains the following information from each TPB.
  - Channel Number: (0 to 39)
  - Data bitmap: This the energy information for that channel

  - ϕ,θ information
  - X Information: Energy deposited in that X region
  - Y Information: Energy deposited in that Y region

- *L1EmtSlotIterator:* This iterator class is also required so that the first ChannelTC within the SlotTC is read and then the next through to completion with the total number of TPB's represented within the system.

- *L1EmtBackPb , L1EmtFrontPb:* These classes are used to access and store the contents of the playback memories within the singleton. They also define the maximum size of the data that can be written into them.

- *L1EmtOnlineTemplates:* Due to a bug in the VxWorks compiler for C++ it is necessary to explicitly declare any templates that are used within the library. If this isn't done when loaded onto the ROMs where the code is dynamically linked then unresolved symbols will result.

- *L1EmtOnlineTypeInit:* This class is used in conjunction with L1EmtTypeIds to give each tagged container type a unique identifier. This class registers this with the dataflow system whereas L1EmtTypeIds actually defines the type numbers.

A.2 L1EmtCalOnline

- *L1EmtConfigCycle:* The *Calchoice* variable defines the type of configuration the FSM will run while the *CSERchoice* defines the type of CSER setup that will be used. This sets such things as Front or Back End playback or normal setup. These are listed below.

  - rec
  - fe
  - fec
  - fecc
  - be
  - bec
  - lat
  - norm

- *L1EmtMetaCycle:* This class also contains the CalChoice and CSERChoice variables. This was allowed initially to allow some flexibility in the position within the FSM that the choice of dependent actions would take place. This allows calibrations that need more steps within the FSM to operate correctly to be accommodated more easily.

- *L1EmtMacroCycle, L1EmtMajorCycle & L1EmtMinorCycle:* These classes are built with no configurable options but exist should the need for them ever arise.

As with other packages that are built using the online makefile system it is necessary to declare any and all templates within classes which are used within the package. Also contained are the files that produce the executables for production of cycle tagged container files. These are used by the Run Control system to coordinate the actions of the system at each step of the FSM. There is one of these files per type of calibration run that could be done, the internal structure of these being as follows.

1. Initially an OdfArena is created in memory space. This is used to hold all the cycle tagged containers before they are written to file.

2. A topTC is then created on which the subsystem specific cycleTC's are appended.

3. The ConfigCycleTC is then constructed with the calibration specific *Calchoice* and *CSERChoice* variables as constructor arguments. This is then appended to the topTC. Within this part of the code is also a variable to determine the number of subclass meta cycles to be attached.

4. Then number of Metacycles is then iterated through. Within each Meta cycle is a variable to determine the number of Macro cycles per Meta cycle, Major per Macro and Minor per Major.

5. Within Each Minor Cycle a dataflow command can be issued such as L1Accept. The number issued can also be controlled.

The order of operation for a configuration TC is to first perform all the operations for the 1st of each type of FSM level and then iterate back up the configuration tree to perform the next iteration of the previous level.
The final group of classes within this package are those to store and process the data collected from the Frame Clash calibration. This is described in more detail in section 5.3.4. The classes used are:

- *L1EmtFCScatChan, L1EmtFCSafeChan:* These classes are derivatives of CalScat chan and are used to stire 2 dimensional scatter points. This gives a storage container for the data from the frameclash calibration for the best values of the frameoffset and synchDelay.

- *L1EmtFCErrors:* This class is used to store the raw error words read out for each combination of frameOffset and synchDelay.

A.3 L1EmtOdf

- *L1EmtAbsRead:* This is the EMT base class for all reading of information from the TPB such as Ax, Fcx, Fx, CSER & FIFO buffers through the D-link. Deriving from the odfRead class the constructor is supplied with a pointer to the

calling VxWorks task, the address to determine from where the data is being read and the list of elements that will be read, in the EMT case which boards are present in the system. When the class is first called a check is made to ensure that the element passed is indeed present in the system and then that it does have data to be read. A check is then made for the start-bit after which the header is copied directly into an L1EmtHeader object from the board. The actual data itself is then copied with a word format swap to account for the method of storage on the ROM's. There is also within this class a definition of which C&D-link pair will be used with the EMT only using set A. This is therefore hardcoded into this class. The derivatives of this class are listed below each having its respective raw data type templated into the constructor:

  - L1EmtFcxRead
  - L1EmtCserRead
  - L1EmtAxRead
  - L1EmtFxRead

  In each case the class calls the L1EmtAbsRead constructor templated to the type of raw data that will be transported. The Playback reads though are slightly more complicated since firstly there are more than one per board/element plus after reading they must be cleared automatically. To assist with this it was decided that iterator classes would be needed.

- *L1EmtFrontPbIterator & L1EmtBackPbIterator:* The functionality of these iterators is exactly the same even though they operate over different FIFOs. Since there are 4 FIFOs per TPB, 1 for the backend and 3 for the front there must be an iterator for each. This condenses the output from each of the 3 FIFOs into one object for readout through the VME interface.

- *L1EmtPbRead:* As with the Xylinx configuration data reads this is also templated to AbsRead though it has an interface between to allow for the differing number of FIFO's in the forward and backward system.

- *L1EmtInject:* Within the dataflow platform a command is labelled as an 'inject'. Each subsystem must create a class containing the subsystem dependent definition of all injects. An inject is passed with 2 arguments, the opcode of the command (these are shown in table A.1) and the subAddress. The subAddress is the destination label for the opcode (These are listed in table A.2 specific to the EMT system). To ensure fast operation each possible inject has its own function within this class with these both hardwired into it with the definitions defined within the base class odfInject. Each inject method is also passed a pointer to the odfTask that called the function and to which it will be attached to allow it to run within VxWorks. The simple injects such as set configuremode, setrunmode etc. are broadcast to all boards within the EMT system. To allow for this the fibre pair used is hardwired in (in the EMT case this is A) with this function returning the elements of the EMT system present. To allow for future functionality a generic inject function was also included.

OpCode	Command
0x00	No Operation
0x01	Clear-Readout
0x02	Synchronise-Readout
0x03	Level 1 Accept
0x04	Read-Event
0x05	Calibration-Strobe
0x06	Start-Playback
0x15	Clear Ax Errors
0x16	Clear Spy FIFOs
0x18	Set Configure Mode
0x19	Set Run Mode
0x1a	Read
0x1b	Write
0x1c	Clear Backend FIFO
0x1d	Clear Frontend FIFO
0x1e	User-Reset

Table A.1: *The Opcodes used within the EMT system and their functions*

subAddress	Location
0x00	Algorithm Xilinx 1
0x01	Algorithm Xilinx 2
0x02	Algorithm Xilinx 3
0x03	Algorithm Xilinx 4
0x04	Front End Playback 1
0x05	Front End Playback 2
0x06	Front End Playback 3
0x08	Back End Playback
0x09	Formatter Xilinx
0x0a	Fast Control Xilinx
0x0c	Read from CSER
0x0d	Write to CSER

Table A.2: *The Subcommand Addresses used within the EMT and their corresponding locations*

- *L1EmtHeader:* The format of the header attached to information that will flow in either the C-link or D-link is described in section 5.3.3.1. This class is the concrete implementation of this functionality. It holds each part of the header word in an array which can then be addesd to the front of the daq word.

- *L1EmtLinks:* The *BABAR* standard readout module has two C/D-link pairs A & B. The EMT system only uses A and as such this must be defined. This class has the definition of which pair to use hardcoded in as well as an accessor function to retrieve this information. As with all functions running on the ROM the constructor is passed a pointer to the calling VxWorks task. The main functionality of this class though is to set the global list of elements present in the system for use in all other classes.

- *L1EmtTestInject:* Since the lower value opcodes are not actually issued as software injects by the fast control system it was necessary to create a test class that contained them for use during development of the prototypes and then initial testing of the preproduction boards. To this end this class holds the injects for Synch, L1Accept & Read Event. Normally these are reserved for issue only by the Fast Control System hardware and as such must not be used when the code is run within the main dataflow platform.

- *L1EmtTestStackInject:* During development of the system it was necessary to simulate the closeness that injects would come when operating at a Level 1 rate of 2kHz. To allow for this the StackInject class was developed. This allowed for 2 injects to be loaded into the ROM with a configurable time delay between them. They would then be passed as one command to observe the board behaviour.

- *L1EmtTpbVme:* This class contains all the interface definitions between the hardware boards and the VMS system including the system base address. Since this differs between the setup at SLAC and when testing was done at RAL both of these are still included. Functions are also included for the control of readout of both the CSER and Spy buffers through VME.

- *L1EmtTrgConfig:* It was necessary to add functionality to allow the progress of L1Accepts through the system to be monitored via the Xyplex terminal window. This was used primarily during the interface testing during system integration since at the nominal L1Accept rate of *BABAR* during normal running allowing printout could cause backpressure within the system due to SBC processor usage and then in turn detector deadtime. To allow for this initially this class had functionality to firstly set the interval between printouts and also the amount of printout per L1Accept. This allowed setting the interval to a maximum value of 100000 events which was thought infrequent enough to not cause deadtime.

- *L1EmtWrite:* Unlike the read class the write class has all the individual types of data that could be written (Ax, CSER, Fcx etc.) already hardcoded in. This is due to the preformatting that occurs within the RawData class for that type. The write functionality occurs as a block of unsigned short words. Again the

link to use is hardwired in along with instructions to ignore errors that come from the other link.

- *L1EmtOdfTemplates:* For any package that is to be built within the online dataflow Makefile system any templates that are going to be used must be explicitly declared within a separate class. This was found to be a bug/feature of the VxWorks C++ compiler. To allow for this these files are created. In this case the templates used are the XXRead classes which have the type of raw data included in the word as a template.

It is necessary to encapsulate all the operations of classes working on the Spy system within a suitable executable. This is executed after the standard EMT executable with an appropriate priority. The following classes are used to operate and check the Spy system.

- *L1EmtBackgroundTask:* This class defines the executable that will be actually called by a line in the EMT startup script. Within this is the functionality to initiate the dumping of the contents of the spy memories through VME as well as a visible check on the task running through a check on the CSER to ascertain the board mode, configuration or run. This initiates a printout via the Xyplex terminal window within the same function also starting spy buffer filling through the issuing of a StartPlayback command. All instantiations of later components of the spy simulation are instantiated here to allow for the creation of arrays to hold the outputed spy data from the FIFOs. Within the SpyDump function all outputed data is then formatted into arrays for later comparison with the simulation.

  The actual classes for moving and then storing the data once it has been read from the VME bus are below.

- *L1EmtSpy:* This class is used to collect the output of the Spy task and then output to file if any errors are found. It also contains functions to allow for the reading in of an input file that can be used for the verification of the Spy system.

- *L1EmtSpyTask:* This actually creates the VxWorks format task that is run in the background to control the Spy process within the ROM.

- *L1EmtSpyIterator:* To collect the output from each of the TPB's for input into the spy process it is necessary to use an iterator.

A.4 L1EmtCalOdf

- *L1EmtBase:* There are many functions that are shared with all of the actions classes within this package. These include the specific functions for reading, writing the configuration from the singleton onto the boards. As well as the functions used to setup the different CSER's. The different CSER setups are described below:

- *Configure*
  PlaybackEnable set to playbackOff
  SpyStart set to startOnStartPlayback
  SpyStop set to stopOnFull
- *Configurec*
  PlaybackEnable set to playbackOff
  SpyStart set to startAlways
  SpyStop set to stopOnFull
- *Configfe*
  PlaybackEnable set to playbackOn
  PlaybackPosition set to frontendPlayback
  PlaybackCycle set to playbackCycleOnce
  SpyStart set to startOnStartPlayback
  SpyStop set to stopOnFull
- *Configfec*
  PlaybackEnable set to playbackOn
  PlaybackPosition set to frontendPlayback
  PlaybackCycle set to playbackCycleContinuously
  SpyStart set to startOnStartPlayback
  SpyStop set to stopOnFull
- *Configfecc*
  PlaybackEnable set to playbackOn
  PlaybackPosition set to frontendPlayback
  PlaybackCycle set to playbackCycleContinuously
  SpyStart set to startAlways
  SpyStop set to stopOnFull
- *Configbe*
  PlaybackEnable set to playbackOn
  PlaybackPosition set to backendPlayback
  PlaybackCycle set to playbackCycleOnce
- *Configbec*
  PlaybackEnable set to playbackOn
  PlaybackPosition set to backendPlayback
  PlaybackCycle set to playbackCycleContinuously
- *Configlat*
  PlaybackEnable set to playbackOff
  SpyStart set to startOnStartPlayback
  SpyStop set to stopOnLevel1Accept

The functions to change the system state between configure and run are also here as well as the issuing of the StartPlayback function.

For each input datatype for configuration there is a separate 'Set' function which copies the data from its external storage to the singleton class held is the ROM

memory space. There are 2 types of these functions, one to load from a flat file and the other from the tagged container objects. To wrap these functions for easy use there is an allSet function which simply calls all the other set functions within it.

There are several different types of calibration that the EMT system can run. Several of the classes that correspond to dataflow actions are command to all classes. These are:

- *L1EmtReset:* When the system is first switched on it automatically fires off a reset transition. This is used to issue a userReset to clear the event, playback and spy buffers of any spurious data. The system is then explicitly set to Configure mode (though it is designed to start up in this mode). The CSER is then filled with the default values as hard coded into the Raw data class. All error flags are then cleared.

  The singleton L1EmtTpbCrate class is then created into which the serial number is read from the board and placed within the CSERRawData class. This is then read back and compared with the value on the boards to verify the C/D-link connections.

- *L1EmtCalConfig:* This class is the first in the progression around the finite state machine and has the interfaces within it for the loading of the configuration constants for the 3 Xilinx's as well as the system input mask. Within the constructor the 3 configuration loaders are created which automatically find the configuration tagged containers. These are then passed to the globalconfig function that actually instantiates the configuration TC's in memory space and validates them. The CSERChoice variable is also read from the cycle TC and used to determine which CSER to load. Again for normal data taking CSER 'normal' is used. This has the following attributes:

  - playbackOff
  - Spy startOnStartPlayback
  - Spy stopOnFull

- *L1EmtBeginRun:* This action is used to validate the data that was downloaded onto the TPB's and comparing what is read back with the contents of the singleton class L1EmtTpbCrate (See section 5.3.1 for a description of this). An error is flagged here if there is a discrepancy.

- *L1EmtBeginMeta:* This action makes the actual decision of which type of calibration to do. It was determined that this was the latest that this decision could be made within the FSM.

- *L1EmtEndMeta:* This class must be included to match the Begin Meta since the Dataflow system is only able to replace missing actions within the FSM with

a dataflow standard action for a pair, i.e. you cannot create your own begin action without a complementary end action.

The normal data taking feature extraction has its own set of classes with the standard feature extraction L1Accept collecting data. These classes are:

- *L1EmtFEXBeginMacro, L1EmtFEXBeginMinor, L1EmtFEXEndMacro, L1EmtFEXEndMinor:* These classes are used only to attach the appropriate sub action. These also give the capability to have a small amount of diagnostic code within one of these classes.

- *L1EmtFEXL1Accept:* This class contains all the code used for feature extraction (This is described in more detail in section 5.3.4.1). It is essential that the operation of this code is a quick as possible since the fire method must operate within a time window of 500μs. The internal operation of the code is as follows. The constructor reads the formatter Xilinx configuration data to set the extent of the memory buffer into which the data will be read from the event buffer. The global data buffer & ϕ buffer lengths from the Fast Control Xilinx configuration data is also read. The fire method then copies the data from the event buffers straight into the memory space allocated. There is then a separate method to swap the format between what was read and what will be written into the channel tagged containers.

For diagnostic purposes special configurations have been developed to run using the playback (both back and front end) memories to issue data to validate the trigger. These are described here:

- *L1EmtBEPBBeginMacro, L1EmtBEPBEndMacro, L1EmtBEPBBeginMinor, L1EmtBEPBEndMinor:* These are classes as with the FEX corresponding classes are used purely to attach the correct sub actions. In this case the BEPBL1Accept.

- *L1EmtBEPBL1Accept:* Since the backend playback memories are after the stage where the DAQ data can be written out then it is unnecessary to have a fire method that runs any code. This class has an empty method implemented.

- *L1EmtFEPBBeginMacro, L1EmtFEPBEndMacro, L1EmtFEPBBeginMinor, L1EmtFEPBEndMinor:* As with the BEPB classes these are again used just for attaching the correct L1Accept action to the finite state machine.

- *L1EmtFEPBL1Accept:* Since the playback buffers are of limited size then it is necessary to synchronise the StartPlayback function with the L1ccept. The design is such that every nth time the L1A is called the StartPlayback is issued, the idea being to run with the GLT triggering on M and on the 1Hz random trigger. The random trigger will therefore issue the first L1Accept which then causes a StartPlayback to be issued, to stop a high rate loop within the system the next start playback is then delayed until certain number of random L1Accepts have been issued. The cycle is then repeated.

The data from the EMC system is fed into a dual port memory buffer. As such it can be read and written to at the same time. This is undesirable and to prevent this a calibration has been designed to check for this condition. With the data a frame bit is sent down a separate twisted pair. This must not occur on the same clock pulse as the TPB frame bit. This results in a situation where the same bit can be read/written to in the memory. This calibration is slightly different to the rest since one of the values that are being altered are contained within the EMC UPC configuration data. The operation of the calibration is as follows:

- *L1EmtFCBeginMacro:* This class creates the special calibration system xtc in memory. It also builds the final L1EmtFCData object which will hold the values of the frameoffset and synchDelay which are best to avoid the frameclash condition. The next action is also appended.

- *L1EmtFCBeginMajor:* This class iterates through the value of the Fcx synchDelay. The calibration xtc is passed through this class and a copy of the synchDelay is copied into it.

- *L1EmtFCBeginMinor:* In the corresponding class within the EMC cycle setup the frame bit is iterated through its full range of 16 values. This class attaches a configurable number of L1Accepts. Within this class the value of the frameoffset as copied into the configuration xtc is know through the number of times that the cycle configure function has been called. The the xtc is then transmitted onto the appended L1Accept object.

- *L1EmtFCL1Accept:* The L1Accept class for this calibration is used to read the CSER from each board in turn using the L1EmtFCIterator class. The error register is read and copied into the calibration xtc arrays.

- *L1EmtFCEndMinor:* This class is used to copy the data contained within the calibration xtc into another type of container. This can be used to progress down the configuration tree. For each instance of the value of the frameoffset the saved data is only copied into the accumulated addxtc. These classes of containers are used within the calibration system for storing the raw calibration information.

- *L1EmtL1AcceptIterator:* This iterator is used to iterate over the error registers from each TPB and transfer this data into the calibration xtc's.

- *L1EmtFCEndMajor:* The end macro cycle repeats what was done during the End Minor cycle except this time for the synchDelay cycles. The addxtc's produced for each EndMinor cycle are accumulated for each synchDelay value and then copied into another addxtc. This class also analyses the data and copies the results to a calibration ScatChan.

- *L1EmtFCEndMacro:* This class is used to create an object of type L1EmtFCErrors into which the accumulated value of both frameoffset and synchDelay are put for the combination which gives the lowest occurrence of cable errors.

- *L1EmtFCIterator:* The iterator class is used by both the EndMinor and EndMajor class to iterate over the addxtc's produced by each of the TPB's present in the system.

Several calibrations use alterations to the tower input mask. The most important of these is the Tower calibration. This allows the physical interconnection with the EMC to be checked when using the set pattern output of the EMC UPC's as well as system noise when reading directly from the front end electronics.

- *L1EmtTCALBeginMacro:* This class contains the code which alters the mask as loaded in the singleton. This is then transferred onto the boards. The actual change occurring is that for the first 100 L1Accepts the mask is set to only readout from θ=0, this is then iterated through the range in θ every 100 L1Accepts.

- *L1EmtTCALEndMacro:* This class is built just to connect the correct non-default action onto the finite state machine.

- *L1EmtTCALBeginMinor:* To allow the configuration mask to be reset the system must be set to configuration mode. This class then resets the mode to run to allow data taking. The standard L1Accept action is attached. This can be set to allow a configurable number of L1Accepts to be added.

- *L1EmtTCALEndMinor:* The End minor action for this calibration resets the system state to configure mode to allow the BeginMacro action to change the input mask.

  The Phi calibration is used to check the connection between the EMT & GLT. With the overall trigger mask set to take triggers resulting from the EMT system then the output of the GLT should exactly match the input mask loaded. The synchronised systems then run changing the ϕ sectors unmasked every set number of L1Accepts passed.

- *L1EmtPHICALBeginMacro, L1EmtPHICALEndMinor:* Unlike the tower calibration the usage of these classes is just to ensure the correct connection of the next transition to the FSM.

- *L1EmtPHICALBeginMinor:* This transition for the ϕ calibration contains both the code to change the input mask as well as the resetting of runmode. For the the input mask setting the following configuration is setup. For the first 400 events the mask is set so that a single ϕ sector is unmasked which rotates around the input channels with 10 L1Accepts per sector. The next 200 events have 2 directly opposite sectors unmasked. A standard L1Accept is appended to this action so that the data is read into standard output tagged containers.

- *L1EmtPHICALEndMacro:* This class as with the TCALEndMinor class changes the system state back to configure mode to allow the input mask to be changed.

The idea behind the FcX calibration was to monitor the system response to a change in the synchDelay variable within the FcX configuration data. There are 16 possible values for this and so 10 L1Accepts are taken for each value.

- *L1EmtFCXCALBeginMacro, L1EmtFCXCALEndMacro:* Again these classes are needed to attach the correct Minor cycle action.

- *L1EmtFCXCALBeginMinor:* This class holds the code used to iterate over the different values of the synchDelay as well as reseting the system back to runMode to allow L1Accepts to be taken. As with other calibrations of this type the standard L1Accept action is used.

- *L1EmtFCXCALEndMinor:* This again sets the system back into configureMode to allow resetting of the synchDelay.

As described in section 5.4.1 for the development of the prototype TPB's there were many diagnostic tests developed to run from the VxWorks command line. The Board Test calibration was developed to allow these to again be run but from within the dataflow finite state machine. This would quickly automate the process of failure detection. The operation of each of these tests is given in more detail in above section.

- *L1EmtBTBeginMacro:* VmeTest. This test must be setup to operate first within the chain since the rest of the tests all depend on the VME readout being reliable. These tests are setup so that should one fail then the sequence will terminate.

- *L1EmtBTBeginMajor* SpeedTest. The necessity for the system to be able to handle odfInjects very close together is shown especially when the L1Accepts are being sent at 2kHz.

- *L1EmtBTBeginMinor:* OpSaTest. The correct response of the system to the injects when sent to different subAddress is especially necessary when loading the different configuration constants and then reading them back.

- *L1EmtBTEndMacro, L1EmtBTEndMajor, L1EmtBTEndMinor:* These classes as with many other End actions are attached in unison with their respective Begin actions.

During the development of the new version of the output tagged containers it was necessary to run with 2 copies of the tagged containers being written, one each of the old and new versions for comparison.

- *L1EmtTCBeginMacro, L1EmtTCEndMacro, L1EmtTCBeginMinor, L1EmtTCEndMinor:* These classes are again used to connect the correct L1Accept action to the FSM.

- *L1EmtTCL1Accept:* This class actually does both the construction of the old version of the output TaggedContainer objects as well as the new containers. These are given totally different type identification numbers so that they can be compared offline.

- *L1EmtCalSegTest:* This code builds at the segment level of dataflow and is called by the startup script. Its firstly calls the L1EmtReset action to initialise the system and then attaches the CalConfig and BeginRun actions to the FSM. The actions of actually triggering the Reset action attaches the FSM created within the system ROM to the main dataflow FSM.

- *L1EmtCalOdfTemplates:* As with any online built package this file holds explicit declarations of the templates that are used within this package.

- *TestEmtCycles:* During development of the code it was necessary to have a means of testing the system behaviour during the transition from the non-action based FSM to the calibration code based actions classes. As such this small Unix/VxWorks files was used to create an initial VxWorks process to run the system.

A.5 L1EmtSpy

Contains the code that is used to sample the input data fed into the boards and apply a software simulation of the algorithm design to it to generate its own set of outputs. These are then periodically checked during runtime. Currently this requires an expert to view text-files created when the system finds an error present.

- *L1Emt:* This class defines all the common definitions of structures used within the EMT simulation. It contains the enumeration for the global maps as well as defining the array space used to store these objects.

- *L1EmtAxSim:* This class contains all the code which collects the output from various sub classes to construct an object which accurately duplicates the Xilinx algorithm for performing the trigger processing. It contains all aspects of the functionality of the algorithm as defined in the hardware system.

- *L1EmtAxSimParms:* The algorithm running in hardware is supplied with a set of configuration constants. This class is used to interface between the configuration data as stored within the configuration database and the simulation and then store it in a way compatible for the simulation.

- *L1EmtDaqSector:* This class contains the code for construction of the trigger sums before nearest neighbour addition. It contains all the theta discriminator functionality.

- *L1EmtHistory:* This class is a wrapper for already processed data and the input that generated it. It stores data of type L1EmtTowerSumHistory.

- *L1EmtTowerSumHistories:* This class contains tower sum information already processed.

- *L1EmtSpyApp:* This is an interface for running the simulation code within VxWorks. It initially loads the configuration constants held within L1EmtAxSimParam into a newly created L1EmtTpbCrate object running within the spy framework. The tower sum histories are then read from their objects and run through the simulation. The results are the L1EmtSpySector objects of which there are 40, these are then compared with the actual algorithm output for errors.

- *L1EmtSpySector:* Objects of this class actually contain the ϕ sum data after processing.

- *L1EmtSpyTemplates:* As with all other packages that are built within the online makefile system this file contains all the templates that are used within the package explicitly defined.

Glossary

ADC Analogue to Digital Converter

ADB Analogue to Digital Board

CMOS C Metal Oxide Silicon

DCH Drift Chamber

DCT Drift Chamber Trigger

DFB DIRC Front-end Boards

DIRC Detector of Internally Reflected Cherenkov radiation.

EMC ElectroMagnetic Calorimeter

FADC Fast Analogue to Digital Converter

GLT Global Level-1 Trigger

HER High Energy Ring

IFR Instrumented Flux Return

IFT Instrumented Flux return Trigger

IP Interaction Point

LER Low Energy Ring

PMT Photo Multiplier Tube

ROM Read Out Module

SVT Silicon Vertex Tracker

TDC Time to Digital Converter

TPB Trigger Processor Board

UPC Untriggered Personality Card, Type of readout module used exclusively by the EMC

References

[1] Final Design Report The BaBar Collaboration (March, 1995)

[2] K. Lande *et al. Phys. Rev.* , **D103**(1956):1901

[3] M. Gell-Mann & A. Pais. *Phys. Rev.* 97(1955):1387

[4] J. H. Christenson, J.W. Cronin, V.L. Fitch and R. Turlay, *Phys. Rev. Lett.* **13** (1964) 138.

[5] C. Caso et al., Review of Particle physics,*Eur. Phys. J.*, **C3**(1998)

[6] M. Neubert. B Physics and *CP* violation *Int. Jour. Mod. Phys.* , A11(1996):4173 - 4240

[7] M. Kobayashi and T. Maskawa, Prog. Theor. Phys. **49**, No. 2 652

[8] N. Cabbibo, *Phys. Rev. Lett.* **10**, 531 (1963)

[9] M. Kobayashi and T. Maskawa, Prog. Th. Phys. **49** (1973) 652.

[10] L. L. Chau and W. Y. Keung, *Phys. Rev. Lett.* ,**53**, 1802(1984)

[11] C. Jarlskog. *Phys. Rev. Lett.* ,55(1985):1039

[12] L.Wolfenstein, Phys. Rev. D. **39** No. 9 2381 and Phys. Rev. Lett. **51** 1945

[13] D.E. Groom,*Eur. Phys. J.*, **C15**, 1 (2000)

[14] H. Abele *et al.*, *Phys. Lett.* , **B407**, 212 (1997):
J.Reich *et al.*, ILL Worksop, October 1998:
E. Bopp *et al.*, *Phys. Rev. Lett.* , **56**, 919 (1986):
P. Liaud, *Nucl. Phys.* , **A612**, 53 (1997)

[15] C. Sbarra, talk at the *Rencontres de Moriond, Les Arcs, Savoie, France*, March 11-18 2000

[16] R. Alexsan, B. Kayser, and D. London, *Phys. Rev. Lett.* **73**, 18 (1994)

[17] J.P. Silva, G.C. Branco & L. Lavoura, *CP* violation, Chapter18. Oxford Uni Press, 1999.

[18] D. Boutigny *et al.* The *BABAR* collaboration, "Physics at the *BABAR* experiment", eds P. F. Harrison and H. Quinn

[19] Y. Nir and Helen R. Quinn, Ann. Rev. Nucl. Part. Sci. **42** (1992) 211

[20] *B* Factories: The State of the Art in Accelerators, Detectors and Physics, ed. D. Hitlin, SLAC-400 (1992)

[21] P.Odddone, in *Proceedings of the UCLA Workshop: Linear Collider B $\bar{B}$ Factory Conceptual Design*, edited by D. Stork, World Scientific (1987), p243.

[22] S. Henderson, CLNS 97/1528, (1997)

[23] PEP-II, An Asymmetric *B*-Factory, Conceptual Design Report, SLAC-418/LBL-PUB-5379/CALT-68-1869/UCRL-ID-114055/UC-IRPA-93-01

[24] D. Boutigny *et al.*, The *BABAR* Collaboration, Letter of Intent, SLAC-443 (1992)

[25] F. LeDiberder, "Precision on *CP* violation measurements and requirements on the vertex resolution", *BABAR Note* # 34, 1990

[26] J. D. Richman. The *BABAR* Silicon Vertex Tracker. *Nucl. Instr. and Methods* **A409** 1998

[27] R. Johnson *et al*, "Silicon Vertex Detector Readout Chip (Target Design Specifications)," *BABAR* Note # 214 (1995)

[28] G. Sciolla *et al*, The *BABAR* Drift Chamber, *Nucl. Instr. and Methods* **A409** 310 (1998)

[29] J. Albert *et al.* Electronics for the *BABAR* central drift chamber. (1998). IEEE 1998 Nuclear Science Symposium (NSS) and Medical Imaging Conference (MIC), Toronto, Ontario, Canada, 8-14t Nov, 1998.
D. Coupal et al. The *BABAR* drift chamber electronics group, Drift Chamber technical note TNDC-97-68 v4.0.

[30] B. N. Ratcliff, SLAC-PUB-5946 (1992); P. Coyle *et al*, *Nucl. Instr. Methods A* **A343**, 292 (1994)

[31] D. Boutigny *et al.*, The *BABAR* Collaboration, The *BABAR* Technical Design Report, SLAC-R-95-457 (1995)

[32] J. Dowdell, *BABAR* Calorimeter DAQ system overview (*BABAR* Calorimeter internal note, August 1997), J. Dowdell, *BABAR* Calorimeter DAQ ADC Board Description, (*BABAR* Calorimeter internal note, May 1997), G. M. Haller and D. R. Freytag, "Analogue Floating Point BiCMOS Sampling Chip and Architecture of the *BABAR* CsI Calorimeter Front End Electronics System at the SLAC B-Factory", *BABAR Note* # 285

[33] R. Bernet *et al*, "Callibration and monitoring for the *BABAR* Calorimeter," *BABAR* Note # 363

[34] P. Clark, *BABAR Light Pulser System*, D. Phil Thesis, University of Edinburgh, 2000.

[35] F. Anulli *et al*, The Muon and Neutral Hadron Detector for *BABAR*. *Nucl. Instr. and Methods* **A409** 542 (1988)

[36] R. Santonico and R. Cardarelli, *Nucl. Instr. Methods A* **187** (1981), R. Cardarelli *et al. Nucl. Instr. Methods A* **263** (1988)

[37] See for example L. Antonazzi *et al.* (E771 collaboration), *Nucl. Instr. Methods A* **315** 92 (1992) , C. Bacci *et al.* (RD 5 collaboration) *ibid.* 102, A. Anotelli *et al.* (FENICE collaboration), *Nucl. Instr. Methods A* **337** 34 (1993)

[38] A. Boyarski *et al.*, *BABAR Note* # 514 (2000)

[39] N. Dyce *et al.*, The *BABAR* Trigger Group, "The *BABAR* Trigger System Design Requirements", V4.00 (1997)

[40] S. Gehrig, "Design and Simulated Performance of the Level 1 Trigger System", *BABAR Note* # 380 (1997)

[41] F.A. Kirsten *et al*, *BABAR* Level 1 Drift Chamber and Global Trigger Implementation, 1998

[42] D. Piccolo. The IFT Level 1 Trigger System, *BABAR*Note # 420

[43] E. Frank *et al*, Architecture of the *BABAR* Level 3 Software trigger, *BABAR* Note # 463 (1998)

[44] M. Huffer, For the Dataflow group, *BABAR* Data Aquisition, 1997

[45] I. Scott, Private Communication, September 1997

[46] Motorola Computer Group division of Motorola, Inc., 2900 South Diablo Way, tempe, AZ 85282, USA.

[47] Sun Microsystems, Inc., 901 San Antonio Rd., Palo Alto, CA 94303, USA.

[48] The VxWorks RTOS & Tornado Development interface are products of Wind River Systems, Inc., 1010 Atlantic Ave., CA 94501-1153, USA.

[49] P. Grosso, Reverse Dataflow and Late Binding, *BABAR* Collabporation Talk, Oct 1998

[50] Raw Data flow management in OEP, http://www.slac.stanford.edu/BFROOT/www/Computing 970828/OEPRawData.html .

[51] P. Dauncey *et al*, BaBar Level 1 Calorimeter Trigger Design

[52] S. Galagedera, Functional Description of the EMC Trigger Processor Board, Iss 1.1, 13/6/98

[53] Level 1 Calorimeter Trigger Energy Selection Processor Algorithm, J Andress, *BABAR Note* # 508

[54] Viewlogic FPGA Design Software, Innoveda Inc., 293 Boston Post Road West, Marlborough, MA 01752, USA

[55] A. Mass, Fast Control Xilinx Users Manual, V1.0, 1998

[56] S. Galagedera, Functional Description of the Formatter Xilinx, Iss 1.2, 14/6/98

[57] S. Galagedera, Functional Description of the VME Xilinx (Vx), Iss 1.1, 9/6/98

[58] J. Dowdell, *BABAR* EMC DAQ System, WWW Page from EMC electronics homepage at SLAC.

[59] S. Nash, Private Communication.

[60] G. Booch, Object Oriented Analysis and Design (2nd Edition), Addison-Wesley, California, 1994

[61] The Objectivity Database, Object Orientated Database Product supplied by Objectivity Inc., Mountainview, California.

[62] J.D. McFall and D. Wallom, L1 EMT Online Help, http://www.slac.stanford.edu/BFROOT/www/detector/Trigger/emt/software/emtOnline.html .

[63] P. Mcgrath, FrameClash Calibration, WWW page off *BABAR* Trigger homepage at SLAC.

[64] R.T. Hamilton, DAQ Programmers Guide, V1.1, 1997

[65] P. Dauncey, Test Results of Level 1 Calorimeter Trigger Prototype, 1998

[66] Java Analysis Studio Homepage, http://www-sldnt.slac.stanford.edu/jas/

[67] N. Chevalier, EMT Efficiency Study, http://www.slac.stanford.edu/∼phnic/EMTefficiency.html

[68] Y. Kubota et al. (The CLEO Collaboration), *Nucl. Instr. Methods A* **320** 66 (1992)

[69] J. Back, "Track cluster matching for the Electromagnetic Calorimeter using Detector Model", *BABAR Note* # 440 and "Track cluster matching for the Electromagnetic Calorimeter using a Simple Model", *BABAR Note* # 439

[70] J. Tinslay, Photon ID, *BABAR* April 1999 Collaboration Meeting, 1999

[71] *BABAR* Analysis Document # 20, Reconstruction of π^0 in *BABAR*.

[72] D. Antreasyan, "An algorithm for tagging photon and merged π^0 showers in the crystal ball", Crystal Ball note 321, 1983

[73] P. F. Harrison, "Consistencies: definition and usage", Internal *BABAR* physics note, 1997

[74] K. Flood, http://www.slac.stanford.edu/∼kflood/MergedPi0PID.ps

[75] C. Touramanis, The WalkFitter for K_s^0, Private Communication.

[76] D Hitlin, First Physics Results From Babar, 30th International Conference On High Energy Physics, Osaka, Japan. 31/07/2000.

[77] *BABAR* Analysis Document #139, Measurement of Inclusive production of Charmonium Final States in B meson Decays,

[78] *BABAR* Analysis Document #90, Cut based Electron Identification.

[79] *BABAR*Analysis Document #60, Muon Identification in the *BABAR* Experiment.

[80] R. Faccini. Vertexing/Kinematic Fitting User's Guide. WWW page at SLAC.

[81] *BABAR* Analysis Document # 134, Measurement of the number of $\Upsilon(4s)$ Mesons Produced in Run 1.

[82] *BABAR* Analysis Document # 157, Measurement of the GoodTrackLoose efficiency using SVT tracks.

[83] *BABAR* Analysis Document # 113, Measurement of Branching Ratios of Charged and Neutral B Mesons into Exclusive Charmonium States.